
Measurement of Branching Ratios
and CP Asymmetries for the decays

$$B^0 \rightarrow \pi^+ \pi^-$$

$$B^0 \rightarrow K^+ \pi^-$$

$$B^0 \rightarrow K^+ K^-$$

Kolja Andreas Prothmann



München 2012

Measurement of Branching Ratios
and CP Asymmetries for the decays

$$\mathbf{B}^0 \rightarrow \pi^+ \pi^-$$

$$\mathbf{B}^0 \rightarrow \mathbf{K}^+ \pi^-$$

$$\mathbf{B}^0 \rightarrow \mathbf{K}^+ \mathbf{K}^-$$

Kolja Andreas Prothmann

Dissertation
an der Fakultät für Physik
der Ludwig-Maximilians-Universität
München

vorgelegt von
Kolja Andreas Prothmann
aus München

München, den 19.12.2012

Erstgutachter: Prof. Dr. Christian Kiesling

Zweitgutachter: Prof. Dr. Jochen Schieck

Tag der mündlichen Prüfung: 30.1.2013

Contents

1	Introduction	1
2	<i>CP</i> Violation in the Standard Model	7
2.1	The Standard Model of Particle Physics	7
2.2	The CKM Matrix and the Unitarity Triangle	13
2.3	$B^0\bar{B}^0$ Mixing	14
2.3.1	Time Evolution of the neutral B Meson	15
2.3.2	Types of CP Violation	17
2.3.3	Coherent $B^0\bar{B}^0$ Mixing	20
2.4	CP violation in B Decays into light Hadrons	22
2.4.1	CP violation in $b \rightarrow u\bar{d}$ Transitions	22
2.5	Determination of ϕ_2 using Isospin correlated $B \rightarrow \pi\pi$ decays	24
2.5.1	CP violation in $b \rightarrow sud$ transitions	27
2.6	Searches on Physics beyond the Standard Model in $B^0 \rightarrow K\pi$ Decays	28
2.7	The Decay $B^0 \rightarrow K^+K^-$	29
2.8	Theory Predictions on Branching Fractions and CP Parameters	29
2.9	Current Status of the Experimental Measurements	31
3	The Belle Experiment	35
3.1	The KEKB Accelerator	35
3.2	The Belle Detector	36
3.2.1	The Beam Pipe	38
3.2.2	The Silicon Vertex Detector	38
3.2.3	The Central Drift Chamber (CDC)	42
3.2.4	The Aerogel Cherenkov Counter (ACC)	44
3.2.5	The Time of Flight Counter (TOF)	46
3.2.6	The Electromagnetic Calorimeter (ECL)	47
3.2.7	The Solenoid Magnet	49
3.2.8	The K_L^0 and Muon Detector (KLM)	50
3.3	Trigger and Data Acquisition	51
4	Analysis of $B^0 \rightarrow h^+h^-$	57

4.1	Introduction to the Technique of a “Blind Analysis”	57
4.2	Data Set	60
4.3	Event Selection	61
4.3.1	Track Selection	61
4.3.2	Analysis Window	62
4.3.3	Vertexing and Tagging	62
4.3.4	Continuum Discriminating Variables	64
4.3.5	Time Dependent Event Selection	69
4.3.6	Detection Efficiency	69
4.4	Data Models	70
4.4.1	Signal $B^0 \rightarrow \pi^+\pi^-$	70
4.4.2	Signal $B^0 \rightarrow K^+\pi^-$	76
4.4.3	Signal $B^0 \rightarrow K^+K^-$	82
4.4.4	Continuum Background	87
4.4.5	Background from charmless B^+B^- decays	94
4.4.6	Background of charmless $B^0\bar{B}^0$ decays	100
4.5	Full Data Model - all Components combined	105
4.6	Study of Fit Biases	108
4.6.1	Pseudo-Experiment Setup	108
4.6.2	Fit Results and Pull Distributions	109
4.6.3	Interpretation	114
4.6.4	Possible Sources of the Fit Biases	114
5	Differences between Monte-Carlo and Data	117
5.1	Control Sample Measurement	117
5.1.1	Control Sample $B \rightarrow D\pi, D \rightarrow K\pi$	117
5.1.2	Event Selection	118
5.1.3	Data Model	118
5.1.4	Fit of $D\pi$ Model to the Control Sample	132
5.2	Corrections to the Particle Identification	135
6	Results from $B^0 \rightarrow h^+h^-$	141
6.1	Measurement of $B^0 \rightarrow h^+h^-$ from the full Data Sample	141
6.1.1	Box Opening	141
6.1.2	Comparison with previous Results	144
6.2	Estimation of Systematic Uncertainties	161
6.2.1	Number of $B\bar{B}$ pairs	161
6.2.2	Tracking Systematics	161
6.2.3	IP Profile	161
6.2.4	Selection Criteria of the B -tagging Algorithm	162
6.2.5	Track Helix Error	162
6.2.6	Δt Selection	162
6.2.7	Vertex Quality	162

6.2.8	Δz Bias	163
6.2.9	Misalignment	163
6.2.10	Physics Parameters	163
6.2.11	Data/MC Shape	163
6.2.12	Δt Resolution Function	164
6.2.13	Flavour Tagging	164
6.2.14	Parametric Shape	164
6.2.15	Non-parametric Shape	164
6.2.16	Fit Bias	165
6.2.17	Tag-side Interference	165
6.2.18	Discussion of the Contributions of the total Systematic Error	166
6.3	Upper Limit Calculation for $B^0 \rightarrow K^+K^-$	169
6.4	Results from Isospin Analysis of $B \rightarrow \pi\pi$	171
6.5	Results from the $K\pi$ Sum Rule	175
7	Summary and Outlook	177
A	Toy Monte-Carlo Plotting Method	181
B	Flavour Tagging	183
B.1	Track-Level Flavour Tagging	183
B.1.1	Slow Pion Category	183
B.1.2	Lambda Category	184
B.1.3	Kaon Category	185
B.1.4	Lepton Category	185
B.2	Event-Level Flavour Tagging	185
B.2.1	Flavour Tagging Performance	186
C	Δt Resolution Function	189
C.1	Detector Resolution	189
C.2	B_{Tag} Vertex Smearing from Non-Primary Tracks	190
C.3	Kinematic Approximation	191
C.4	Outlier	193
C.5	Combined Resolution Function	194
D	Parameters of the Fit Model for all Components	195

Zusammenfassung

Diese Doktorarbeit stellt eine Messung der Verzweungsverhältnisse und CP Parameter der Zerfallskanäle $B^0 \rightarrow \pi^+\pi^-$, $B^0 \rightarrow K^+\pi^-$ und $B^0 \rightarrow K^+K^-$ vor. Der gesamte Belle Datensatz mit 772 Millionen $B\bar{B}$ Paaren wird untersucht. Die $B\bar{B}$ Paare wurden am KEKB e^+e^- Speicherring bei einer Schwerpunktsenergie, die der Masse der $\Upsilon(4S)$ Resonanz entspricht, erzeugt.

Die Analyse liefert folgende Ergebnisse für die Verzweungsverhältnisse

$$\begin{aligned}\mathcal{B}(B^0 \rightarrow \pi^+\pi^-) &= (5.63 \pm 0.16(\text{stat}) \pm 0.16(\text{syst})) \times 10^{-6}, \\ \mathcal{B}(B^0 \rightarrow K^\pm\pi^\mp) &= (18.71 \pm 0.25(\text{stat}) \pm 0.37(\text{syst})) \times 10^{-6}, \\ \mathcal{B}(B^0 \rightarrow K^+K^-) &< 14 \times 10^{-8} \text{ at } 90\% \text{ CL}.\end{aligned}$$

Für die CP -Asymmetrien ergeben sich folgende Werte

$$\begin{aligned}\mathcal{A}_{CP}(B^0 \rightarrow \pi^+\pi^-) &= 0.33 \pm 0.06 (\text{stat}) \pm 0.03 (\text{syst}), \\ \mathcal{S}_{CP}(B^0 \rightarrow \pi^+\pi^-) &= -0.64 \pm 0.08 (\text{stat}) \pm 0.03 (\text{syst}), \\ \mathcal{A}_{CP}(B^0 \rightarrow K^\pm\pi^\mp) &= -0.061 \pm 0.014 (\text{stat}) \pm 0.008 (\text{syst}),\end{aligned}$$

wobei die Parameter \mathcal{A}_{CP} und \mathcal{S}_{CP} jeweils die direkte und die durch Mischung induzierte CP Verletzung messen. Unsere Ergebnisse schließen einen Winkel ϕ_2 des Unitaritätsdreiecks zwischen 23.8° und 66.8° mit einer Signifikanz von 1σ aus. Eine Modell unabhängige Suche nach neuer Physik beim Zerfall von $B^0 \rightarrow K^+\pi^-$ zeigt eine kleine Abweichung vom Standardmodell von $-0.289 \pm 0.139(\text{stat}) \pm 0.064(\text{syst})$ mit einer Signifikanz von 1.9σ .

Abstract

We present measurements of the branching fractions and CP violation parameters for the decay channels $B^0 \rightarrow \pi^+\pi^-$, $B^0 \rightarrow K^+\pi^-$ and $B^0 \rightarrow K^+K^-$. The final Belle dataset of 772 million $B\bar{B}$ pairs produced at the $\Upsilon(4S)$ resonance at the KEKB asymmetric-energy e^+e^- collider is used. For the branching fractions, we obtain

$$\begin{aligned}\mathcal{B}(B^0 \rightarrow \pi^+\pi^-) &= (5.63 \pm 0.16(\text{stat}) \pm 0.16(\text{syst})) \times 10^{-6}, \\ \mathcal{B}(B^0 \rightarrow K^\pm\pi^\mp) &= (18.71 \pm 0.25(\text{stat}) \pm 0.37(\text{syst})) \times 10^{-6}, \\ \mathcal{B}(B^0 \rightarrow K^+K^-) &< 14 \times 10^{-8} \text{ at } 90\% \text{ CL}.\end{aligned}$$

For the CP -asymmetries, we obtain following values:

$$\begin{aligned}\mathcal{A}_{CP}(B^0 \rightarrow \pi^+\pi^-) &= 0.33 \pm 0.06 (\text{stat}) \pm 0.03 (\text{syst}), \\ \mathcal{S}_{CP}(B^0 \rightarrow \pi^+\pi^-) &= -0.64 \pm 0.08 (\text{stat}) \pm 0.03 (\text{syst}), \\ \mathcal{A}_{CP}(B^0 \rightarrow K^\pm\pi^\mp) &= -0.061 \pm 0.014 (\text{stat}) \pm 0.008 (\text{syst}),\end{aligned}$$

where \mathcal{A}_{CP} and \mathcal{S}_{CP} represent direct and mixing-induced CP violation, respectively. For the CP -violating weak phase ϕ_2 we exclude the region $23.8^\circ < \phi_2 < 66.8^\circ$ at the 1σ level. A model independent test of new physics using a sum rule in the $K\pi$ system yields a mild deviation from the standard model of $-0.289 \pm 0.139(\text{stat}) \pm 0.064(\text{syst})$ with a 1.9σ significance.

Chapter 1

Introduction

Astrophysical observations show that the universe today consists entirely out of matter. According to the Big Bang theory [1, 2], equal amounts of matter and antimatter were created initially. Without an asymmetry in particle and antiparticle production or decays, they should either have annihilated each other leaving the universe composed only of photons and neutrinos. Alternatively, one can imagine an Anti-Universe, made of antimatter. But this Anti-Universe would have to coexist spatially separated since we do not observe any hints for matter anti-matter annihilation. While this latter possibility seems quite artificial, the exact mechanism that created the presently observed matter dominance in the universe is still unknown. In the Big Bang model the universe starts with a very high energy density and expands. Because of this expansion the energy density shrinks. In current particle accelerator and collider experiments, we can reach an energy density corresponding to that at 1×10^{-10} s after the Big Bang. Particle physics is a good model for the history of the universe from 1×10^{-10} s until the present (Fig. 1.1). But how can we obtain a matter antimatter asymmetry? The Russian physicist, Andrei Sakharov, postulated in 1967 [3] that there are three necessary conditions that must be fulfilled to produce matter and antimatter at different rates. The baryon number must not be conserved and the universe must be in a state out of a thermal equilibrium. But most important for our searches is that the symmetry of the C and CP operator must be violated. But what does CP violation mean? There are three fundamental discrete symmetry operators, \mathbf{C} , \mathbf{P} , \mathbf{T} , that can be applied on a quantum mechanical state. The charge conjugate operator, \mathbf{C} , basically transforms a particle into its anti-particle. The parity operator, \mathbf{P} , and the time reversal operator, \mathbf{T} , change the 4-vector of a particle. The operator \mathbf{P} transforms $(x, t) \rightarrow (-x, t)$, which is a mirroring around the origin, while the operator \mathbf{T} transforms $(x, t) \rightarrow (x, -t)$. If a process is equal before and after applying one of the operators, then the process conserves the corresponding symmetry. Every Lorentz invariant quantum field theory conserves the combined \mathbf{CPT} symmetry [5].

Historically the violation of \mathbf{C} or \mathbf{P} or \mathbf{CP} symmetry in elementary reactions was not expected. Historically the $\theta - \tau$ puzzle was the first hint of parity violation. A particle, τ ,

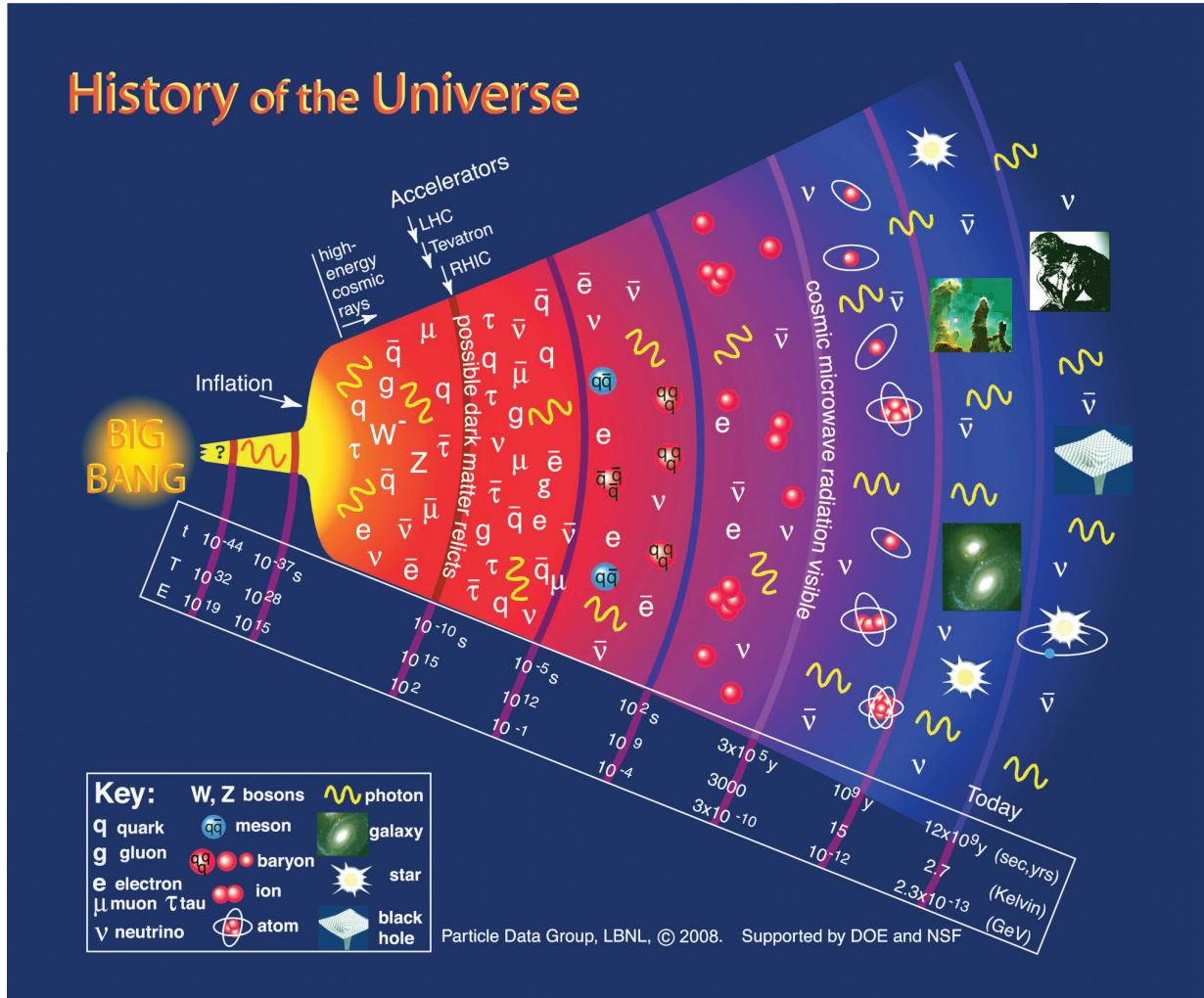


Figure 1.1: History of the universe in the Standard Model of cosmology [4].

decaying into three pions was observed in cosmic rays. The parity of the pion is known to be -1 . Therefore the parity of the τ particle is calculated to be $(-1)(-1)(-1) = -1$. Another particle, θ , was observed to decay into two pions, which consequently had to have a parity of $(-1)(-1) = 1$. The puzzle is the fact that θ and τ had the same mass and lifetime but because of their different parity could not be the same particle. Two theoretical physicists Lee and Yang questioned parity conservation in weak interaction in 1956 [6]. The $\theta - \tau$ puzzle is resolved as the θ and τ can be the same particle which is nowadays called K^0 . Lee and Yang also suggested an experiment to test parity using Co^{60} atoms.

In 1957, Wu *et al.* [7] indeed observed parity violation in the decay of $\text{Co}^{60} \rightarrow \text{Ni}^{59} + e^- + \bar{\nu}_e$. The experimental setup involved a sample of Co^{60} with aligned spins and detection of the decay products. It was observed that almost all electrons were emitted opposite to the spin direction. If one applies the \mathbf{P} operator to this reaction, the space but not the spin

direction of the atom is mirrored. Then, in the new coordinate system, the electrons will be emitted in the opposite direction. This means that the physical law is not invariant under \mathbf{P} transformation in this process. Later, this was explained by the weak force which only couples to left-handed particles and right-handed-antiparticles. Therefore, \mathbf{C} is also maximally violated as a massless right-handed particle does not couple to the weak force after \mathbf{C} transformation when it becomes a left-handed antiparticle. After the shock of observing that \mathbf{C} and \mathbf{P} symmetry are not preserved in elementary processes, the idea that the combined symmetry CP seemed to be conserved appealed to physicist sensibilities. But only a few years later, in 1964, small deviations to a perfect CP symmetry were observed at the level of $\epsilon \approx 2.3 \cdot 10^{-3}$ [8]. This corresponds to a difference of the decay rates of

The Standard Model [9–11] is our currently best theory of particle physics. With a small set of elementary particles and force carriers, it can describe all elementary processes except gravity with good accuracy up to the currently reachable energy. In the Standard Model, the source of CP violation is a mixing matrix that describes the mixture of quantum mechanical flavour and mass eigenstates, the so called Cabibbo-Kobayashi-Maskawa (**CKM**) matrix [12]. In 2008, the Nobel Prize was awarded to Kobayashi and Maskawa for this discovery which predicted 3 generations of quarks and CP violation which was proven by the B -factory experiments Belle and BaBar. The amount of CP violation predicted by the Standard Model, however, is much too small to explain the lack of anti-matter in the universe [13]. Thus we are looking for new sources of CP violation beyond the Standard Model that could explain the matter asymmetry. These new sources are likely to show up as deviations from the predictions of the Standard Model.

One way to find deviations from the Standard Model is to test the unitarity of the **CKM** matrix. If the **CKM** matrix is not unitary, the theory does not conserve total probability and can therefore be basically falsified. The unitarity condition can be visualized as a triangle in the complex space (Fig. 1.2). By measuring the sides and angles of the triangle independently we can overconstrain the triangle and look for “tensions”. These tensions may be a hint for new physics beyond the Standard Model.

The Standard Model predicts the largest CP violation in the decay of B mesons. To make precision measurements of B decays, two “B-factories” were built. BaBar at the PEP storage ring in Stanford, USA, and the Belle experiment at the KEKB storage ring in Tsukuba, Japan. The KEKB storage ring is the world record holder on both instantaneous luminosity ($2.11 \times 10^{34} \text{ cm}^{-2} \text{ s}^{-1}$) and integrated luminosity (1 ab^{-1}). We have the unique possibility to analyse the final data set of Belle.

There are several ways of measuring CP violation at B-factories: A difference in the decay rates of B mesons and \bar{B} mesons to a specific final state is called direct CP violation, which constrains the sides of the unitarity triangle. Quite challenging is the measurement of a time-dependent difference in the decay rates of B mesons and \bar{B} mesons. This mixing-induced CP violation can be observed even in the absence of direct CP violation.

The analysis which is presented in this thesis focusses on $B \rightarrow h^+h^-$ decays where the

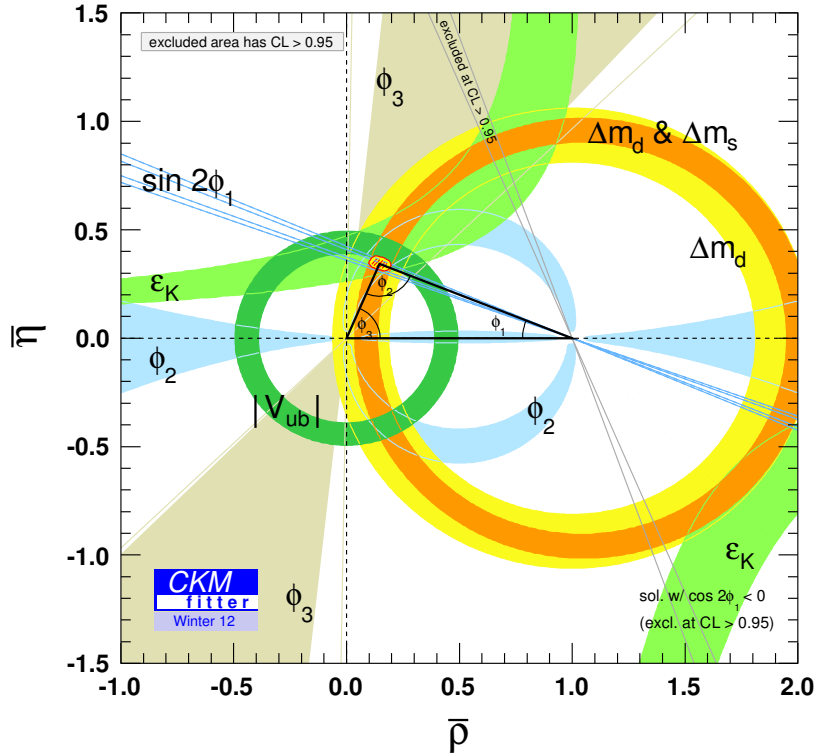


Figure 1.2: Summary of experimental results to constrain the unitarity triangle by the CKMfitter group [14]

h^\pm represents a charged pion or kaon. These decays are especially interesting because the decay rates cannot be predicted precisely by theory calculation and the experimental input is therefore required. Also a tension exists in the measurements of the direct CP violation between the two B-factory experiments in this channel that we hope to resolve.

We have measured the branching ratio of $B^0 \rightarrow \pi^+\pi^-$ and achieved the worlds most precise measurement of direct and mixing induced CP violation in this channel. The result is used to determine one of the angles of the unitarity triangle, ϕ_2 . To perform a model independent search for new physics beyond the Standard Model (BSM) we obtain the direct CP violation in the channel $B \rightarrow K\pi$ and the branching ratio. Theories beyond the Standard Model predict high branching fractions for the process $B^0 \rightarrow K^+K^-$. Our search places a very restrictive limit on this process.

In the first chapter (Sec. 2), the Standard Model is introduced describing the mechanism for CP violation in particular. A brief introduction to the Belle detector and the KEKB storage ring is given in chapter 3. The technique of a “blind” analysis is presented in chapter 4. We start with an introduction to the basic principles of analysis (Sec. 4.1) and

the data set (Sec. 4.2) that is analysed. This is followed by a detailed description of the reconstruction and event selection in section 4.3. A maximum likelihood fit is used to extract the physics observables from the data set. The necessary models for the various signal and background components are obtained from simulation. This is explained in detail in section 4.4. Furthermore, we present a study of possible fit biases (Sec. 4.6) on the branching fraction measurement and the CP parameters. The following chapter 5 demonstrates methods for correcting differences between simulation and data in the likelihood fit models. We performed an unblinded analysis on a control sample (Sec. 5.1) to obtain corrections from data for our signal model obtained from simulation. Also, a new method is demonstrated (5.2), which corrects histograms which are used as data models. Finally in chapter 6, the branching fractions and CP parameters are presented. The discussion includes the estimation of systematic uncertainties (Sec. 6.2) and calculation of the upper limit for the branching fraction of $B^0 \rightarrow K^+K^-$ (Sec. 6.3). The combination with other results measured with the Belle detector enables us to perform an analysis to extract the angle ϕ_2 of the unitarity triangle (Sec. 6.4). Model independent searches for new physics beyond the Standard Model in the decay $B^0 \rightarrow K^+\pi^-$ are performed exploiting a sum rule using CP parameters and branching fractions from various $B \rightarrow K\pi$ decays (Sec. 6.5). The thesis concludes with chapter 7.

Chapter 2

CP Violation in the Standard Model

2.1 The Standard Model of Particle Physics

The Standard Model is a quantum mechanical theory that postulates a set of elementary particles shown in Tbl. 2.1 and force carriers Tbl. 2.2. The elementary particles are spin-1/2 particles, fermions, and the constituents of matter. The force carries can be described by integer spin bosons.

The electron and the neutrino, two fermions, form the first generation of the leptons. More heavy versions of the electron, the muon and the tau with their corresponding neutrinos form the second and third generations of leptons, respectively. In weak production and decay processes the lepton and its associated neutrino are produced as pairs. Finally the quarks are the constituents of compound particles (hadrons) e.g. the proton and the neutron. The quarks do not have an integer charge but are charged $-1/3$ and $+2/3$ with respect to the electron charge. Also the quarks can be ordered by their mass and charge into three generations, where each generation is much more heavy than the preceding one. The six quarks are labeled by the flavour quantum number u, d, c, s, t, b . In addition we can assign every quark a quantum number, called colour. Every quark can carry red, green or blue and the corresponding anti colours. There are two ways of combining the quarks to colour less hadrons. The combination of three quarks (red, green, blue) forms a baryon. The best known example of these is the proton which consists of two up-quarks and one down-quark ($u u d$). The other possibility is to combine a quark (colour) with an anti-quark (anti-colour) to obtain a meson (colour-less). The combination of an up-quark (u) with an anti-down-quark (\bar{d}) with the lowest energy is called pion (π^+). Two more important examples are the K^+ meson, which consists of an up-quark (u) and an anti-strange-quark (\bar{s}), and the B meson which consists of a bottom-quark (b) and an anti-down-quark (\bar{d}).

Four forces, or interactions, are known in nature: electromagnetic, weak force, strong force

Table 2.1: *Elementary spin-1/2 particles (fermions) in the Standard Model.*

charge	1st gen.	2nd gen.	3rd gen.
+2/3	u	c	t
-1/3	d	s	b
-1	e^-	μ^-	τ^-
0	ν_e	ν_μ	ν_τ

Table 2.2: *Integer-spin bosons in the Standard Model.*

charge	spin	abbreviation
0	1	γ
+1	1	W^+
-1	1	W^-
0	1	Z^0
0	1	g
0	0	H^0

and gravity. The Standard Model describes the first three. In a quantum field theory a force is described by the exchange of gauge bosons. The electromagnetic force is responsible for all the atomic properties and shapes our daily experience the most. The mediator of the electromagnetic force is the photon which couples only to charged particles. The weak force is the source of e.g. the β -decays. The mediators of the weak force are either charged or neutral with only the charged mediators having the possibility to change the flavour of the quarks and leptons. The electromagnetic and the weak force can be unified to a combined electroweak force [11]. The strong force is the dominant force in the atomic core. It keeps the protons in the atomic core from exploding due to coulomb repulsion. The attractive force between the quarks in the nucleon is mediated by the gluon. The last boson to be described is the Higgs boson. It is not a mediator of a force, but it is rather the source of mass for the fermions in the Standard Model. In every gauge invariant quantum field theory, like the Standard Model, all particles have to be massless. Since measurements show us that the particle do have mass, the theory has to be modified. Therefore a coupling to the Higgs boson is introduced that yields mass to all remaining particles.

The Standard Model groups two major theories into a common description, the Quantum-Chromo-Dynamics (QCD) which governs the strong interaction of quarks and gluons, and the unification of electromagnetic and weak interactions, quantum flavour dynamics (QFD), set up by Glashow, Weinberg and Salam [11]. The Standard Model is a locally gauge-invariant theory, incorporating the gauge symmetry groups $SU(3)_{\text{colour}} \times SU(2)_L \times U(1)$ essentially defines the Standard Model, where $SU(3)_{\text{colour}}$ and $SU(2)_L \times U(1)$ are the QCD and the electroweak part respectively. The Lagrangian of the Standard Model is given by

$$\mathcal{L}_{\text{SM}} = \mathcal{L}_{\text{EW}} + \mathcal{L}_{\text{QCD}}.$$

The fundamental representation of $SU(3)_{\text{colour}}$ are triplets in the form $Q_i = \begin{pmatrix} Q_i^{\text{red}} \\ Q_i^{\text{green}} \\ Q_i^{\text{blue}} \end{pmatrix}$

where the index i identifies the quarks $i = 1, \dots, 6 \rightarrow u, d, s, c, b, t$. In addition we have an adjointed representation of $SU(3) \rightarrow N^2 - 1 = 8$ massless gluons which always carry two colours. The Gell-Mann's matrices T^a act as generators for the group.

The electroweak part of the Standard Model is modelled as a spontaneously broken Yang-Mills theory based on $SU(2)_L \times U(1)_Y$ [11]. The electroweak Lagrangian is composed by four parts: The Lagrangian of the fermion fields, $\mathcal{L}_{\text{EW}}^{\text{ferm}}$, the Lagrangian of the gauge-fields, $\mathcal{L}_{\text{EW}}^{\text{gauge}}$, which gives rise to the bosons of the electroweak theory, the Lagrangian of the spontaneously broken symmetry, $\mathcal{L}_{\text{EW}}^{\text{SSB}}$, which describes the Higgs sector, and the gauge invariant Yukawa couplings, which generate the masses for the fermions, are described in $\mathcal{L}_{\text{EW}}^{\text{Yukawa}}$.

$$\mathcal{L}_{\text{EW}} = \mathcal{L}_{\text{EW}}^{\text{ferm}} + \mathcal{L}_{\text{EW}}^{\text{gauge}} + \mathcal{L}_{\text{EW}}^{\text{SSB}} + \mathcal{L}_{\text{EW}}^{\text{Yukawa}}.$$

The $SU(2)_L$ is the weak isospin group with a gauge coupling g and the three generators $T^i = \sigma^i/2$ ($\sigma^i =$ Pauli matrices, $i = 1, 2, 3$). The three gauge bosons W_1^μ , W_2^μ and W_3^μ are required to be massless in order not to break the gauge symmetry. The fermion fields are divided into left-handed doublets of $SU(2)$ and right-handed singlets,

$$\Psi_l = \frac{1}{2}(1 - \gamma_5)\Psi \quad \Psi_r = \frac{1}{2}(1 + \gamma_5)\Psi$$

The $U(1)_Y$ group is the gauge group of the weak hypercharge ($Q = T_3 + Y$) with a gauge coupling g' . The group has only one generator which assigns the hypercharge Y to each field and one gauge boson B^μ .

For the first generation of fermions the following tuples can be written.

$$L_L = \begin{pmatrix} \nu_{eL} \\ e_L \end{pmatrix}_{Y=-1/2} \quad (\nu_{eR})_{Y=0} \quad (e_R)_{Y=-1},$$

$$Q_L = \begin{pmatrix} u_L \\ d_L \end{pmatrix}_{Y=1/6} \quad (u_R)_{Y=2/3} \quad (d_R)_{Y=-1/3}.$$

Staying with the example of the first generation of particles we can write the following Lagrangian for the fermion fields,

$$\mathcal{L}_{\text{EW}}^{\text{ferm}} = \bar{Q}_L i \not{D} Q_L + \bar{L}_L i \not{D} L_L + \bar{u}_R i \not{D} u_R + \bar{d}_R i \not{D} d_R + \bar{e}_R i \not{D} e_R + \bar{\nu}_R i \not{D} \nu_R.$$

Here, the covariant derivative D_μ is given by

$$D_\mu = \partial_\mu - ig W_\mu^i T_\mu^i - ig' \frac{1}{2} Y B_\mu,$$

where the index i identifies the quarks $i = 1, \dots, 6 \rightarrow u, d, s, c, b, t$. Now rewriting the Lagrangian $\mathcal{L}_{\text{EW}}^{\text{ferm}} = \mathcal{L}_{\text{kin}} + \mathcal{L}_{\text{CC}} + \mathcal{L}_{\text{NC}}$, in terms of charged current and neutral current, we can identify the bosons coupling to those currents.

$$\begin{aligned}\mathcal{L}_{\text{kin}}^{\text{ferm}} &= \bar{L}_L(i\cancel{D})L_L + \bar{e}_R(i\cancel{D})e_R + \dots, \\ \mathcal{L}_{\text{CC}} &= \frac{g}{\sqrt{2}}W_\mu^+\bar{\nu}_{eL}\gamma^\mu e_L + \frac{g}{\sqrt{2}}W_\mu^-\bar{e}_L\gamma^\mu\nu_{eL}, \\ \mathcal{L}_{\text{NC}} &= \frac{g}{2}W_\mu^3[\bar{\nu}_{eL}\gamma^\mu\nu_{eL} - \bar{e}_L\gamma^\mu e_L] + \frac{g'}{2}B_\mu[Y(L)(\bar{\nu}_{eL}\gamma^\mu\nu_{eL} \\ &\quad + \bar{e}_L\gamma^\mu e_L) + Y(e_R)\bar{\nu}_{eR}\gamma^\mu\nu_{eR} + Y(e_R)\bar{e}_R\gamma^\mu e_R] + \dots,\end{aligned}$$

where $W^\pm = \frac{1}{\sqrt{2}}(W_\mu^1 \mp iW_\mu^2)$ are the mediators of the charged currents and W_μ^3 and B_μ are the mediators of the neutral currents. But none of the neutral Gauge-Bosons W_μ^3 or B_μ can be identified as the photon field A_μ because they couple to neutral fields while the photon does not. Weinberg solved this problem by introducing a rotation by the weak mixing angle (Weinberg angle) θ_W ,

$$\begin{aligned}B_\mu^3 &= \sin(\theta_W)A_\mu + \cos(\theta_W)Z_\mu, \\ W_\mu^3 &= \sin(\theta_W)A_\mu - \cos(\theta_W)Z_\mu.\end{aligned}$$

The rotation is chosen so that the kinetic terms are still diagonal. The Lagrangian for the neutral current then becomes

$$\mathcal{L}_{\text{NC}} = \bar{\psi}\gamma^\mu \left(g \sin \theta_W T^3 + g' \cos \theta_W \frac{Y}{2} \right) \psi A_\mu + \bar{\psi}\gamma^\mu \left(g \cos \theta_W T^3 + g' \sin \theta_W \frac{Y}{2} \right) \psi Z_\mu.$$

One can identify the electric charge Q , for $\psi^T = (\nu_{eL}, e_L, \nu_{eR}, e_R, \dots)$ to be

$$eQ = g \sin \theta_W T^3 + g' \cos \theta_W \frac{Y}{2}.$$

Using the information from e.g. the leptonic doublet L_L , one can derive a relation between the Weinberg angle and g

$$g \sin \theta_W = g' \cos \theta_W = e,$$

which is the electroweak unification.

The Lagrangian of the gauge fields can be derived by dimensional analysis of the gauge fields

$$\mathcal{L}_{\text{EW}}^{\text{gauge}} = -\frac{1}{4}W_{\mu\nu}^a W^{a,\mu\nu} - \frac{1}{4}B_{\mu\nu}B^{\mu\nu},$$

where

$$\begin{aligned} B_{\mu\nu} &= \partial_\mu B_\nu - \partial_\nu B_\mu, \\ W_{\mu\nu}^a &= \partial_\mu W_\nu^a - \partial_\nu W_\mu^a + g\epsilon^{abc}W_\mu^b W_\nu^c. \end{aligned}$$

So far all fermions are massless in the Standard Model. The Higgs mechanism [10] provides masses by spontaneously breaking the $SU(2)_L \times U(1)_Y$ symmetry (SSB). Therefore, a complex scalar doublet of $SU(2)_L$ with $Y = \frac{1}{2}$ is introduced:

$$\phi = \begin{pmatrix} \phi^+ \\ \phi^0 \end{pmatrix}.$$

The Lagrangian for a scalar particle is as follows

$$\mathcal{L}_{\text{EW}}^{\text{SSB}} = (D^\mu \phi)^\dagger D_\mu \phi - \mu^2 \phi^\dagger \phi - \lambda(\phi^\dagger \phi)^2.$$

Following reference [10], the expectation value is chosen to be

$$\langle \phi \rangle = \frac{1}{\sqrt{2}} \begin{pmatrix} 0 \\ v \end{pmatrix} \quad \text{with} \quad v = \left(\frac{-\mu^2}{\lambda} \right)^{-1/2} \quad (\mu^2 < 0, \lambda > 0),$$

in order to spontaneously break the symmetry. The mass terms for the Gauge-bosons arise from the term $(D^\mu \phi)^\dagger D_\mu \phi$. We obtain the following masses.

$$\begin{aligned} W_\mu^\pm &= \frac{1}{\sqrt{2}}(W_\mu^1 \mp iW_\mu^2) \rightarrow M_W = g\frac{v}{2}, \\ Z_\mu &= \frac{1}{\sqrt{g^2 + g'^2}}(gW_\mu^3 - g'B_\mu) \rightarrow M_Z = \sqrt{g^2 + g'^2}\frac{v}{2}, \\ A_\mu &= \frac{1}{\sqrt{g^2 + g'^2}}(g'W_\mu^3 + gB_\mu) \rightarrow M_A = 0. \end{aligned}$$

Using the definition of $\cos \theta_W = g/\sqrt{g^2 + g'^2}$, the relation between the W and Z mass are obtained,

$$M_W = M_Z \cos \theta_W.$$

Using the unitarity Gauge it is possible to derive

$$\phi = \frac{1}{\sqrt{2}} \begin{pmatrix} 0 \\ v + H \end{pmatrix}$$

where H is the only remaining scalar field, the Higgs boson, with a mass $M_H^2 = -2\mu^2 = 2\lambda v^2$.

The entire Higgs sector, $\mathcal{L}_{\text{EW}}^{\text{SSB}}$, depends only on two theory parameters v and M_H . The v parameter can be measured in decays of the muon, while the Higgs mass is measured at the LHC experiments [15–18]. In a press conference at CERN on the 4. July 2012 the ATLAS and the CMS collaboration announced the discovery of a boson compatible with the Standard Model Higgs Boson. The Higgs mass is found to be approximately $M_H \approx 126 \text{ GeV}$ [19, 20].

Coming back to the fermions in the Standard Model, we know from gauge symmetry that the Standard Model forbids mass terms. But all fermions are massive from experimental evidence. Therefore the fermion masses are generated via gauge invariant Yukawa couplings

$$\mathcal{L}_{\text{EW}}^{\text{Yukawa}} = -\Gamma_{\mu}^{ij} \bar{Q}_L^i \phi^c u_R^j - \Gamma_d^{ij} \bar{Q}_L^i \phi d_R^j - \Gamma_e^{ij} \bar{L}_L^i \phi l_R^j + \text{h.c.}$$

Upon spontaneous symmetry breaking, we obtain

$$\begin{aligned} \mathcal{L}_{\text{EW}}^{\text{Yukawa}} &= -\Gamma_{\mu}^{ij} \bar{u}_L^i \frac{v+H}{\sqrt{2}} u_R^j - \Gamma_d^{ij} \bar{d}_L^i \frac{v+H}{\sqrt{2}} d_R^j - \Gamma_e^{ij} \bar{l}_L^i \frac{v+H}{\sqrt{2}} l_R^j + \text{h.c.} \\ &= -\sum_{f,i,j} \bar{f}_L^i M_f^{ij} f_R^j \left(1 + \frac{H}{v}\right) + \text{h.c.} \end{aligned}$$

where

$$M_f^{ij} = \Gamma_f^{ij} \frac{v}{\sqrt{2}},$$

is a non-diagonal mass matrix. To extract the fermion masses we have to diagonalize the matrix. This is done using the unitary transformations U_L and U_R ,

$$M_D = (U_L^f)^\dagger M_f U_R^f.$$

We can then define the mass eigenstates and extract the fermion masses as the eigenvalues,

$$f_L^i = (U_L^f)_{ij} f_L^j \quad \text{and} \quad f_R^i = (U_R^f)_{ij} f_R^j.$$

Inserting the definitions in the Lagrangian,

$$\begin{aligned} \mathcal{L}_{\text{EW}}^{\text{Yukawa}} &= \sum_{f,i,j} \bar{f}_L^i [(U_L^f)^\dagger M_f U_R^f] f_R^j \left(1 + \frac{H}{v}\right) + \text{h.c.} \\ &= \sum_{f,i,j} m_f (\bar{f}_L^i f_R^j + \bar{f}_R^j f_L^i) \left(1 + \frac{H}{v}\right). \end{aligned}$$

In terms of the new mass eigenstates, the quark component of \mathcal{L}_{CC} now reads

$$\mathcal{L}_{CC} = \frac{g}{\sqrt{2}} \bar{u}_L^i [(U_L^u)^\dagger U_R^d] \gamma^\mu d_L^j + \text{h.c.}$$

where

$$V_{CKM} = (U_L^u)^\dagger U_R^d,$$

is the Cabibbo-Kobayashi-Maskawa matrix (**CKM**) [12] which is the origin of flavour mixing in the Standard Model.

2.2 The CKM Matrix and the Unitarity Triangle

The Standard Model describes the mixing of mass and flavour eigenstates by the so called **CKM** matrix. The elements of this matrix are not given by the theory, but must be determined by experiment. There are some constraints on the matrix from the theory. A very basic constraint is that the equations should preserve the total probability to be unity. This property of the CKM matrix is called unitarity. The unitarity condition can be geometrically represented as a triangle in the complex plane. All sides and angles can be determined by experiment to overconstrain the unitarity triangle. If deviations from a triangle shape appear it would be a clear hint on the failure of the mechanism. The CKM matrix which is derived in section 2.1, describes the mixture of flavour and mass eigenstates:

$$\begin{pmatrix} |d'\rangle \\ |s'\rangle \\ |b'\rangle \end{pmatrix} = \begin{pmatrix} V_{ud} & V_{cd} & V_{td} \\ V_{us} & V_{cs} & V_{ts} \\ V_{ub} & V_{cb} & V_{tb} \end{pmatrix} \begin{pmatrix} |d\rangle \\ |s\rangle \\ |b\rangle \end{pmatrix} \quad (2.1)$$

For three or more generations of quarks it can be shown that the CKM matrix is complex (irreducible complex phase) in general. This is in contrast to the 2 generation case, where the CKM matrix is a simple rotation matrix. It should be noted that the Lagrangian of the electroweak force is not invariant under CP transformation if the matrix is complex, which is the source of CP violation in the Standard Model.

The elements of the **CKM** matrix describe the transition probability of a quark into a different flavour. To make the interaction strength of flavour changing weak currents visible, the Wolfenstein parametrisation of the CKM matrix is used [21]

$$V_{CKM} = \begin{pmatrix} 1 - \frac{1}{2}\lambda^2 & \lambda & A\lambda^3(\rho - i\eta + \frac{i}{2}\eta\lambda^2) \\ -\lambda & 1 - \frac{1}{2}\lambda^2 - i\eta A^2\lambda^4 & A\lambda^2(1 + i\eta\lambda^2) \\ A\lambda^3(1 - \rho - i\eta) & -A\lambda^2 & 1 \end{pmatrix} + \mathcal{O}(\lambda^6), \quad (2.2)$$

where λ is the sine of the Cabibbo angle [22] $\lambda = \sin \theta_C \approx 0.23$. The degrees of freedom of the **CKM** matrix are 3 real numbers λ , ρ , A and one complex $i\eta$. The unitarity condition can be written as $\sum_k V_{ik}V_{jk}^* = 0$ for all $i \neq j$. Every condition consists of 3 terms that can be graphically represented as a triangle in complex plane. For the B -system (1. and 3. row) this leads to the following condition

$$\underbrace{V_{ud}V_{ub}^*}_{\mathcal{O}(\lambda^3)} + \underbrace{V_{cd}V_{cb}^*}_{\mathcal{O}(\lambda^3)} + \underbrace{V_{td}V_{tb}^*}_{\mathcal{O}(\lambda^3)} = 0. \quad (2.3)$$

The 3 complex numbers can be graphically represented as a triangle in complex space. It is worth mentioning that all sides similar length $\mathcal{O}(\lambda^3)$ which implies that all angles in the triangle are large. That is not the case for the kaon triangle (1. and 2. column) which is almost degenerate. The B^0 decays are therefore the preferred laboratory for studying CP violation. For convenience reasons, we normalize Eq. (2.3) by the magnitude of one

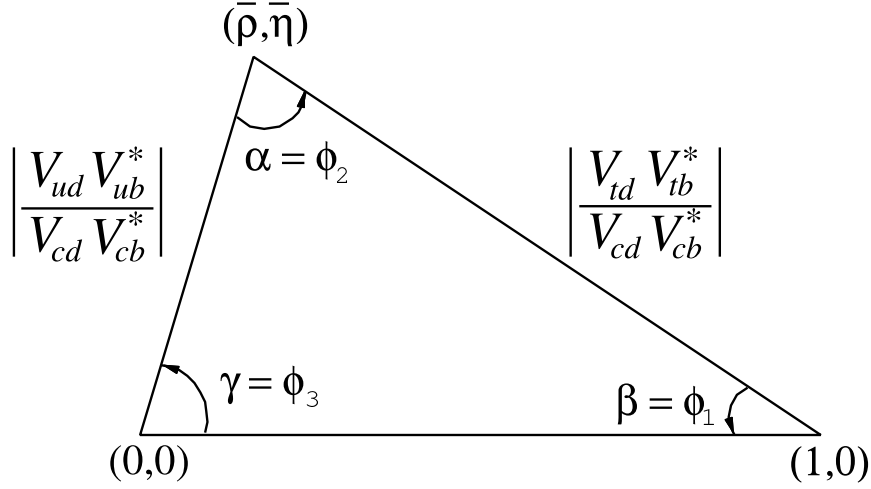


Figure 2.1: *The normalized unitarity triangle.*

side $|V_{cd}V_{cb}^*|$. This side becomes aligned with the real axis and its magnitude becomes unity. The normalized triangle is shown in figure 2.1 where we introduce η and ρ to be

$$\bar{\rho} \equiv \left(1 - \frac{\lambda^2}{2}\right) \rho, \quad \bar{\eta} \equiv \left(1 - \frac{\lambda^2}{2}\right) \eta. \quad (2.4)$$

The angles in the unitarity triangle are described by the following equations,

$$\phi_1 \equiv \pi - \arg\left(\frac{-V_{td}V_{tb}^*}{-V_{cd}V_{cb}^*}\right), \quad \phi_2 \equiv \arg\frac{V_{td}V_{tb}^*}{-V_{ud}V_{ub}^*}, \quad \phi_3 \equiv \arg\frac{V_{ud}V_{ub}^*}{-V_{cd}V_{cb}^*}. \quad (2.5)$$

Two sides and the three angles can be measured independently in B -decays. By measuring all 5 parameters which over constrains the triangle, we can test the unitarity of the CKM matrix. The current limits on this measurement can be found in Fig. 1.2.

2.3 $B^0\bar{B}^0$ Mixing

We are looking for CP violation in the decays of B mesons. There are two possible types of CP violation in B meson decays. We can observe direct CP violation, which means that the decay rates of a B meson and a \bar{B} meson into a specific final state are different. The other possibility is to observe mixing induced CP violation or mixing induced CP violation. The mixing induced CP violation exhibits a time-dependent decay rate difference between B^0 and \bar{B}^0 decays although the time-integrated decay rate can be the same. Indirect CP violation can be observed only if both the B^0 and the \bar{B}^0 meson can decay into the same final state, a CP eigenstate. Measurements of direct and mixing induced CP violation have to take into account the time evolution of the neutral B meson which is explained in the next section.

2.3.1 Time Evolution of the neutral B Meson

In this section we are deriving the flavour oscillations of the neutral B meson. Neutral B mesons B^0 (\bar{b}, d) and \bar{B}^0 (b, \bar{d}) are pseudo-scalar mesons ($J^P = 0^-$) and C -conjugates. In the strong interaction the mesons are produced as pure flavour eigenstates. Since the mass-Eigenstate and the flavour-Eigenstate are different and both can reach the same final states there is the possibility for time-dependent flavour oscillations in the Standard Model. This can be observed for other heavy neutral mesons as well. This $B\bar{B}$ mixing is mediated mainly by a second order process where the b and d quarks couple to W boson and a top quarks, t (see Fig. 2.2). The time evolution of a quantum state is governed by the

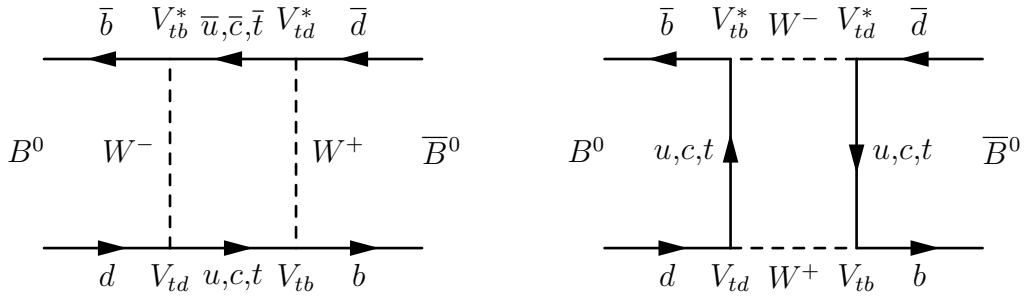


Figure 2.2: Feynman box diagram showing the predominant time-dependent flavour mixing diagrams

Schrödinger equation. A general B meson state can be written as a linear combination of the flavour Eigenstates

$$|B(t)\rangle = a(t)|B^0\rangle + b(t)|\bar{B}^0\rangle, \quad (2.6)$$

and by applying the Schrödinger equation on the state, we obtain

$$i\frac{d}{dt}\begin{pmatrix} |B(t)\rangle \\ |\bar{B}(t)\rangle \end{pmatrix} = \mathbf{H}\begin{pmatrix} |B(t)\rangle \\ |\bar{B}(t)\rangle \end{pmatrix}. \quad (2.7)$$

The weak effective Hamiltonian \mathbf{H} , is the sum of a hermitian 2×2 mass matrix and a anti-hermitian 2×2 decay matrix,

$$\mathbf{H} = \mathbf{M} - \frac{i}{2}\mathbf{\Gamma} = \begin{pmatrix} M_{11} - \frac{i}{2}\Gamma_{11} & M_{12} - \frac{i}{2}\Gamma_{12} \\ M_{21} - \frac{i}{2}\Gamma_{21} & M_{22} - \frac{i}{2}\Gamma_{22} \end{pmatrix}, \quad (2.8)$$

where \mathbf{M} is the mass matrix and $\mathbf{\Gamma}$ is the decay matrix. The hermiticity of \mathbf{H} ($\mathbf{H} = \mathbf{H}^\dagger$) dictates for the off-diagonal elements $H_{12} = H_{21}^*$. The off-diagonal elements are associated with flavour changing transitions, meaning $B^0 \leftrightarrow \bar{B}^0$. CP symmetry is violated when $H_{21} \neq H_{12}^*$. The diagonal elements are associated with flavour conserving transitions, $B^0 \rightarrow B^0$ and $\bar{B}^0 \rightarrow \bar{B}^0$. If CPT invariance is imposed, then $H_{11} = H_{22} = M - 1/2\Gamma$, which means that the self coupling is independent of the flavour. The eigenvalues μ_\pm , can be determined from diagonalizing \mathbf{H} ,

$$\mu_\pm \equiv M - \frac{i}{2}\Gamma \pm \sqrt{\left(M_{12} - \frac{i}{2}\Gamma_{12}\right)\left(M_{12}^* - \frac{i}{2}\Gamma_{12}^*\right)}. \quad (2.9)$$

The eigenstates corresponding to the eigenvalues are

$$\begin{aligned} |B_L\rangle &\equiv p |B^0\rangle + q |\bar{B}^0\rangle \text{ for } \mu_-, \\ |B_H\rangle &\equiv p |B^0\rangle - q |\bar{B}^0\rangle \text{ for } \mu_+, \end{aligned} \quad (2.10)$$

where

$$\frac{q}{p} \equiv \sqrt{\frac{M_{12}^* - \frac{i}{2}\Gamma_{12}^*}{M_{12} - \frac{i}{2}\Gamma_{12}}} \text{ and } \sqrt{p^2 + q^2} = 1. \quad (2.11)$$

The eigenstates $|B_{L,R}\rangle$, are the physical mass eigenstates. The L and H are a short-hand notation for the light and heavy mass eigenstates, respectively. The masses and the decay rates for $|B_{L,R}\rangle$ are given by

$$m_L = \text{Re}(\mu_-), \quad \Gamma_L = -2 \text{Im}(\mu_-), \quad (2.12)$$

$$m_H = \text{Re}(\mu_+), \quad \Gamma_H = -2 \text{Im}(\mu_+). \quad (2.13)$$

The difference and the average of the masses and decay rates are given by

$$\Delta m_d \equiv m_H - m_L, \quad \Delta \Gamma \equiv \Gamma_L - \Gamma_H, \quad \frac{m_H + m_L}{2} = M, \quad \frac{\Gamma_H + \Gamma_L}{2} \equiv \Gamma. \quad (2.14)$$

The time evolution of this two-state system, using equation 2.10 and 2.13, is as follows

$$\begin{aligned} |B_L(t)\rangle &= e^{i\mu_- t} |B_L\rangle = e^{-im_L t} e^{-\Gamma_L t/2} (p |B^0\rangle + q |\bar{B}^0\rangle), \\ |B_H(t)\rangle &= e^{i\mu_+ t} |B_H\rangle = e^{-im_H t} e^{-\Gamma_H t/2} (p |B^0\rangle + q |\bar{B}^0\rangle). \end{aligned} \quad (2.15)$$

By using Eq. 2.10, one can absorb the time dependency in the flavour state $|B^0\rangle$,

$$\begin{aligned} |B_L(t)\rangle &= p |B^0(t)\rangle + q |\bar{B}^0(t)\rangle, \\ |B_H(t)\rangle &= p |B^0(t)\rangle - q |\bar{B}^0(t)\rangle. \end{aligned} \quad (2.16)$$

With Eq. 2.15, Eq. 2.16 and 2.14, the time evolution of B^0 and \bar{B}^0 can then be extracted,

$$\begin{aligned} |B^0(t)\rangle &= g_+(t) |B^0\rangle + \frac{q}{p} g_-(t) |\bar{B}^0\rangle, \\ |\bar{B}^0(t)\rangle &= g_+(t) |B^0\rangle - \frac{q}{p} g_-(t) |\bar{B}^0\rangle, \end{aligned} \quad (2.17)$$

where

$$g_{\pm} \equiv \frac{1}{2} e^{iMt} e^{-\Gamma t/4} \left(e^{i\Delta m_d t/2} e^{-\Delta\Gamma t/4} \pm e^{-i\Delta m_d t/2} e^{\Delta\Gamma t/4} \right). \quad (2.18)$$

Commonly the lifetime difference between the light and heavy state is assumed to be zero ($\Delta\Gamma = 0$) because the difference is so small ($\Delta\Gamma/\Gamma = \mathcal{O}(10^{-3})$). The decay rate is redefined as $\Gamma_L = \Gamma_H = \Gamma$, and therefore, Eq. 2.18 becomes

$$g_{\pm}(t) = e^{-\Gamma t/2} \left(\frac{e^{i\Delta m_d t/2} \pm e^{-i\Delta m_d t/2}}{2} \right), \quad (2.19)$$

where the phase e^{iMt} is removed by convention. Thus, the simplified time evolution of the flavour states is

$$\begin{aligned} |B^0(t)\rangle &= e^{-\Gamma t/2} \left(\cos \frac{\Delta m_d t}{2} |B^0\rangle + i \frac{q}{p} \sin \frac{\Delta m_d t}{2} |\bar{B}^0\rangle \right), \\ |\bar{B}^0(t)\rangle &= e^{-\Gamma t/2} \left(\cos \frac{\Delta m_d t}{2} |\bar{B}^0\rangle - i \frac{q}{p} \sin \frac{\Delta m_d t}{2} |B^0\rangle \right). \end{aligned} \quad (2.20)$$

2.3.2 Types of CP Violation

When observing CP violation, we are measuring a difference in the decay of a particle and its anti-particle. For the decay probability one has to square the complex amplitude for the decay. CP violation is observed in general when the magnitude of the amplitude is different for the particle and its anti-particle. This is possible when the process is the sum of two amplitudes with a weak and a strong phase where the weak phase is changed by the CP transformation and the strong phase stays invariant.

When considering CP violation we can observe CP in three different processes. CP violation can occur in the mixing amplitude itself and is called CP violation in mixing. This is negligible in the case of the neutral B mesons because the masses of the B_H and B_L meson are almost the same. Another possibility is to observe CP violation in the decay. This is possible e.g. when there is a contribution from a weak and strong phase. The strong phase is invariant under CP transformation while the weak phase changes sign when going from particle to anti-particle decay. This phenomenon is called direct CP violation and it can be empirically observed by different decay rates for the particle and its anti-particle. For neutral B mesons there is a third possibility to have CP violation in the interference between the mixing and decay amplitudes. Since the mixing amplitude is time-dependent also the decay rate difference is time dependent. In this case we are talking about mixing induced CP violation.

Consider the case where both B^0 and \bar{B}^0 decay into the same CP eigenstate, f_{CP} . The decay amplitudes are

$$\begin{aligned} A_{CP} &= \langle f_{CP} | \mathbf{H} | B^0 \rangle, \\ \bar{A}_{CP} &= \langle f_{CP} | \mathbf{H} | \bar{B}^0 \rangle. \end{aligned} \quad (2.21)$$

Generalizing Eq. 2.21 to incorporate the time evolution (Eq. 2.20), one obtains the time dependent amplitudes

$$\begin{aligned} A_{CP}(t) &= A_{CP} e^{-\Gamma t/2} \left(\cos \frac{\Delta m_d t}{2} + i \lambda_{CP} \sin \frac{\Delta m_d t}{2} \right), \\ \bar{A}_{CP}(t) &= \bar{A}_{CP} e^{-\Gamma t/2} \left(\cos \frac{\Delta m_d t}{2} - \frac{i}{\lambda_{CP}} \sin \frac{\Delta m_d t}{2} \right), \end{aligned} \quad (2.22)$$

where

$$\lambda_{CP} \equiv \frac{q \bar{A}_{CP}}{p A_{CP}}. \quad (2.23)$$

To simplify Eq. 2.23, we take a look at the Feynman diagram showing $B\bar{B}$ mixing (Fig. 2.2). The b and d quarks couple to the W boson and u, c, t quarks. The t quark dominates here because of Glashow, Iliopoulos and Maiani (GIM) cancellations. Theory indicates that[[23],[24],[25],[26]],

$$M_{12} \propto (V_{tb}V_{td}^*)^2 m_t^2, \quad (2.24)$$

$$\Gamma_{12} \propto (V_{tb}V_{td}^*)^2 m_b^2, \quad (2.25)$$

where $m_{t,b}$ is the mass of the t and b quark. If we expand Eq. (2.11),

$$\begin{aligned} \frac{q}{p} &\simeq \sqrt{\frac{M_{12}^*}{M_{12}}} + \mathcal{O}\left(\frac{\Gamma_{12}}{M_{12}}\right) \\ \Rightarrow \left|\frac{q}{p}\right| &= \left|\frac{V_{td}V_{tb}^*}{V_{td}^*V_{tb}}\right| + \mathcal{O}\left(\frac{m_b^2}{M_t^2}\right), \quad \text{but } m_b^2/M_t^2 \ll 1, \\ \Rightarrow \left|\frac{q}{p}\right| &\simeq 1. \end{aligned} \quad (2.26)$$

Using this information, we can simplify the equation for λ_{CP} (2.23) to

$$|\lambda_{CP}|^2 = \frac{|\bar{A}_{CP}|^2}{|A_{CP}|^2}, \quad (2.27)$$

The time-dependent decay rates are therefore

$$\begin{aligned} \Gamma[B^0(t) \rightarrow f_{CP}] &= |\langle f_{CP} | B^0(t) \rangle|^2 \\ &= \frac{e^{-\Gamma t}}{2} |A_{CP}|^2 [(|\lambda_{CP}|^2 + 1) - (|\lambda_{CP}|^2 - 1) \cos \Delta m_d t - 2Im(\lambda_{CP}) \sin \Delta m_d t], \end{aligned} \quad (2.28)$$

$$\begin{aligned} \Gamma[\bar{B}^0(t) \rightarrow f_{CP}] &= |\langle f_{CP} | \bar{B}^0(t) \rangle|^2 \\ &= \frac{e^{-\Gamma t}}{2} |A_{CP}|^2 [(|\lambda_{CP}|^2 + 1) + (|\lambda_{CP}|^2 - 1) \cos \Delta m_d t + 2Im(\lambda_{CP}) \sin \Delta m_d t]. \end{aligned} \quad (2.29)$$

We define the time-dependent CP rate asymmetry as

$$\begin{aligned} a_{CP}(t) &\equiv \frac{\Gamma(\bar{B}^0(t) \rightarrow f_{CP}) - \Gamma(B^0(t) \rightarrow f_{CP})}{\Gamma(\bar{B}^0(t) \rightarrow f_{CP}) + \Gamma(B^0(t) \rightarrow f_{CP})} \\ &= \frac{(|\lambda_{CP}|^2 - 1) \cos \Delta m_d t + 2Im(\lambda_{CP}) \sin \Delta m_d t}{|\lambda_{CP}|^2 + 1} \\ &= \mathcal{A}_{CP} \cos \Delta m_d t + \mathcal{S}_{CP} \sin \Delta m_d t, \end{aligned} \quad (2.30)$$

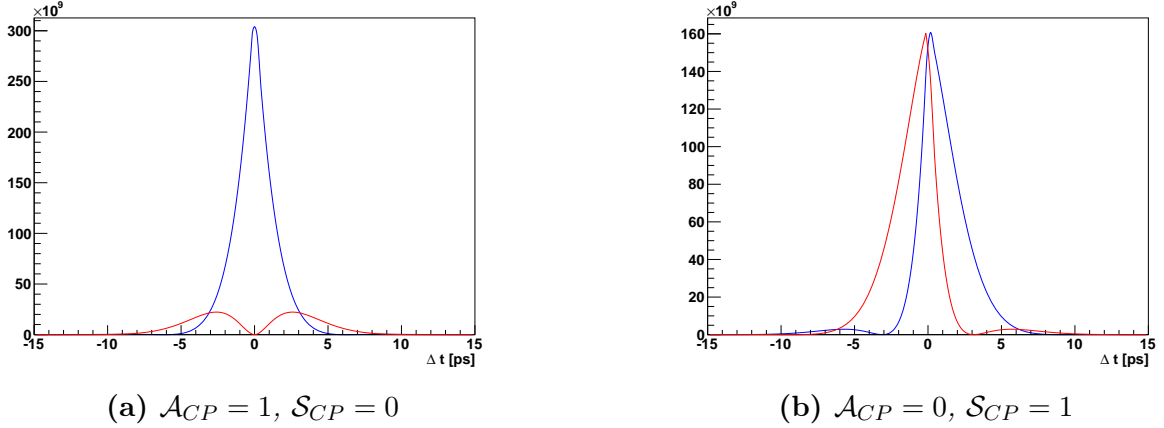


Figure 2.3: Theoretical Δt distribution for maximal direct (a) and mixing induced (b) CP violation. The red line indicates the distribution for B^0 mesons while the blue line indicates the distribution for \bar{B}^0 mesons. (a), [(b)] shows the Δt distributions for a decay to a CP final state with the CP parameters $\mathcal{A}_{CP} = 1$ and $\mathcal{S}_{CP} = 0$ [$\mathcal{A}_{CP} = 0$ and $\mathcal{S}_{CP} = 1$].

where the CP parameters are defined as

$$\mathcal{A}_{CP} \equiv \frac{|\lambda_{CP}|^2 - 1}{|\lambda_{CP}|^2 + 1}, \quad \mathcal{S}_{CP} \equiv \frac{2\text{Im}(\lambda_{CP})}{|\lambda_{CP}|^2 + 1}. \quad (2.31)$$

To get an intuitive feeling about the CP parameters, it is useful to recall λ_{CP} (Eq. 2.23) being defined as the product of q/p and \bar{A}_{CP}/A_{CP} . These complex numbers can be written as amplitude and phase of the mixing and decay part,

$$\lambda_{CP} \propto e^{-i\phi_M} \frac{|\bar{A}_{CP}|}{|A_{CP}|} e^{-i\phi_D} = \frac{|\bar{A}_{CP}|}{|A_{CP}|} e^{-i(\phi_M + \phi_D)}, \quad (2.32)$$

where ϕ_M is the phase difference from mixing and ϕ_D is the phase difference from the decay amplitude.

Now consider a different decay rate for $\Gamma(B^0 \rightarrow f_{CP})$ and $\Gamma(\bar{B}^0 \rightarrow f_{CP})$. As a consequence, $|\bar{A}_{CP}|^2/|A_{CP}|^2 \neq 1 \Rightarrow \mathcal{A}_{CP} \neq 0$.

If there is a phase difference between the mixing and decay phase $\phi_M + \phi_D \neq 0$, then $\text{Im}(\lambda_{CP}) \neq 0 \Rightarrow \mathcal{S}_{CP} \neq 0$. This is called mixing induced CP violation.

For both cases ($\mathcal{A}_{CP}, \mathcal{S}_{CP} = 1, 0$ and $\mathcal{A}_{CP}, \mathcal{S}_{CP} = 0, 1$), the expected distributions of the time-dependent decay rates are shown in Figure 2.3. The red line indicates the probability for B^0 decays and the blue line shows the probability for \bar{B}^0 decays to a CP final state. From Fig. 2.3a it is clear that one does not need a time-dependent analysis to extract the direct CP violation. Fig. 2.3b show the shift of the decay probability in time if mixing induced CP violation is present. It becomes obvious that timing information is essential the observe mixing induced CP violation.

2.3.3 Coherent $B^0\bar{B}^0$ Mixing

The rate asymmetry (Eq. 2.30) assumes that the flavour of the B -meson (b - or \bar{b} -quark) is known at the decay time. This is true for a decay like $B^0 \rightarrow K^+\pi^-$ or $\bar{B}^0 \rightarrow K^-\pi^+$ because we can determine from the final state which flavour the decaying B -meson had at the moment of the decay. If the B -meson, however, decays into a CP eigenstate the flavour of that B -meson is unknown. This is the case for e.g. the decay $B^0 \rightarrow \pi^+\pi^-$. At the Belle experiment we can, however, exploit that the B mesons are produced in quantum mechanically entangled states. This means the B and the \bar{B} mesons oscillate coherently. If one of the B mesons decays into a CP eigenstate and the other B mesons decays into a flavour specific final state then we can determine the flavour of both B mesons at the decay time of the flavour specific state. Afterwards, the remaining B meson continues to oscillate as already demonstrated in section 2.3.1.

At electron-positron colliders the B -mesons are exclusively produced from the $\Upsilon(4S)$ resonance which is a $J^{PC} = 1^{--}$ state. The B mesons are pseudoscalar mesons ($J^P = 0^-$). In order to preserve the total angular momentum of the $\Upsilon(4S)$ meson, the B mesons must have a relative angular momentum $L = 1$ (p-wave). The state is therefore antisymmetric. Because of Bose-Einstein-statistics, the states $|B^0_1\rangle|B^0_2\rangle$ and $|\bar{B}^0_1\rangle|\bar{B}^0_2\rangle$ are forbidden. Therefore the only possibility is that the $B^0\bar{B}^0$ -pair oscillates coherently. The quantum mechanically entangled state is

$$|B_1(t_1), B_2(t_2)\rangle = \frac{1}{\sqrt{2}} (|B^0_1(t_1)\rangle|\bar{B}^0_2(t_2)\rangle - |\bar{B}^0_1(t_1)\rangle|B^0_2(t_2)\rangle). \quad (2.33)$$

Substituting Eq. 2.33 into Eq. 2.20, we obtain the following time evolution

$$|B_1(t_1), B_2(t_2)\rangle = \frac{1}{\sqrt{2}} e^{-\Gamma(t_1+t_2)/2} \left[\cos \frac{\Delta m_d \Delta t}{2} (|B^0_1\rangle|\bar{B}^0_2\rangle - |\bar{B}^0_1\rangle|B^0_2\rangle) + i \frac{q}{p} \sin \frac{\Delta m_d \Delta t}{2} (|B^0_1\rangle|\bar{B}^0_2\rangle - |\bar{B}^0_1\rangle|B^0_2\rangle) \right], \quad (2.34)$$

where $\Delta t = t_2 - t_1$. Let t_i be the decay time of each B meson. If we can determine the flavour of one B meson at the time t_1 , then we know the flavour of the other B meson at the time t_1 . Given the time evolution we derived here, a probability for the flavour at the time t_2 can be calculated. In the case of our analysis, we pick events where one of the B mesons decays into a CP eigenstate. We can reconstruct the CP eigenstate and determine the decay time of one B mesons, the so-called CP -side. If the other B meson decays into a flavour specific final state, we can find the flavour at the moment of the decay and the corresponding decay time. The procedure of determining the flavour of the other B meson is called tagging. Therefore the other B meson is also called tag-side. Experimentally, a lifetime measurement in the order of ps is impossible with current technology. The B physics experiments use a Lorentz boosted center-of-mass system to translate the time measurement into a spatial measurement. The precision of the spatial measurement has to

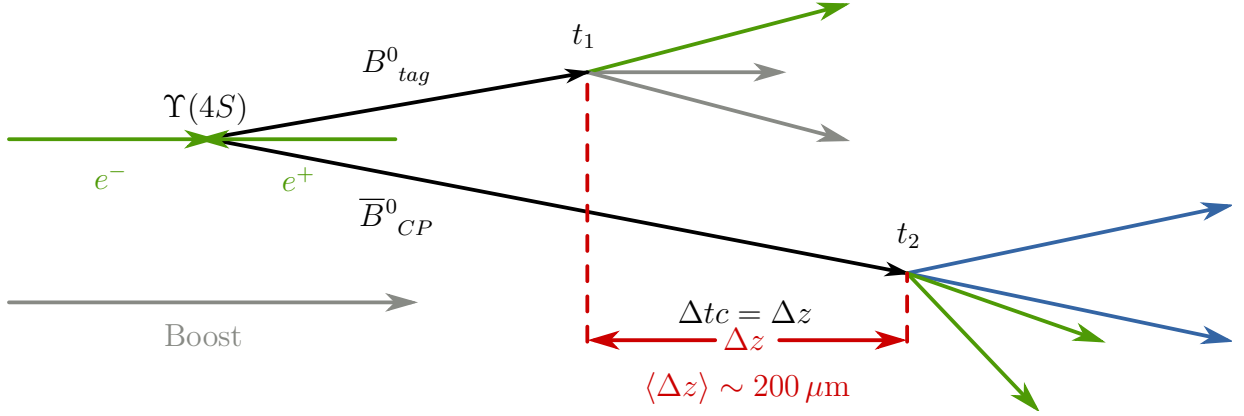


Figure 2.4: Two entangled B mesons are produced from the $\Upsilon(4S)$ resonance. One decays into CP eigenstate at time t_2 (CP -side). The other B meson decays into a flavour specific state at time t_1 (tag-side). From the charge of the decay products on the tag-side, the flavour of both B mesons can be determined at time t_1 .

be in the order of $100 \mu\text{m}$ for low energy e^+e^- experiments which is technically achievable with modern silicon detectors. Figure 2.4 is a diagram summarising the essential idea of the measurement. The time dependent decay rates take the form

$$\begin{aligned} \Gamma(f_{CP}, f_{\text{Tag}}) &= |\langle f_{CP}, f_{\text{Tag}} | B_{CP}^0(t_{CP}), B_{\text{Tag}}^0(t_{\text{Tag}}) \rangle|^2 \\ &= \frac{1}{4} e^{-\Gamma(t_{CP}+t_{\text{Tag}})} A_{CP}^2 A_{\text{Tag}}^2 \\ &\quad [(|\lambda_{CP}|^2 + 1) - (|\lambda_{CP}|^2 - 1) \cos \Delta m_d \Delta t - \text{Im}(\lambda_{CP}) \sin \Delta m_d \Delta t], \end{aligned} \quad (2.35)$$

$$\begin{aligned} \Gamma(f_{CP}, \bar{f}_{\text{Tag}}) &= |\langle f_{CP}, \bar{f}_{\text{Tag}} | B_{CP}^0(t_{CP}), \bar{B}_{\text{Tag}}^0(t_{\text{Tag}}) \rangle|^2 \\ &= \frac{1}{4} e^{-\Gamma(t_{CP}+t_{\text{Tag}})} A_{CP}^2 A_{\text{Tag}}^2 \\ &\quad [(|\lambda_{CP}|^2 + 1) - (|\lambda_{CP}|^2 - 1) \cos \Delta m_d \Delta t - \text{Im}(\lambda_{CP}) \sin \Delta m_d \Delta t]. \end{aligned} \quad (2.36)$$

λ_{CP} retains its definition from the non-coherent case. It is also noteworthy that the resulting time dependent CP -asymmetry,

$$\begin{aligned} a_{CP}(\Delta t) &\equiv \frac{\Gamma(f_{CP}, f_{\text{Tag}}) - \Gamma(f_{CP}, \bar{f}_{\text{Tag}})}{\Gamma(f_{CP}, f_{\text{Tag}}) + \Gamma(f_{CP}, \bar{f}_{\text{Tag}})} \\ &= \mathcal{A}_{CP} \cos \Delta m_d \Delta t + \mathcal{S}_{CP} \sin \Delta m_d \Delta t, \end{aligned} \quad (2.37)$$

keeps its form with t replaced by Δt . Equation (2.30) is the corresponding equation for the non-coherent decay. In the next step we want to obtain the physical limits of the parameters \mathcal{A}_{CP} and \mathcal{S}_{CP} . The left side of Eq. 2.37 exposes the limits for a_{CP} being $-1 \leq a_{CP}(\Delta t) \leq 1$ by definition. The condition for $a_{CP} = 1$ is found by solving

$$\mathcal{A}_{CP}^2 + \mathcal{S}_{CP}^2 + \left(\frac{2 \text{Re} \lambda^2}{|\lambda|^2 + 1} \right)^2 = 1. \quad (2.38)$$

When we ignore the unknown third term of Eq.2.38 we obtain the inequality

$$\mathcal{A}_{CP}^2 + \mathcal{S}_{CP}^2 \leq 1, \quad (2.39)$$

which limits the physical allowed values for \mathcal{A}_{CP} and \mathcal{S}_{CP} to the area of the unit circle in the *CP* parameter plane.

To extract the parameters \mathcal{A}_{CP} and \mathcal{S}_{CP} from the Δt distribution we need a probability density function (PDF). To obtain this PDF, one has to integrate over the unmeasurable values of $t_{\text{Tag}} + t_{CP}$ in Eq. 2.36. Also the function must be normalized in the region $-\text{inf} < a_{CP} < +\text{inf}$. The probability for finding a final state f_{CP} at a time Δt , for a given flavour tag q , is

$$\mathcal{P}(\Delta t, q) = \frac{e^{-|\Delta t|/\tau_{B^0}}}{4\tau_{B^0}} [1 + q(\mathcal{A}_{CP} \cos \Delta m_d \Delta t + \mathcal{S}_{CP} \sin \Delta m_d \Delta t)], \quad (2.40)$$

where $q = +1(-1)$ for $B_{\text{Tag}} = B^0(\bar{B}^0)$. To understand the *CP* violation parameters \mathcal{A}_{CP} and \mathcal{S}_{CP} better, the phenomenology of the extreme cases of only direct *CP* violation and only mixing induced *CP* violation are shown in figure 2.3.

2.4 *CP* violation in *B* Decays into light Hadrons

Charmless two-body decay branching fractions have been studied in various theoretical approaches, but predictions for the expected *CP* violation vary widely [27–33]. $b \rightarrow u, s$ transitions are only possible through higher order processes and therefore very sensitive to theoretical approximations but also new physics. Thus, increasingly precise measurements are important for our understanding of hadronic *B* decays. The decays that are mediated predominantly by $b \rightarrow u\bar{u}d$ transitions are sensitive to the angle ϕ_2 (Sec. 2.4.1). The decay rates for the $K\pi$ channels can also be used to place a constraint on ϕ_3 [34–37] (Sec. 2.5.1). A puzzling result that has been observed is that the amount of direct *CP* violation differs for $B^0 \rightarrow K^+\pi^-$ and $B^+ \rightarrow K^+\pi^0$ although the leading diagrams differ only by the spectator quark [38]. The *CP* parameters and branching ratios from these $K\pi$ channels can be used for a model independent search for new physics using a sum rule (Sec. 2.6).

2.4.1 *CP* violation in $b \rightarrow u\bar{u}d$ Transitions

Belle [39] and BaBar [38] have reported time-dependent *CP* asymmetries in the channels, $B^0 \rightarrow \pi^+\pi^-, \rho^\pm\pi^\mp, \rho^+\rho^-$. The decay channels which are mediated by $b \rightarrow u\bar{u}d$ transition are sensitive to the angle ϕ_2 of the unitarity triangle as we will show in the following.

One important channel of this analysis is the decay $B^0 \rightarrow \pi^+\pi^-$. The decay amplitudes can be visualised as Feynman diagrams. The charged current transitions are known as

tree level diagram and the second order neutral current transitions are named “penguin diagram”. The Feynman diagrams for the tree level decay and the penguin are shown in Fig. 2.5. We can look at the suppression of the decay due to factors originating from the **CKM** matrix in terms of the Cabibbo angle $\lambda = \sin \theta_C$. We find a suppression of order λ^3 for the tree diagram and λ^3 for the penguin diagram. Since the magnitude of the tree amplitude and the penguin amplitude are of almost same size we are expecting a relatively large direct CP violation, but theoretical predictions vary widely [27–33]. In addition, interference between the mixing amplitude and the decay amplitudes occurs which results in time-dependent CP violation. The $\pi^+\pi^-$ final state is an eigenstate of CP , with

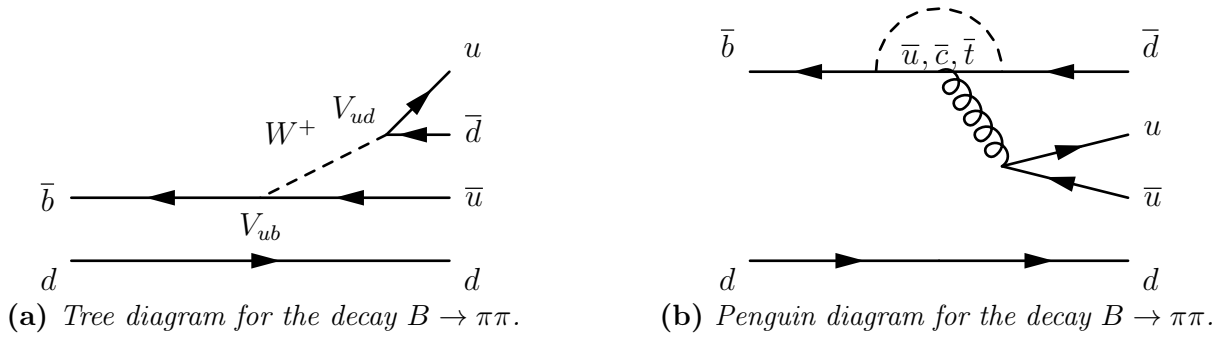


Figure 2.5: Feynman diagrams illustrating the tree and penguin decay of the decay $B \rightarrow \pi\pi$.

an eigenvalue of $CP = +1$. As we know from Eq. 2.37, the time dependent rate asymmetry is described with two parameters only, \mathcal{A}_{CP} and \mathcal{S}_{CP} . For the special case of the tree decay of $B^0 \rightarrow \pi^+\pi^-$, we can derive their expected values in terms of the **CKM** matrix elements and therefore also in terms of the angle ϕ_2 of the unitarity triangle. This is explicitly done in Sec. 2.4.1. Because \mathcal{A}_{CP} and \mathcal{S}_{CP} are also accessible by measuring the time dependent rate asymmetry we can determine the angle ϕ_2 . The parameters \mathcal{A}_{CP} and \mathcal{S}_{CP} determine the direct and the mixing-induced CP violation. In the case of no direct CP violation, the angle ϕ_2 is related to \mathcal{S}_{CP} in the following way [40]:

$$\mathcal{S}_{CP} = \frac{2 \operatorname{Im} \lambda_{CP}}{|\lambda_{CP}|^2 + 1} = \sin(2\phi_2).$$

In general, where tree and penguin diagrams contribute to the amplitude, \mathcal{S}_{CP} for $B \rightarrow \pi^+\pi^-$ is given by [40]

$$\mathcal{S}_{CP} = \sqrt{1 - \mathcal{A}_{CP}^2} \sin(2\phi_2^{eff}).$$

Because of contributions from penguin decays we can only measure an effective angle ϕ_2^{eff} . To extract the pure ϕ_2 angle, we can perform an isospin analysis using the various charge combinations in the di-pion final states, which are related by isospin symmetry. Using the isospin analysis, the $\Delta\phi_2 = \phi_2 - \phi_2^{eff}$ can be determined. Details about the isospin analysis procedure are shown in the next section 2.5.

2.5 Determination of ϕ_2 using Isospin correlated $B \rightarrow \pi\pi$ decays

In the previous section, we showed that it is possible to measure the angle $\sin\phi_2^{eff}$ with the decay $B^0 \rightarrow \pi^+\pi^-$. But the angle ϕ_2^{eff} is equal to the angle ϕ_2 of the unitarity triangle only if there is no contribution from loop corrections like penguin-diagrams in the decay. To measure the value of $\Delta\phi_2$ coming from the penguin diagrams we can utilize isospin symmetry. This was shown by Gronau and London in 1990 [41] and we will follow their derivation. Bose-Einstein statistics dictates that the $\pi\pi$ mesons, which are necessarily on an S wave can have a total isospin $I = 0$ or $I = 2$, $I = 1$ is forbidden. The tree diagram (see Fig. 2.5a) can lead to both a $I = 0$ and a $I = 2$ final state. The penguin diagram (2.5b), however, can only lead to $\pi\pi$ states with $I = 0$ because the gluon carries no isospin [41]. Since the B meson is isospin $I = 1/2$, the $\Delta I = \frac{3}{2}$ operator occurs only in the tree level diagram while the $\Delta I = \frac{1}{2}$ operator is present in the tree-level and the penguin diagrams. Finally, the $\pi^\pm \pi^0$ final state can have only $I = 2$. For this reason the process $B^\pm \rightarrow \pi^\pm\pi^0$ is mediated by the tree diagram only. The amplitudes A^{+-} , A^{+0} and A^{00} for the decays $B^0 \rightarrow \pi^+\pi^-$, $B^0 \rightarrow \pi^0\pi^0$ and $B^+ \rightarrow \pi^+\pi^0$, respectively, can be expanded in terms of isospin $I = 0$ and $I = 2$ components. Writing $\pi^+\pi^-$ as a linear combination $\pi^+\pi^- = (\pi^+_1\pi^-_2 + \pi^-_1\pi^+_2)/\sqrt{2}$ and similar for $\pi^+\pi^0$ and using the Clebsch-Gorden coefficients, we find

$$\frac{1}{\sqrt{2}}A^{+-} = A_2 - A_0, \quad (2.41)$$

$$, A^{00} = 2A_2 + A_0, A^{+0} = 3A_2 \quad (2.42)$$

where A_0 and A_2 denote the amplitude contributing to the isospin $I = 0$ and $I = 2$ di-pion final state. These equations can be rewritten to yield a complex triangle relation.

$$\frac{1}{\sqrt{2}}A^{+-} + A^{00} = A^{+0}. \quad (2.43)$$

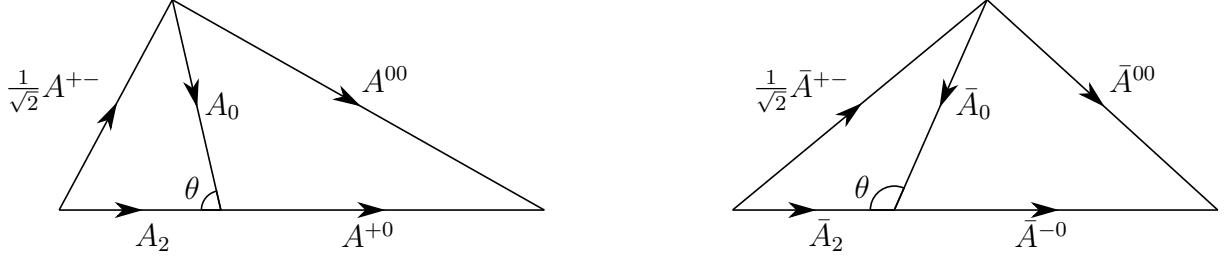
The corresponding triangle relation for the charge conjugated process reads:

$$\frac{1}{\sqrt{2}}\bar{A}^{+-} + \bar{A}^{00} = \bar{A}^{-0}. \quad (2.44)$$

The amplitudes \bar{A}^{+-} , \bar{A}^{00} and \bar{A}^{-0} , correspond to the processes $\bar{B}^0 \rightarrow \pi^+\pi^-$, $\bar{B}^0 \rightarrow \pi^0\pi^0$ and $B^- \rightarrow \pi^-\pi^0$. One can obtain the amplitudes A from the amplitudes \bar{A} by changing the sign of the **CKM** weak phase. The strong phase, however, stays the same. The A_2 amplitude has only contributions from the tree level diagram, so that

$$A_2 = |A_2|e^{i(\delta_2+\phi_t)}, \quad \bar{A}_2 = |A_2|e^{i(\delta_2-\phi_t)}, \quad (2.45)$$

where δ_2 is the final-state-interaction phase coming from the $I = 2$ final state, and ϕ_t is the tree-level **CKM** phase. We can conclude that the magnitude of the amplitudes A^{+0} and



(a) The isospin triangle for the Eq. 2.43.

(b) The isospin triangle for the Eq. 2.44.

Figure 2.6: Isospin triangles.

A^{-0} are the same ($|A^{+0}| = |A^{-0}|$). Also, it should be stated that there is no easy relation between the other amplitudes. The magnitudes of the decay amplitudes are obtainable from experiment. For the charged B meson, we obtain $|A^{+0}|$ and $|A^{-0}|$ directly from the branching ratio. For the neutral B mesons, one has to take mixing into account. The magnitude of the amplitudes $|A^{+-}|$, $|\bar{A}^{+-}|$, $|A^{00}|$, $|\bar{A}^{00}|$ can be measured using Eq. 2.36.

Looking at the triangles defined in Eq. 2.43 and Eq. 2.44, we observe that the triangles are congruent and have identical orientation in this limit.

The $\sin \Delta m_d t$ term arises due to interference of A_f and \bar{A}_f in the mixing. For the $\pi^+\pi^-$ final state, the interference λ_{CP} is given by

$$\lambda_{CP} = \frac{q}{p} e^{-2i\phi_t} \left[\frac{1 - \bar{z}}{1 - z} \right] = e^{-2i(\phi_t + \phi_M)} \left[\frac{1 - \bar{z}}{1 - z} \right], \quad (2.46)$$

where Eq. 2.42 and Eq. 2.45 have been used and

$$z \equiv \frac{A_0}{A_2}, \quad \bar{z} \equiv \frac{\bar{A}_0}{\bar{A}_2}. \quad (2.47)$$

In the next step, we want to express the phases of the amplitudes with the angles of the unitarity triangle (given in Eq. 2.5). We are using $\phi_M = \phi_1$ and $\phi_t = \phi_3$ where each equations can be checked with the mixing or tree Feynman diagrams, respectively. The CKM matrix elements in the diagram are corresponding to the angle definition. Assuming a closed unitarity triangle ($\phi_3 + \phi_1 = \pi - \phi_2$) we find

$$\text{Im } \lambda_{CP+-} = \text{Im} \left(e^{2i\phi_2} \left[\frac{1 - \bar{z}}{1 - z} \right] \right). \quad (2.48)$$

If penguin contribution can be neglected ($z = \bar{z}$) Eq. 2.48 simplifies to $\text{Im } \lambda_{CP+-} = \sin 2\phi_2$. In the general case of contributions from penguins. z is not equal to \bar{z} . In this case. the knowledge of their phases and magnitudes is necessary to evaluate ϕ_2 . To obtain z and \bar{z} we perform a simple geometrical consideration on the isospin triangle. Looking at the

triangle from Eq. 2.43 which are shown in figure 2.6a, we can see all the amplitudes in the complex plane. Please note that the magnitudes of the sides can be extracted from the branching ratios of the isospin related processes. With the knowledge of A^{+0} , one can immediately determine A_2 with Eq. 2.42. With additional information of the magnitude of the other two sides, one can determine the magnitude of A_0 or more conveniently $\cos \theta$. It is important to state that it is not possible to determine the sign of θ . This leaves us with a twofold ambiguity where one solution is the triangle shown in the figure and the other solution being the triangle mirrored at the A^{+0} axis. In an analogous way, we can proceed with the *CP*-conjugated processes shown in figure 2.6b. Equation 2.48 can be parametrised with the magnitude $|z|$ and a phase θ to be

$$\text{Im } \lambda_{CP+-} = \text{Im} \left(e^{2i\phi_2} \left[\frac{1 - |\bar{z}|e^{\pm i\bar{\theta}}}{1 - |z|e^{\pm i\theta}} \right] \right), \quad (2.49)$$

with $|z|$, $|\bar{z}|$, θ and $\bar{\theta}$ all known in principle. We convert the term between the square brackets into a magnitude m_{+-} which is unambiguously known from the four parameters and four phases which are dependent on the choice of signs in Eq. 2.49. These four phases are denoted by $\pm\epsilon_{+-}$ and $\pm\eta_{+-}$. The unbiased ϕ_2 is a solution to one of the following four equations,

$$\sin(2\phi_2 \pm \epsilon_{+-}) = (\text{Im } \lambda_{CP+-})/m_{+-}, \quad (2.50)$$

$$\sin(2\phi_2 \pm \eta_{+-}) = (\text{Im } \lambda_{CP+-})/m_{+-}. \quad (2.51)$$

This leaves us with a four fold ambiguity in total.

Luckily, we can disentangle this ambiguity using the process $B^0 \rightarrow \pi^0\pi^0$. In a similar approach the coefficient of the $\sin \Delta m_d t$ term is given by

$$\text{Im } \lambda_{CP00} = \text{Im} \left(e^{2i\phi_2} \left[\frac{1 - |\bar{z}|e^{\pm i\bar{\theta}}}{1 - |z|e^{\pm i\theta}} \right] \right). \quad (2.52)$$

Denoting the magnitude and phase of the quantity within the square brackets gives us a magnitude m_{00} and the four phases $\pm\epsilon_{00}$ and $\pm\eta_{00}$. Analogous to the above, ϕ_2 must be a solution to one of the four equations,

$$\sin(2\phi_2 \pm \epsilon_{00}) = (\text{Im } \lambda_{CP00})/m_{00}, \quad (2.53)$$

$$\sin(2\phi_2 \pm \eta_{00}) = (\text{Im } \lambda_{CP00})/m_{00}. \quad (2.54)$$

These two sets of equations determine $\sin \phi_2$ unambiguously in general. Only in the very special case where solutions of Eq. 2.51 and Eq. 2.54 overlap, we are left with a twofold ambiguity.

The isospin analysis using our measured results is performed in section 6.4.

2.5.1 CP violation in $b \rightarrow sud$ transitions

A very puzzling observation in recent years has been made in $b \rightarrow sud$ transitions. Although the decay $B^0 \rightarrow K^+\pi^-$ and the decay $B^+ \rightarrow K^+\pi^0$ only differ by the spectator quark (u,d), a sizeable difference between the branching ratios and direct CP violation is observed. To solve this so called “ $K\pi$ puzzle” [42], we need to further reduce the uncertainties on our measurements. Our analysis contributes the measurement of the decay $B^0 \rightarrow K^+\pi^-$. The

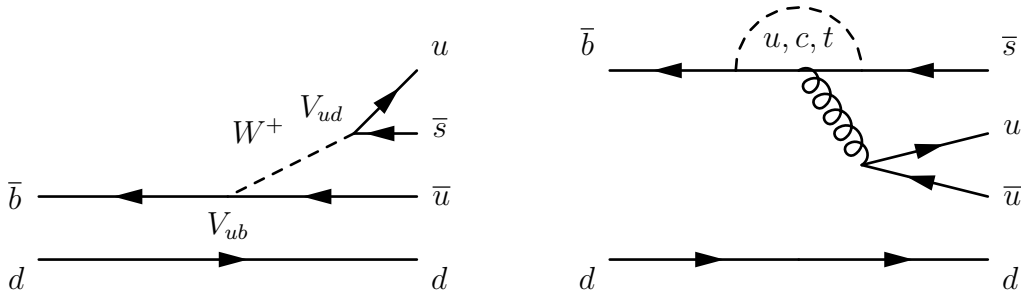


Figure 2.7: tree and penguin diagram of the decay $B^0 \rightarrow K^+\pi^-$

decay of $B^0 \rightarrow K^+\pi^-$ is mediated by a tree level diagram and a penguin diagram shown in Fig. 2.7. We can roughly determine the relative size of the amplitude of the tree diagram and the penguin diagram by looking at the **CKM** factors in terms of $\lambda = \sin\theta_C$, at the vertices. In the tree diagram, we obtain a suppression factor of λ^3 for the $b \rightarrow u$ transition and a factor of λ in the $W^+ \rightarrow su$ transition. The total suppression factor from the **CKM** matrix is therefore λ^4 . For the penguin diagram, however, we find a λ^2 suppression only. This means that the $B^0 \rightarrow K^+\pi^-$ decay is dominated by a penguin diagram and not a tree level diagram. This has several implications. First, we expect direct CP violation since a tree amplitude and a penguin amplitude contribute to the decay. But because the magnitudes of the tree and penguin decay are so different a small \mathcal{A}_{CP} is expected. As we have seen earlier, the direct CP violation can be measured without timing information. Also we do not have to find the B -tag of the other B meson because the $K^+\pi^-$ and $K^-\pi^+$ final states are flavour specific (self-tagging). This means that we can determine the flavour of the decaying B meson by examining the charge of the final state particles the kaon and pion. The direct CP violation can be measured using

$$\mathcal{A}_{CP} = \frac{N(\bar{B}^0 \rightarrow K^-\pi^+) - N(B^0 \rightarrow K^+\pi^-)}{N(\bar{B}^0 \rightarrow K^-\pi^+) + N(B^0 \rightarrow K^+\pi^-)}. \quad (2.55)$$

Last but not least, the dominant penguin amplitude enhances our sensitivity to new physics (NP). Heavy particles as virtual particles in the loop have measurable contributions to the branching ratios and CP parameters. These NP particles can have a mass much higher than the energy available in the collision. The mass reach is then limited by the available statistics [40]. To test for new physics beyond the Standard Model, we are using the methods described in the next section 2.6.

2.6 Searches on Physics beyond the Standard Model in $B^0 \rightarrow K\pi$ Decays

In this section we are going to present two ways to search for new physics beyond the Standard Model in $B^0 \rightarrow K\pi$ decays. In the first case, we are creating ratios of branching fractions of all possible charged and neutral $B^0 \rightarrow K\pi$ decays. We can compare the resulting numbers with the predictions from the Standard Model. In the second case, we are evaluating a $K\pi$ sum rule [43–46]. If the sum rule is not fulfilled within the uncertainties, we have a hint for new physics beyond the SM. In both cases we are exploiting the isospin symmetry in the decays of $B^0 \rightarrow K\pi$.

Historically a discrepancy of the measured difference $R_c - R_n$ and the SM expectation of zero has been observed at a 2σ level. This 2σ discrepancy, also known as the “ $K\pi$ puzzle” has gradually disappeared once more precise measurements have been published. This analysis is contributing to solve the $K\pi$ puzzle. The difference of the ratios R_c and R_n is used to reduce systematics in both the theoretical and the experimental calculations. One uses the following definitions [44]

$$R_c = \frac{2\mathcal{B}(B^+ \rightarrow K^0\pi^+)}{\mathcal{B}(B^+ \rightarrow K^+\pi^0)} \quad (2.56)$$

$$R_n = \frac{\mathcal{B}(B^0 \rightarrow K^+\pi^-)}{2\mathcal{B}(B^0 \rightarrow K^0\pi^0)} \quad (2.57)$$

Turning away from the branching ratios and having a look at the direct CP violation parameters $\mathcal{A}_{CP}(B^0 \rightarrow K^+\pi^-) = -0.094 \pm 0.018 \pm 0.008$ [38] and $\mathcal{A}_{CP}(B^+ \rightarrow K^+\pi^0) = +0.07 \pm 0.03 \pm 0.01$ [38], we find that they have a different magnitude and sign although they differ only by the spectator quark. But the expectation is that the direct CP violation in these channels should be of approximately the same magnitude and sign [47]. The difference is $\Delta\mathcal{A}_{CP} = \mathcal{A}_{CP}(B^+ \rightarrow K^+\pi^0) - \mathcal{A}_{CP}(B^0 \rightarrow K^+\pi^-) = +0.148 \pm 0.028$, which is 5.3σ different from the SM which predicts a vanishing difference. There are attempts to explain this “ $\Delta\mathcal{A}_{CP}$ puzzle” with an enhanced colour-suppressed tree [30] or electroweak penguin processes [48] or a combination [49] that may contribute only to $B^+ \rightarrow K^+\pi^0$ decays. But all these explanations have in common that the predicted strong phase does not fit into the theoretical framework of factorisation.

Gronau *et. al.* [43–46] suggested to evaluate a $K\pi$ sum rule (Eq. 2.58)

$$\mathcal{A}_{CP}(K^+\pi^-) + \mathcal{A}_{CP}(K^0\pi^+) \frac{\mathcal{B}(K^0\pi^+) \tau_0}{\mathcal{B}(K^+\pi^-) \tau_+} = \mathcal{A}_{CP}(K^+\pi^0) \frac{2\mathcal{B}(K^+\pi^0) \tau_0}{\mathcal{B}(K^+\pi^-) \tau_+} + \mathcal{A}_{CP}(K^0\pi^0) \frac{2\mathcal{B}(K^0\pi^0)}{\mathcal{B}(K^+\pi^-)}, \quad (2.58)$$

where $\tau_0(\tau_+)$ is the lifetime of the B^0 (B^+) meson. The derivation mainly exploits the isospin symmetry and $SU(3)$ flavour symmetry. No assumptions are made upon the size of the colour-suppressed tree and electroweak penguin amplitudes. If NP is found it is most

likely that a $\Delta I = 1$ operator in the effective Hamiltonian, forbidden in the SM (see above), is present [44].

2.7 The Decay $B^0 \rightarrow K^+K^-$

The Standard Model provides an expectation for the branching ratio of the $B^0 \rightarrow K^+K^-$ decay of roughly $\mathcal{B}(K^+K^-) = (0.013_{-0.013}^{+0.088}) \times 10^{-6}$ [28, 50, 51]. The dominant Feynman diagram is shown in Fig. 2.8. The main difficulty in making theory predictions on the branching ratio is the hadronisation (see next section 2.8). It is not calculable perturbatively and therefore can only be taken from experiments.

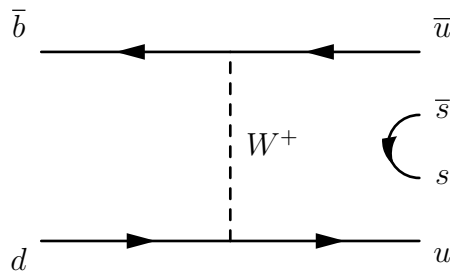


Figure 2.8: The dominant Feynman diagram for the decay $B^0 \rightarrow K^+K^-$

2.8 Theory Predictions on Branching Fractions and CP Parameters

The first studies to calculate predictions for the branching ratios and CP parameters of $B^0 \rightarrow h^+h^-$ decays use effective field theories [28]. The effective field theory usually works in the limit of a meson containing one heavy quark (heavy quark limit) decaying into two bodies (quasi two-body decays). The calculation is factorized into a perturbatively calculable part, the Wilson coefficients, and a hadronization part. We summarise the theory predictions of the branching fractions and direct CP violation in table 2.3 and 2.4 respectively.

Results from Beneke *et al.* [28] use QCD factorisation and determination of the Wilson coefficients. Ciuchini *et al.* [31] contra dicts this approach and proposes to use charming and GIM penguin contributions to reconcile the theoretical predictions with the experimental evidence.

An extensive study performed by Buras *et al.* [29] claims to explain all features of $B^0 \rightarrow h^+h^-$ decays using the Standard Model. The experimental results can be accommodated within the SM through non-factorisable hadronic interference effects. The study uses the branching ratios and CP parameters of $B^0 \rightarrow \pi^+\pi^-$ as input.

Table 2.3: *Theory predictions for CP averaged branching fractions*

Mode	branching ratio[10^{-6}]	source
$B^0 \rightarrow \pi^+\pi^-$	$8.9^{+5.5}_{-4.7}$	[28]
$B^0 \rightarrow \pi^+\pi^-$	4.7 ± 0.8	[31]
$B^0 \rightarrow \pi^+\pi^-$	$7.0^{+2.0}_{-1.5}$	[47]
$B^0 \rightarrow K^+\pi^-$	$16.3^{+15.2}_{-8.5}$	[28]
$B^0 \rightarrow K^+\pi^-$	18.4 ± 1.3	[31]
$B^0 \rightarrow K^+\pi^-$	$15.5^{+3.1}_{-2.5}$	[47]
$B^0 \rightarrow K^+K^-$	$0.013^{+0.088}_{-0.013}$	[28]
$B^0 \rightarrow K^+K^-$	0.06	[47]

Table 2.4: *Theory predictions for direct CP violation*

Mode	$\mathcal{A}_{CP}[10^{-2}]$	source
$B^0 \rightarrow \pi^+\pi^-$	$-6.5^{+13.7}_{-13.3}$	[28]
$B^0 \rightarrow \pi^+\pi^-$	$ 52 \pm 18 $	[31]
$B^0 \rightarrow \pi^+\pi^-$	23 ± 7	[47]
$B^0 \rightarrow K^+\pi^-$	$4.5^{+9.1}_{-9.9}$	[28]
$B^0 \rightarrow K^+\pi^-$	$ 21 \pm 10 $	[31]
$B^0 \rightarrow K^+\pi^-$	-17 ± 5	[47]
$B^0 \rightarrow K^+\pi^-$	$14.0^{+13.9}_{-8.7}$	[29]

2.9 Current Status of the Experimental Measurements

The Belle collaboration as well as the BaBar collaboration performed these branching fraction measurements. Since very recent we also have results from the CDF and LHCb collaborations.

Belle: [52, 53]

$$\mathcal{B}(B^0 \rightarrow \pi^+\pi^-) = (5.1 \pm 0.2(\text{stat}) \pm 0.2(\text{syst})) \times 10^{-6}, \quad (2.59)$$

$$\mathcal{B}(B^0 \rightarrow K^+\pi^-) = (19.9 \pm 0.4(\text{stat}) \pm 0.8(\text{syst})) \times 10^{-6}, \quad (2.60)$$

$$\mathcal{B}(B^0 \rightarrow K^+K^-) = (9 \pm 18(\text{stat}) \pm 1(\text{syst})) \times 10^{-8}. \quad (2.61)$$

BaBar: [54, 55]

$$\mathcal{B}(B^0 \rightarrow \pi^+\pi^-) = (5.5 \pm 0.4(\text{stat}) \pm 0.3(\text{syst})) \times 10^{-6}, \quad (2.62)$$

$$\mathcal{B}(B^0 \rightarrow K^+\pi^-) = (19.1 \pm 0.6(\text{stat}) \pm 0.6(\text{syst})) \times 10^{-6}, \quad (2.63)$$

$$\mathcal{B}(B^0 \rightarrow K^+K^-) = (4 \pm 15(\text{stat}) \pm 8(\text{syst})) \times 10^{-8}, \quad (2.64)$$

CDF: [56, 57]

$$\mathcal{B}(B^0 \rightarrow \pi^+\pi^-) = (5.0 \pm 0.3(\text{stat}) \pm 0.4(\text{syst})) \times 10^{-6}, \quad (2.65)$$

$$\mathcal{B}(B^0 \rightarrow K^+K^-) = (23 \pm 10(\text{stat}) \pm 10(\text{syst})) \times 10^{-8}, \quad (2.66)$$

LHCb: [58]

$$\mathcal{B}(B^0 \rightarrow \pi^+\pi^-) = (5.1 \pm 0.2(\text{stat}) \pm 0.4(\text{syst})) \times 10^{-6}, \quad (2.67)$$

$$\mathcal{B}(B^0 \rightarrow K^+K^-) = (11 \pm 5(\text{stat}) \pm 6(\text{syst})) \times 10^{-8}. \quad (2.68)$$

A summary of all measurements of B decays into light hadrons is shown in Fig. 2.9.

Historically, Belle determined values for \mathcal{A}_{CP} incompatible with zero while BaBar determined values compatible with zero. This historical discrepancy is not existing any more but a tension remains. Fig. 2.10 show the status of the tension before the update of the CP parameters by this analysis. Also some of the measurements could be performed by the CDF and LHCb collaboration. We will also report their results here. Belle: [38, 39]

$$\mathcal{A}_{CP}(B^0 \rightarrow \pi^+\pi^-) = +0.55 \pm 0.08(\text{stat}) \pm 0.05(\text{syst}) \quad (2.69)$$

$$\mathcal{S}_{CP}(B^0 \rightarrow \pi^+\pi^-) = -0.61 \pm 0.10(\text{stat}) \pm 0.04(\text{syst}) \quad (2.70)$$

$$\mathcal{A}_{CP}(B^0 \rightarrow K^+\pi^-) = -0.094 \pm 0.018(\text{stat}) \pm 0.008(\text{syst}) \quad (2.71)$$

BaBar: [55]

$$\mathcal{A}_{CP}(B^0 \rightarrow \pi^+\pi^-) = +0.21 \pm 0.09(\text{stat}) \pm 0.02(\text{syst}) \quad (2.72)$$

$$\mathcal{S}_{CP}(B^0 \rightarrow \pi^+\pi^-) = -0.60 \pm 0.11(\text{stat}) \pm 0.03(\text{syst}) \quad (2.73)$$

$$\mathcal{A}_{CP}(B^0 \rightarrow K^+\pi^-) = -0.107 \pm 0.018(\text{stat})|_{-0.004}^{+0.008}(\text{syst}) \quad (2.74)$$

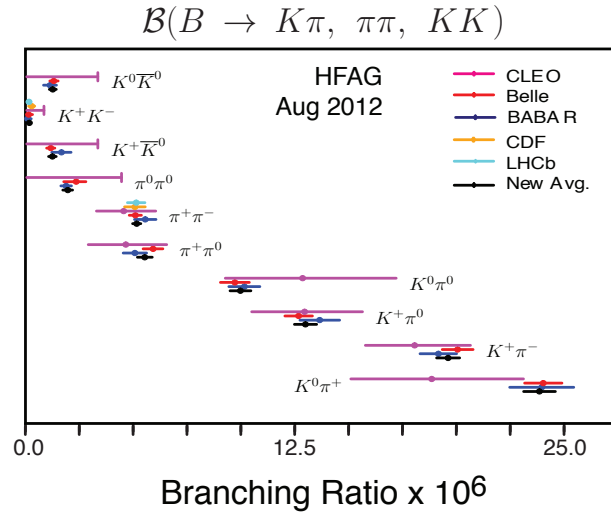


Figure 2.9: Current results of branching fraction measurements from various experiments [59]

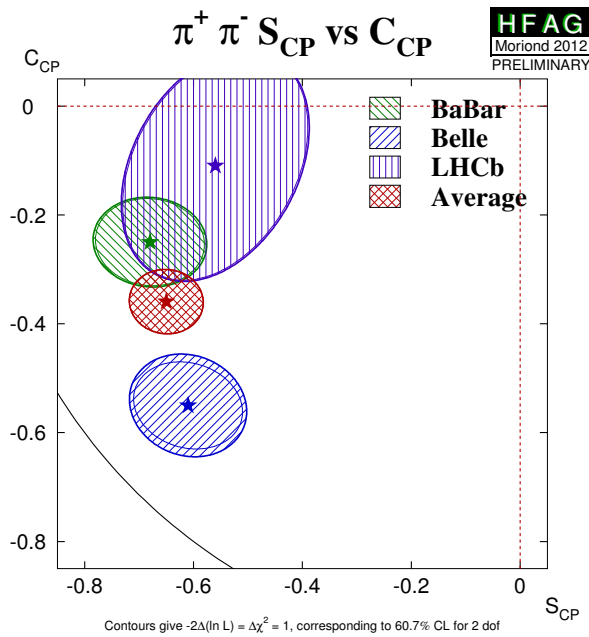


Figure 2.10: Direct CP violation vs. mixing induced CP violation parameters for the decay $B^0 \rightarrow \pi^+ \pi^-$ determined from the Belle, BaBar and LHCb experiments [59]. Other experiments use a different definition of the direct CP violation parameter $\mathcal{A}_{CP} = -C_{CP}$.

CDF: [60]

$$\mathcal{A}_{CP}(B^0 \rightarrow K^+\pi^-) = -0.083 \pm 0.013(\text{stat}) \pm 0.003(\text{syst}) \quad (2.75)$$

LHCb: [61, 62]

$$\mathcal{A}_{CP}(B^0 \rightarrow \pi^+\pi^-) = +0.11 \pm 0.21(\text{stat}) \pm 0.03(\text{syst}) \quad (2.76)$$

$$\mathcal{S}_{CP}(B^0 \rightarrow \pi^+\pi^-) = -0.56 \pm 0.17(\text{stat}) \pm 0.03(\text{syst}) \quad (2.77)$$

$$\mathcal{A}_{CP}(B^0 \rightarrow K^+\pi^-) = -0.088 \pm 0.011(\text{stat}) \pm 0.008(\text{syst}) \quad (2.78)$$

Chapter 3

The Belle Experiment

The Belle experiment [63] is located at the High Energy Accelerator Research Organization (KEK) in Tsukuba, Japan. It consists of an accelerator, a storage ring (KEKB) and the Belle detector.

The KEKB storage ring [64] is a electron positron collider and the current world record holder in instantaneous luminosity ($2.11 \times 10^{34} \text{ cm}^{-2}\text{s}^{-1}$). The luminosity is proportional to the rate of physics events. The center-of-mass energy of the electrons and positrons is 10.58 GeV which corresponds to the mass of the $\Upsilon(4S)$ resonance. The interesting physics events are decays of the $\Upsilon(4S)$ resonance into $B\bar{B}$ pairs. These events are recorded by the Belle detector. To perform high precision CP measurements we need high event statistics because many processes are very rare. This goes hand-in-hand with the high luminosity delivered by KEKB.

The Belle detector is built around the interaction point of the positron and the electron beam. The Belle detector is a large-solid-angle magnetic spectrometer. It is especially designed to have a good spatial vertex resolution which is important for CP analysis. An important competing experiment is the BaBar experiment [65] at the PEP-II storage ring. BaBar is very similar to the Belle experiment, but completely independent. Having a second experiment gives us a unique possibility to compare our results.

3.1 The KEKB Accelerator

The KEKB accelerator consists of a particle source, several pre-accelerators, a linear accelerator (LINAC) and the KEKB storage ring [64]. The electrons and positrons are accelerated in the LINAC to an energy of 3.5 GeV and 8 GeV respectively. After acceleration, the electrons are injected into the High Energy Ring (HER) and the positrons are injected into the Low Energy Ring (LER). The circumference of both rings is 3012 m and about 5000 bunches of particles reside in each ring when the storage ring is completely filled

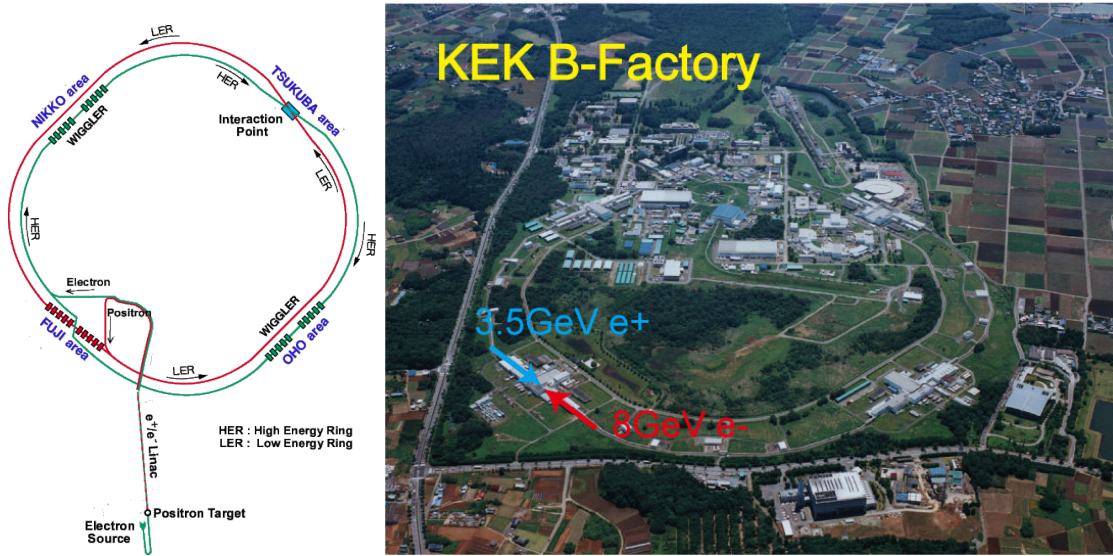


Figure 3.1: The KEKB accelerator ring. The Belle detector is located at the Tsukuba area.

(Fig. 3.1). At the interaction point (IP), the bunches from the HER and LER collide at a finite angle of 22 mrad. To compensate for the drop in luminosity due to the finite crossing angle, crab cavities were installed. These crab cavities tilt the bunches before colliding in a way that the luminosity of a head on collision can be restored (Fig. 3.2). The asymmetric energy of the electrons and positrons leads to a Lorentz boost of the center-of-mass reference frame of $\beta\gamma = 0.425$. This boost can be used later in the analysis to translate a spatial difference between two points into a decay time difference. The center-of-mass energy is tuned to be $\sqrt{s} = 10.58$ GeV which is the mass of the $\Upsilon(4S)$. The mass of the $\Upsilon(4S)$ is right above the production threshold of $B\bar{B}$ pairs and decays exclusively into a pair of quantum mechanically entangled B mesons.

3.2 The Belle Detector

The Belle detector is a large-solid-angle magnetic spectrometer built asymmetrically around the interaction point (IP). It is built to identify most of the final state particles that can occur in B meson decays. Figure 3.3 shows a cut-out of the detector with all important subdetector components. The coordinate system of the Belle detector has the nominal IP as the origin. The z -axis is defined to be opposite to the positron beam direction. The y -axis points vertically upwards which defines the x -axis to be $x \equiv y \times z$.

Starting from inside the detector consists out of a 4 layer silicon strip vertex detector (SVD) to precisely measure the traces of charged particles coming from the decay at the IP. The start point of a particle track is called its vertex. The main goal of the SVD is to

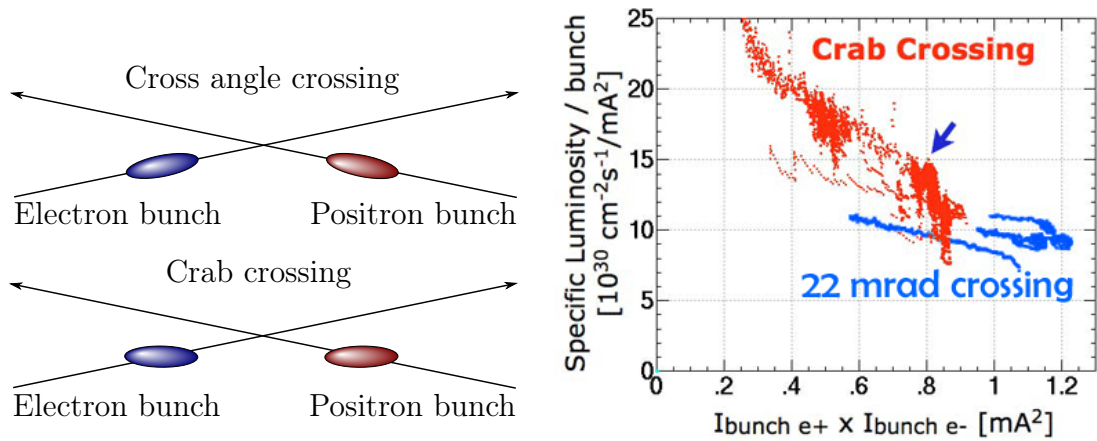


Figure 3.2: In the left diagram, crab cavities compensate for the finite crossing angle. Effectively, the whole bunch collides head-on, as would be the case without a crossing angle. The right diagram shows luminosity improvements as a function of the bunch current.

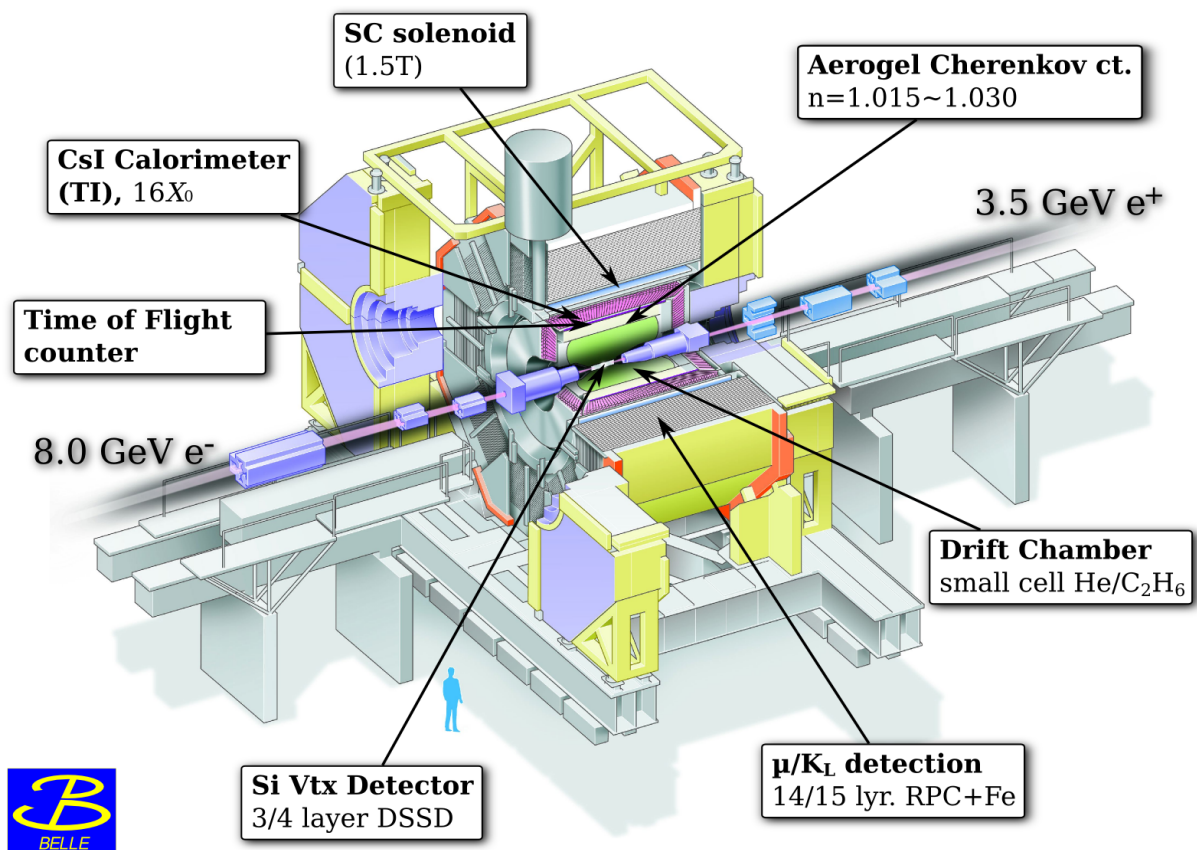


Figure 3.3: The Belle detector with all subdetector components.

precisely measure these vertices. Together with the central drift chamber (CDC), which determines the momentum of particles, the SVD and the CDC form the tracking system. To identify the particle species, aerogel threshold Cherenkov counters (ACC) and time-of-flight scintillation counters (TOF) are positioned in front of the calorimeter. The electromagnetic calorimeter (ECL), which measures photon energy deposits, consists of CsI (Ti) crystals. The ECL is located inside a superconducting solenoidal magnet with a strength of 1.5 T. The iron return yoke is instrumented to detect K_L^0 and muons. The KLM information is used in particle identification. The individual detectors are described briefly in the following sections. We follow the detailed Belle detector description from reference [63] here. In the first phase of the Belle experiment, a 2.0 cm beam pipe and a 3-layer silicon vertex detector (SVD1) was used to take 152×10^6 $B\bar{B}$ pairs data. In a second phase, the inner detectors were upgraded to provide a better spatial resolution by moving the new components closer to the IP. A 1.5 cm beam pipe, a 4-layer silicon vertex detector (SVD2) and a small-cell inner drift chamber was used to record the remaining 620×10^6 $B\bar{B}$ pairs. The geometry and the detector response of both phases SVD1 and SVD2 have been transferred into a Monte Carlo simulation. We use a GEANT3-based [66] Monte Carlo (MC) simulation to model the response of the detector.

3.2.1 The Beam Pipe

The IP is in a vacuum inside the beam pipe. The beam pipe has to obey two constraints. On one hand, it must keep the vacuum and therefore has to withstand the pressure from the atmosphere. On the other hand, it should be thin to minimize the disturbance of the traversing particles. The main cause of the disturbance is multiple scattering at the atom cores. To reduce the effect, a material with a low atomic number, Beryllium, is chosen. The beam pipe is made of two cylinders with a wall thickness of 0.5 mm at a radius of 20 mm and 23 mm respectively (Fig. 3.4). The gap is filled with paraffin for cooling. The outer cylinder contains a $50 \mu\text{m}$ thick gold layer to catch low energetic photons. These photons could, if not absorbed by the beam pipe, cause serious radiation damage to the silicon detectors just outside of the beam pipe. The total thickness of the beam pipe corresponds to 1% of a radiation length.

During the upgrade of the inner detector in 2003 (SVD2), the beam pipe was also replaced. To get better spatial resolution, the inner silicon detectors were move closer to the IP. Therefore, the beam pipe outer radius was shrunk to 15 mm.

3.2.2 The Silicon Vertex Detector

The innermost tracking detector plays a crucial role in determining the vertex resolution because it is closest to the IP. Since we are interested in measuring time dependent CP violation, we need to know the decay time difference of the B mesons which is in

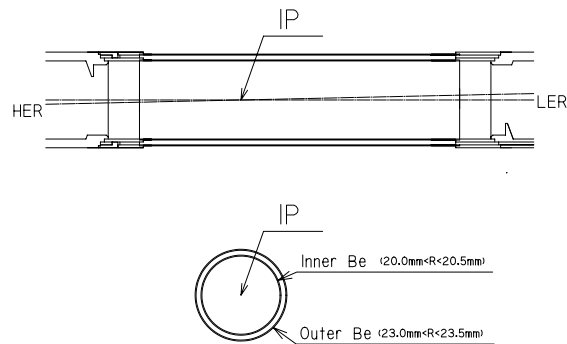


Figure 3.4: Geometry of the Belle beam pipe used for data taking of the first 152×10^6 million $B\bar{B}$ pairs.

the order of ps. We use the Lorentz boost of the asymmetric collider to translate this immeasurably small time difference into a spatial difference in the order of $100 \mu\text{m}$. This spatial displacement is measurable with a good vertex detector.

Three concentric cylindrical layers make up the SVD1 [67]. The radii are 30 mm, 45.5 mm and 60.5 mm, respectively. The region $23^\circ < \theta < 80^\circ$, in the polar angle is covered, corresponding to a large 86% of the solid angle. The SVD1 layer 1, 2 and 3 consist of 8, 10 and 14 ladders (Fig. 3.5), respectively, which are made up by two electrically independent half-ladders. A support structure holds the two half-ladders together mechanically. Each ladder consists of one or two double-sided strip detectors (DSSD) manufactured by Hamamatsu Photonics. The geometrical shape of the DSSD is 57.5 mm times 33.5 mm, with a thickness of $300 \mu\text{m}$. The DSSD consists of 1280 sense strips and 640 readout pads on each side. One side is p -doped, grounded and the strips are parallel to the beam to measure the ϕ coordinate of a traversing charged particle, whereas the other side is n -doped, biased with 75 V, with the strips perpendicular to the beam and measure the z coordinate of a traversing charged particle. In addition, p stops are implanted between the n doped strips to provide better separation. The pitch of the strips is $42 \mu\text{m}$ in z and $35 \mu\text{m}$ in ϕ . A charged particle traversing the DSSD will create electron-hole pairs. The charge carriers, electrons and holes, will travel in the electrical bias field and create a signal which can be read-out.

After the accumulation of 152×10^6 $B\bar{B}$ pairs, the SVD1 detector was replaced by the successor SVD2. The SVD2 comes with many improvements. Among them is an additional 4th layer that is placed closer to the beam pipe. The new innermost layer moved 1 cm closer to the IP to a radius of 2 cm. The acceptance was also increased to a polar angle coverage of $17^\circ < \theta < 150^\circ$. In addition, the central drift chamber (CDC) which is the outer shell of the SVD had to be redesigned to accommodate the now larger SVD. A comparison in the number of ladders and DSSDs between SVD1 and SVD2 can be found by viewing Tbl. 3.1 and Tbl 3.2.

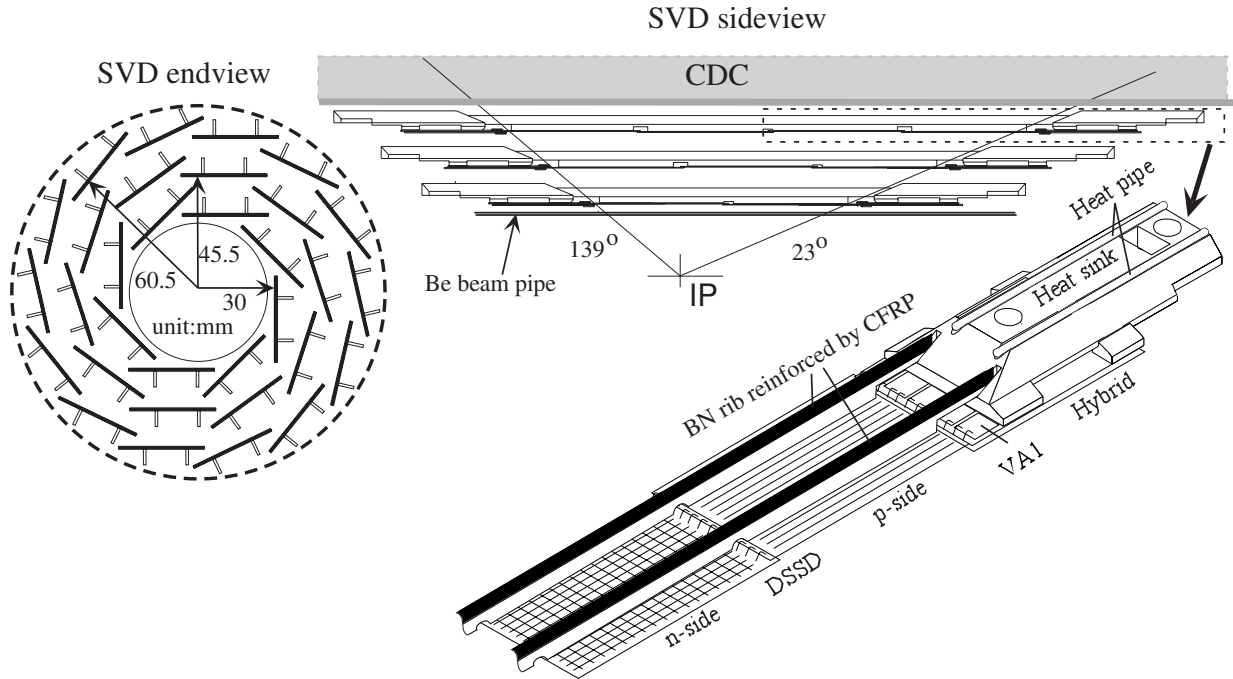


Figure 3.5: Geometry of the Silicon vertex detector (SVD1) of Belle is illustrated on the upper left. Acceptance of the Belle tracking system and the mechanical setup of a SVD ladder is shown in the upper right and lower center respectively.

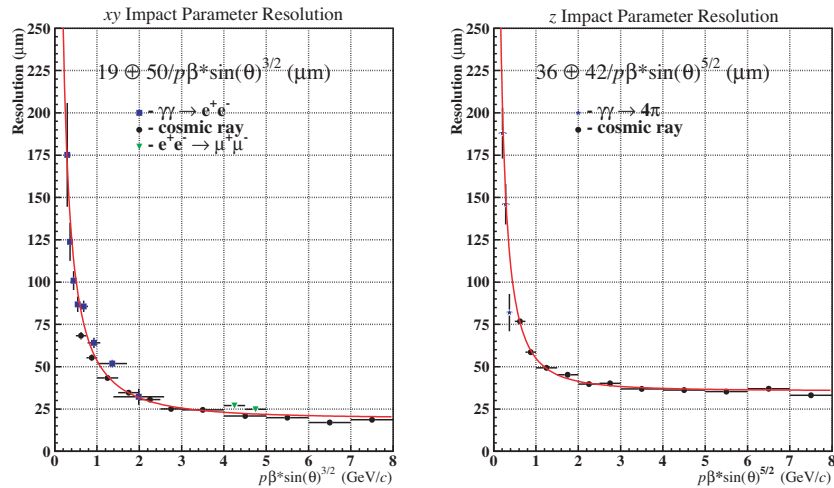


Figure 3.6: Impact parameter resolution for charged muons from cosmic ray data for SVD1. Each track is required to have associated SVD hits. The effective momentum \hat{p} is $\hat{p} \equiv p\beta \sin^{3/2} \theta$ in the left plot and $\hat{p} \equiv p\beta \sin^{5/2} \theta$ in the right plot. The red solid line indicates a fit to the data points with the parameters shown in the plot.

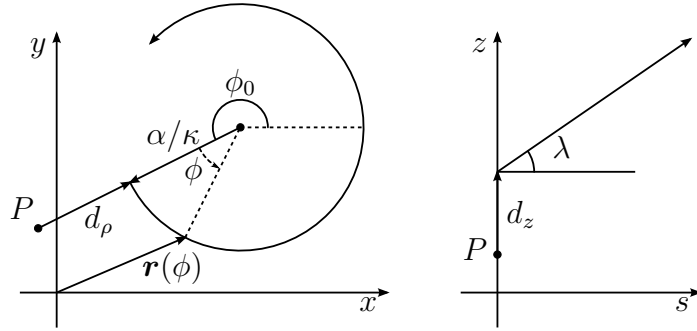
Table 3.1: *Number of ladders in each layer and number of DSSDs in each half-ladder of the SVD1*

Layers	# Ladders	# DSSDs in forward/backward half-ladder
1	8	1/1
2	10	1/2
3	14	2/2

Table 3.2: *Number of ladders in each layer and number of DSSDs in each half-ladder of the SVD2*

Layers	# Ladders	# DSSDs in forward/backward half-ladder
1	6	1/1
2	12	1/2
3	18	2/3
4	18	3/3

The particles traversing the SVD and the other tracking detectors follow a helix trajectory. The reason for the bending of the tracks is the 1.5 T magnetic field which is generated by a large solenoidal magnet (Sec. 3.2.7). The particle track helix is parametrised using 5 parameters. The 6 degrees of freedom, three from the position and three from the momentum, can be expressed by 5 parameters because we assume the magnetic field to be aligned to the detector z -axis. The track parametrization can be seen in Fig. 3.7. The

**Figure 3.7:** *The track parameters d_ρ , d_z , κ , ϕ , λ .*

best way to estimate the SVD performance is to look at the impact parameter resolution. The resolution is determined from the distribution of the track parameters d_ρ and d_z . The resolution in z and ϕ is dependent on the momentum p and the polar-angle θ and can be extracted from cosmic muon data to be

$$\sigma_z = \left(42.2 \oplus \frac{44.3}{p\beta \sin^{5/2} \theta} \right) \mu m, \quad \sigma_\phi = \left(19.2 \oplus \frac{54.0}{p\beta \sin^{3/2} \theta} \right) \mu m, \quad (3.1)$$

for SVD1 where \oplus is defined as the quadratic sum. Figure 3.6 shows the plot used for

extracting the resolution parameters [67]. For SVD2 we obtain the following parameters

$$\sigma_z = \left(27.8 \oplus \frac{31.9}{p\beta \sin^{5/2} \theta} \right) \mu m, \quad \sigma_\phi = \left(21.9 \oplus \frac{35.5}{p\beta \sin^{3/2} \theta} \right) \mu m. \quad (3.2)$$

For a time-dependent CP analysis, the z -separation between the B vertices, should be known to an accuracy of at least $100 \mu m$. It can be verified in Fig. 3.6 that this is possible in a wide momentum range with the Belle silicon detector system. To show the resolution independent of the polar angle θ a effective momentum, \hat{p} , is introduced which incorporates the polar angle.

3.2.3 The Central Drift Chamber (CDC)

The Central Drift Chamber (CDC) is an instrumented gas volume used for measuring the tracks of charged particles. The traversing particles ionize the gas volume and the ions are measured by wires, which gives the measurement concept the name “wire chamber”. It is situated around the SVD but still inside the solenoid magnet of Belle. The tracks of the charged particles are bent by the magnetic field (Sec. 3.2.7) to follow a helix path. From the curvature of these tracks and the exact knowledge of the magnetic field strength, it is possible to calculate the momentum of particles. Another quantity which can be measured is the energy loss (dE/dx) of the particles in the gas volume. This information is used to provide an additional input to the particle identification.

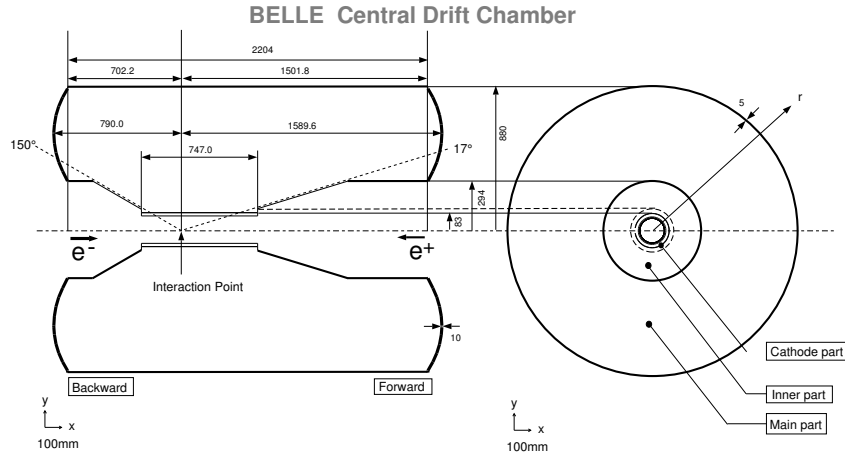
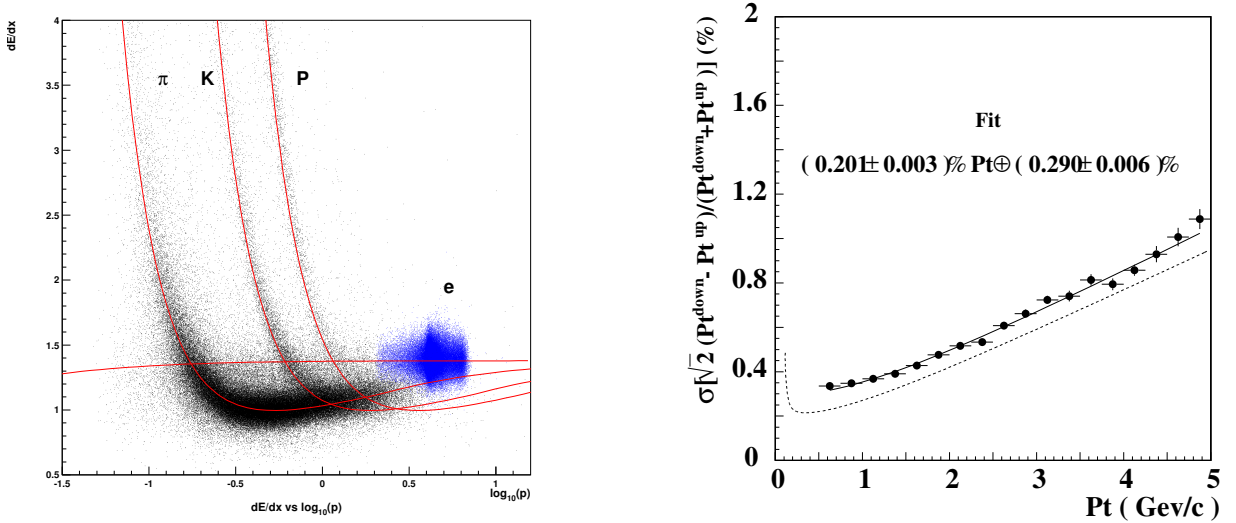


Figure 3.8: Mechanical design of the CDC including the acceptance angles.

The CDC covers a polar angle of $17^\circ < \theta < 150^\circ$ which corresponds to a solid angle of 92%. The geometrical layout can be studied in Fig. 3.8. The CDC is divided into 50 layers of sense wires and has 8400 drift cells in total. A drift cell is defined to be a positively charged sense wire surrounded by 8 negatively biased field wires. If a traversing particle ionizes the gas in the CDC the electrons drift along the field lines to a sense wire. The

bias is adjusted to generate a sufficiently strong electric field for the drifting electrons to generate secondary ionizations. These secondary ionisations result in a signal gain of about 10^6 . Wires parallel to the z -axis are primarily used to measure the transverse momentum p_T . Other so called stereo-wires are rotated by ± 50 mrad to the z -axis to deliver a spatial information on the z -direction or the θ angle in the helix representation of the track. The electronics readout uses the amplitude of the signal for measuring dE/dx . The drift time is used to determine the distance of the particle, passing a sense wire. The different energy depositions for different particle species are shown in Fig. 3.9a. A special gas mixture



(a) Energy depositions in the CDC for different particle species. Blue dots indicate the energy deposition for electrons. The red curves and their corresponding black dots show the theoretical curve and the distribution from data.

(b) CDC p_T resolution for cosmic rays depending on the p_T of the incoming particle. The dotted line showing the optimal curve for a particle with $\beta = 1$.

Figure 3.9: Energy depositions and tracking performance of the CDC.

composed of atoms with a low atomic number Z is used to reduce the effect of Coulomb scattering which would degrade momentum resolution. A mixture with 50% helium and 50% ethane is chosen. The p_T resolution is found to be

$$\sigma(p_T) = (0.2p_T \oplus 0.29/\beta)\%, \quad (3.3)$$

where \oplus indicates the quadratic sum. Figure 3.9b shows the measurement of cosmic ray data and the fit to extract the p_T resolution.

To achieve this resolution the hits from the CDC are combined with the hits from the SVD. A Kalman filter is used to get a very good track fit. The average track matching efficiency between SVD and CDC is better than 98%.

3.2.4 The Aerogel Cherenkov Counter (ACC)

The Aerogel Cherenkov counter (ACC) is used to identify different particle types. It is especially effective to discriminate electrons and charged pions against kaons. The ACC uses the Cherenkov effect. A particle emits light when traversing a medium with a velocity v_p , greater than the speed of light in this medium. The speed of light in a medium is $v_{em} = c/n$, where n is the refraction index of the material. Then,

$$v_p > v_{em} \Rightarrow n > \frac{1}{\beta} = \sqrt{1 + \left(\frac{m}{p}\right)^2}, \quad (3.4)$$

where β is the ratio between the particle velocity and the light speed in vacuum $\beta = v_p/c$. It is important to note here that the condition for Cherenkov light to be emitted, depends on the mass and momentum of the particle. The angle of the Cherenkov light emission is

$$\cos \theta = \frac{1}{n\beta}. \quad (3.5)$$

The refraction index is chosen in a way such that kaons of typical momentum do not emit light but electrons and pions of typical momentum do emit light. Because the center-of-mass system is boosted in the lab frame, the mean of the momentum distribution of the particles is not uniform in the detector. The choice of the refraction index, however, is dependent on the mean momentum. Therefore, the refraction index of the material has to change with the θ ang

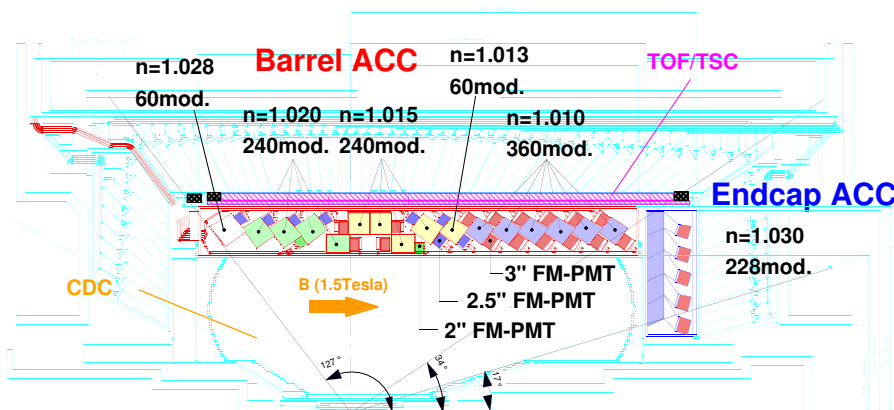


Figure 3.10: Arrangement of the ACC modules in the barrel part and the endcap.

The ACC is divided into the barrel part and the forward endcap. The barrel part consists of 960 counter modules separated into sets of 60 in the ϕ direction. The endcap is divided into 5 concentric layers with 228 modules in total. Each counter is geometrically arranged in a way that it points to the IP. Fig. 3.10 shows the geometry of the ACC.

A counter module consists of silica aerogel encased in an aluminium box of roughly $12 \times 12 \times 12 \text{cm}^2$. One or two photomultiplier tubes capable of operating in the 1.5 T magnetic field are attached to the sides of each aluminium case. Light pulses can be detected and the number of photo electrons is assigned to the particle traversing the ACC. As stated earlier, the refractive indices have to change as a function of the polar angle. In the barrel region, these refractive indices $n = 1.010, 1.013, 1.015, 1.020$ and 1.028 , are used. The ACC system gives the only particle identification in the forward endcap region. To also encompass low momentum particles, a refractive index of $n = 1.030$ is chosen. The backward endcap is not equipped with ACC modules because no high momentum tracks are expected in this region because of the boosted center-of-mass system.

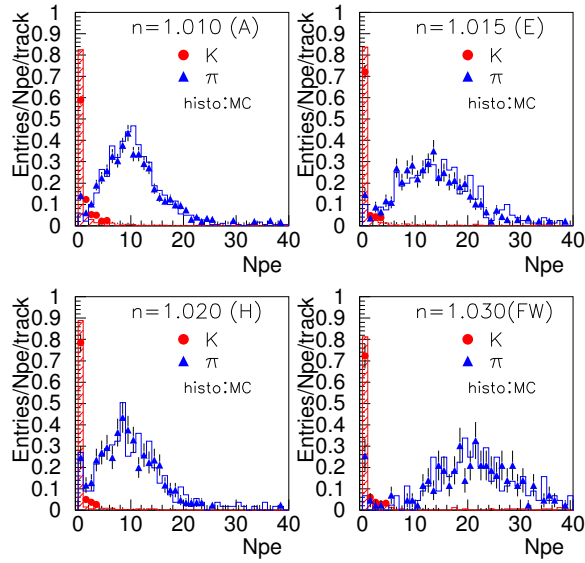


Figure 3.11: Plot showing the distribution of pulse heights for pions (in blue) and kaons (in red) in units of photo electrons. The four plots show the discrimination between pions and kaons for different optical densities.

Figure 3.11 shows the measured pulse height distribution in the ACC barrel for π^\pm and K^\pm candidates from $D^*(2010)^\pm$ decays. The clear separation between kaons and pions can be seen, and the good agreement between Monte Carlo simulation and data is also demonstrated. The overlap region between pions and kaons is the area where the identification is ambiguous or, in other words, the separation is imperfect. The ACC is operated as a threshold device. The number of photo-electrons N_{pe} from the photomultiplier is compared to a threshold $N_{\text{pe}}^{\text{thres}}$. The likelihood for an unknown particle to be of type i is given by the step function

$$\mathcal{L} = \begin{cases} \epsilon_i^{\text{Exp}} & \text{if } N_{\text{pe}} \geq N_{\text{pe}}^{\text{thres}} \\ 1 - \epsilon_i^{\text{Exp}} & \text{if } N_{\text{pe}} < N_{\text{pe}}^{\text{thres}}, \end{cases} \quad (3.6)$$

where the efficiency ϵ_i^{Exp} is determined from simulation.

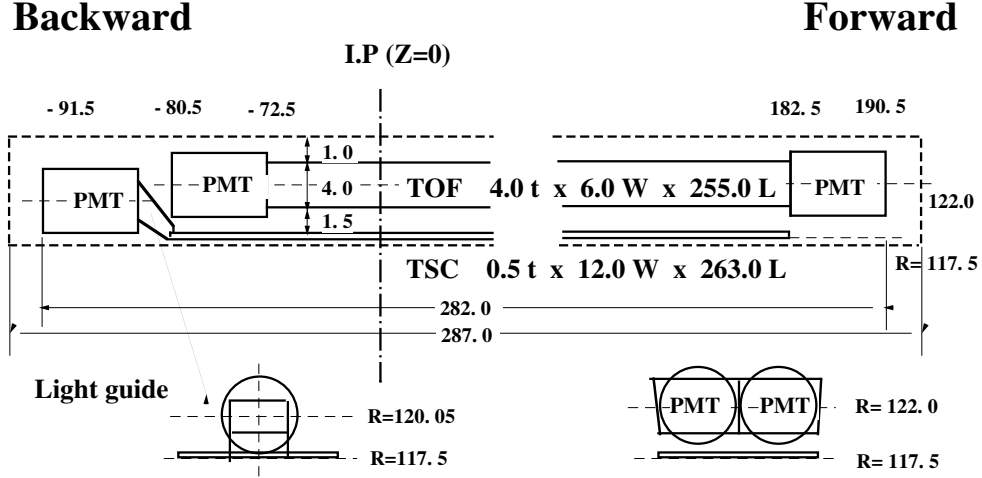


Figure 3.12: TOF module mechanical design.

3.2.5 The Time of Flight Counter (TOF)

In the momentum region below $1.2 \text{ GeV}/c$, the Belle experiment uses a Time of Flight counter (TOF) to discriminate between different particle types e.g. pions and kaons. By measuring the flight time T , of a particle from the collision to the TOF counter, we can determine its mass m , with

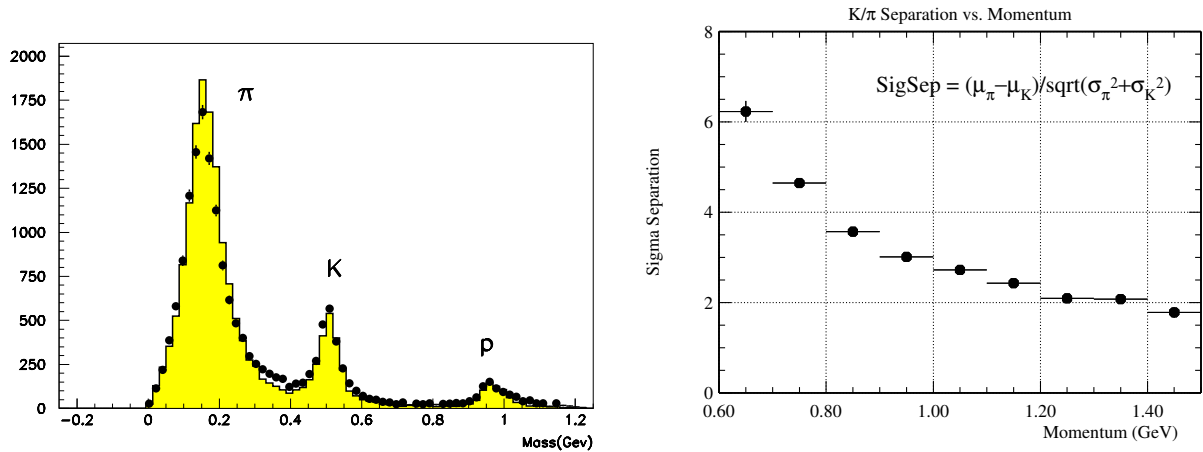
$$T = \frac{L}{c\beta} = \frac{L}{c} \sqrt{1 + \left(\frac{m}{p}\right)^2}, \quad (3.7)$$

where p is the momentum of the track and L is the flight length.

The TOF modules consist of two plastic scintillators with a photomultiplier tube attached to each. The pair of TOF counters is accompanied by a Trigger Scintillation Counter (TSC) which is mounted directly in front. The TSC is a very thin plastic scintillator which is connected to a photomultiplier tube via light guides. It provides an input for the data acquisition trigger system. Figure 3.12 shows the layout of the TOF module.

To cover the acceptance of $34^\circ < \theta < 120^\circ$ in polar angle, 64 TOF modules are located in the barrel region at a radius of 1.2 m from the IP. Fig. 3.13a shows the mass distribution that is obtained from data and compares it to the expectations from Monte-Carlo simulation. It is note-worthy that the data points are consistent with the simulation predictions that assume a time resolution of 100 ps. Figure 3.13b shows the K/π separation performance as a function of the particle's momentum.

The TOF information is not used in the reconstruction of the signal modes studied in this thesis. In the two body decay $B \rightarrow h^+h^-$, where the heavy B decays into two light hadrons. The hadrons have a high momentum because of the high mass of the B meson. With a



(a) Mass distribution obtained from TOF data. Expectations from MC match the data recorded.

(b) Separation of kaons and pions achieved with the TOF subdetector.

Figure 3.13: Performance plots for the TOF.

minimal momentum of about 1.7 GeV for pions, these particles are out of the momentum region which is accessible for the TOF.

3.2.6 The Electromagnetic Calorimeter (ECL)

The Electromagnetic Calorimeter (ECL) is used to measure the energy of electrons, positrons and photons. In a dense material, the electromagnetically interacting particles induce an electromagnetic shower. The typical decay length of electromagnetic interacting particles is X_0 . The decay products in the cascade carry a fraction of the energy of the primary particle. The number of decay products is roughly proportional to the energy of the primary particle.

The ECL consists of 8736 thallium-doped (Tl) CsI crystal counters. Each CSI(Tl) crystal has a tower shape and a height of 30 cm. This corresponds to 16.2 radiation length. Each CSI(Tl) crystal is also pointing towards the IP. The ECL is divided into the barrel region with 6624 crystals and the forward and backward endcap with 1152 and 960 crystals, respectively. The detailed geometry is shown in Fig. 3.14.

When an electron or photon hits a crystal, its energy is deposited in electromagnetic showers produced by bremsstrahlung and pair production. Scintillation photons are guided to the photomultiplier tubes and measured. Other particles like protons do not start an electromagnetic shower because their interaction is governed by the strong interaction (λ_I).

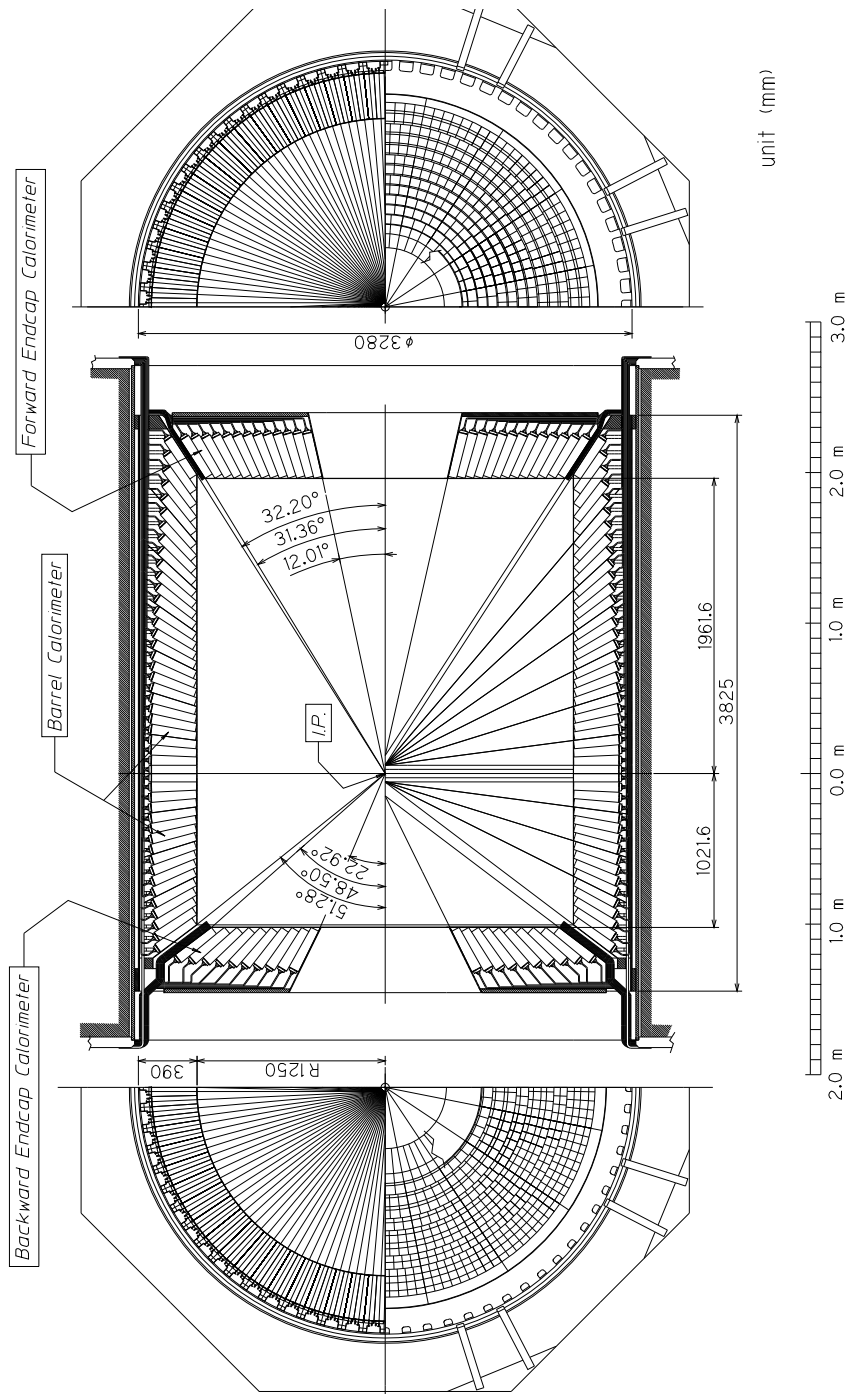


Figure 3.14: The overall geometrical layout of the ECL.

By calculating the ratio of measured cluster energy in the ECL and momentum in the tracking system E/p for charged tracks, one can distinguish between particle types. For electrons, the ratio E/p is close to unity while it is smaller for other particles e.g. the proton. The electron identification exploits this behaviour. The energy resolution is given by

$$\frac{\sigma_E}{E} \left(1.34 \oplus \frac{0.066}{E} \oplus \frac{0.81}{E^{1/4}} \right) \%, \quad (3.8)$$

and the position resolution is

$$\sigma_{\text{pos}} = \left(0.27 + \frac{3.4}{E^{1/2}} + \frac{1.8}{E^{1/4}} \right) \text{ mm}, \quad (3.9)$$

where E is in units of GeV. Figure 3.15 shows the energy and position resolution of the ECL.

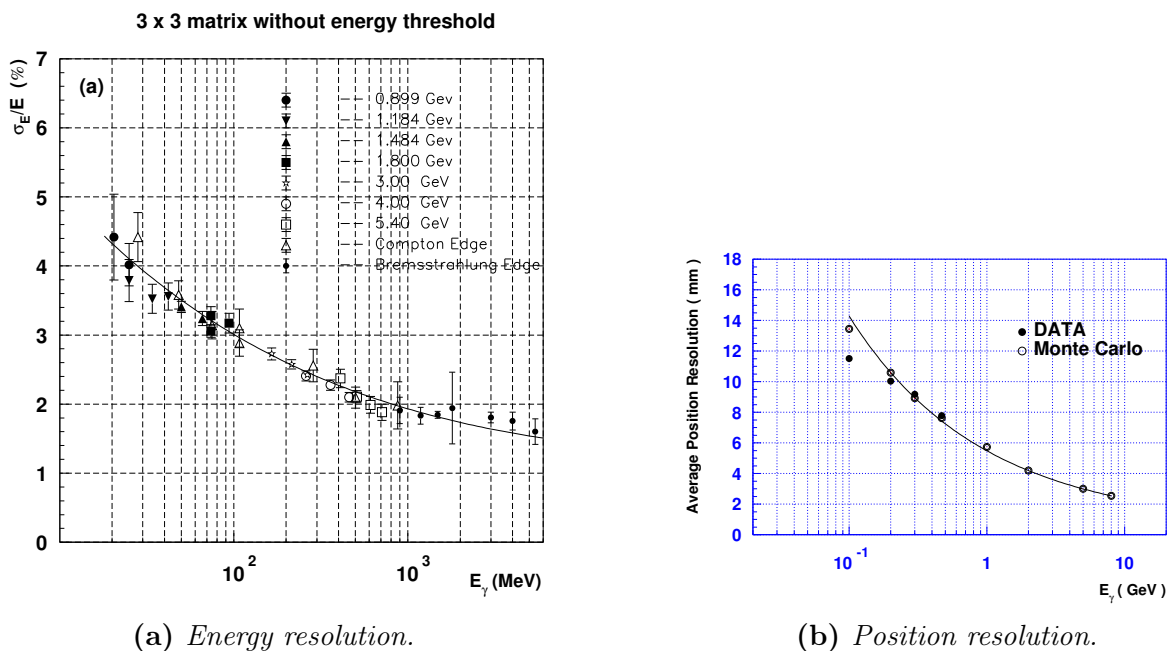


Figure 3.15: Energy and position resolution of the ECL.

3.2.7 The Solenoid Magnet

To bend the tracks of charged particles in the tracking system, a superconducting solenoid magnet with a field strength of 1.5 T is used. From the helix path of the particle, the momentum can be determined in the CDC. The superconducting coil consists of a single layer of niobium-titanium-copper alloy embedded in a high purity aluminium stabiliser. The coil is wound around an aluminium support cylinder of 3.4 m in diameter and 4.4 m

in length. To cool the niobium alloy to superconducting temperature, it is immersed in circulating liquid helium. Figure 3.16 shows the layout of the superconducting solenoid and the cryostat which is the thermal encapsulation.

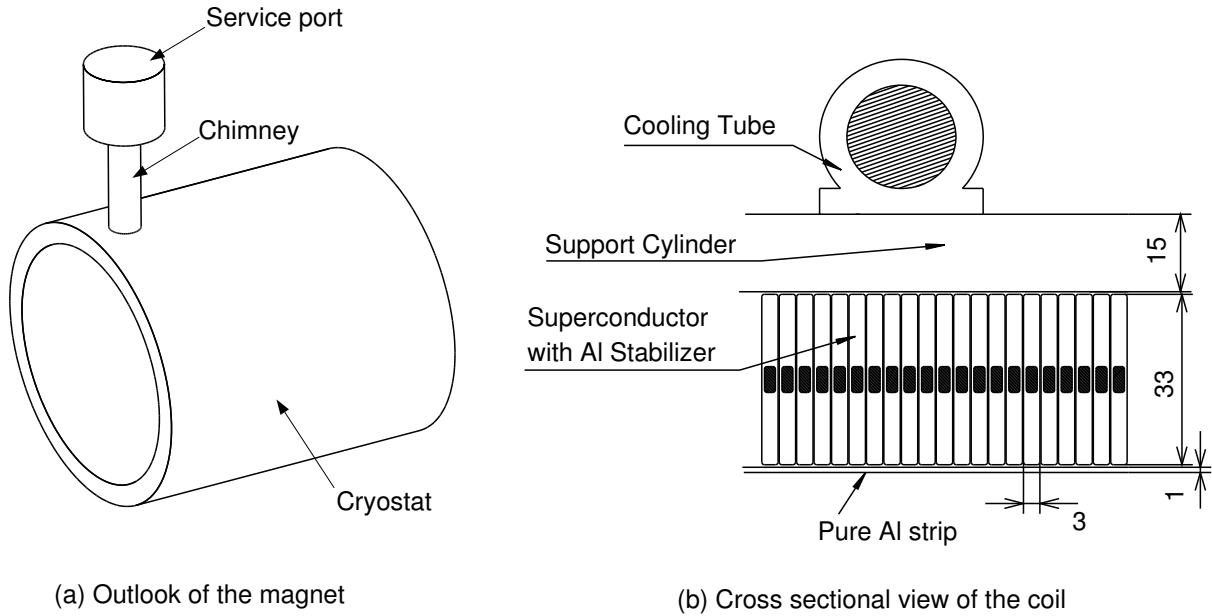


Figure 3.16: *Layout of the superconducting solenoid magnet of Belle including the cryostat.*

3.2.8 The K_L^0 and Muon Detector (KLM)

The K_L^0 and muon detector (KLM) is mainly used for muon identification. The momentum of a charged particle must be higher than $p_T > 0.6 \text{ GeV}/c$ to reach the KLM detector. It is also used to identify neutral K_L^0 particles which do not generate electromagnetic showers in the ECL. The interaction of the K_L^0 mesons is governed by the strong interaction. The typical interaction length of the strong force is λ_I which is much larger than the electron magnetic interaction length X_0 . These particle types only seldom interact with material and therefore need a dense and large detector to be detected efficiently.

The KLM is geometrically embedded into the iron return yoke of the solenoid magnet (instrumented return yoke). A return yoke is needed for the solenoid magnet to minimise the stray field in the experimental hall. This return yoke is made of iron and guides the magnetic field lines. It is a so-called instrumented return yoke which consists of alternating layers of 4.7 cm thick iron plates and resistive plate counters (RPC). There are 15 RPC superlayers interleaved by 14 steel plates in the barrel region and 14 RPC superlayers in the two endcap region. This geometrical setup yields a coverage of the polar angle of

$20^\circ < \theta < 155^\circ$. Two perpendicular RPC layers are combined to a superlayer which is then capable of giving $\theta - \phi$ positional information. A cut-out of an RPC superlayer is shown in Fig. 3.17.

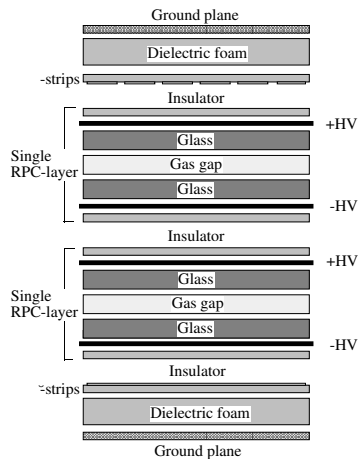


Figure 3.17: *Cut-out of a KLM super layer.*

The operation principle for the KLM is the following. Amongst the few particles that can leave the electromagnetic calorimeter (ECL), the muon and the K_L^0 are the most common at Belle. The muon interacts electromagnetically with the material of the ECL and the KLM. Because of its higher mass it does not initialize electromagnetic showers in the ECL like the electron does. Therefore, the ionisation of the muon track can be measured in the KLM. The K_L^0 , however, produces a hadronic shower in the KLM due to the strong interaction with the atomic nuclei in the KLM material. The ionising secondary particles in the shower can be detected by the RPCs. The cluster formation is fundamentally different for muons and K_L^0 particles. The muons generate clusters which are thin and have a long penetration depth while the K_L^0 particles generate wider and shorter clusters.

3.3 Trigger and Data Acquisition

The trigger system is used to identify physics events using the information of several sub detectors. The data acquisition system, which works hand-in-hand with the trigger, is responsible for reading out the data from all subdetectors. The trigger system is needed to distinguish the interesting physics events from the huge amount of beam background using fast signals from the subdetectors (data reduction). The background events result from the high beam current of the KEKB accelerator which is needed to keep the luminosity high. The background level is very sensitive to the accelerator conditions, demanding a flexible solution for the trigger system. On one hand, the trigger has to keep the rate of

accepted events at a tolerable level for the data acquisition which stores the event data. On the other hand, the trigger must be efficient by using redundant information from different subdetectors to keep the efficiency for interesting physics events high.

The Belle trigger system reduces the data rate in several steps. The first trigger is a Level-1 hardware trigger followed by a Level-3 software trigger that both operate in real-time. A Level-4 trigger, event reconstruction and classification is performed offline. Fig. 3.18 shows a flow diagram of the event data through the various triggers.

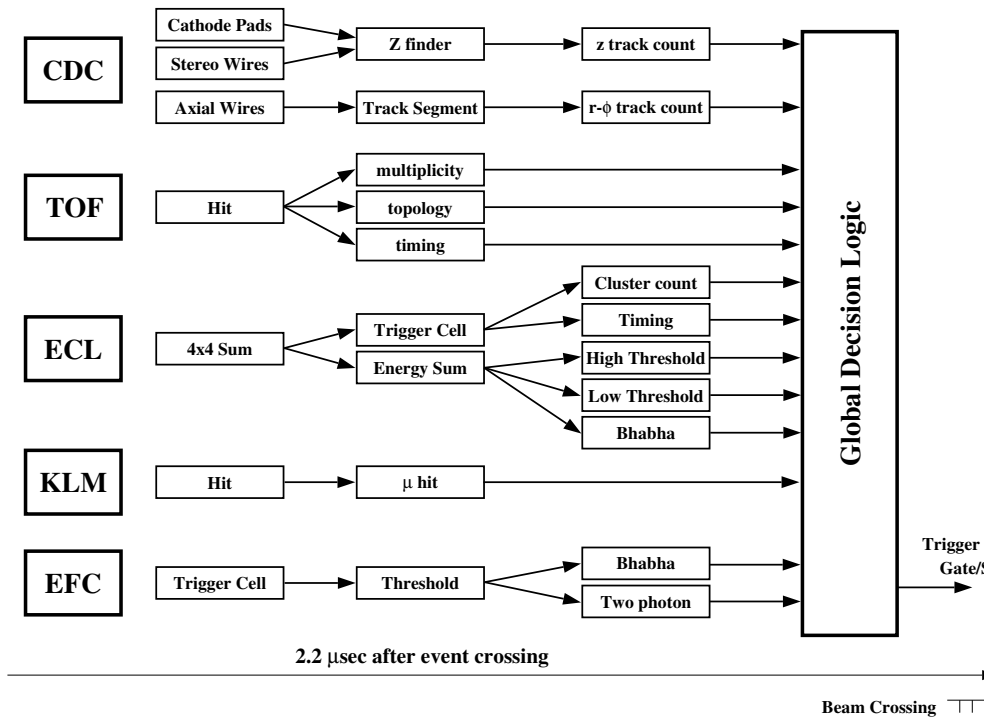


Figure 3.18: *Trigger system of the Belle detector.*

The Level-1 trigger, Global Decision Logic (GDL), uses input from subdetector trigger systems. The subdetector trigger systems can be grouped into track triggers and energy triggers. The CDC and TSC, which is a component of the TOF, are responsible for the charged track trigger while the ECL and the Extreme Forward Calorimeter (EFC) provides triggers based on the total energy deposit. Information about the muon is collected from the KLM. A summary of all trigger input to the GDL is provided in Fig. 3.19.

The GDL is build up by four main sub-triggers, namely the two track trigger, the three track trigger, the cluster number trigger and the energy sum trigger. The two track trigger requires two tracks with an opening angle greater than 135° and z vertex information for at least one of the two tracks. In addition a minimum of 2 hits are required in the TOF. The three track trigger is similar to the two track trigger, but no opening angle condition is required. Furthermore hits in the inner tracking subdetector are required. The cluster

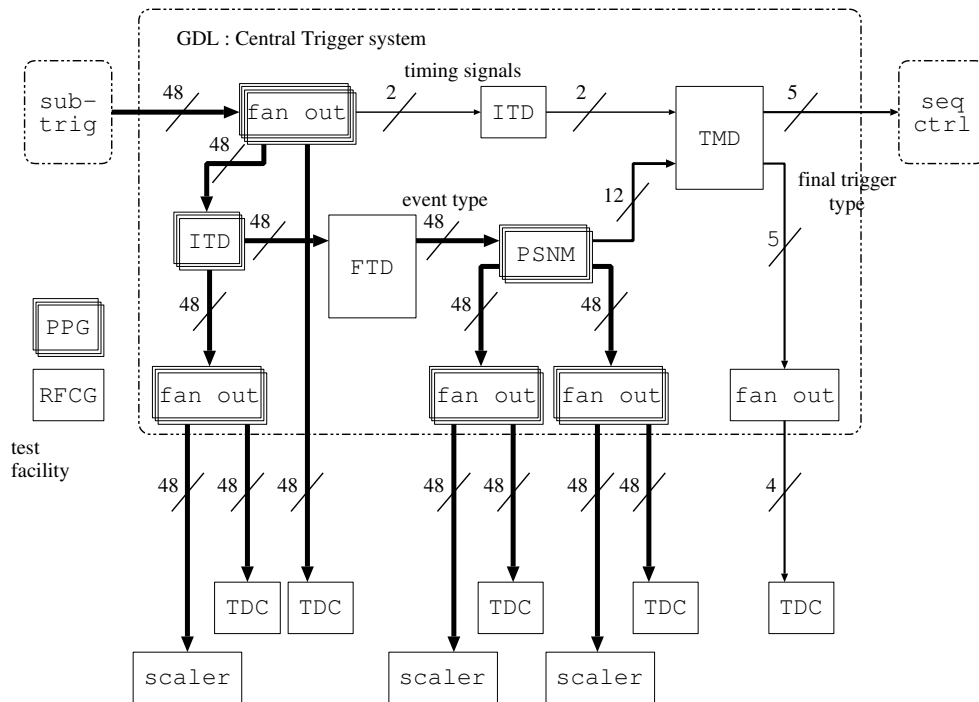


Figure 3.19: Flow chart of the global decision logic (GDL) of the Belle trigger.

number trigger requires at least 4 isolated clusters in the ECL. If at least 1 GeV is deposited in the ECL, the energy sum trigger is activated.

Within 2.2 us after the beam crossing, the GDL has to deliver a final decision to initiate the readout of all subdetectors to the DAQ. Due to the exploitation of redundant triggers, the trigger efficiency for $B\bar{B}$ events can be kept above 99.5%, while keeping the trigger rate in average at 200 – 250 Hz.

The design goal of the Data Acquisition system (DAQ) is stay operational up to a trigger rate of 500 Hz. The dead time fraction should not become bigger than 10%. The following tasks have to be carried out for every trigger event. First the data from all subdetectors for a given event are collected on a central event builder machine. Then the events are handed over to the Level-3 trigger. The Level-3 trigger is an online computing farm where every event is assigned to a single computer for processing. The online computer performs basic tracking and cluster reconstruction and rejects unwanted events according to the information that was not available in the Level-1 trigger. The remaining events are sent to a computer centre for offline processing.

The Level-4 trigger is the first step applied during offline processing. Events passing the Level-4 trigger undergo full event reconstruction. Tracks are reconstructed using CDC and SVD information. These tracks are also extrapolated to the outer detectors to search for associated clusters. Further cuts are applied to ensure the quality of the recorded events. Every event is required to have at least one track originating from the IP, meaning

$dr < 1.0$ cm and $dz < 4.0$ cm, with a $p_T > 300$ MeV/c. In addition to the improved tracking, the particle identification information is assigned to the tracks. Clusters in the ECL are reconstructed to form photons. All the calculated information from this full reconstruction is stored together with the raw event data and is stored in a format available to the collaborators for analysis.

To close the chapter about detector physics, data acquisition and reconstruction, we present a plot of a reconstructed golden channel $B \rightarrow J/\psi K_S^0$ event in Fig. 3.20.

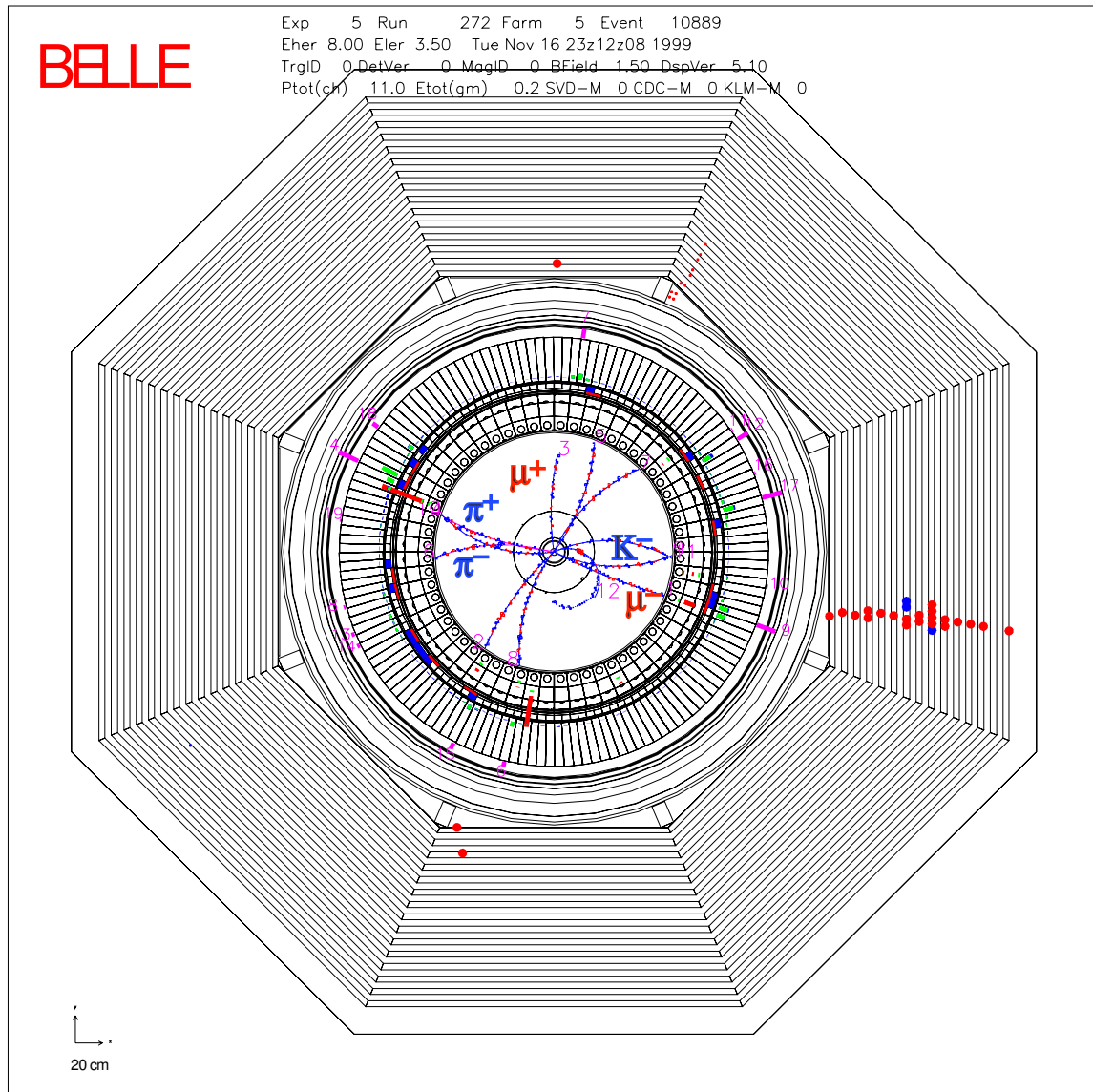


Figure 3.20: Event display of a $B \rightarrow J/\psi K_S^0$ decay candidate (<http://www.belle.jp/belle/events/>). Cut through the detector $r - \phi$ plane.

Chapter 4

Analysis of $B^0 \rightarrow h^+h^-$

4.1 Introduction to the Technique of a “Blind Analysis”

In this analysis we are measuring the branching ratios of $B^0 \rightarrow h^+h^-$, where the h^\pm represents a light charged hadron; either a pion or kaon. The measurement of the branching ratio of $B^0 \rightarrow K^+K^-$ would be a first observation. In addition to this, we are also extracting CP parameters from these decays. The direct CP violation $\mathcal{A}_{CP}(K\pi)$ is measured along with the time-dependent CP parameters for direct ($\mathcal{A}_{CP}(\pi^+\pi^-)$) and mixing-induced ($\mathcal{S}_{CP}(\pi^+\pi^-)$) CP violation. This is the first time at Belle that one is attempting to extract branching fractions and time-dependent CP parameters in a combined maximum likelihood fit.

The following section explains how to obtain the above physics observables using a maximum likelihood fit. The analysis is performed as a blind analysis. The goal of a blind analysis is to obtain an unbiased physics result. This means that we do not look into the data until we have verified on generated data samples (Monte-Carlo samples) that the analysis procedure works. If we would tune the analysis on the data sample, we could modify the analysis until it yields desired results. As this would practically introduce a bias due to our expectations, this is therefore forbidden in a blind analysis. After an internal referee approval of the analysis method, the analysis software is run on the data set a single time. This is referred to as the box-opening because we have treated the data as a black-box, and after the box-opening have access to what is inside. After the box-opening, the analysis method may not be changed to prevent us from biasing the results.

At the KEKB collider, electrons and positrons are brought to collision at a center-of-mass energy corresponding to the mass of the $\Upsilon(4S)$ resonance. About three quarters of the $q\bar{q}$ cross section consists of $q\bar{q}$ pairs, where $q = u, d, s, c$. These events are called continuum. In the remaining quarter, an $\Upsilon(4S)$ is produced, which exclusively decays into a $B\bar{B}$ pair (see section 4.2). In total, 772×10^6 $B\bar{B}$ pairs are collected at Belle. From this data set

we want to single out a few thousand signal events. The first step to reduce the amount of background is the so-called event selection. The $\Upsilon(4S)$ decays exclusively into a $B\bar{B}$ pair and we try to reconstruct one of the B mesons. Reconstruction in this context means that we try to combine the four momentum of the final state particles to build the parent particles in the decay chain. For the decay of $B^0 \rightarrow h^+h^-$, we only sum up the four momenta of two oppositely charged tracks and obtain a B meson candidate. Now many criteria (cuts) are applied to every decay event that is recorded. Details can be found in section 4.3. The next step is to select variables that give good discrimination between our signal and the various backgrounds in this analysis, especially the continuum background. The variable M_{BC} , is the mass of the reconstructed B meson calculated by using the momentum of the reconstructed B meson and the beam energy in the center-of-mass system. This trick avoids using the relatively imprecise measurement of the particle's momentum in the tracking detectors compared to the well-known beam energy. A similar but almost orthogonal variable is ΔE , which is defined as the difference between the reconstructed energy and the beam energy in the center-of-mass system. For calculation of this quantity, only the precise particle tracking detectors are needed. So to obtain the energy from the momentum measurement, we have to use a particle hypothesis for the final state particles. This analysis assumes every particle to be a pion. Therefore only the decays of $B^0 \rightarrow \pi^+\pi^-$ generate a distribution centered around zero in ΔE . For the decays containing one or two kaons, too little energy is reconstructed. This means that the decay of $B \rightarrow K\pi$ is shifted in ΔE by $m(\pi^\pm) - m(K^\pm)$ and the decay of $B \rightarrow K^+K^-$ is shifted by $2 \times (m(\pi^\pm) - m(K^\pm))$. For the positive and the negatively charged final state particles that are reconstructed to the B meson, we obtain particle identification information. The likelihood ratio constructed from the likelihood to be a kaon and the likelihood to be a pion is used in the fit later on. It is denoted $\mathcal{L}_{K/\pi}^+$ and $\mathcal{L}_{K/\pi}^-$, depending on whether it was obtained for the positive or the negative particle. Signal events decay in a spherical uniform directions, while continuum events decay with a jet-like topology. The event shape variables are measures for the sphericity and the jet-likeness of a event. For these inputs, we use a multivariate analysis to calculate a single variable, the fisher discriminant, $\mathcal{F}_{S/B}$ (Sec. 4.3.4). The distribution of the fisher discriminant is different for signal events and continuum background events providing discrimination between the two. Finally for the time-dependent CP violation measurement, we reconstruct the vertex and flavour of the other B meson or tag-side. From examining the decay topology of the other B meson, we obtain the decay vertex using an iterative fitting procedure [68]. The flavour of the other B , q ($q = +1$ for B^0 and $q = -1$ for \bar{B}^0), can be determined if the other B decays into a flavour specific final state [69]. The spatial distance Δz , between the decay vertices of the reconstructed B and the other B is calculated and translated into a decay time difference Δt , using the known boost of the center-of-mass system. Overall, we are using 7 variables for the maximum likelihood fit: M_{BC} , ΔE , $\mathcal{L}_{K/\pi}^+$, $\mathcal{L}_{K/\pi}^-$, $\mathcal{F}_{S/B}$, Δt and q .

The next step in the analysis is to obtain probability density functions (PDFs) for signal and background events. The three signal components are $B^0 \rightarrow \pi^+\pi^-$, $B^0 \rightarrow K^+\pi^-$ and $B^0 \rightarrow K^+K^-$. The dominant background by far, are continuum events. Continuum events

are produced in $e^+ e^-$ collisions that go directly into $q \bar{q}$ pairs, where $q = u, d, s, c$. Another background consists of misreconstructed B and B^\pm decays which happen to be in the same kinematic region, especially three body decays into light hadrons. For all these 6 components, we have to find a probability density function which is a function of the 7 variables. Finding the PDFs through the fit procedure is called model building.

This is done using a maximum likelihood approach. In the special case of no correlations between the 7 variables, the PDF factorizes and we can model every distribution individually. For example, ΔE in one of the signal components can be described by a Gaussian function with the mean and the sigma being the free parameters. A maximum likelihood fit on a pure Monte-Carlo sample of the signal component yields us the parameters (mean and sigma) for the Gaussian model. The maximum likelihood fit method varies the free parameters and uses a gradient descending method to find the parameters that maximize the likelihood. The pure Monte-Carlo sample which is needed for obtaining the PDFs, is taken from Monte-Carlo full detector simulation for the signal components and the B decay backgrounds. For the continuum component, a data sample recorded slightly below the $\Upsilon(4S)$ resonance (off-resonance) is used. One advantage of parametric over non-parametric model descriptions is the possibility to check and correct for differences between the Monte-Carlo full simulation and the data. This can be done by investigating a second similar decay, a control sample (Sec. 5.1). The correction factors for the parameters of the model can be determined there and applied to the main analysis without biasing the results. For the non-parametric models, we developed a bin-wise method for correcting the histogram for the differences between data and Monte-Carlo (Sec. 5.2).

4.2 Data Set

The branching fraction measurement and the time dependent CP violation measurement are based on the final data sample of Belle containing 772×10^6 $B \bar{B}$ pairs. The data sample was collected with the Belle detector at the KEKB storage ring using $e^- e^+$ collisions at the energy of the $\Upsilon(4S)$ resonance ($\sqrt{s} = 10.58$ GeV).

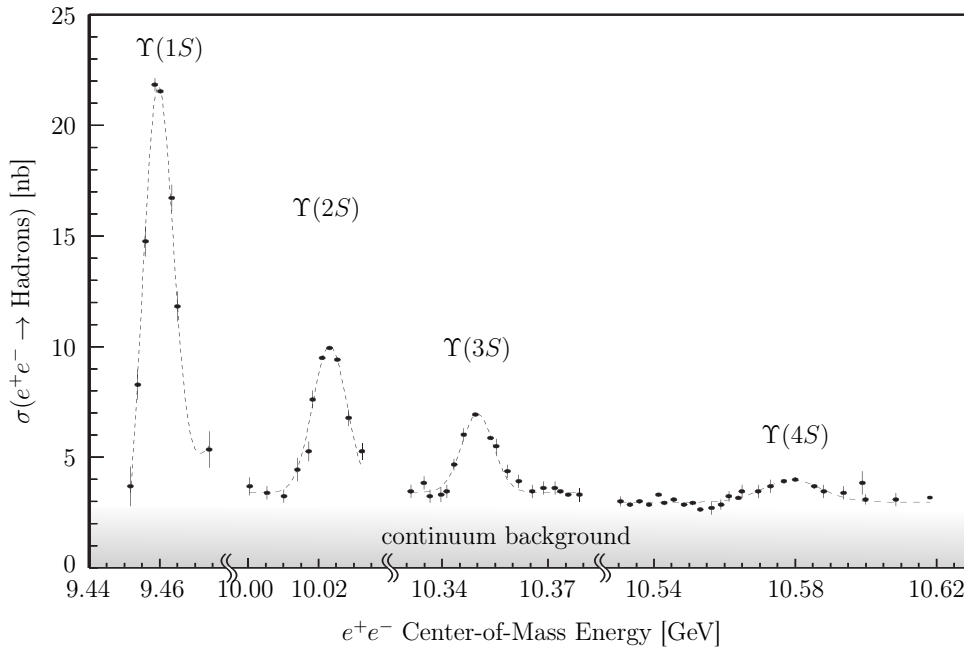


Figure 4.1: Production cross sections around the center-of-mass energies of the Υ resonances.

The production cross section of the $\Upsilon(4S)$ resonance is about 1/4 of the total hadronic production cross section (Fig. 4.1). The remaining part of the production cross section is called continuum. It is an irreducible physics background coming mainly from the process where the electron and the positron produce $q \bar{q}$ pairs, where $q = \{u, d, s, c\}$. The KEKB storage ring is operated at asymmetric beam energies of 3.5 GeV for the positrons and 8 GeV for the electrons, giving the center-of-mass system a Lorentz boost of $\beta\gamma = 0.425$ opposite to the positron beam direction, z . The peak instantaneous luminosity achieved by KEKB is $2.11 \times 10^{34} \text{ cm}^{-2}\text{s}^{-1}$ which is the current world record. In total, an integrated luminosity of 1 ab^{-1} was accumulated.

Another data sample which is used in the analysis is the off-resonance data sample. The off-resonance data sample is recorded with a center-of-mass energy 80 GeV below the $\Upsilon(4S)$ resonance ($\sqrt{s} = 10.50$ GeV). The physics of the continuum events is unchanged by the small shift in center-of-mass energy, but the energy is not sufficient to generate $B\bar{B}$ events. Therefore the off-resonance data sample is a pure continuum event sample.

The integrated luminosity of the off-resonance data sample corresponds to a tenth of the integrated luminosity of the on-resonance data sample.

4.3 Event Selection

The event selection is the first step in the analysis of B mesons decaying as $B^0 \rightarrow \pi^+\pi^-$, $B^0 \rightarrow K^\pm\pi^\mp$ and $B^0 \rightarrow K^+K^-$. The purpose of the event selection is to reduce the number of events that are going to be analysed from the total Belle statistics of 772×10^6 $B \bar{B}$ events to a much smaller data set, which happens to be in the order of one million events. It is noteworthy that we try to apply loose criteria on the selection to keep all interesting events, but do not necessarily reject all background events. In other words this means we do not want to obtain a very pure sample, but we want to keep the reconstruction efficiency high.

The event selection is done in a two step procedure. First we perform a coarse search for events that contain high momentum tracks, a skim. In the skim, we are requiring that any two oppositely charged particles in the event can be reconstructed to a B meson. The event is required to have $M_{BC} > 5.17 \text{ GeV}/c^2$ and $|\Delta E| < 0.55 \text{ GeV}$. After the skim, we obtain a much smaller data sample where we can use more elaborate techniques for event selection. We are concentrating the event selection now on the specific decays of $B^0 \rightarrow \pi^+\pi^-$, $B^0 \rightarrow K^\pm\pi^\mp$ and $B^0 \rightarrow K^+K^-$ in the sample remaining after the skim. In the reconstruction, we again combine the 4 vectors of a positively and negatively charged particle. The energy is calculated from the momentum of the particles using a pion hypothesis for the mass. All other particles in the event are assumed to be the other B . The following sections describe in detail the criteria (cuts) we use to obtain the data sample for extracting the branching ratios and CP parameters.

4.3.1 Track Selection

A very loose cut is placed on the impact parameters of the tracks. This helps to suppress cosmic particles or beam gas events.

$$\begin{aligned}\Delta r &< 0.4 \text{ cm}, \\ \Delta z &< 4 \text{ cm}.\end{aligned}$$

We require that the track was not produced by an electron. Therefore, we cut at 0.9 on the electron-pion likelihood ratio. The electron-pion likelihood ratio is calculated from several likelihoods. The ratio of energy deposited in the calorimeter and the particle's momentum measured in the drift chamber is used. The vertical spread of a calorimeter cluster is quantized as the ratio of energy deposited in 3×3 crystals and 5×5 crystals

at the calorimeter. Also we can extrapolate the track into the calorimeter assuming the mass of an electron and compare the extrapolated position with the cluster position in the calorimeter by calculating the χ^2 . Furthermore information from the ACC (Sec. 3.2.4), the TOF (Sec. 3.2.5) and the central drift chamber (Sec. 3.2.3) is used. From the CDC the energy loss, $\Delta E/\Delta x$, is used to distinguish between electrons and pions.

It is also a requirement for the tracks to have hits in the SVD to improve the vertex resolution. We apply the same cuts as those used to extract the official Belle detector resolution description of Δt , to be used:

$$\begin{aligned} &\text{number of hits in } Z \geq 2, \\ &\text{number of hits in } r - \phi \geq 1. \end{aligned}$$

4.3.2 Analysis Window

We place some criteria on every event, which if passed, is included in the analysis. The most important ones are on M_{BC} and ΔE ,

$$M_{BC} = \sqrt{E_{\text{beam}}^2 - \mathbf{p}^2}. \quad (4.1)$$

M_{BC} has a upper bound of the beam energy in the center-of-mass system. We choose the lower limit to be $5.24 \text{ GeV}/c^2$. This window includes the full distribution of our signal modes $\pi^+ \pi^-$, $K^+ \pi^-$ and $K^+ K^-$ without loss of efficiency.

Almost independent to the variable M_{BC} is ΔE ,

$$\Delta E = E_{\text{reco}} - E_{\text{beam}}. \quad (4.2)$$

The reconstructed energy is taken from the momentum of the two tracks assuming a pion particle hypothesis. In a first approximation, ΔE should be symmetric around 0 GeV . There is, however, a tail to lower energies due to final state radiation. For the decay modes $K^\pm \pi^\mp$ and $K^+ K^-$, too little energy is reconstructed due to the pion hypothesis. To fully include those two decay channels we used an asymmetric analysis windows in ΔE . It ranges from -0.2 GeV to 0.15 GeV .

4.3.3 Vertexing and Tagging

The two tracks of the particles that form the B mesons are fitted to a common vertex with a "beam tube constraint" to increase the energy and vertex resolution. The "beam tube constraint" is a method to take advantage of our knowledge about the interaction point(IP) without biasing the measurement of Δt . The additional constraint also enables us to find a vertex if vertex information is only available from one track. A virtual track

originating from the IP and pointing at 11 mrad angle with respect to the detector z axis is added to the other two tracks in the vertex fit. The IP is determined regularly from pre-scaled hadronic events as it varies with time and accelerator conditions. It is modelled by a three dimensional Gaussian with a typical spread of $\sigma_x = 100 \mu\text{m}$, $\sigma_y = 5 \mu\text{m}$ and $\sigma_z = 3 \mu\text{m}$. To account for the finite flight length of the B mesons we introduce an additional smearing in the $r - \phi$ plane, $IP_{\text{smear}} = 21 \mu\text{m}$.

The other B or tag side B is fitted by the TagVK algorithm and B-tagging is performed by the Hamlet algorithm [69]. The TagVK algorithm uses the tracks that are not used for the reconstructed B meson and estimates the decay vertex of the other B with a vertex fit without actually reconstructing the tag side. Therefore initially all tracks with a bad position measurement, $\sigma_z < 0.5 \text{ mm}$, are excluded from the vertex fit. Also it is required that the tracks originate from a position close to the reconstructed vertex of the reconstructed B meson. Therefore a cut is placed on the impact parameter of the track helix, $dr < 0.5 \text{ mm}$, with respect to the reconstructed B .

The vertex fit of the tag-side B meson is an iterative procedure starting with the remaining tracks and the IP constraint. The χ^2 of the vertex fit is determined and compared to an empirical value of 20. If the $\chi^2 > 20$ the track which yields the highest contribution to the χ^2 is determined. The geometric interpretation is that we determine the track that is displaced the most from the majority of the tracks. This track is removed and the vertex fit, including the χ^2 evaluation, is redone. It is noteworthy to state that the high momentum leptons, $p_l^{\text{CMS}} > 1.1 \text{ GeV}/c$, are always kept because they are likely to originate from semi-leptonic $b \rightarrow cl\nu_l$ decays. The re-fitting continues until a $\chi^2 < 20$ is reached. The vertex from the last iteration is accepted as vertex of the other B .

The spatial difference in the z detector direction between the vertices of the reconstructed B_{Rec} meson and the other B meson, B_{Tag} , is defined to be,

$$\Delta z \equiv z_{\text{Rec}} - z_{\text{Tag}}. \quad (4.3)$$

We obtain the decay time difference Δt by applying the Lorentz transformation with the known boost of the center of mass frame,

$$\Delta t = \frac{\Delta z}{\beta\gamma}. \quad (4.4)$$

Eq. 4.4 is a kinematic approximation exploiting that the $B\bar{B}$ pair is practically at rest in the $\Upsilon(4S)$ rest frame. The Lorentz boost of the $\Upsilon(4S)$ is $\beta\gamma = 0.425$ at the Belle experiment.

The flavour tagging routine, Hamlet, determines two values q and r . A description of the flavour tagging algorithm can be found in Appendix B. The flavour tag q of the B_{Tag} is -1 or 1 for \bar{B} or B respectively. The variable r , is associated flavour-tagging dilution factor. It ranges from no information about the flavour $r = 0$ to unambiguous flavour assignment

$r = 1$. The data for the time dependent CP analysis is divided into 7 regions in r (r -bins) defined in table 4.1. The total effective tagging efficiency is determined to be 0.29 ± 0.01 .

All B mesons and events that do not successfully finish this procedure are discarded.

Table 4.1: *Definition of the r -bins regions.*

r -bin,l	r-region
0	$0.0 \leq r \leq 0.1$
1	$0.1 < r \leq 0.25$
2	$0.25 < r \leq 0.5$
3	$0.5 < r \leq 0.625$
4	$0.625 < r \leq 0.750$
5	$0.750 < r \leq 0.875$
6	$0.875 < r \leq 1.0$

4.3.4 Continuum Discriminating Variables

To further remove continuum background, we want to exploit the geometry of the decay. In continuum events, the collision energy is distributed among the quark and the anti-quark. In the center-of-mass system, the momentum of the quark and the anti-quark is basically back-to-back. Therefore the continuum events have a more jet-like structure. The two B mesons decay with no spatial preference and the decay topology is more spherical.

We used a set of variables that exploit the geometrical differences in the events to discriminate between $B\bar{B}$ events and continuum events. These variables are combined to a single quantity using a multivariate method. The performances of neuronal networks, boosted decision trees and a fisher discriminant were estimated. Since we found no significant differences in the discrimination performance, we used the most simple method, the fisher discriminant [70]. The following variables are used as an input to the fisher discriminant.

We make use of the thrust of an set of particles, which is close to unity if the event is jet-like. The thrust is given by

$$T = \frac{\sum_i |\mathbf{n} \cdot \mathbf{p}_i|}{\sum_i |\mathbf{p}_i|}, \quad (4.5)$$

where p_i is the momentum of the particles and \mathbf{n} is an arbitrary vector. The thrust axis is the vector \mathbf{n} which maximizes the thrust T . To get a more intuitive feeling of the thrust and the thrust axis, we want explain two limit cases. Imagine a particle at rest decays into two daughter particles. The momentum of the particles is back to back (180°). In this case the thrust axis is parallel to the momentum of the particles. Now imagine the mother particle has a little initial momentum p_m , perpendicular to the daughter particle momentum p_i , mathematically $\mathbf{p}_m \cdot \mathbf{p}_i = 0$ and $p_m \ll p_i$. This will not change the direction

of the thrust axis. For the second case we want the same scenario, except $p_m \gg p_i$. In this case, the thrust axis is aligned with the momentum of the mother particle p_m .

Another event shape variable we use is the Legendre Polynomial

$$\mathcal{L} = \sum_i |\mathbf{p}_i| \left| \left(\frac{\mathbf{n} \cdot \mathbf{p}_i}{|\mathbf{n}| |\mathbf{p}_i|} \right)^R \right|, \quad (4.6)$$

where \mathbf{n} is an arbitrary axis, p_i is the momentum of the particles of interest and R is the order of the Legendre Polynomial. The order zero Legendre Polynomial is the sum of the absolute momentum of the particles. The second order Legendre polynomial weights every particle momentum by the angle between the particle momentum and the axis \mathbf{n} . Particle momenta being closer to aligned are weighted up and more perpendicular ones are weighted down.

Another important difference is the angular distribution of the momentum of the two B mesons. The $\Upsilon(4S)$ is produced via an electromagnetic interaction from a electron and a positron. The photon can only be transversally polarized and carries spin one. The $\Upsilon(4S)$ inherits the spin of the photon and is therefore polarized parallel to the beam axis, which is close to the detector z axis. In the decay of the $\Upsilon(4S)$ into two spin zero B mesons, the total angular momentum must be preserved, which means that the two B mesons are in a p-wave configuration. As a consequence, the decay perpendicular to the detector z axis is the most probable one.

The following event shape variables, F_i , are used to discriminate between $B\bar{B}$ events and continuum events,

$$F_1 = \frac{|\mathbf{t}_B \cdot \mathbf{t}_{OB}|}{|\mathbf{t}_B| |\mathbf{t}_{OB}|} \quad (4.7)$$

$$F_2 = \frac{|\mathbf{t}_B \cdot \mathbf{z}|}{|\mathbf{t}_B| |\mathbf{z}|} \quad (4.8)$$

$$F_3 = \frac{|\mathbf{p}(B) \cdot \mathbf{z}|}{|\mathbf{p}(B)| |\mathbf{z}|} \quad (4.9)$$

$$F_4 = \sum |\mathbf{p}_T| \quad (4.10)$$

$$F_5 = \mathcal{L}(0, \mathbf{p}(B) \cdot \mathbf{p}(\text{OB charged})) \quad (4.11)$$

$$F_6 = \mathcal{L}(0, \mathbf{p}(B) \cdot \mathbf{p}(\text{OB neutral})) \quad (4.12)$$

$$F_7 = \mathcal{L}(2, \mathbf{p}(B) \cdot \mathbf{p}(\text{OB charged})) \quad (4.13)$$

$$F_8 = \mathcal{L}(2, \mathbf{p}(B) \cdot \mathbf{p}(\text{OB neutral})) \quad (4.14)$$

where B denotes the reconstructed B meson and OB denotes the other B meson.

Figure 4.2 shows the distribution of the event shape variables for signal Monte-Carlo events from the decay $B^0 \rightarrow \pi^+ \pi^-$ and from off-resonance data. Off-resonance data is recorded with a center-of-mass energy 80 MeV below the threshold of producing $\Upsilon(4S)$. Because of

the lower center-of-mass energy, the off-resonance sample contains all the continuum decays but no $B\bar{B}$ pairs are produced.

- The F_1 (Eq. 4.7) event shape variable shows the cosine of the angle between the thrust axis of the reconstructed B and the thrust axis of the other B , which are all the charged and neutral particles not used in the reconstruction procedure. Because the decays of the two B mesons are independent, we expect a flat distribution. For continuum background, we know that it is created from the primary interaction. The $q\bar{q}$ quarks create jets that are back-to-back in the center-of-mass system. When reconstructing a fake B meson from these tracks, we expect the thrust axis to be aligned with the jet axis. The same is true for the other B . Because of this, the expectation for the continuum background is a cosine of one.
- When exchanging the thrust of the other B with the detector z axis we obtain the event shape variable F_2 (Eq. 4.8). If the B meson decays into two particles and one is outside the Belle detector acceptance limit (see Sec. 3.2), the event can not be reconstructed. Therefore we note a cut-off close to 0.85 which can be calculated using the acceptance and the Lorentz boost. Because the jets from $q\bar{q}$ do have some angular spread, we expect to catch more events close to the cut off region.
- The distribution of F_3 (Eq. 4.9) is the angular distribution of the momentum of the B meson. Here we can directly test the spin properties of the $\Upsilon(4S)$ decay into the two B mesons as explained above. The theoretically expected $1 - \cos^2 \theta$ shape and the flat distribution for continuum are shown in Fig. 4.2.
- The distribution F_4 is showing the sum of the transversal momentum of all particles on the tag side. The continuum distribution has in average a higher momentum with respect to the $B\bar{B}$ distribution. The reason is the lower multiplicity of the continuum events. Because of that the chance of loosing a track is lower in continuum events compared to $B\bar{B}$ events. The reconstructed momentum of the continuum is higher in average.
- The Legendre Polynomials utilise the thrust of the reconstructed B as the reference axis. F_5 sums over the momentum vector of the charged tracks of the other B and F_6 sums over the neutral clusters of the other B . These distributions exhibit a similar behaviour as the previous variable, F_4 .
- The variables F_7 and F_8 are constructed the same way as F_5 and F_6 but using a second order Legendre Polynomial. The second order Legendre Polynomial incorporates a weighting by the square of the cosine of the angle between the thrust of the reconstructed B and the momentum vectors (Eqn. 4.6). In addition to the factors explained in the previous variables the angular distribution of the momenta of the other B plays a role here. For continuum events the momenta are aligned with the thrust of the other B . From F_1 we know that the thrust of the other B is parallel to the thrust of the reconstructed B of jet-like continuum events. This explains the additional discrimination visible in F_7 and F_8 .

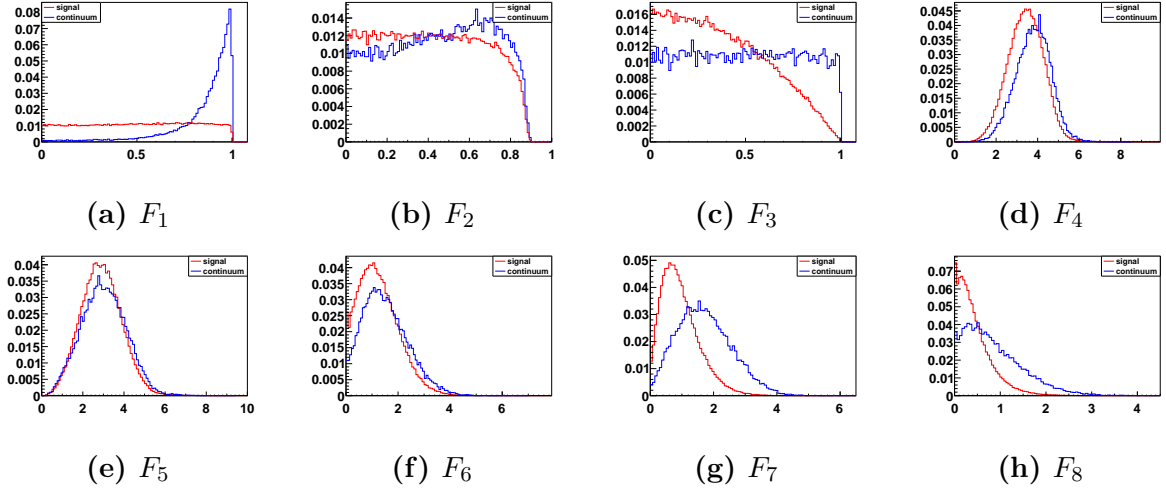


Figure 4.2: Distribution of input variables for the Fisher discriminant. We are showing normalized distributions of Monte-Carlo $B^0 \rightarrow \pi^+\pi^-$ events and off-resonance data in red and blue, respectively.

When studying the continuum suppression variables, F_1 4.7 was observed to give the best discriminating power between B decays and $q\bar{q}$ events (Ref. 4.2). The variable is the cosine of the angle between the thrust axis of the reconstructed B and the other B . Only events are taken into account with $F_1 \leq 0.9$. Approximately 90% of the signal events and 50% of the background events survive this cut. A significance optimization on the cut would suggest performing a harder cut on F_1 . However, we do not want to follow this path because we intend to fit the shape of the resulting fisher discriminant rather than cutting on it. Nevertheless applying this cut relieves us of having one order of magnitude more background. Therefore we can relax the accuracy requirements of the background model.

When combining the four-vectors of charged hadron tracks with a pion hypothesis to a B^0 , it is possible to get more than one combination that have an invariant mass and energy in the analysis region. The analysis region is defined by the cuts on M_{BC} and ΔE and all other event selection criteria mentioned earlier. If we reconstruct more than one event then a track from the other B^0 (tag side) was used and misinterpreted as a CP side track. In the case of this analysis, the average number of reconstructed B^0 candidates is close to 1 as shown in table 4.2. The plots in figure 4.3 show the distribution of the event multiplicity for the different decay channels. In case we have more than one B^0 candidate reconstructed

Table 4.2: Event multiplicity for different channels from Monte-Carlo.

	SVD1	SVD2
$\pi^+ \pi^-$	1.017	1.017
$K^+ \pi^-$	1.017	1.016
$K^+ K^-$	1.016	1.016

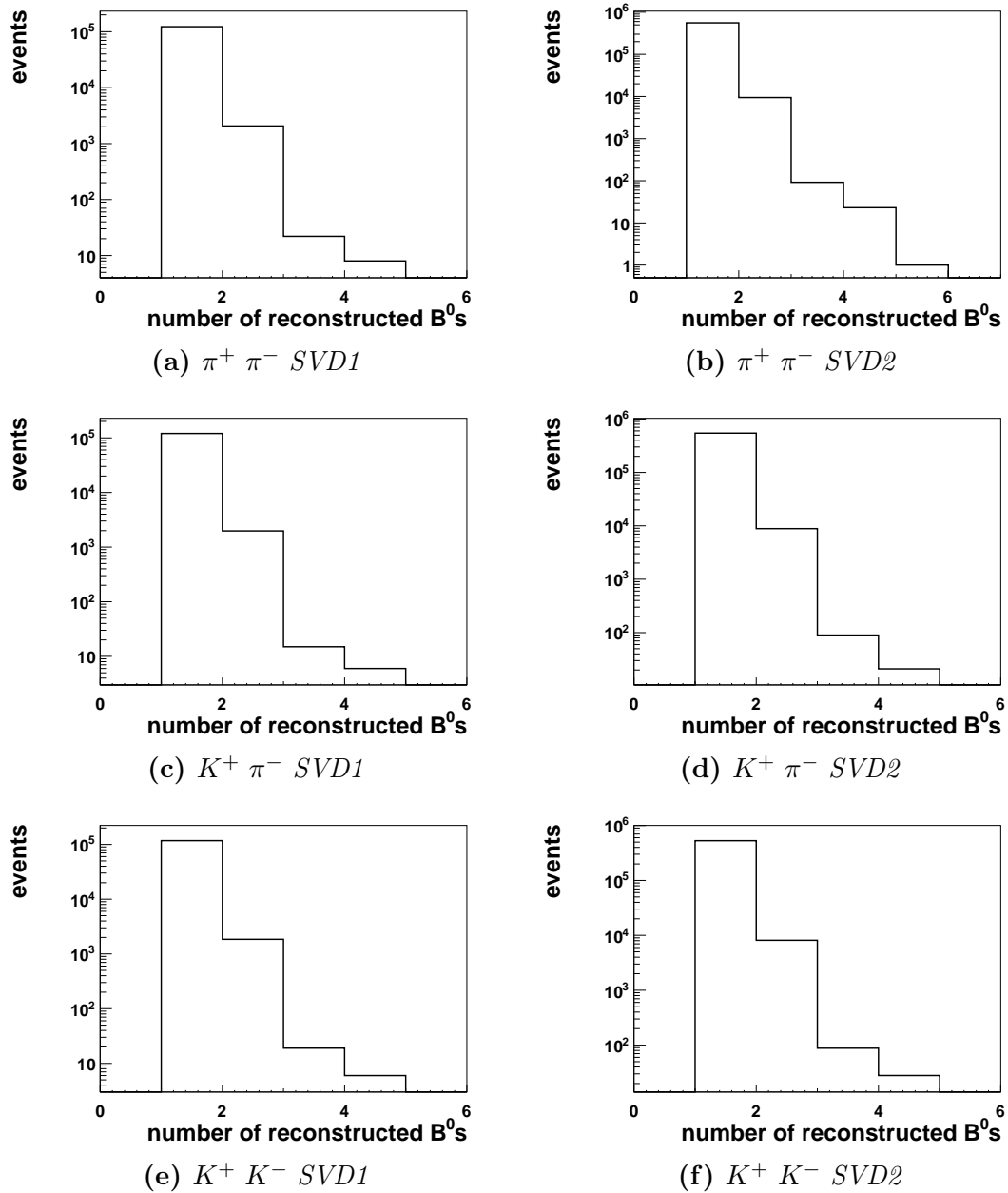


Figure 4.3: Event multiplicity for different channels.

we have to perform a best B^0 selection. Our method is to keep the B^0 candidate that is reconstructed from the highest momentum tracks. This seems to be a good assumption as we expect that the tag side B^0 decays, in general, into more than two final state particles. The total momentum is then distributed over more final state particles and is in average lower per particle.

4.3.5 Time Dependent Event Selection

As shown in Sec. 4.3.3, we can translate the spatial difference Δz , between the decay vertex of the reconstructed B , z_{Rec} , and the vertex of the other B , z_{Tag} , into a decay time difference Δt . The B mesons travel mainly in the boost direction, z , because the B mesons are almost at rest in the center-of-mass frame,

$$\Delta t \equiv \frac{(z_{Rec} - z_{Tag})}{\beta\gamma c} = \frac{\Delta z}{\beta\gamma c}.$$

The Δt distribution is determined in the range $|\Delta t| < 70$ ps. The goodness-of-fit $h = \chi^2/\text{NDF}$, is required to be $h_{Rec,Tag} < 500$ for multi-track vertices. More information about the vertex fitting quality and the detector resolution can be found in Appendix C. The goodness-of-fit cannot be calculated for single track vertices although vertex information can be obtained from single track events (Sec. 4.3.3). In order to reduce fitting biases from event dependent PDFs, the Punzi effect [71], the vertex uncertainty must be $\sigma_z^{Rec,Tag} < 200 \mu\text{m}$ for multi-track vertices and $\sigma_z^{Rec,Tag} < 500 \mu\text{m}$ for single-track vertices.

4.3.6 Detection Efficiency

After applying all the selection criteria above, we obtain the efficiencies shown in Tbl. 4.3. Because we are fitting the particle identification information and do not cut on the distribu-

Table 4.3: *Reconstruction efficiencies for all decay channels.*

decay channel	$\epsilon(\text{SVD1})$	$\epsilon(\text{SVD2})$
$B^0 \rightarrow \pi^+\pi^-$	0.605 ± 0.002	0.677 ± 0.001
$B^0 \rightarrow K^\pm\pi^\mp$	0.593 ± 0.002	0.662 ± 0.001
$B^0 \rightarrow K^+K^-$	0.581 ± 0.002	0.647 ± 0.001

tion we have no further uncertainties and corrections. Please note that the reconstruction efficiency is about 10% higher than in the previous Belle analysis [39]. The downside of this high reconstruction efficiency is that the purity of the data sample is very low. To still obtain an excellent fit, we are building a complex model of the signal and background. This is demonstrated in the following section 4.4.

4.4 Data Models

The aim of this analysis is to obtain the branching fractions and CP parameters for the signal channels $B^0 \rightarrow \pi^+\pi^-$, $B^0 \rightarrow K^+\pi^-$ and $B^0 \rightarrow K^+K^-$. We first want to demonstrate the basic principle here with a one dimensional example. Therefore we are looking into the distribution of the variable ΔE , the difference between the reconstructed and the beam energy. The ΔE distribution is different for all the signal components and for the background components. We are describing the shape of the individual distributions for every component. In the example of the ΔE distribution, we model the signal modes with a Gaussian and the continuum background with a straight line. We are using these parametrisations as probability distribution functions (PDFs), implying that they are normalised in the fit region. The determination of the yields of the individual components is performed using an extended unbinned maximum likelihood fit. The fit is a procedure where we are determining the maximum likelihood by varying the floating parameters of the PDFs including the yields and the CP parameters. Using the reconstruction efficiency we can determine the branching fractions from the yield measurement.

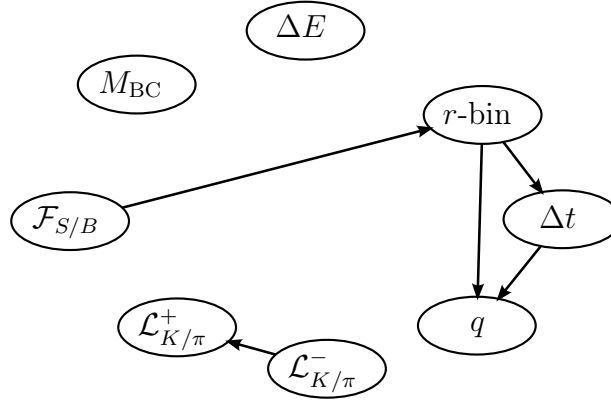
Now we are leaving the example of a one dimensional fit and are coming back to the analysis. Here, the branching fractions and CP parameters are determined using the same procedure as described in the one dimensional ΔE example, except that the physics parameters are extracted from a 7 dimensional extended unbinned maximum likelihood fit. We fit ΔE , M_{BC} , $\mathcal{L}_{K/\pi}^+$, $\mathcal{L}_{K/\pi}^-$, $\mathcal{F}_{S/B}$, q and Δt in every r -bin and SVD configuration, l and s , respectively. The complete Belle dataset was recorded in two run periods with different tracking subsystems. We are calling the run period from experiment 7 to 29, SVD1 and from experiment 31 to 65, SVD2. The probability density functions (PDFs) are built independently in the two run periods. Every signal channel and background is modelled as a independent component, l . In the following we are describing in detail how the PDFs for the different components are build.

4.4.1 Signal $B^0 \rightarrow \pi^+\pi^-$

The model is determined from correctly reconstructed signal MC events. A sample of 1×10^6 events were generated taking final state radiation into account. Then all events were processed according to the event selection described in section 4.3. In the remaining events, only 0.29% were found to be misreconstructed according to Monte-Carlo truth information. Therefore we do not need to implement a misreconstructed model. The same is true for the models of $K^+\pi^-$ and K^+K^- . The correlation table 4.4 shows very small correlations except for $\mathcal{L}_{K/\pi}^+$ with $\mathcal{L}_{K/\pi}^-$, and the fisher discriminant $\mathcal{F}_{S/B}$ with qr . The probability density function (PDF) is constructed as a product of individual PDFs for all variables except $\mathcal{L}_{K/\pi}^+$ and $\mathcal{L}_{K/\pi}^-$ where a combined 2 dimensional PDF is used. For better illustration of the correlations, Fig. 4.4 shows a Bayesian-probability network where the modelled correlations are shown as arrows.

Table 4.4: Correlation matrix for the $\pi^+ \pi^-$ signal Monte-Carlo.

	M_{BC}	ΔE	$\mathcal{L}_{K/\pi}^+$	$\mathcal{L}_{K/\pi}^-$	$\mathcal{F}_{S/B}$	q	qr	Δt
M_{BC}	1.00	-0.03	-0.00	-0.00	0.00	-0.00	-0.00	-0.00
ΔE		1.00	0.02	0.03	0.00	0.00	0.00	0.00
$\mathcal{L}_{K/\pi}^+$			1.00	0.05	-0.03	0.00	0.00	0.00
$\mathcal{L}_{K/\pi}^-$				1.00	-0.03	-0.00	0.00	0.00
$\mathcal{F}_{S/B}$					1.00	0.00	0.05	0.00
q						1.00	0.01	0.05
qr							1.00	0.01
Δt								1.00

**Figure 4.4:** Bayesian probability network for the component $\pi^+ \pi^-$. The directed acyclic graph shows the fit variables as nodes and the modelled correlations as arrows.

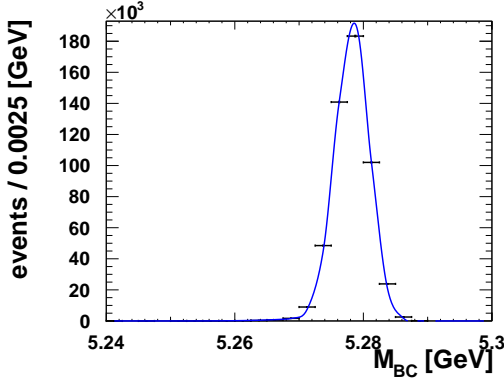
The PDF for M_{BC} and ΔE is modelled by a triple Gaussian which is the sum of three Gaussians which are defined in the following way,

$$\begin{aligned}
 \mathcal{P}_{\pi^+\pi^-}(M_{\text{BC}}) \equiv & f_1 \cdot G(M_{\text{BC}}, \mu_1^l + \mu_1^{\text{CF},l}, \sigma_1^l \cdot \sigma_1^{\text{CF},l}) \\
 & + f_2 \cdot G(M_{\text{BC}}, \mu_1^l + \mu_1^{\text{CF},l} + \mu_2^l, \sigma_1^l \cdot \sigma_1^{\text{CF},l} \cdot \sigma_2^l) \\
 & + (1 - f_1 - f_2) \cdot G(M_{\text{BC}}, \mu_1^l + \mu_1^{\text{CF},l} + \mu_2^l + \mu_3^l, \sigma_1^l \cdot \sigma_1^{\text{CF},l} \cdot \sigma_2^l \cdot \sigma_3^l), \quad (4.15)
 \end{aligned}$$

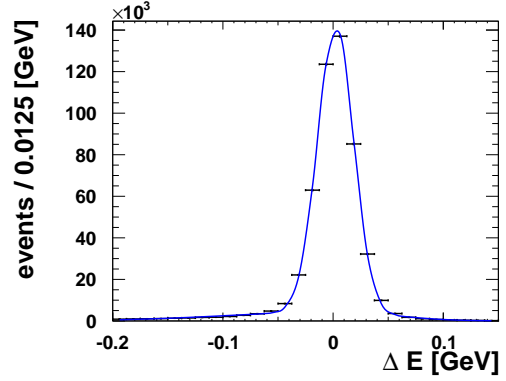
$$\begin{aligned}
 \mathcal{P}_{\pi^+\pi^-}(\Delta E) \equiv & f_1 \cdot G(\Delta E, \mu_1^l + \mu_1^{\text{CF},l}, \sigma_1^l \cdot \sigma_1^{\text{CF},l}) \\
 & + f_2 \cdot G(\Delta E, \mu_1^l + \mu_1^{\text{CF},l} + \mu_2^l, \sigma_1^l \cdot \sigma_1^{\text{CF},l} \cdot \sigma_2^l) \\
 & + (1 - f_1 - f_2) \cdot G(\Delta E, \mu_1^l + \mu_1^{\text{CF},l} + \mu_2^l + \mu_3^l, \sigma_1^l \cdot \sigma_1^{\text{CF},l} \cdot \sigma_2^l \cdot \sigma_3^l). \quad (4.16)
 \end{aligned}$$

The triple Gaussian also incorporates correction factors (labelled with a superscript CF) that may be floated in a final fit to data to compensate differences between data and Monte-Carlo (MC). The correction factors may be determined by a fit to a control sample

(Sec. 5.1). For the fit to $\pi^+ \pi^-$ signal Monte-Carlo, the correction factors that modify the mean are fixed to zero while the correction factors that change the width are fixed to unity. The fit results can be found in figure 4.5.



(a) Fit projection of the variable M_{BC} from full detector simulation Monte-Carlo.



(b) Fit projection of the variable ΔE from full detector simulation Monte-Carlo.

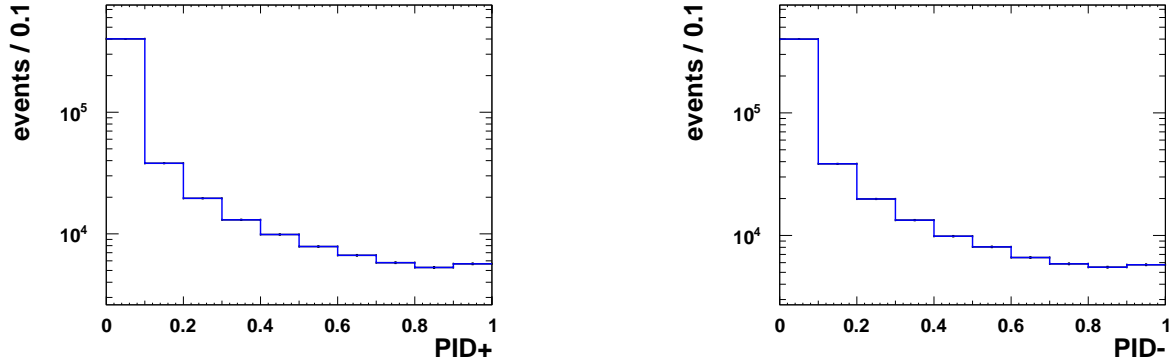
Figure 4.5: Fit results for the variables M_{BC} and ΔE for component $\pi^+ \pi^-$. Data points with errors represent the MC from full detector simulation and the solid blue line represents the fit result.

As the $\mathcal{L}_{K/\pi}^+$ and $\mathcal{L}_{K/\pi}^-$ variables are correlated, we model them with a two dimensional histogram. Correction factors for cuts on $\mathcal{L}_{K/\pi}^+$ or $\mathcal{L}_{K/\pi}^-$ are available from a previous analysis. Starting with these correction factors, an algorithm explained in section 5.2 is used to correct the histogram obtained from Monte-Carlo to resemble the data. The $\mathcal{F}_{S/B}$ fit results can be found in figure 4.6.

The Fisher discriminant that distinguishes between signal (B decays) and continuum ($e^+e^- \rightarrow q\bar{q}$, where $q = u, d, s, c$), $\mathcal{F}_{S/B}$, is modelled by a triple Gaussian in every r -bin, l . This procedure handles the correlation of $\mathcal{F}_{S/B}$ with the r -bin and is used for all components, j . The parameters of the triple Gaussian are determined from Monte-Carlo of the decay $B^0 \rightarrow \pi^+\pi^-$. The same parameters are used for the other signal decays $B \rightarrow K\pi$ and $B^0 \rightarrow K^+K^-$. The triple Gaussian is a sum of three individual Gaussians, containing correction factors which can be applied to incorporate the differences between data and MC where necessary,

$$\begin{aligned} \mathcal{P}_j^l(\mathcal{F}_{S/B}) \equiv & f_1 \cdot G(\mathcal{F}_{S/B}, \mu_1^l + \mu_1^{\text{CF},l}, \sigma_1^l \cdot \sigma_1^{\text{CF},l}) \\ & + f_2 \cdot G(\mathcal{F}_{S/B}, \mu_1^l + \mu_1^{\text{CF},l} + \mu_2^l, \sigma_1^l \cdot \sigma_1^{\text{CF},l} \cdot \sigma_2^l) \\ & + (1 - f_1 - f_2) \cdot G(\mathcal{F}_{S/B}, \mu_1^l + \mu_1^{\text{CF},l} + \mu_2^l + \mu_3^l, \sigma_1^l \cdot \sigma_1^{\text{CF},l} \cdot \sigma_2^l \cdot \sigma_3^l). \end{aligned} \quad (4.17)$$

The fit results can be found in figure 4.7.



(a) Fit projection of the variable $\mathcal{L}_{K/\pi}^+$ from full detector simulation Monte-Carlo.

(b) Fit projection of the variable $\mathcal{L}_{K/\pi}^-$ from full detector simulation Monte-Carlo.

Figure 4.6: Fit results for the variables $\mathcal{L}_{K/\pi}^+$ and $\mathcal{L}_{K/\pi}^-$ for component $\pi^+ \pi^-$. Data points with errors represent the MC from full detector simulation and the solid blue histogram represents the fit result.

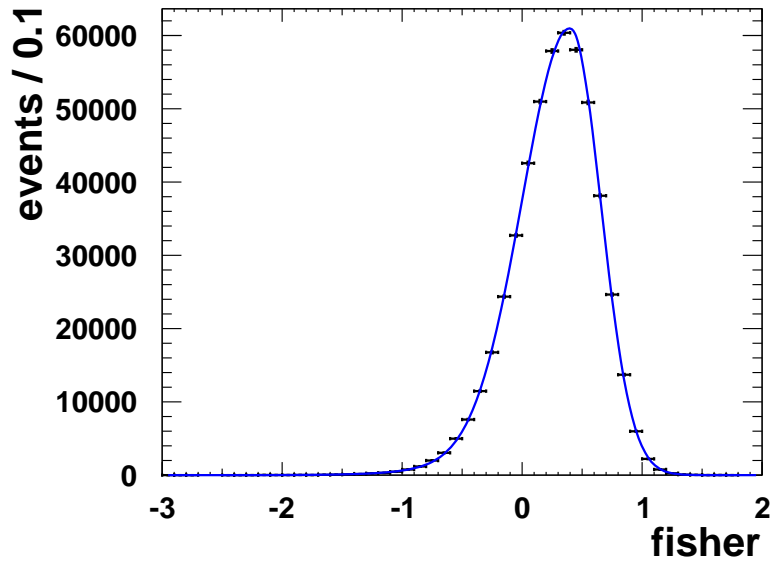


Figure 4.7: Fit results for the variable $\mathcal{F}_{S/B}$ for component $\pi^+ \pi^-$. The PDF is shown in blue while the full detector simulation Monte-Carlo is plotted in black including errors.

The time dependent CP parameters \mathcal{A}_{CP} and \mathcal{S}_{CP} are determined by including the following PDF,

$$\mathcal{P}_{\pi^+\pi^-}^l(\Delta t, q) \equiv \frac{e^{-|\Delta t|/\tau_{B^0}}}{4\tau_{B^0}} \left\{ (1 - q\Delta w_l + q(1 - 2w_l)) \times \left[(\mathcal{A}_{CP} \cos \Delta m_d \Delta t + \mathcal{S}_{CP} \sin \Delta m_d \Delta t) \right] \right\} \otimes R_{B^0\bar{B}^0}(\Delta t). \quad (4.18)$$

The PDF accounts for the dilution from probability of incorrect flavour tagging, w_l and the difference between wrong flavour tagging in B^0 and \bar{B}^0 decays, Δw_l . The CP asymmetry PDF is convoluted with the detector resolution function $R_{B^0\bar{B}^0}(\Delta t)$, for neutral B mesons. The resolution function [68] is explained in appendix C. The PDF also depends on the B lifetime τ_{B^0} , and the mass difference between B_H and B_L , Δm_d . The following values were used to generate the $\pi^+ \pi^-$ signal Monte-Carlo,

$$\begin{aligned} \tau_{B^0} &= 1.534\,39 \text{ ps}, \\ \Delta m_d &= 0.507 \times 10^{12} \text{ } \hbar\text{s}^{-1}, \\ \mathcal{A}_{CP} &= 0.36, \\ \mathcal{S}_{CP} &= -0.65. \end{aligned}$$

The fit results can be found in figure 4.8.

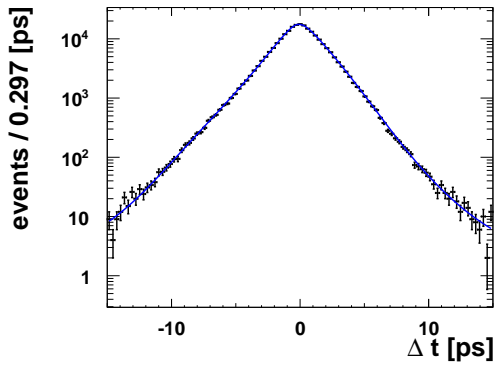
The total PDF for the $\pi^+ \pi^-$ component is constructed to be

$$\begin{aligned} \mathcal{P}_{\pi^+\pi^-}^l(M_{BC}, \Delta E, \mathcal{L}_{K/\pi}^+, \mathcal{L}_{K/\pi}^-, \mathcal{F}_{S/B}, q, \Delta t) \equiv \\ \mathcal{P}_{\pi^+\pi^-}(M_{BC}) \mathcal{P}_{\pi^+\pi^-}(\Delta E) \mathcal{P}_{\pi^+\pi^-}(\mathcal{L}_{K/\pi}^+, \mathcal{L}_{K/\pi}^-) \\ \mathcal{P}_{\pi^+\pi^-}^l(\mathcal{F}_{S/B}) \mathcal{P}_{\pi^+\pi^-}^l(q, \Delta t). \end{aligned} \quad (4.19)$$

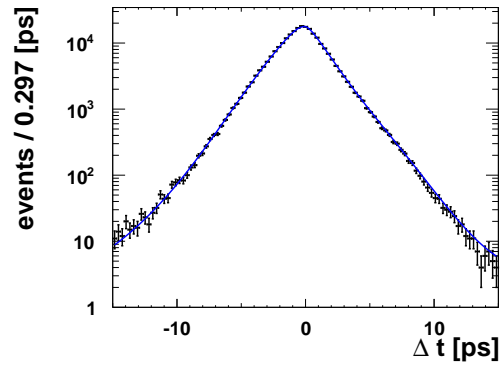
Its shape can be determined by maximizing the following likelihood,

$$\mathcal{L}_j \equiv \prod_{l,s} \frac{e^{N_j^s \sum_{l,s} f_j^{l,s}}}{N_{l,s}!} \prod_{i=0}^{N_{l,s}} N_j^s f_j^{l,s} \mathcal{P}_j^{l,s}(M_{BC}^i, \Delta E^i, \mathcal{L}_{K/\pi}^{+,i}, \mathcal{L}_{K/\pi}^{-,i}, \mathcal{F}_{S/B}^i, q^i, \Delta t^i), \quad (4.20)$$

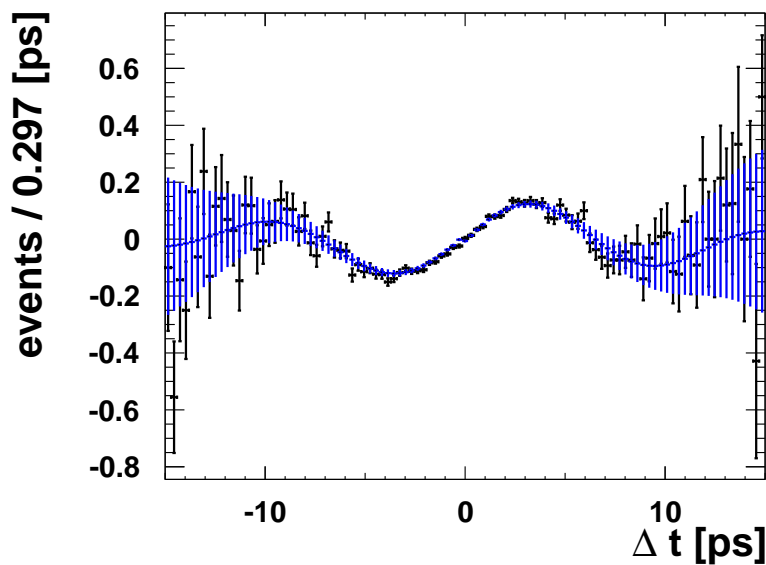
where j is the component. The parameter N is the signal yield, f is the fraction of events in r -bin and SVD configuration l, s . The fit results to $\pi^+ \pi^-$ signal Monte-Carlo are shown in Figs. 4.5, 4.6, 4.7, 4.8.



(a) Δt PDF projection on full detector simulation Monte-Carlo for events tagged as B^0 ($q = 1$).



(b) Δt PDF projection on full detector simulation Monte-Carlo for events tagged as \bar{B}^0 ($q = -1$).



(c) $\pi^+ \pi^- \Delta t$ asymmetry (normalized difference of the above histograms.)

Figure 4.8: Fit results for the variable Δt for component $\pi^+ \pi^-$. Data points with errors represent the MC from full detector simulation and the solid blue line (or histogram) represents the fit result.

4.4.2 Signal $B^0 \rightarrow K^+\pi^-$

In analogy to the signal model for $B^0 \rightarrow \pi^+\pi^-$, we are building the signal model for $B^0 \rightarrow K^+\pi^-$. In fact we are creating two models, one model for the component $K^+\pi^-$, and one model for the component $K^-\pi^+$. The relative fraction of the two components is parametrised using \mathcal{A}_{CP} . The definition of \mathcal{A}_{CP} in Eq. 2.55 is used. Unlike for the channel $B^0 \rightarrow \pi^+\pi^-$ where we are determining the CP parameters from the Δt distribution, we can obtain $\mathcal{A}_{CP}K\pi$ from the relative branching fraction measurement. The models for the two components of $B^0/\bar{B}^0 \rightarrow K^\pm\pi^\mp$ share all parameters except the particle identification (PID) PDFs. Furthermore, the parameters for the $\mathcal{F}_{S/B}$, that discriminates between $B\bar{B}$ events and continuum events, are identical to that we used to model $B^0 \rightarrow \pi^+\pi^-$.

Table 4.5: Correlation matrix for the $K^+\pi^-$ signal Monte-Carlo.

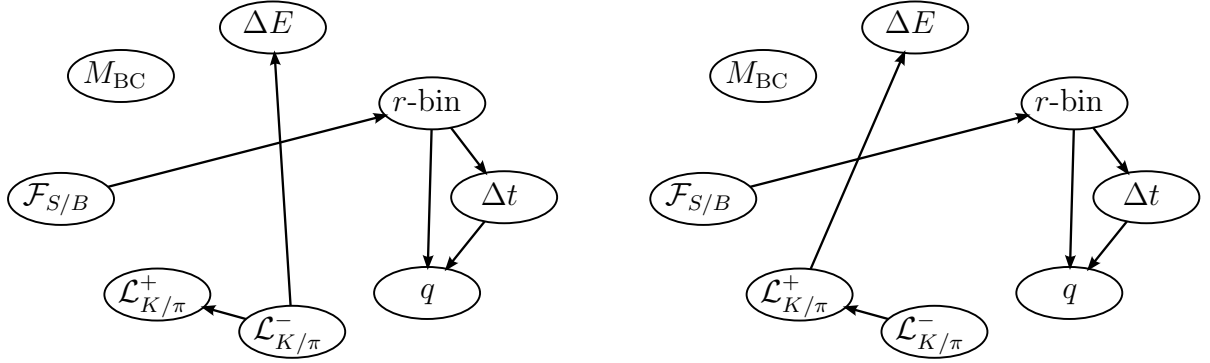
	M_{BC}	ΔE	$\mathcal{L}_{K/\pi}^+$	$\mathcal{L}_{K/\pi}^-$	$\mathcal{F}_{S/B}$	q	qr	Δt
M_{BC}	1.00	-0.09	0.01	-0.00	0.01	-0.00	0.00	-0.02
ΔE		1.00	0.00	0.04	-0.00	0.00	-0.00	0.00
$\mathcal{L}_{K/\pi}^+$			1.00	-0.02	0.03	-0.00	0.01	0.00
$\mathcal{L}_{K/\pi}^-$				1.00	-0.03	0.00	-0.00	0.00
$\mathcal{F}_{S/B}$					1.00	-0.01	0.05	-0.00
q						1.00	-0.21	-0.01
qr							-0.38	0.01
Δt								1.00

Table 4.6: Correlation matrix for the $K^-\pi^+$ signal Monte-Carlo.

	M_{BC}	ΔE	$\mathcal{L}_{K/\pi}^+$	$\mathcal{L}_{K/\pi}^-$	$\mathcal{F}_{S/B}$	q	qr	Δt
M_{BC}	1.00	-0.10	-0.00	0.01	0.01	0.00	0.00	-0.02
ΔE		1.00	0.04	0.01	-0.00	0.00	0.00	0.01
$\mathcal{L}_{K/\pi}^+$			1.00	-0.02	-0.03	-0.00	-0.00	-0.00
$\mathcal{L}_{K/\pi}^-$				1.00	0.03	0.00	0.01	0.00
$\mathcal{F}_{S/B}$					1.00	0.01	0.05	-0.00
q						1.00	0.22	0.00
qr							0.38	0.01
Δt								1.00

For the $K\pi$ model, we have to split up the data sample in the $K^+\pi^-$ component and the $K^-\pi^+$ component. The correlation tables(4.5,4.6) look very similar except the correlation of ΔE with the particle identification Likelihood ratio. We can see that only the pion-like track is correlated with ΔE . Both components share the correlations M_{BC} with ΔE , and $\mathcal{L}_{K/\pi}^+$ with $\mathcal{L}_{K/\pi}^-$. The probability density function (PDF) is constructed as a product of

individual PDFs for all variables except $\mathcal{L}_{K/\pi}^+$, $\mathcal{L}_{K/\pi}^-$ where a combined 2 dimensional PDF is used. We construct two PDFs for $K^+ \pi^-$ and $K^- \pi^+$, respectively. The two models share the PDF models and parameters for all variables except $\mathcal{L}_{K/\pi}^+$ and $\mathcal{L}_{K/\pi}^-$. For better illustration of the correlations, figure 4.9 shows a Bayesian-probability network where the modelled correlations are shown as arrows.



(a) Bayesian probability network for the component $K^+ \pi^-$.

(b) Bayesian probability network for the component $K^- \pi^+$.

Figure 4.9: Bayesian probability network for the $K \pi$ components. The directed acyclic graph shows the fit variables as nodes and the modelled correlations as arrows.

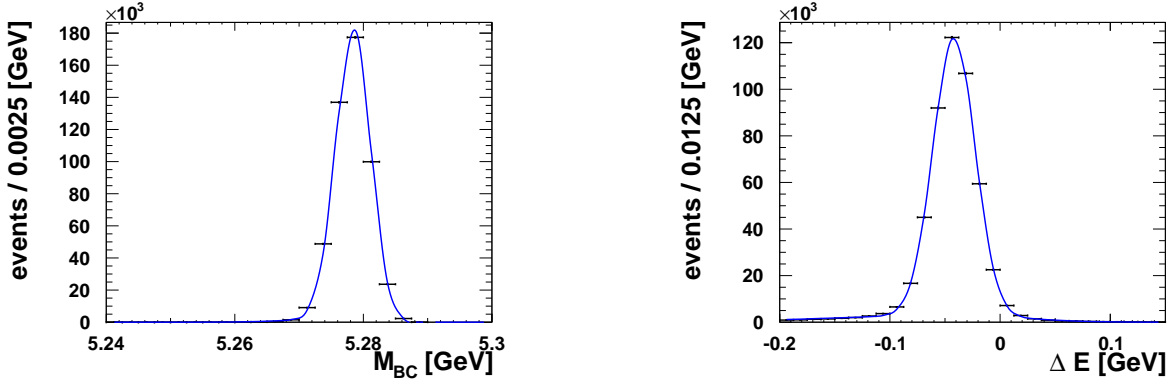
The PDF for M_{BC} and ΔE is modelled by the sum of three Gaussians that are defined the following way analogous to the model of $B^0 \rightarrow \pi^+ \pi^-$,

$$\begin{aligned} \mathcal{P}_{\pi^+ \pi^-}(M_{BC}) \equiv & f_1 \cdot G(M_{BC}, \mu_1^l + \mu_1^{\text{CF},l}, \sigma_1^l \cdot \sigma_1^{\text{CF},l}) \\ & + f_2 \cdot G(M_{BC}, \mu_1^l + \mu_1^{\text{CF},l} + \mu_2^l, \sigma_1^l \cdot \sigma_1^{\text{CF},l} \cdot \sigma_2^l) \\ & + (1 - f_1 - f_2) \cdot G(M_{BC}, \mu_1^l + \mu_1^{\text{CF},l} + \mu_2^l + \mu_3^l, \sigma_1^l \cdot \sigma_1^{\text{CF},l} \cdot \sigma_2^l \cdot \sigma_3^l), \end{aligned} \quad (4.21)$$

$$\begin{aligned} \mathcal{P}_{\pi^+ \pi^-}(\Delta E) \equiv & f_1 \cdot G(\Delta E, \mu_1^l + \mu_1^{\text{CF},l}, \sigma_1^l \cdot \sigma_1^{\text{CF},l}) \\ & + f_2 \cdot G(\Delta E, \mu_1^l + \mu_1^{\text{CF},l} + \mu_2^l, \sigma_1^l \cdot \sigma_1^{\text{CF},l} \cdot \sigma_2^l) \\ & + (1 - f_1 - f_2) \cdot G(\Delta E, \mu_1^l + \mu_1^{\text{CF},l} + \mu_2^l + \mu_3^l, \sigma_1^l \cdot \sigma_1^{\text{CF},l} \cdot \sigma_2^l \cdot \sigma_3^l). \end{aligned} \quad (4.22)$$

The triple Gaussian also incorporates correction factors that may be floated in a fit to control sample data to compensate differences between data and Monte-Carlo (MC). We use the same method for obtaining the correction factors as for the $\pi^+ \pi^-$ model. The fit results can be found in figure 4.10.

As the $\mathcal{L}_{K/\pi}^+$ and $\mathcal{L}_{K/\pi}^-$ are correlated, we model them with a two dimensional histogram. We construct two 2D histograms for $K^+ \pi^-$ ($g = 1$) and $K^- \pi^+$ ($g = 2$), respectively. Correction factors for cuts on $\mathcal{L}_{K/\pi}^+$ or $\mathcal{L}_{K/\pi}^-$ are available from an independent analysis.



(a) Fit projection of the variable M_{BC} from full detector simulation Monte-Carlo.

(b) Fit projection of the variable ΔE from full detector simulation Monte-Carlo.

Figure 4.10: Fit results for the variables M_{BC} and ΔE , for component $K^+ \pi^-$. Data points with errors represent the MC from full detector simulation and the solid blue line represents the fit result.

Starting with these correction factors, an algorithm explained in section 5.2 is used to correct the histogram obtained from Monte-Carlo to resemble the data,

$$\mathcal{P}_{K^+\pi^-}^g(\mathcal{L}_{K/\pi}^+ \mathcal{L}_{K/\pi}^-) \equiv \mathcal{H}(\mathcal{L}_{K/\pi}^{+g}, \mathcal{L}_{K/\pi}^{-g}). \quad (4.23)$$

The fit results can be found in figure 4.11.

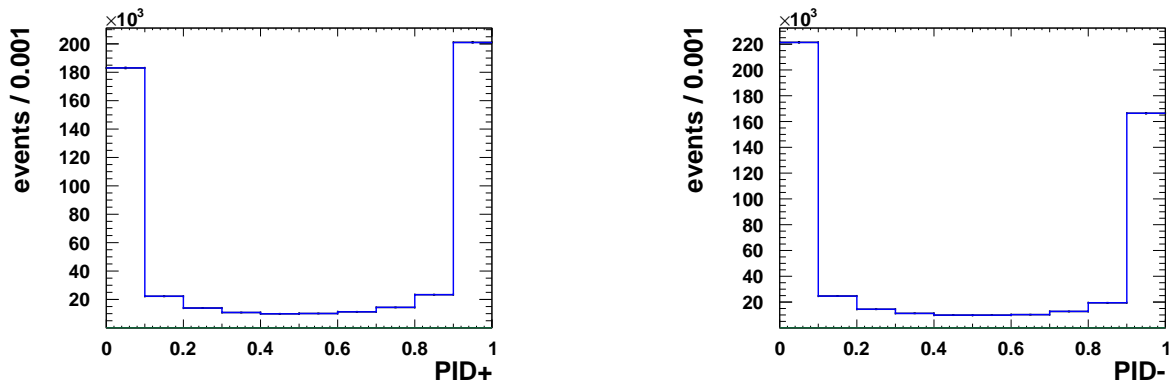
For the $\mathcal{F}_{S/B}$ variable, we use the same model as for all B decays. It is described for the $\pi^+\pi^-$ model above,

$$\begin{aligned} \mathcal{P}_j^l(\mathcal{F}_{S/B}) \equiv & f_1 \cdot G(\mathcal{F}_{S/B}, \mu_1^l + \mu_1^{\text{CF},l}, \sigma_1^l \cdot \sigma_1^{\text{CF},l}) \\ & + f_2 \cdot G(\mathcal{F}_{S/B}, \mu_1^l + \mu_1^{\text{CF},l} + \mu_2^l, \sigma_1^l \cdot \sigma_1^{\text{CF},l} \cdot \sigma_2^l) \\ & + (1 - f_1 - f_2) \cdot G(\mathcal{F}_{S/B}, \mu_1^l + \mu_1^{\text{CF},l} + \mu_2^l + \mu_3^l, \sigma_1^l \cdot \sigma_1^{\text{CF},l} \cdot \sigma_2^l \cdot \sigma_3^l), \end{aligned} \quad (4.24)$$

The fit results can be found in figure 4.12.

The channel $K^+ \pi^-$, is not an eigenstate of the CP symmetry. For this reason, a mixing-induced asymmetry \mathcal{S}_{CP} , cannot be observed. The direct \mathcal{A}_{CP} is determined from the ratio between the $K^+ \pi^-$ and $K^- \pi^+$ PDFs. The best discriminant is not Δt , but the particle identification likelihoods of the positively and negatively charges particles ($\mathcal{L}_{K/\pi}^+, \mathcal{L}_{K/\pi}^-$). Nevertheless we have to model the Δt PDF account for neutral $B^0 \bar{B}^0$ mixing,

$$\begin{aligned} \mathcal{P}_{K^+\pi^-}^{l,g}(\Delta t, q) \equiv & \frac{e^{-|\Delta t|/\tau_{B^0}}}{4\tau_{B^0}} \\ & (1 - q\Delta w_l + q(1 - 2w_l) \cdot \mathcal{A}_{CP}^{\text{eff},g} \cdot \cos \Delta t \Delta m) \\ & \otimes R_{B^0 \bar{B}^0}(\Delta t). \end{aligned} \quad (4.25)$$



(a) Fit projection of the variable $\mathcal{L}_{K/\pi}^+$ from full detector simulation Monte-Carlo.

(b) Fit projection of the variable $\mathcal{L}_{K/\pi}^-$ from full detector simulation Monte-Carlo.

Figure 4.11: Fit results for the variables $\mathcal{L}_{K/\pi}^+$ and $\mathcal{L}_{K/\pi}^-$ for component $K^+ \pi^-$. Data points with errors represent the MC from full detector simulation and the solid blue histogram represents the fit result.

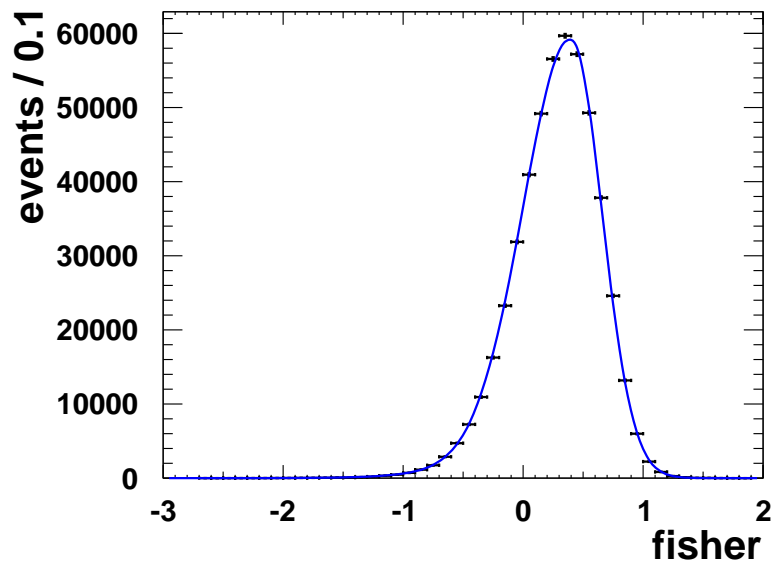


Figure 4.12: Fit results for the variable $\mathcal{F}_{S/B}$ for component $K^+ \pi^-$. The PDF is shown in blue while the full detector simulation Monte-Carlo is plotted in black including errors.

The effective \mathcal{A}_{CP} is dependent on the component ($K^+ \pi^-$ or $K^- \pi^+$), g , which means:

$$\mathcal{A}_{CP}^{\text{eff}} = -1 \quad \text{for } K^+ \pi^- \text{ } g = 1, \quad (4.26)$$

$$\mathcal{A}_{CP}^{\text{eff}} = 1 \quad \text{for } K^- \pi^+ \text{ } g = 2. \quad (4.27)$$

The PDF also depends on the B lifetime τ_{B^0} , and the mass difference between B_H and B_L Δm_d . The following values were used to generate the $K^+ \pi^-$ signal Monte-Carlo,

$$\begin{aligned} \tau_{B^0} &= 1.534 \text{ } 39 \text{ ps,} \\ \Delta m_d &= 0.507 \times 10^{12} \text{ } \hbar s^{-1}, \\ \chi_d &= 0.1878, \\ \mathcal{A}_{CP} &= -0.087. \end{aligned}$$

The fit result from the Δt dimension can be found in figure 4.13. The total PDF for the $K^+ \pi^-$ component is constructed to be

$$\begin{aligned} \mathcal{P}_{K^+ \pi^-}^{l,g}(M_{\text{BC}}, \Delta E, \mathcal{L}_{K/\pi}^+, \mathcal{L}_{K/\pi}^-, \mathcal{F}_{S/B}, q, \Delta t) \equiv \\ \mathcal{P}_{K^+ \pi^-}(M_{\text{BC}}) \mathcal{P}_{K^+ \pi^-}(\Delta E) \mathcal{P}_{K^+ \pi^-}^g(\mathcal{L}_{K/\pi}^+, \mathcal{L}_{K/\pi}^-) \mathcal{P}_{K^+ \pi^-}^l(\mathcal{F}_{S/B}) \mathcal{P}_{K^+ \pi^-}^l(q, \Delta t). \end{aligned} \quad (4.28)$$

The likelihood is constructed differently for this channel than for the other channels. Basically the $B^0 \rightarrow K^+ \pi^-$ and $B^0 \rightarrow K^- \pi^+$ components are treated as two independent channels interconnected by \mathcal{A}_{CP} .

$$\begin{aligned} \mathcal{L}_j \equiv \prod_{l,s} \frac{e^{N_j^s \sum_{l,s} f_j^{l,s}}}{N_{l,s}!} \times \\ \prod_{i=0}^{N_{l,s}} N_j^s f_j^{l,s} (1 - \mathcal{A}_{CP}^j) \mathcal{P}_j^{l,s,g=1}(M_{\text{BC}}^i, \Delta E^i, \mathcal{L}_{K/\pi}^{+,i,g}, \mathcal{L}_{K/\pi}^{-,i}, \mathcal{F}_{S/B}^i, q^i, \Delta t^i) \times \\ \prod_{i=0}^{N_{l,s}} N_j^s f_j^{l,s} (1 + \mathcal{A}_{CP}^j) \mathcal{P}_j^{l,s,g=2}(M_{\text{BC}}^i, \Delta E^i, \mathcal{L}_{K/\pi}^{+,i,g}, \mathcal{L}_{K/\pi}^{-,i}, \mathcal{F}_{S/B}^i, q^i, \Delta t^i), \end{aligned} \quad (4.29)$$

where j is the component. The parameter N is the signal yield and f is the fraction of events in r -bin and SVD configuration l, s . The fit results to $K^+ \pi^-$ signal Monte-Carlo are shown in Figs. 4.10, 4.11, 4.12, 4.13.

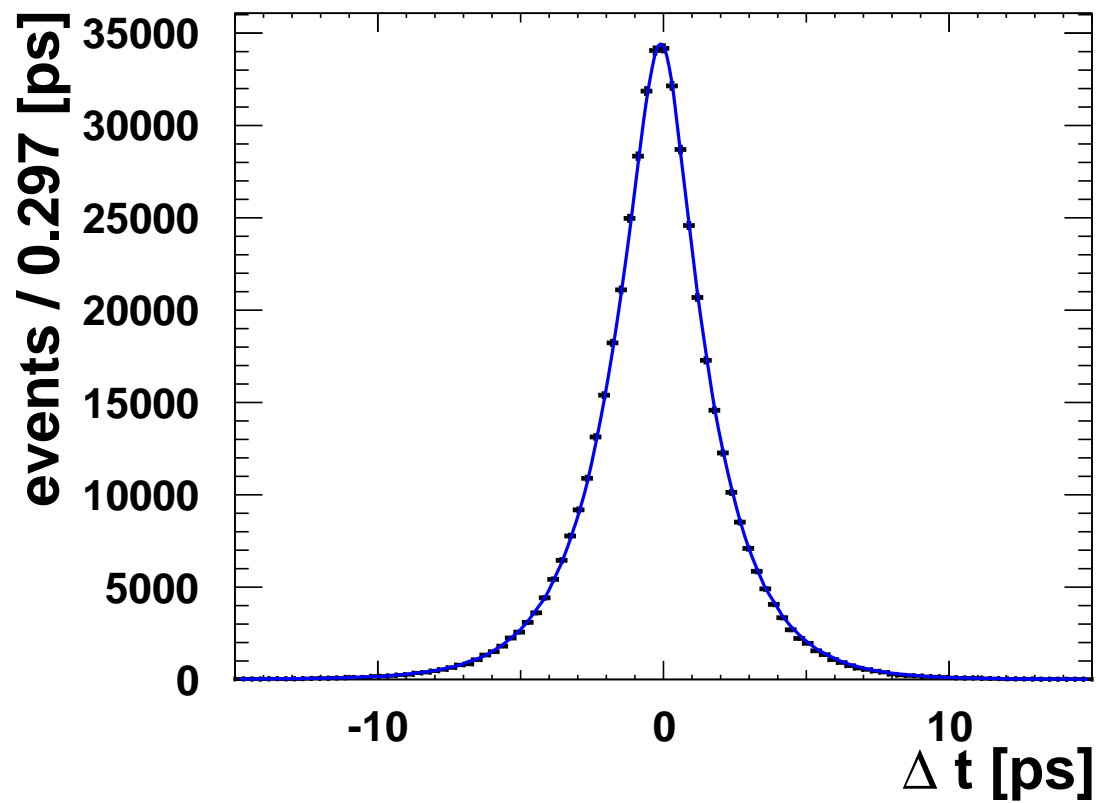


Figure 4.13: Fit results for variable Δt , for component $K^+ \pi^-$. Data points with errors represent the MC from full detector simulation and the solid blue line represents the fit result.

4.4.3 Signal $B^0 \rightarrow K^+K^-$

The decay $B^0 \rightarrow K^+K^-$ is kinematically similar to the decay of $B^0 \rightarrow \pi^+\pi^-$ except for the mass difference between the kaon and the pion. Therefore, also the parametrisation forms are identical in all dimensions. The ΔE distributions differs between the two channels. The reconstruction and event selection (Sec. 4.3) assumes the pion mass as mass of the two charged particles that are combined to a B meson. Therefore the reconstructed energy is shifted by two times the mass difference between the kaon and the pion, $2 \cdot (m(K) - m(\pi)) = 2 \cdot 354 \text{ MeV} = 708 \text{ MeV}$, with respect to the channel $B^0 \rightarrow \pi^+\pi^-$. In addition, the PID likelihood peaks at the opposite side. The correlation table 4.7 shows correlations for M_{BC}

Table 4.7: Correlation matrix for the $K^+ K^-$ signal Monte-Carlo.

	M_{BC}	ΔE	$\mathcal{L}_{K/\pi}^+$	$\mathcal{L}_{K/\pi}^-$	$\mathcal{F}_{S/B}$	q	qr	Δt
M_{BC}	1.00	-0.16	0.01	0.01	0.03	-0.00	-0.00	-0.03
ΔE		1.00	-0.01	-0.01	-0.01	0.00	0.00	0.01
$\mathcal{L}_{K/\pi}^+$			1.00	0.02	0.03	-0.00	0.01	-0.00
$\mathcal{L}_{K/\pi}^-$				1.00	0.03	0.00	0.01	-0.00
$\mathcal{F}_{S/B}$					1.00	0.00	0.05	-0.01
q						1.00	0.00	-0.00
qr							-0.00	0.01
Δt								1.00

with ΔE , and $\mathcal{L}_{K/\pi}^+$ with $\mathcal{L}_{K/\pi}^-$. The probability density function (PDF) is constructed as a product of individual PDFs for all variables except for $\mathcal{L}_{K/\pi}^+$ and $\mathcal{L}_{K/\pi}^-$, where a combined 2 dimensional PDF is used. For better illustration of the correlations, figure 4.14 shows a Bayesian-probability network where the modelled correlations are shown as arrows.

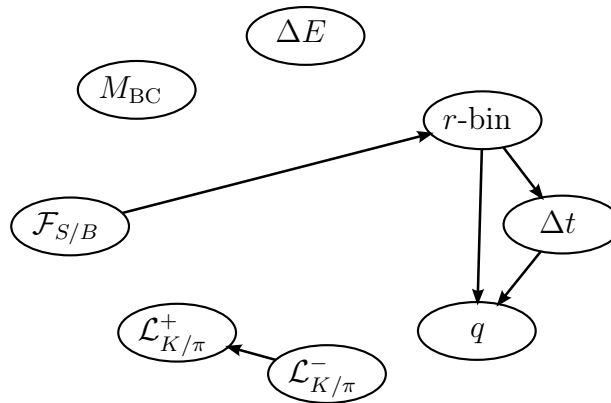


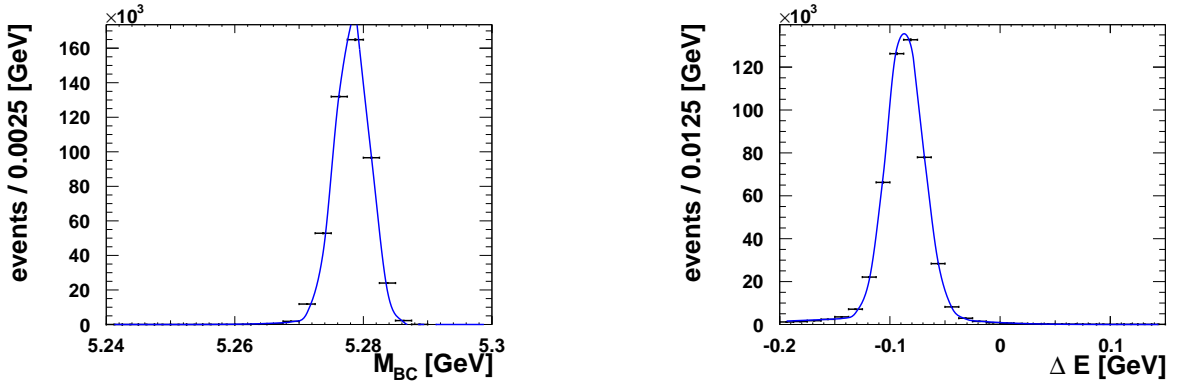
Figure 4.14: Bayesian probability network for the component $K^+ K^-$. The directed acyclic graph shows the fit variables as nodes and the modelled correlations as arrows.

The PDF for M_{BC} and ΔE is modelled by the sum of three Gaussians that are defined in analogy to the $\pi^+\pi^-$ model the following way,

$$\begin{aligned} \mathcal{P}_{\pi^+\pi^-}(M_{BC}) \equiv & f_1 \cdot G(M_{BC}, \mu_1^l + \mu_1^{\text{CF},l}, \sigma_1^l \cdot \sigma_1^{\text{CF},l}) \\ & + f_2 \cdot G(M_{BC}, \mu_1^l + \mu_1^{\text{CF},l} + \mu_2^l, \sigma_1^l \cdot \sigma_1^{\text{CF},l} \cdot \sigma_2^l) \\ & + (1 - f_1 - f_2) \cdot G(M_{BC}, \mu_1^l + \mu_1^{\text{CF},l} + \mu_2^l + \mu_3^l, \sigma_1^l \cdot \sigma_1^{\text{CF},l} \cdot \sigma_2^l \cdot \sigma_3^l), \end{aligned} \quad (4.30)$$

$$\begin{aligned} \mathcal{P}_{\pi^+\pi^-}(\Delta E) \equiv & f_1 \cdot G(\Delta E, \mu_1^l + \mu_1^{\text{CF},l}, \sigma_1^l \cdot \sigma_1^{\text{CF},l}) \\ & + f_2 \cdot G(\Delta E, \mu_1^l + \mu_1^{\text{CF},l} + \mu_2^l, \sigma_1^l \cdot \sigma_1^{\text{CF},l} \cdot \sigma_2^l) \\ & + (1 - f_1 - f_2) \cdot G(\Delta E, \mu_1^l + \mu_1^{\text{CF},l} + \mu_2^l + \mu_3^l, \sigma_1^l \cdot \sigma_1^{\text{CF},l} \cdot \sigma_2^l \cdot \sigma_3^l). \end{aligned} \quad (4.31)$$

The triple Gaussian also incorporates correction factors that may be floated in a fit to control sample data to compensate differences between data and Monte-Carlo (MC). For the fit to $K^+ K^-$ signal Monte-Carlo, the correction factors that modify the mean are fixed to zero while the correction factors that change the width are fixed to unity. The fit results can be found in figure 4.15.

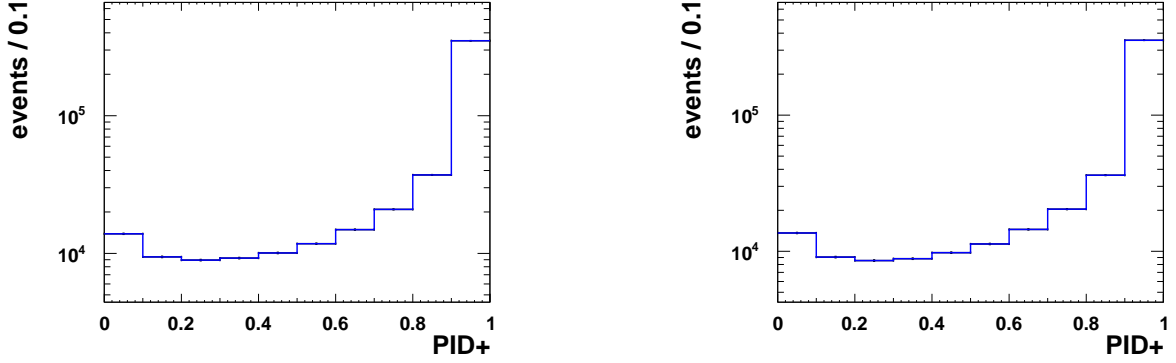


(a) Fit projection of the variable M_{BC} , from full detector simulation Monte-Carlo.

(b) Fit projection of the variable ΔE , from full detector simulation Monte-Carlo.

Figure 4.15: Fit results for the variables M_{BC} and ΔE , for component $K^+ K^-$. Data points with errors represent the MC from full detector simulation and the solid blue line represents the fit result.

As the $\mathcal{L}_{K/\pi}^+$ and $\mathcal{L}_{K/\pi}^-$ variables are correlated, we model them with a two dimensional histogram. Correction factors for cuts on $\mathcal{L}_{K/\pi}^+$ or $\mathcal{L}_{K/\pi}^-$ are available from an independent analysis. Starting with these correction factors, an algorithm explained in section 5.2 is used to correct the histogram obtained from Monte-Carlo to resemble the data. The fit results can be found in figure 4.16.



(a) Fit projection of the variable $\mathcal{L}_{K/\pi}^+$, from full detector simulation Monte-Carlo.

(b) Fit projection of the variable $\mathcal{L}_{K/\pi}^-$, from full detector simulation Monte-Carlo.

Figure 4.16: Fit results for the variables $\mathcal{L}_{K/\pi}^+$ and $\mathcal{L}_{K/\pi}^-$, for component $K^+ K^-$. Data points with errors represent the MC from full detector simulation and the solid blue histogram represents the fit result.

For the $\mathcal{F}_{S/B}$ variable, we use the same model as for all B decays. It is described for the $\pi^+\pi^-$ model above,

$$\begin{aligned} \mathcal{P}_j^l(\mathcal{F}_{S/B}) \equiv & f_1 \cdot G(\mathcal{F}_{S/B}, \mu_1^l + \mu_1^{\text{CF},l}, \sigma_1^l \cdot \sigma_1^{\text{CF},l}) \\ & + f_2 \cdot G(\mathcal{F}_{S/B}, \mu_1^l + \mu_1^{\text{CF},l} + \mu_2^l, \sigma_1^l \cdot \sigma_1^{\text{CF},l} \cdot \sigma_2^l) \\ & + (1 - f_1 - f_2) \cdot G(\mathcal{F}_{S/B}, \mu_1^l + \mu_1^{\text{CF},l} + \mu_2^l + \mu_3^l, \sigma_1^l \cdot \sigma_1^{\text{CF},l} \cdot \sigma_2^l \cdot \sigma_3^l). \end{aligned} \quad (4.32)$$

The $\mathcal{F}_{S/B}$ fit results can be found in figure 4.17.

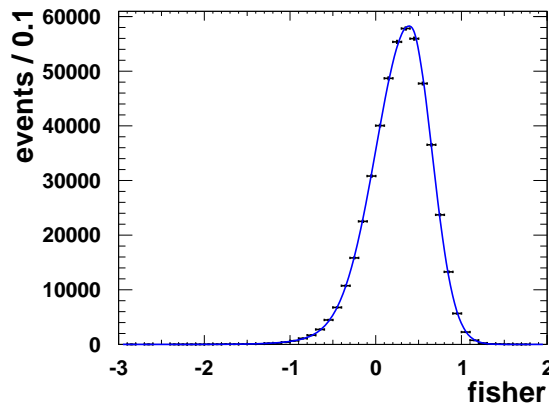


Figure 4.17: Fit results for the variable $\mathcal{F}_{S/B}$ for component $K^+ K^-$. The PDF is shown in blue while the full detector simulation Monte-Carlo is plotted in black including errors.

The time dependent CP parameters \mathcal{A}_{CP} and \mathcal{S}_{CP} are determined by multiplying by the following PDF, The Δt distribution is modeled with the same parametrisation as in the $\pi^+\pi^-$ model. Since we expect to have very low statistics in the final fit, \mathcal{A}_{CP} and \mathcal{S}_{CP} are fixed to zero. We use the Δt PDF of

$$\mathcal{P}_{K^+K^-}^l(\Delta t, q) \equiv \frac{e^{-|\Delta t|/\tau_{B^0}}}{4\tau_{B^0}} \left\{ (1 - q\Delta w_l + q(1 - 2w_l)) \times \left[(\mathcal{A}_{CP} \cos \Delta m_d \Delta t + \mathcal{S}_{CP} \sin \Delta m_d \Delta t) \right] \right\} \otimes R_{B^0\bar{B}^0}(\Delta t). \quad (4.33)$$

The PDF accounts for the dilution from probability of incorrect flavour tagging, w_l and the difference between wrongly tagging B^0 and \bar{B}^0 , Δw_l . The CP asymmetry PDF is convoluted with the detector resolution function $R_{B^0\bar{B}^0}(\Delta t)$, for neutral B mesons. The resolution function [68] is explained in appendix C. The PDF also depends on the B lifetime τ_{B^0} , and the mass difference between B_H and B_L , Δm_d . The following values were used to generate the $K^+ K^-$ signal Monte-Carlo,

$$\begin{aligned} \tau_{B^0} &= 1.534\,39 \text{ ps}, \\ \Delta m_d &= 0.507 \times 10^{12} \text{ } \hbar\text{s}^{-1}, \\ \mathcal{A}_{CP} &= 0.0, \\ \mathcal{S}_{CP} &= 0.0. \end{aligned}$$

The fit results for the Δt dimension can be found in figure 4.18.

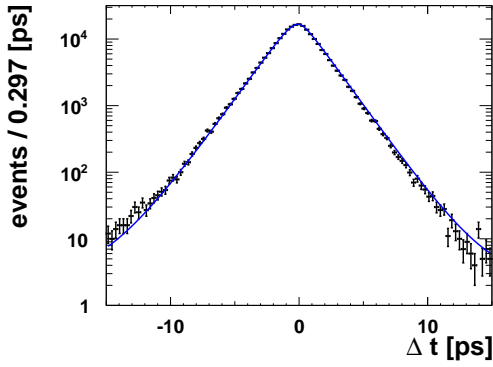
The total PDF for the $K^+ K^-$ component is constructed to be

$$\begin{aligned} \mathcal{P}_{K^+K^-}^l(M_{BC}, \Delta E, \mathcal{L}_{K/\pi}^+, \mathcal{L}_{K/\pi}^-, \mathcal{F}_{S/B}, q, \Delta t) \equiv \\ \mathcal{P}_{K^+K^-}(M_{BC}) \mathcal{P}_{K^+K^-}(\Delta E) \mathcal{P}_{K^+K^-}(\mathcal{L}_{K/\pi}^+, \mathcal{L}_{K/\pi}^-) \\ \mathcal{P}_{K^+K^-}^l(\mathcal{F}_{S/B}) \mathcal{P}_{K^+K^-}^l(q, \Delta t). \end{aligned} \quad (4.34)$$

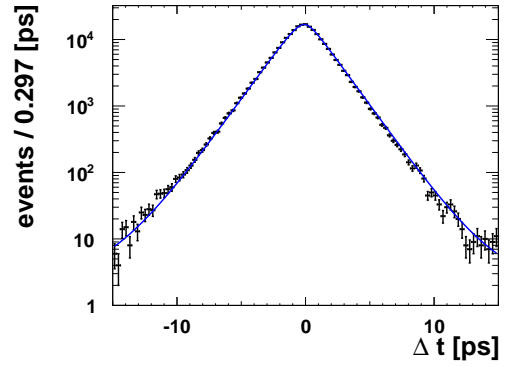
Its shape can be determined by maximizing the following likelihood

$$\mathcal{L}_j \equiv \prod_{l,s} \frac{e^{N_j^s \sum_{l,s} f_j^{l,s}}}{N_{l,s}!} \prod_{i=0}^{N_{l,s}} N_j^s f_j^{l,s} \mathcal{P}_j^{l,s}(M_{BC}^i, \Delta E^i, \mathcal{L}_{K/\pi}^{+,i}, \mathcal{L}_{K/\pi}^{-,i}, \mathcal{F}_{S/B}^i, q^i, \Delta t^i), \quad (4.35)$$

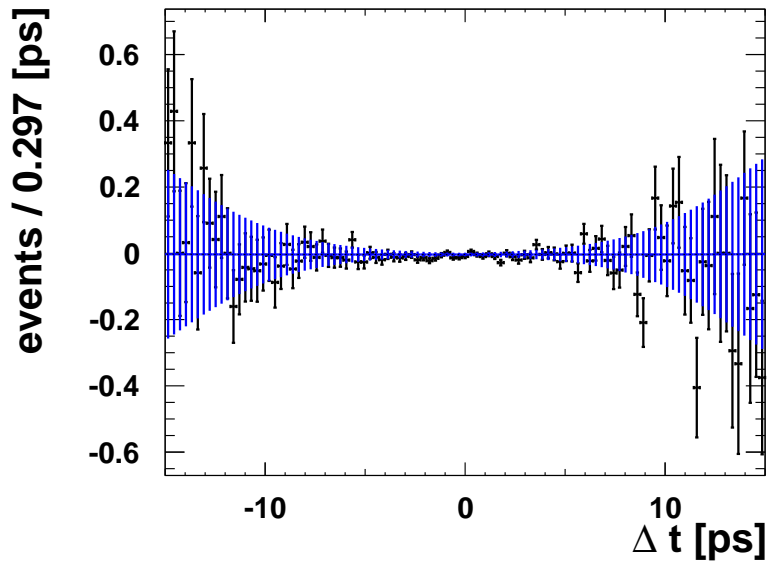
where j is the component. The parameter N is the signal yield and f is the fraction of events in r -bin and SVD configuration l, s . The fit results to $K^+ K^-$ signal Monte-Carlo are shown in Figs. 4.15, 4.16, 4.17, 4.18.



(a) Δt PDF and full detector simulation Monte-Carlo for events tagged as B^0 ($q = 1$).



(b) Δt PDF and full detector simulation Monte-Carlo for events tagged as \bar{B}^0 ($q = -1$).



(c) $K^+ K^- \Delta t$ asymmetry

Figure 4.18: Fit results for variable Δt for component $K^+ K^-$. Data points with errors represent the MC from full detector simulation and the solid blue line represents the fit result.

4.4.4 Continuum Background

The by far dominant background is the combinatorial background from continuum events. The continuum model is determined from off-resonance data taken 80 MeV below the $\Upsilon(4S)$ resonance. The event selection criteria described in Sec. 4.3 is used. Because the continuum

Table 4.8: *Correlation matrix for the continuum data taken from off resonance data.*

	M_{BC}	ΔE	$\mathcal{L}_{K/\pi}^+$	$\mathcal{L}_{K/\pi}^-$	$\mathcal{F}_{S/B}$	q	qr	Δt
M_{BC}	1.00	-0.00	0.01	-0.00	-0.01	0.00	-0.01	0.00
ΔE		1.00	-0.00	-0.00	0.06	-0.00	-0.02	-0.00
$\mathcal{L}_{K/\pi}^+$			1.00	0.15	0.03	-0.06	0.01	-0.01
$\mathcal{L}_{K/\pi}^-$				1.00	0.05	0.06	0.01	-0.01
$\mathcal{F}_{S/B}$					1.00	-0.00	-0.03	0.00
q						1.00	0.01	0.01
qr							1.00	0.00
Δt								1.00

is the largest background, we take into account as many correlations from table 4.8 as possible. In the following, we describe our procedure to incorporate the correlations into the model. For better illustration of the correlations, figure 4.19 shows a Bayesian-probability network where the modelled correlations are shown as arrows.

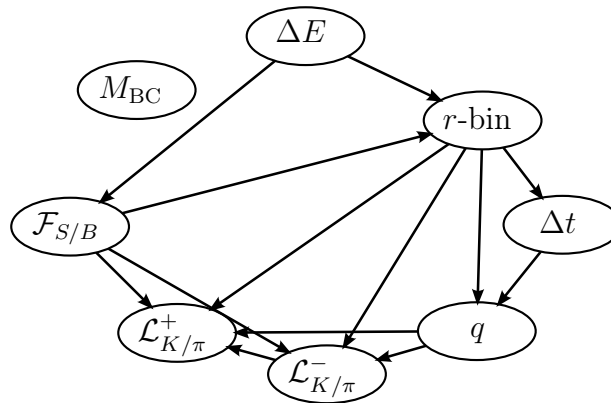
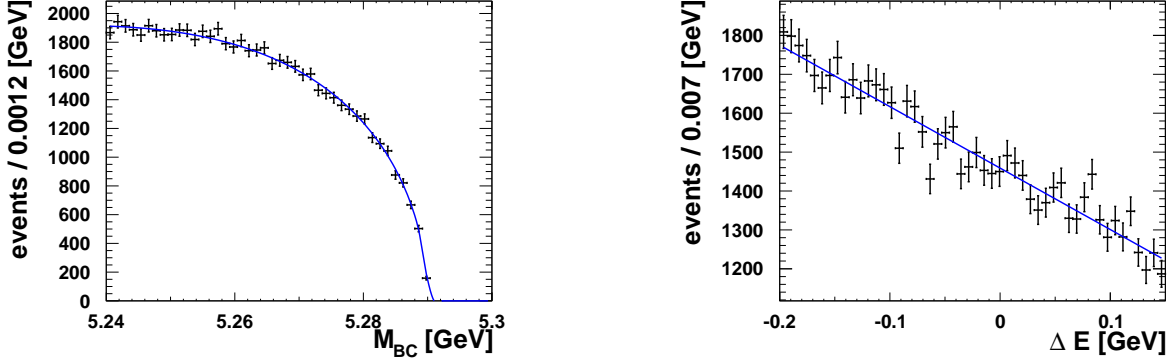


Figure 4.19: *Bayesian probability network for the continuum component. The directed acyclic graph shows the fit variables as nodes and the modelled correlations as arrows.*

The PDF for M_{BC} is modelled by an Argus function [72],

$$\mathcal{P}_{\text{cont}}(M_{\text{BC}}) \equiv M_{\text{BC}} \cdot \sqrt{1 - \left(\frac{M_{\text{BC}}}{E_{\text{beam}}}\right)^2} \cdot e^{a_{\text{eff}} \cdot \left(1 - \left(\frac{M_{\text{BC}}}{E_{\text{beam}}}\right)^2\right)}. \quad (4.36)$$

There is one event-dependent parameter in the M_{BC} PDF, the E_{beam} , which is the beam energy of this event. The fit results for M_{BC} can be found in figure 4.20a.



(a) Fit results of the variable M_{BC} , for the continuum component.

(b) Fit results of the variable ΔE , for the continuum component.

Figure 4.20: Fit results of M_{BC} and ΔE for continuum. Data points with errors represent the off-resonance data and the solid blue line represents the fit result.

Because ΔE exposes a flat structure in the signal region, we model it by a first order Chebyshev polynomial. To incorporate the correlation between ΔE and the B -tag quality qr , we fit ΔE in each r -bin,

$$\mathcal{P}_{\text{cont}}^l(\Delta E) \equiv 1 + c_{\text{eff}}^l \Delta E. \quad (4.37)$$

We take into account the correlation of ΔE and $\mathcal{F}_{S/B}$ by using a first order Chebyshev polynomial and determine a correction to the slope of the ΔE straight line. All r -bins have a separate correlation factor $c_{\Delta E}^{\text{fish},l}$,

$$c_{\text{eff}}^l \equiv \left(1 + c_{\Delta E}^{\text{fish},l}\right) \cdot \mathcal{F}_{S/B}. \quad (4.38)$$

The free parameters are c_1 and the correlation factor between ΔE and $\mathcal{F}_{S/B}$, $c_{\Delta E}^{\text{fish}}$. The fit results for ΔE can be found in figure 4.20b. In addition, figure 4.21 shows the fits of ΔE in every r -bin.

As the $\mathcal{L}_{K/\pi}^+$ and $\mathcal{L}_{K/\pi}^-$ variables are correlated, we model them with a two dimensional histogram. Correction factors for cuts on $\mathcal{L}_{K/\pi}^+$ or $\mathcal{L}_{K/\pi}^-$ are available from an independent analysis. On top of this, we model the correlation between $\mathcal{L}_{K/\pi}^+$, $\mathcal{L}_{K/\pi}^-$ and q in each r -bin, l . For a value of $q = 1$, we get an excess on $K^+\pi^-$ on the reconstructed side and for $q = -1$, we get an excess of $K^-\pi^+$. We model this with the manta-ray function we introduced in Eq. 4.45 (see also Fig. 4.31). The c parameter defines the size of the plateau where mr is almost zero, while a defines the amplitude at the points $(1, 0)$ and $(0, 1)$. a and c are free

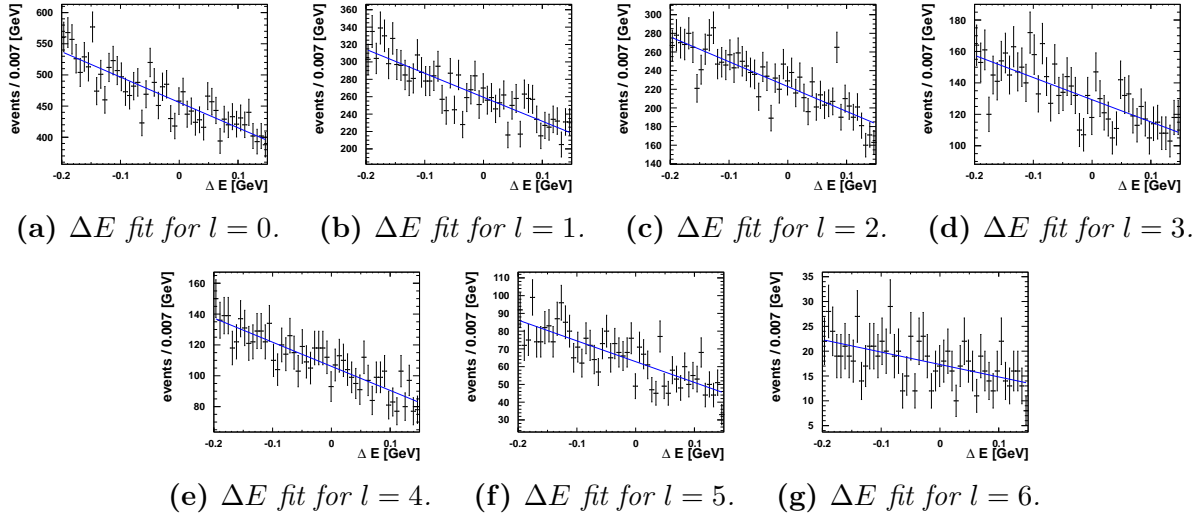


Figure 4.21: Fit results of the variable ΔE , for the continuum component. Data points with errors represent the off-resonance data and the solid blue line represents the fit result. The slope of the first order Chebyshev polynome is different in every r -bin. This is especially visible in plot (g), the r -bin with the best B tagging purity, compared to the other plots.

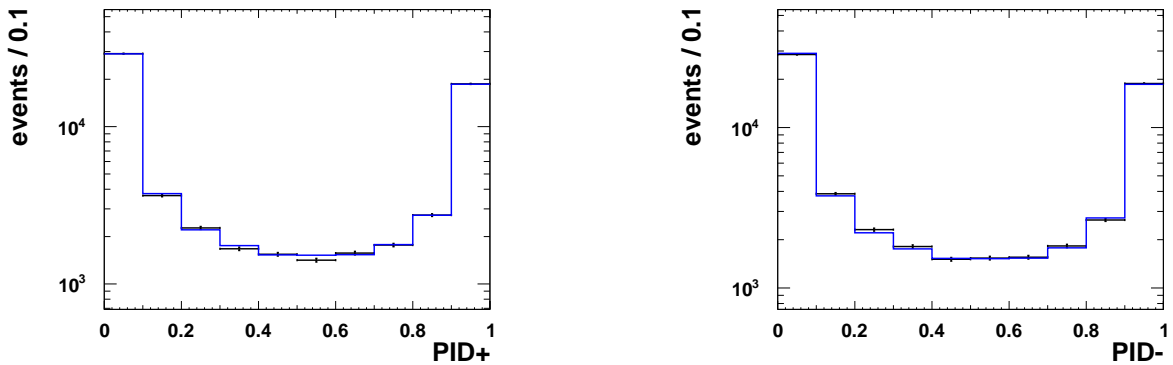


Figure 4.22: Fit results for the variables $\mathcal{L}_{K/\pi}^+$ and $\mathcal{L}_{K/\pi}^-$, for the continuum component cumulated integrated over all r -bins. Data points with errors represent the off-resonance data and the solid blue histogram represents the fit result.

Table 4.9: Borders of the k -bin which are used to take into account the correlation between $\mathcal{L}_{K/\pi}^+, \mathcal{L}_{K/\pi}^-$ and $\mathcal{F}_{S/B}$. The bin borders are located where no discrimination between pion and kaon is possible.

k -bin	borders
1	$\mathcal{L}_{K/\pi}^+ < 0.5 \wedge \mathcal{L}_{K/\pi}^- < 0.5$
2	$\mathcal{L}_{K/\pi}^+ \geq 0.5 \vee \mathcal{L}_{K/\pi}^- > 0.5$

parameters in the fit to the continuum sample. The parameters a and c are determined independently in every r -bin, l ,

$$\mathcal{P}_{\text{cont}}^l(\mathcal{L}_{K/\pi}^+, \mathcal{L}_{K/\pi}^-, q) \equiv \mathcal{H}(\mathcal{L}_{K/\pi}^+, \mathcal{L}_{K/\pi}^-) \cdot \frac{1}{2}(1 + q \cdot mr^l(\mathcal{L}_{K/\pi}^+, \mathcal{L}_{K/\pi}^-)). \quad (4.39)$$

The fit results can be found in figure 4.22 and figure 4.26. The latter one contains the PDF projections in every r -bin. The Fisher discriminant $\mathcal{F}_{S/B}$, distinguishes between signal (B

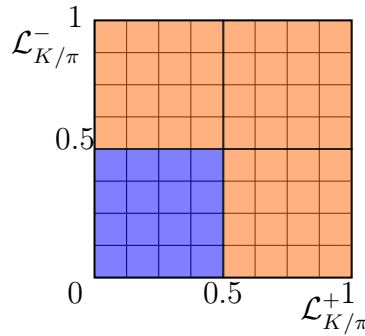


Figure 4.23: The figure shows the bins of a 2D histogram of $\mathcal{L}_{K/\pi}^+$ and $\mathcal{L}_{K/\pi}^-$. The area is divided according to the conditions from Tbl. 4.9. The blue area corresponds to $k = 1$ while the larger orange area corresponds to $k = 2$.

decays) and continuum ($e^+e^- \rightarrow q\bar{q}$, where $q = u, d, s, c$). $\mathcal{F}_{S/B}$ is modelled by a triple Gaussian in every r -bin, l . To incorporate a correlation of $\mathcal{L}_{K/\pi}^+$ and $\mathcal{L}_{K/\pi}^-$ with $\mathcal{F}_{S/B}$, we decided to split the data into two bins, k . The bin $k = 1$, contains the events which look like $\pi^+\pi^-$ events. All other events are in bin $k = 2$. The k -bin borders are located exactly at 0.5, where no discrimination between pion and kaon is possible. The parameters are shown in Tbl. 4.9 and we added Fig. 4.23 to display the k -bin region geometrically. The parameters of the triple Gaussian are determined from a fit to the off-resonance data separately in every r -bin and every k -bin,

$$\begin{aligned} \mathcal{P}_j^l(\mathcal{F}_{S/B}) &\equiv f_1 \cdot G(\mathcal{F}_{S/B}, \mu_1^l, \sigma_1^l) \\ &+ f_2 \cdot G(\mathcal{F}_{S/B}, \mu_1^l + \mu_2^l, \sigma_1^l \cdot \sigma_2^l) \\ &+ (1 - f_1 - f_2) \cdot G(\mathcal{F}_{S/B}, \mu_1^l + \mu_2^l + \mu_3^l, \sigma_1^l \cdot \sigma_2^l \cdot \sigma_3^l) \end{aligned} \quad (4.40)$$

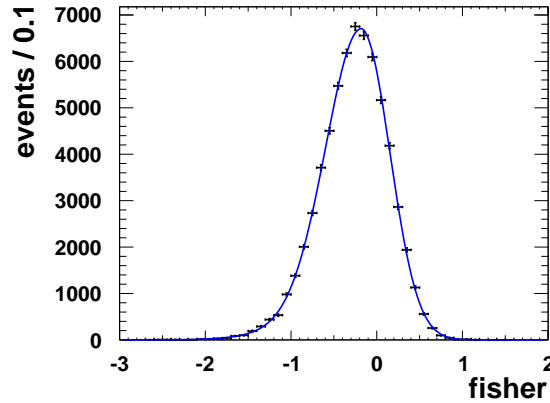


Figure 4.24: *Fit results for the variable $\mathcal{F}_{S/B}$ for the continuum component. The PDF is shown in blue while the off-resonance data is plotted in black including errors.*

There is no need for correction factors because the model parameters are directly obtained from data. The fit results can be found in figure 4.24.

The Δt for continuum consists of a broad lifetime component which accounts for long lived particles, for example charmed particles, and a delta function for single vertex events (prompt decays),

$$\mathcal{P}_{\text{cont}}^l(\Delta t) \equiv \frac{1}{2} \left[f_{\delta} \cdot \delta(\Delta t - \mu_{\delta}) + (1 - f_{\delta}) \cdot \frac{e^{-|\Delta t|/\tau_{\text{eff}}}}{4\tau_{\text{eff}}} \right] \otimes R_{q\bar{q}}(\Delta t). \quad (4.41)$$

As a model for the detector resolution $R_{q\bar{q}}(\Delta t)$, the sum of two Gaussians is used,

$$R_{q\bar{q}}(\Delta t) \equiv fG(\Delta t; \mu_{\text{main}}, \sigma_{\text{main}}) + (1 - f)G(\Delta t; \mu_{\text{main}}, \sigma_{\text{main}}\sigma_{\text{tail}}). \quad (4.42)$$

The fit results can be found in figure 4.25.

The total PDF for the continuum component is constructed to be

$$\mathcal{P}_{\text{cont}}^l(M_{\text{BC}}, \Delta E, \mathcal{L}_{K/\pi}^+, \mathcal{L}_{K/\pi}^-, \mathcal{F}_{S/B}, q, \Delta t) \equiv \mathcal{P}_{\text{cont}}(M_{\text{BC}}, \Delta E) \mathcal{P}_{\text{cont}}^l(\mathcal{L}_{K/\pi}^+, \mathcal{L}_{K/\pi}^-) \mathcal{P}_{\text{cont}}^l(\mathcal{F}_{S/B}) \mathcal{P}_{\text{cont}}^l(\Delta t). \quad (4.43)$$

The fit results to off-resonance data are shown in Figs. 4.20a, 4.20b, 4.22, 4.24, 4.25.

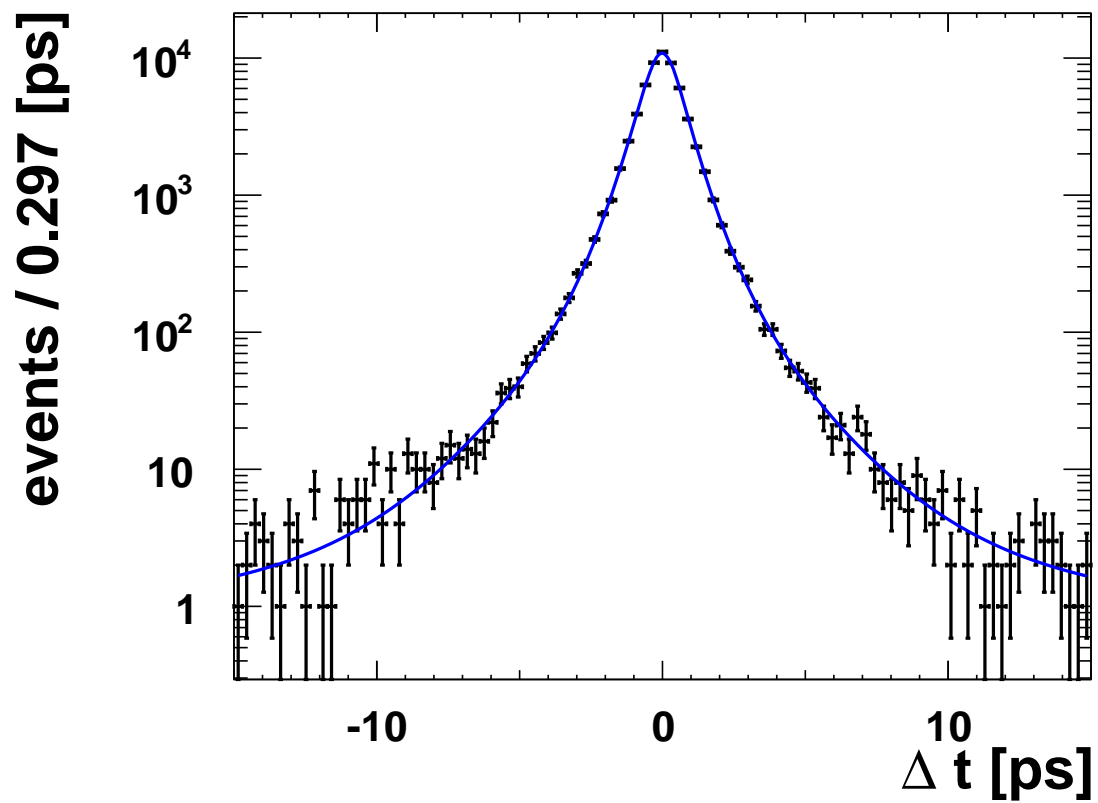


Figure 4.25: Δt fit results for the continuum component. Data points with errors represent the off-resonance data and the solid blue line represents the fit result.

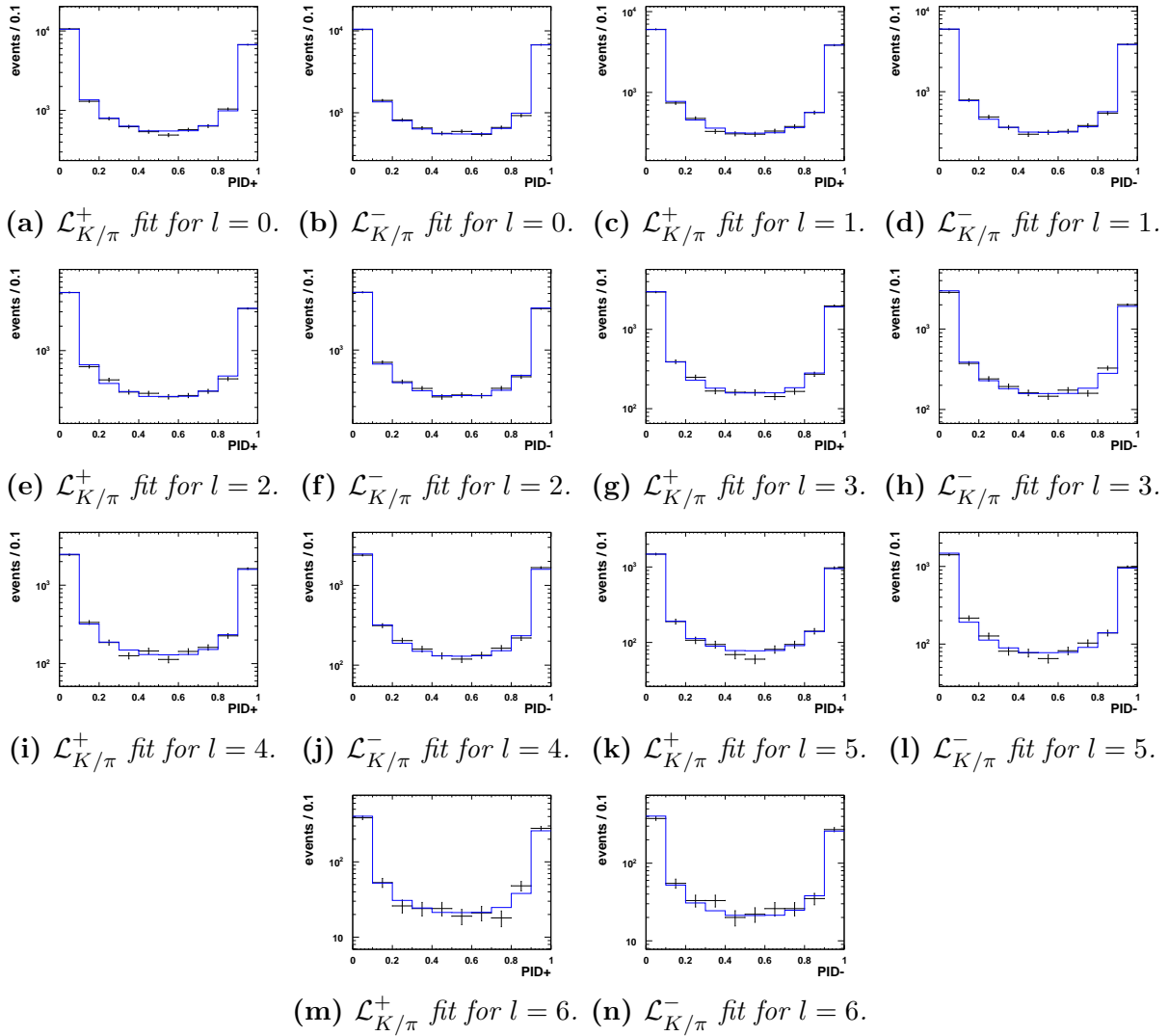


Figure 4.26: Detailed fit results of the variables $\mathcal{L}_{K/\pi}^+$ and $\mathcal{L}_{K/\pi}^-$, for the continuum component in every r -bin. Data points with errors represent the off-resonance data and the solid blue line represents the fit result.

4.4.5 Background from charmless B^+B^- decays

The charmless B^+B^- model describes a minor background and is determined from a Monte-Carlo sample which is approximately 50 times the expected number of events. The event selection criteria explained in Sec. 4.3 was used. The correlation table 4.10 show the

Table 4.10: *Correlation matrix for the charmless B^+B^- Monte-Carlo.*

	M_{BC}	ΔE	$\mathcal{L}_{K/\pi}^+$	$\mathcal{L}_{K/\pi}^-$	$\mathcal{F}_{S/B}$	q	qr	Δt
M_{BC}	1.00	-0.18	-0.05	-0.05	0.04	0.00	0.01	-0.01
ΔE		1.00	0.04	0.03	-0.06	0.00	-0.01	-0.01
$\mathcal{L}_{K/\pi}^+$			1.00	0.03	-0.03	-0.09	-0.00	0.00
$\mathcal{L}_{K/\pi}^-$				1.00	-0.03	0.09	0.01	-0.01
$\mathcal{F}_{S/B}$					1.00	0.01	0.04	0.01
q						1.00	0.01	0.01
qr							1.00	0.01
Δt								1.00

correlations between the fit variables. Because of the large size of the background, we have to model it very well and take correlations above 2% into consideration. This leaves us with a large number of correlations to treat. In the following, we show how we incorporate the correlations into the model. For better illustration of the correlations, figure 4.27 shows a Bayesian-probability network where the modelled correlations are shown as arrows.

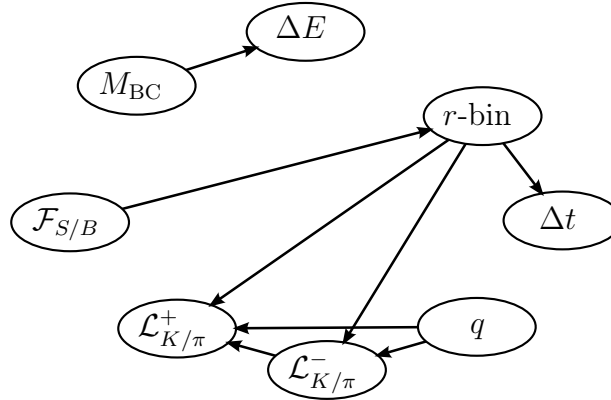


Figure 4.27: *Bayesian probability network for the charmless B^+B^- component. The directed acyclic graph shows the fit variables as nodes and the modelled correlations as arrows.*

The PDF for M_{BC} and ΔE is modelled by a 2D histogram to incorporate the correlation between M_{BC} and ΔE . In figure 4.28, the resulting fit and projections into 1D M_{BC} and ΔE histograms are shown.

$$\mathcal{P}_{\text{rare}B^+B^-}(M_{BC}, \Delta E) \equiv \mathcal{H}(M_{BC}, \Delta E) \quad (4.44)$$

As the $\mathcal{L}_{K/\pi}^+$ and $\mathcal{L}_{K/\pi}^-$ are correlated, we model them with a two dimensional histogram. Correction factors for cuts on $\mathcal{L}_{K/\pi}^+$ or $\mathcal{L}_{K/\pi}^-$ are known from independent studies. Starting with these correction factors, an algorithm explained in section 5.2 is used to correct the histogram obtained from Monte-Carlo to resemble the data. The fit results can be found in figure 4.29.

On top of this, we model the correlation between $\mathcal{L}_{K/\pi}^+, \mathcal{L}_{K/\pi}^-$ and the B -tag q , in each B -tag quality r -bin, l . For a value of $q = 1$ (B_{tag}^0), we get an excess of $K^+ \pi^-$ on the reconstructed side and for $q = -1$ (\bar{B}_{tag}^0), we get an excess of $K^- \pi^+$. This is graphically shown in Fig. 4.30. We model this with the following function (see also Fig. 4.31),

$$mr(x, y) = \begin{cases} a \cdot (x - y)^c & \text{if } x - y \geq 0 \\ -a \cdot (-x + y)^c & \text{if } x - y < 0. \end{cases} \quad (4.45)$$

The c parameter defines the size of the plateau where mr is almost zero, while a defines the amplitude at the points $(1, 0)$ and $(0, 1)$. a and c are free parameters in the fit to the charmless $B^0 \bar{B}^0$ sample. The parameters a and c , are determined independently in every r -bin, l ,

$$\mathcal{P}_{\text{rare}B^+B^-}^l(\mathcal{L}_{K/\pi}^+, \mathcal{L}_{K/\pi}^-, q) \equiv \mathcal{H}(\mathcal{L}_{K/\pi}^+, \mathcal{L}_{K/\pi}^-) \cdot \frac{1}{2}(1 + q \cdot mr^l(\mathcal{L}_{K/\pi}^+, \mathcal{L}_{K/\pi}^-)). \quad (4.46)$$

For the $\mathcal{F}_{S/B}$ variable we use the same model as for all B decays. It is described for the $\pi^+ \pi^-$ model above,

$$\begin{aligned} \mathcal{P}_j^l(\mathcal{F}_{S/B}) &\equiv f_1 \cdot G(\mathcal{F}_{S/B}, \mu_1^l + \mu_1^{\text{CF},l}, \sigma_1^l \cdot \sigma_1^{\text{CF},l}) \\ &\quad + f_2 \cdot G(\mathcal{F}_{S/B}, \mu_1^l + \mu_1^{\text{CF},l} + \mu_2^l, \sigma_1^l \cdot \sigma_1^{\text{CF},l} \cdot \sigma_2^l) \\ &\quad + (1 - f_1 - f_2) \cdot G(\mathcal{F}_{S/B}, \mu_1^l + \mu_1^{\text{CF},l} + \mu_2^l + \mu_3^l, \sigma_1^l \cdot \sigma_1^{\text{CF},l} \cdot \sigma_2^l \cdot \sigma_3^l). \end{aligned} \quad (4.47)$$

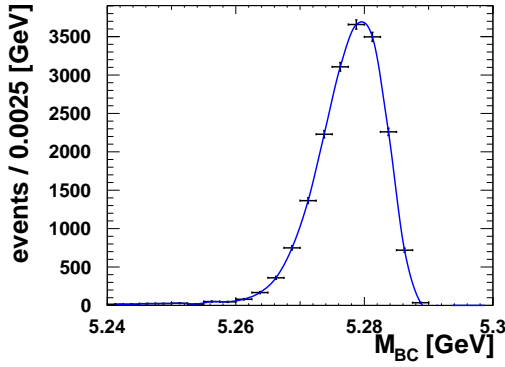
The fit results can be found in figure 4.32.

The Δt PDF is modelled by the lifetime PDF with an effective lifetime τ_{eff} , as free parameter,

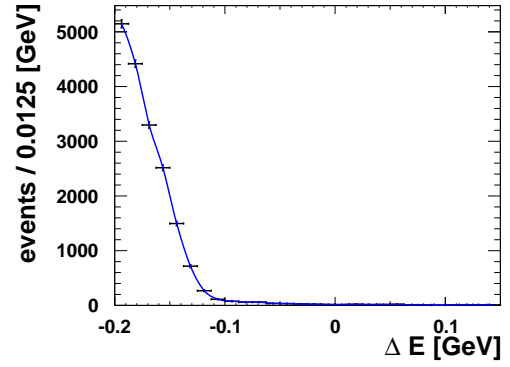
$$\mathcal{P}_{\text{rare}B^+B^-}^l(\Delta t) \equiv \frac{e^{-|\Delta t|/\tau_{\text{eff}}}}{4\tau_{\text{eff}}} \otimes R_{B^0 \bar{B}^0}(\Delta t). \quad (4.48)$$

The life time PDF is convoluted with the detector resolution function $R_{B^+B^-}(\Delta t)$ for charged B mesons. The resolution function [68] is explained in the Appendix C. The fit results can be found in figure 4.33. The total PDF for the charmless B^+B^- component is constructed to be

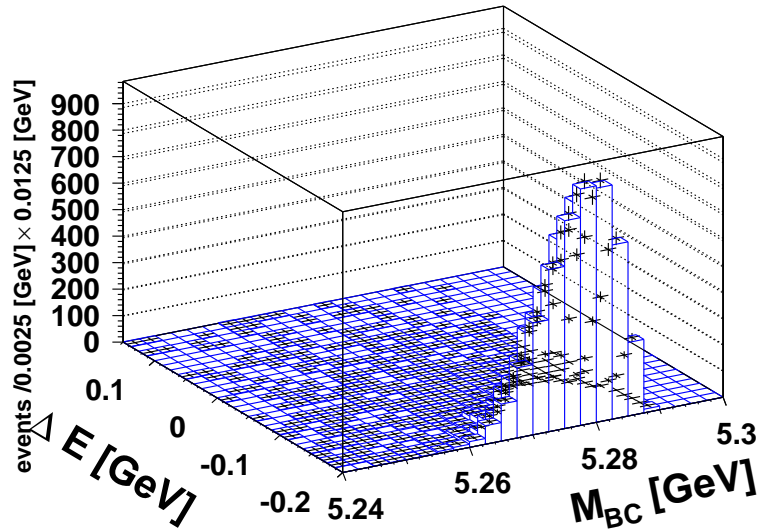
$$\begin{aligned} \mathcal{P}_{\text{rare}B^+B^-}^l(M_{\text{BC}}, \Delta E, \mathcal{L}_{K/\pi}^+, \mathcal{L}_{K/\pi}^-, \mathcal{F}_{S/B}, q, \Delta t) &\equiv \\ \mathcal{P}_{\text{rare}B^+B^-}(M_{\text{BC}}, \Delta E) \mathcal{P}_{\text{rare}B^+B^-}^l(\mathcal{L}_{K/\pi}^+, \mathcal{L}_{K/\pi}^-, q) & \\ \mathcal{P}_{\text{rare}B^+B^-}^l(\mathcal{F}_{S/B}) \mathcal{P}_{\text{rare}B^+B^-}^l(\Delta t). & \end{aligned} \quad (4.49)$$



(a) Fit projection of the variable M_{BC} , from the 2D PDF on full detector simulation Monte-Carlo.

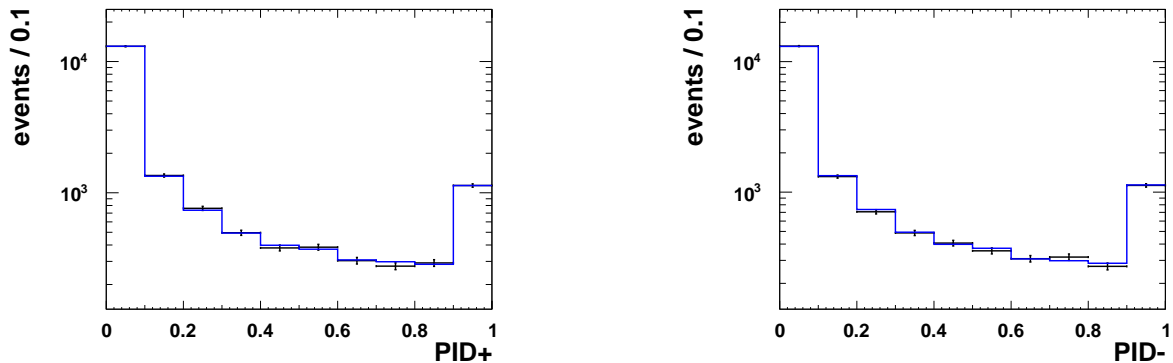


(b) Fit projection of the variable ΔE , from the 2D PDF on full detector simulation Monte-Carlo.



(c) 2D PDF for M_{BC} ΔE .

Figure 4.28: Fit results for the variables M_{BC} and ΔE , for the charmless B^+B^- component. Data points with errors represent the MC from full detector simulation and the solid blue line represents the fit result.



(a) Fit projection of the variable $\mathcal{L}_{K/\pi}^+$, from the 2D PDF on full detector simulation Monte-Carlo.

(b) Fit projection of the variable $\mathcal{L}_{K/\pi}^-$, from the 2D PDF on full detector simulation Monte-Carlo.

Figure 4.29: Fit results for the variables $\mathcal{L}_{K/\pi}^+$ and $\mathcal{L}_{K/\pi}^-$, for the charmless B^+B^- component. Data points with errors represent the MC from full detector simulation and the solid blue histogram represents the fit result.

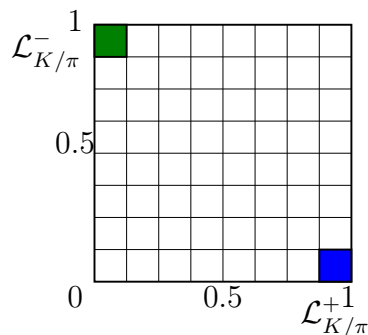


Figure 4.30: The figure shows the bins of a 2D histogram of $\mathcal{L}_{K/\pi}^+$ and $\mathcal{L}_{K/\pi}^-$. We observe an excess of events in the blue bin (1,0) if we select events with a B tag of $q = +1$. For events with a B tag of $q = -1$ an excess in the green bin (0,1) is observed.

The fit results to charmless B^+B^- signal Monte-Carlo are shown in Figs. 4.28, 4.29, 4.32, 4.33.

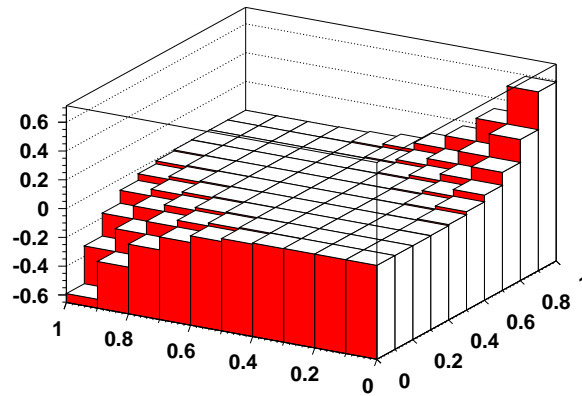


Figure 4.31: Manta-ray function to correct the particle identification histogram for its correlation with q . In the plot, $a = 1$ and $c = 5$ are taken for illustrative purposes.

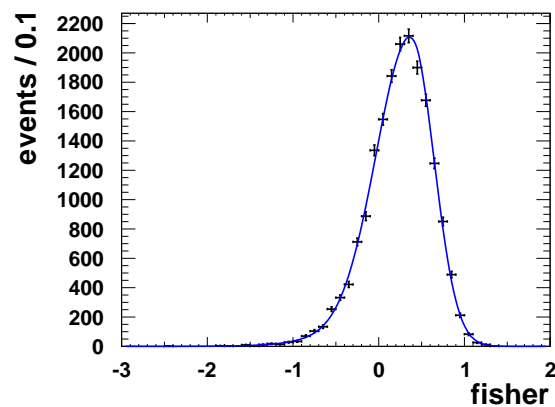


Figure 4.32: Fit results for the variable $\mathcal{F}_{S/B}$ for component charmless B^+B^- . The PDF is shown in blue while the full detector simulation Monte-Carlo is plotted in black including errors.

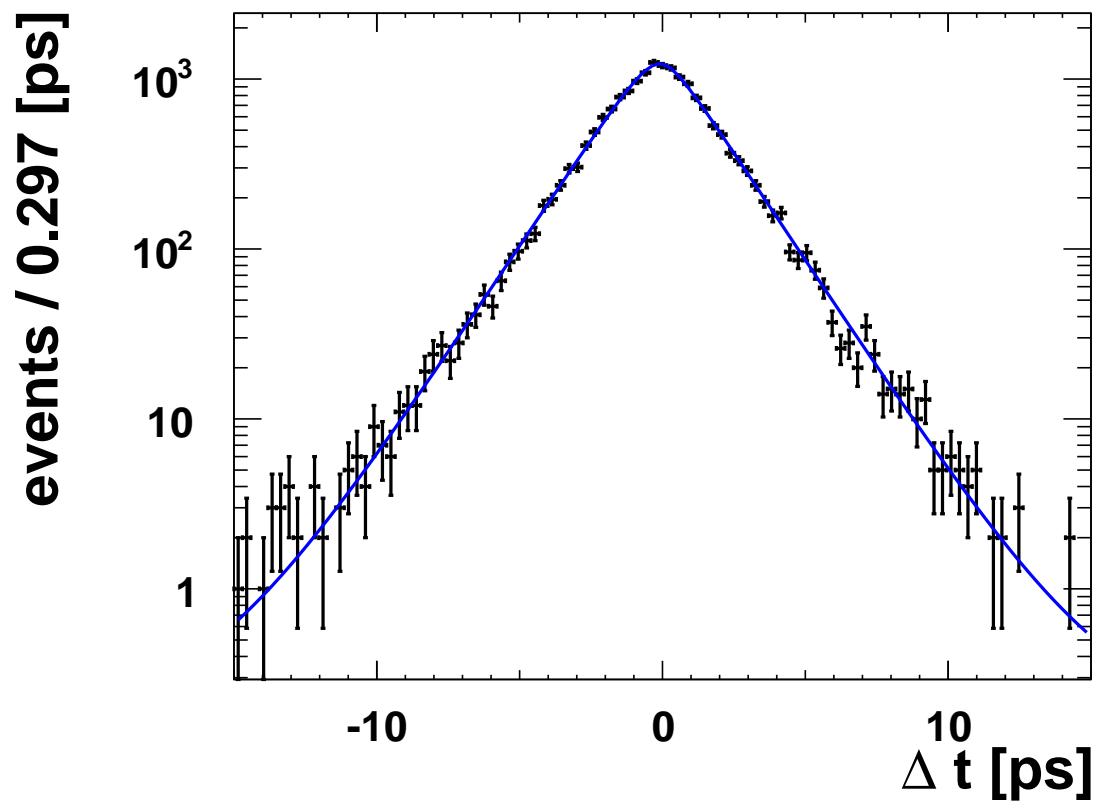


Figure 4.33: Δt fit results for the charmless B^+B^- component. Data points with errors represent the MC from full detector simulation and the solid blue line represents the fit result.

4.4.6 Background of charmless $B^0 \bar{B}^0$ decays

The charmless $B^0 \bar{B}^0$ model describes a minor background and is determined from a Monte-Carlo sample that is approximately 50 times the expected number of events, analogous to the charmless $B^+ B^-$ model. Again the event selection criteria explained in Sec. 4.3 was used.

Table 4.11: Correlation matrix for the charmless $B^0 \bar{B}^0$ Monte-Carlo.

	M_{BC}	ΔE	$\mathcal{L}_{K/\pi}^+$	$\mathcal{L}_{K/\pi}^-$	$\mathcal{F}_{S/B}$	q	qr	Δt
M_{BC}	1.00	-0.10	-0.03	-0.03	0.02	-0.01	-0.00	-0.00
ΔE		1.00	-0.01	-0.02	-0.04	-0.01	0.00	0.01
$\mathcal{L}_{K/\pi}^+$			1.00	0.01	-0.04	-0.05	-0.00	-0.00
$\mathcal{L}_{K/\pi}^-$				1.00	-0.03	0.05	0.00	0.00
$\mathcal{F}_{S/B}$					1.00	0.00	0.05	0.00
q						1.00	0.01	-0.00
qr							0.01	0.01
Δt								1.00

The correlation table 4.11 shows the correlations between the fit variables. Because of the large size of the background, we have to model it very well and take correlations above 2% seriously. The large number of correlations have to be taken into consideration when building the model. For better illustration of the correlations, figure 4.34 shows a Bayesian-probability network where the modelled correlations are shown as arrows.

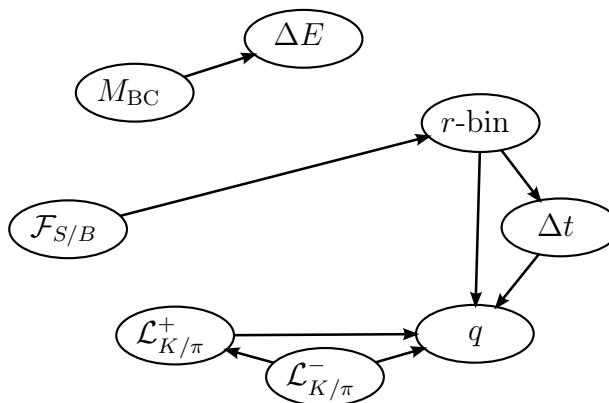
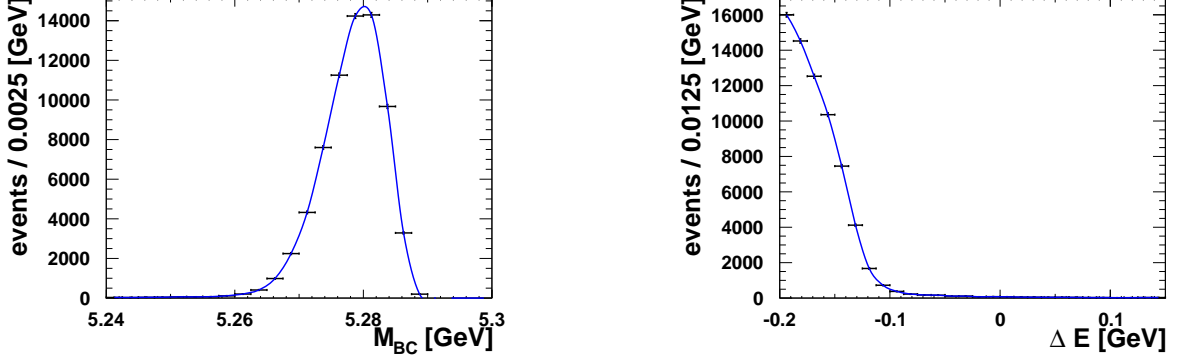


Figure 4.34: Bayesian probability network for the charmless $B^0 \bar{B}^0$ component. The directed acyclic graph shows the fit variables as nodes and the modelled correlations as arrows.

The PDF for M_{BC} and ΔE is modelled by a 2D histogram to incorporate the correlation between M_{BC} and ΔE . In figure 4.35, the resulting fit and projections into 1D M_{BC} and

ΔE histograms are shown.

$$\mathcal{P}_{\text{rare}B^0\bar{B}^0}(M_{BC}, \Delta E) \equiv \mathcal{H}(M_{BC}, \Delta E) \quad (4.50)$$



(a) Fit projection of the variable M_{BC} , from the 2D PDF on full detector simulation Monte-Carlo.

(b) Fit projection of the variable ΔE , from the 2D PDF on full detector simulation Monte-Carlo.

Figure 4.35: Fit results for the variables M_{BC} and ΔE , for the charmless $B^0\bar{B}^0$ component. Data points with errors represent the MC from full detector simulation and the solid blue line represents the fit result.

As the $\mathcal{L}_{K/\pi}^+$ and $\mathcal{L}_{K/\pi}^-$ variables are correlated, we model them with a two dimensional histogram.

$$\mathcal{P}_{\text{rare}B^0\bar{B}^0}^l(\mathcal{L}_{K/\pi}^+, \mathcal{L}_{K/\pi}^-, q) \equiv \mathcal{H}(\mathcal{L}_{K/\pi}^+ \mathcal{L}_{K/\pi}^-). \quad (4.51)$$

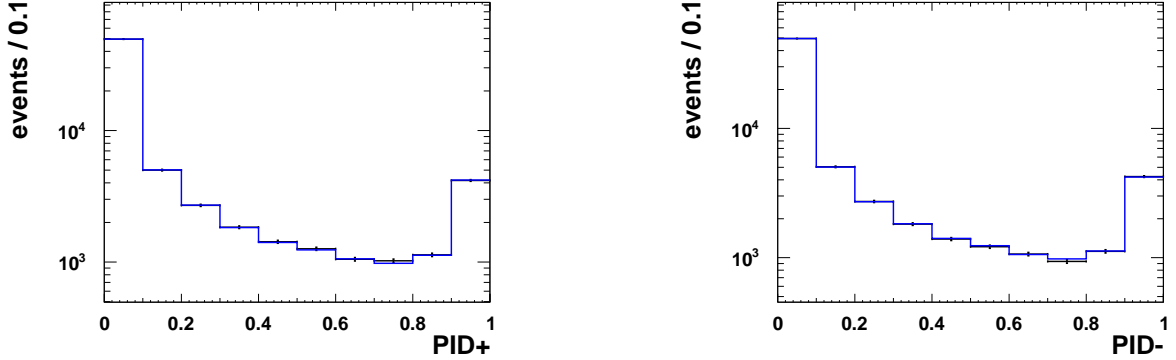
Correction factors for cuts on $\mathcal{L}_{K/\pi}^+$ or $\mathcal{L}_{K/\pi}^-$ are available from independent studies. Starting with these correction factors, an algorithm explained in section 5.2 is used to correct the histogram obtained from Monte-Carlo to resemble the data.

On top of this, we model the correlation between $\mathcal{L}_{K/\pi}^+, \mathcal{L}_{K/\pi}^-$ and the B -tag, q , in each B -tag quality r -bin, l . For a value of $q = 1$, we get an excess on $K^+ \pi^-$ on the reconstructed side and for $q = -1$, we get an excess of $K^- \pi^+$. This correlation is taken into account in the PDF of Δt .

The fit results can be found in figure 4.36.

For the $\mathcal{F}_{S/B}$ variable, we use the same model as for all B decays. It is described for the $\pi^+\pi^-$ model above,

$$\begin{aligned} \mathcal{P}_j^l(\mathcal{F}_{S/B}) \equiv & f_1 \cdot G(\mathcal{F}_{S/B}, \mu_1^l + \mu_1^{\text{CF},l}, \sigma_1^l \cdot \sigma_1^{\text{CF},l}) \\ & + f_2 \cdot G(\mathcal{F}_{S/B}, \mu_1^l + \mu_1^{\text{CF},l} + \mu_2^l, \sigma_1^l \cdot \sigma_1^{\text{CF},l} \cdot \sigma_2^l) \\ & + (1 - f_1 - f_2) \cdot G(\mathcal{F}_{S/B}, \mu_1^l + \mu_1^{\text{CF},l} + \mu_2^l + \mu_3^l, \sigma_1^l \cdot \sigma_1^{\text{CF},l} \cdot \sigma_2^l \cdot \sigma_3^l). \end{aligned} \quad (4.52)$$



(a) Fit projection of the variable $\mathcal{L}_{K/\pi}^+$, from the 2D PDF on full detector simulation Monte-Carlo.

(b) Fit projection of the variable $\mathcal{L}_{K/\pi}^-$, from the 2D PDF on full detector simulation Monte-Carlo.

Figure 4.36: Fit results for the variables $\mathcal{L}_{K/\pi}^+$ and $\mathcal{L}_{K/\pi}^-$, for the charmless $B^0\bar{B}^0$ component. Data points with errors represent the MC from full detector simulation and the solid blue histogram represents the fit result.

The fit results can be found in figure 4.37.

The Δt distribution is described by the following PDF. It takes into account the correlation between $\mathcal{L}_{K/\pi}^+$, $\mathcal{L}_{K/\pi}^-$ and q using the function 4.45. The parameters a and c , of the mr function are determined separately in every r -bin.

$$\mathcal{P}_{\text{rare}B^0\bar{B}^0}^l(\Delta t, q) \equiv \frac{e^{-|\Delta t|/\tau_{\text{eff}}}}{4\tau_{\text{eff}}} \times \left[1 + q \cdot mr(\mathcal{L}_{K/\pi}^+ \mathcal{L}_{K/\pi}^-) \cos \Delta m_d \Delta t \right] \} \otimes R_{B^0\bar{B}^0}(\Delta t). \quad (4.53)$$

Because for $l = 0, 1$, the parameters a and c are consistent with 0 and 1, respectively, we fixed them to these values to obtain a better convergence of the fit model. The Δt distribution is convoluted with the detector resolution function $R_{B^0\bar{B}^0}(\Delta t)$, for neutral B mesons. The resolution function [68] is explained in appendix C. The life time PDF depends on the effective B lifetime τ_{eff} , and the mass difference between B_H and B_L , Δm_d . The following values were used to generate the charmless $B^0\bar{B}^0$ signal Monte-Carlo,

$$\begin{aligned} \tau_{B^0} &= 1.53439 \text{ ps}, \\ \Delta m_d &= 0.507 \times 10^{12} \text{ } \hbar\text{s}^{-1}. \end{aligned}$$

The fit results of the Δt dimension can be found in figure 4.38.

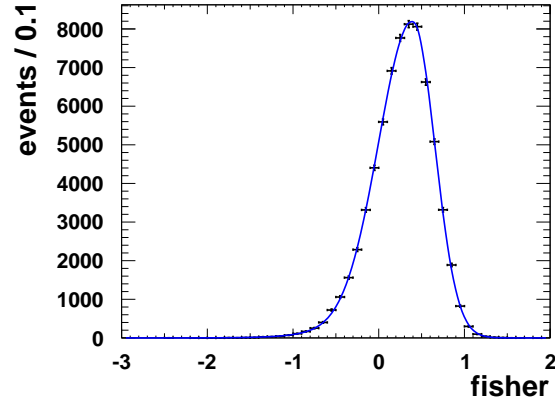
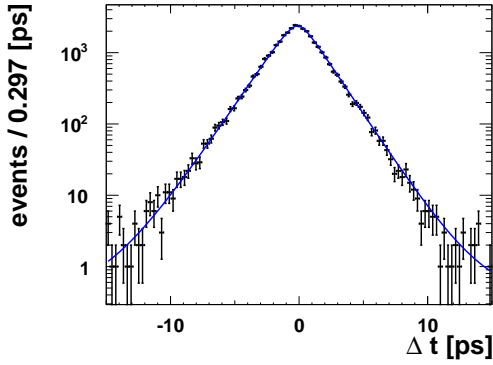


Figure 4.37: Fit results for the variable $\mathcal{F}_{S/B}$, for the charmless $B^0\bar{B}^0$ component. The PDF is shown in blue while the full detector simulation Monte-Carlo is plotted in black including errors.

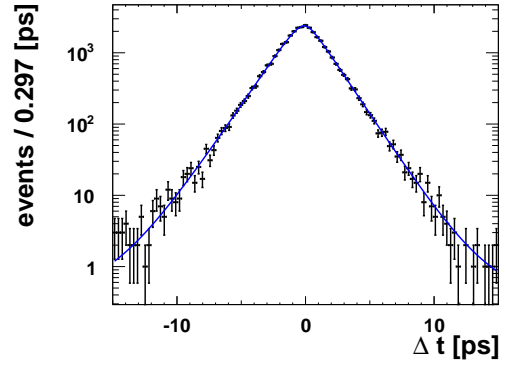
The total PDF for the charmless $B^0\bar{B}^0$ component is constructed to be

$$\begin{aligned} \mathcal{P}_{\text{rare}B^0\bar{B}^0}^l(M_{\text{BC}}, \Delta E, \mathcal{L}_{K/\pi}^+, \mathcal{L}_{K/\pi}^-, \mathcal{F}_{S/B}, q, \Delta t) \equiv \\ \mathcal{P}_{\text{rare}B^0\bar{B}^0}(M_{\text{BC}}, \Delta E) \mathcal{P}_{\text{rare}B^0\bar{B}^0}(\mathcal{L}_{K/\pi}^+, \mathcal{L}_{K/\pi}^-, q) \\ \mathcal{P}_{\text{rare}B^0\bar{B}^0}^l(\mathcal{F}_{S/B}) \mathcal{P}_{\text{rare}B^0\bar{B}^0}^l(q, \Delta t). \end{aligned} \quad (4.54)$$

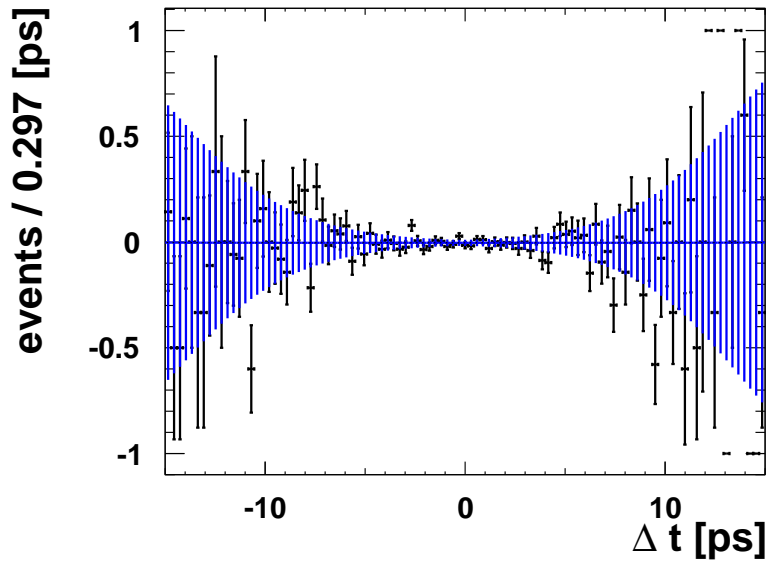
The fit results to charmless $B^0\bar{B}^0$ signal Monte-Carlo are shown in Figs. 4.35, 4.36, 4.37, 4.38.



(a) Δt PDF on full detector simulation Monte-Carlo for events tagged as B^0 ($q = 1$).



(b) Δt PDF on full detector simulation Monte-Carlo for events tagged as \bar{B}^0 ($q = -1$).



(c) Charmless $B^0\bar{B}^0$ Δt asymmetry.

Figure 4.38: Δt fit results for the charmless $B^0\bar{B}^0$ component. Data points with errors represent the MC from full detector simulation and the solid blue line represents the fit result.

4.5 Full Data Model - all Components combined

This section shows the fit of the full model with all components to a toy Monte-Carlo pseudo-experiment. This chapter shows the condensed summary of section 4.4. All components of the fit e.g. $B^0 \rightarrow \pi^+\pi^-$, continuum and $B\bar{B}$ backgrounds are scaled to their expected yields (Tbl. 4.12). The expected yields and a more detailed description of the pseudo-experiments which are performed with the full data model can be found in section 4.6. In this chapter, all plots use the same colour coding. The black dots show the number of events in the corresponding bin from the pseudo-experiment data. The continuum, which is by far the dominant contribution, is shown as red line. The $\pi^+\pi^-$ and $K\pi^-$ component are brown and magenta respectively. The charmless B decays from charged and neutral B decays are colour-coded blue and green, respectively. All plots contain the normalized residuals at the bottom. This sub-plot of the normalized residuals shows the difference between the data bin from a toy Monte-Carlo pseudo-experiment and the PDF, divided by the error of the data bin. The one and two σ bands are highlighted. Counting the bins in the normalized residual plot which deviate from the 2σ band helps to verify how well the PDF fits. This could also be done by calculating a global χ^2 value for the histogram. But our method can observe systematic shifts that are only local in addition e.g. around the signal peak.

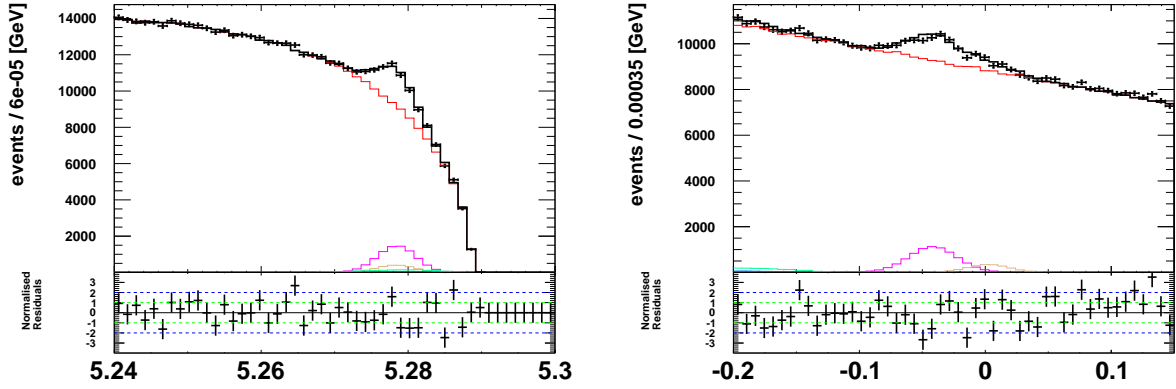


Figure 4.39: M_{BC} and ΔE projections from a fit to Toy Monte-Carlo. The Toy MC is shown as black crosses including the errors. The black histogram represents the summed PDFs of all components. The individual components are the continuum (red), the $B^0 \rightarrow K^+\pi^-$ decay (magenta), the $B^0 \rightarrow \pi^+\pi^-$ decay (gold), the charmless decays of B^0 (green) and B^\pm (blue).

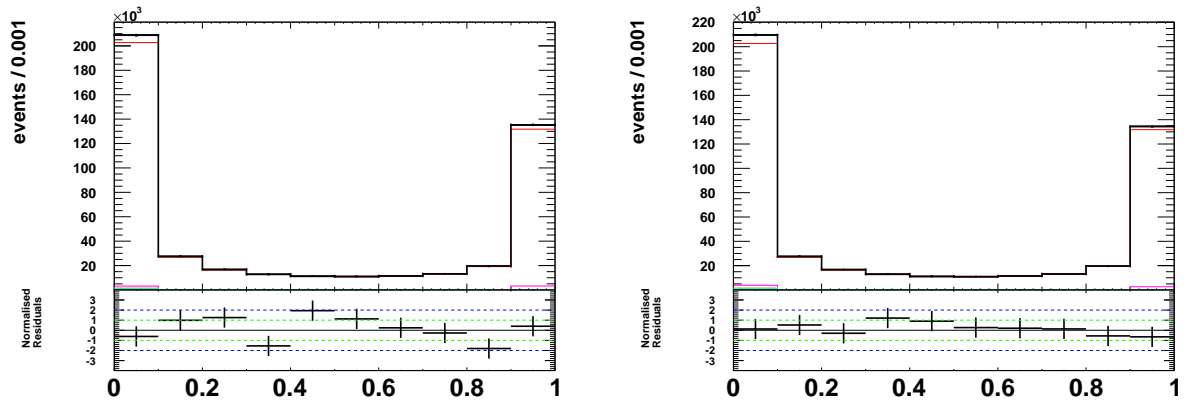


Figure 4.40: $\mathcal{L}_{K/\pi}^+$ and $\mathcal{L}_{K/\pi}^-$ projections from a fit to Toy Monte-Carlo. The Toy MC is shown as black crosses including the errors. The black histogram represents the summed PDFs of all components. The individual components are the continuum (red), the $B^0 \rightarrow K^+\pi^-$ decay (magenta), the $B^0 \rightarrow \pi^+\pi^-$ decay (gold), the charmless decays of B^0 (green) and B^\pm (blue).

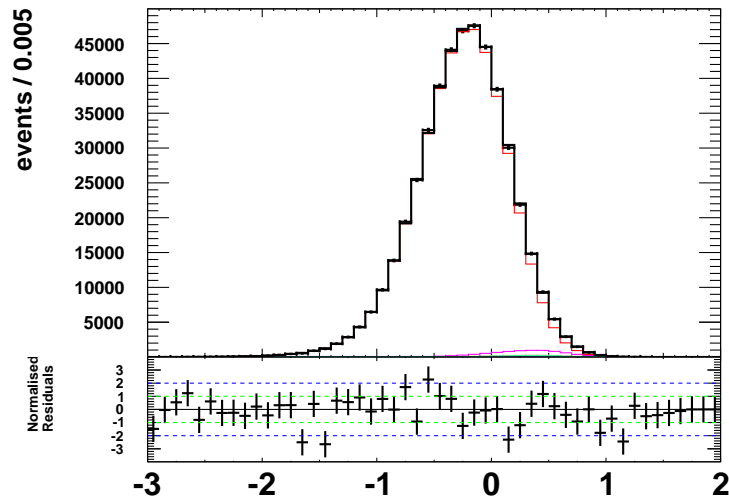


Figure 4.41: $\mathcal{F}_{S/B}$ projection from a fit to Toy Monte-Carlo. The Toy MC is shown as black crosses including the errors. The black histogram represents the summed PDFs of all components. The individual components are the continuum (red), the $B^0 \rightarrow K^+\pi^-$ decay (magenta), the $B^0 \rightarrow \pi^+\pi^-$ decay (gold), the charmless decays of B^0 (green) and B^\pm (blue).

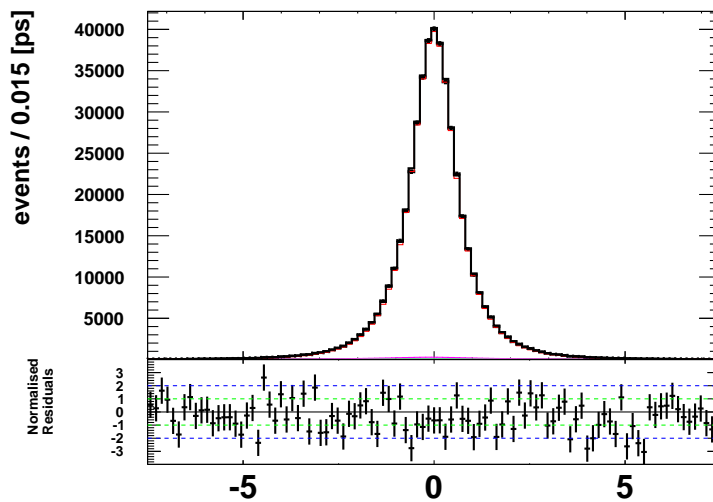


Figure 4.42: Δt projection from a fit to Toy Monte-Carlo. The Toy MC is shown as black crosses including the errors. The black histogram represents the summed PDFs of all components. The individual components are the continuum (red), the $B^0 \rightarrow K^+\pi^-$ decay (magenta), the $B^0 \rightarrow \pi^+\pi^-$ decay (gold), the charmless decays of B^0 (green) and B^\pm (blue).

4.6 Study of Fit Biases

In toy Monte-Carlo ensemble tests, we want to check for biases in the fit results as a result of our procedure. Therefore, we generate a number of pseudo-experiments and use the fitter to extract the physics parameters. This technique is called ensemble tests.

4.6.1 Pseudo-Experiment Setup

For every pseudo-experiment, we determine the number of events per component, the yield, with the following procedure. We use the current world average branching ratios as starting value for the toy Monte-Carlo ensemble tests. The expectations of the event yield are calculated assuming the full Belle statistics and the reconstruction efficiencies described in section 4.3. The resulting yields for every component are shown in table 4.12 and then distributed around these values according to Poisson statistics.

Table 4.12: *Expected yield in every component.*

component	SVD1	SVD2
$\pi^+ \pi^-$	471	2152
$K \pi$	1747	7948
$K^+ K^-$	0	0
charmless B^\pm	82	369
charmless B^0	307	1383
continuum	89353	455907

There are two methods of how to generate the events. We can either pick random events from a big set of events that are generated using full detector simulation, GSIM, or we can generate the events from the PDF. In the following we will refer to event that are picked from a set as GSIM events, and to the other method as PDF events. For the continuum component the number of events in the off resonance sample is not sufficient to apply the picking procedure, so these events will be taken from PDF in any case. For the CP violation parameters, the following values are used in the pseudo-experiments.

$$\mathcal{A}_{CP}(\pi^+\pi^-) = 0.36, \quad (4.55)$$

$$\mathcal{S}_{CP}(\pi^+\pi^-) = -0.65, \quad (4.56)$$

$$\mathcal{A}_{CP}(K\pi) = -0.087. \quad (4.57)$$

A set of 500 pseudo-experiments is generated for both GSIM events and PDF events.

The full fitter is modified to determine a branching ratio for the components $\pi^+ \pi^-$, $K \pi$ and $K^+ K^-$. This is done by replacing the two separate yields for the SVD1 and SVD2

data sample by a common branching ratio times the efficiency and the number of $B\bar{B}$ pairs in this data subsample (Eqn. 4.58).

$$\begin{aligned} Y_{\text{SVD1}} &= \mathcal{B} \times \left(\epsilon_{\text{SVD1}} N_{B\bar{B}}^{\text{SVD1}} \right) \\ Y_{\text{SVD2}} &= \mathcal{B} \times \left(\epsilon_{\text{SVD2}} N_{B\bar{B}}^{\text{SVD2}} \right) \end{aligned} \quad (4.58)$$

We also fixed the ratio between the charmless B^\pm component and the charmless B^0 component because the shapes look very similar in each dimension. In the fit to the pseudo-experiments, all yields and branching ratios are free parameters as well as the CP parameters for the $\pi^+ \pi^-$ and $K \pi$ channels. For all branching ratios and CP parameters, the asymmetric errors are determined. To determine the asymmetric error of a floating parameter of interest we use the following method. The parameter is varied around its central value and fixed. Then the minimization procedure is redone and the $-2 \log \mathcal{L}$ is re-evaluated. With this procedure we scan the $-2 \log \mathcal{L}$ until it changes by exactly one. This position marks the positive or negative error depending on whether the probed value for the parameter was greater or smaller than the central value. For every free physics parameter in the fit, a histogram showing the distribution of the fit result is created. A red line is added to indicate the generated value. This way one can judge the absolute value of possible biases. The results are also shown as distributions of the pull. The pull is determined as

$$\text{pull} = \frac{X_{\text{fit}} - X_{\text{generated}}}{\Delta X_{\text{fit}}}, \quad (4.59)$$

where ΔX is the error of the fit result and the corresponding asymmetric error is chosen according to the equation

$$\Delta X_{\text{fit}} = \begin{cases} \Delta X_{\text{fit}}^- & \text{if } X_{\text{fit}} - X_{\text{generated}} \geq 0 \\ \Delta X_{\text{fit}}^+ & \text{if } X_{\text{fit}} - X_{\text{generated}} < 0. \end{cases} \quad (4.60)$$

4.6.2 Fit Results and Pull Distributions

Figures 4.43 and 4.44 show the pull distributions for the pseudo-experiments using PDF events, and figures 4.45, 4.46 show the results for the pseudo-experiments using GSIM events.

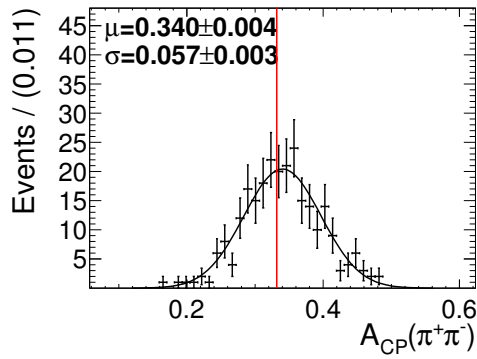
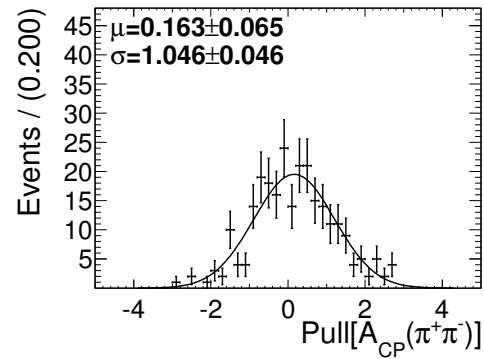
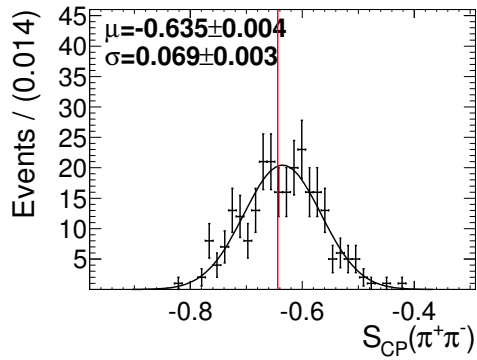
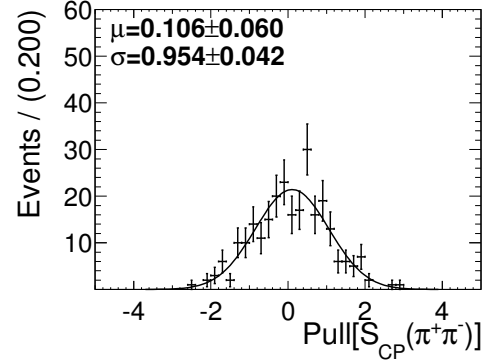
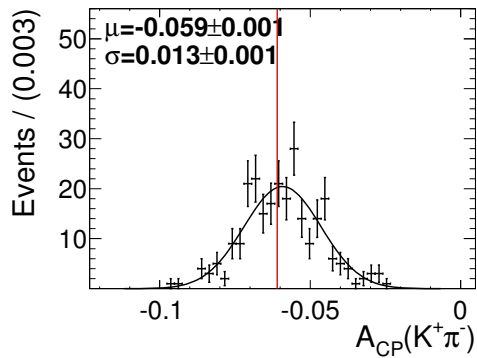
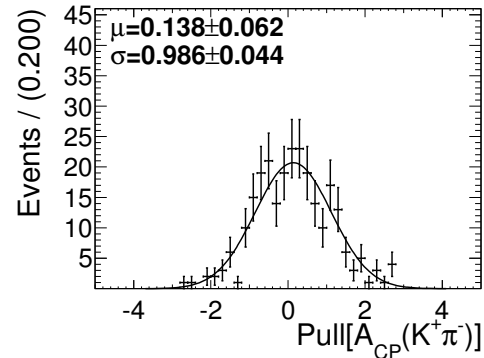
(a) Fit value distribution of $\pi^+ \pi^- \mathcal{A}_{CP}$.(b) Pull distribution of $\pi^+ \pi^- \mathcal{A}_{CP}$.(c) Fit value distribution of $\pi^+ \pi^- \mathcal{S}_{CP}$.(d) Pull distribution of $\pi^+ \pi^- \mathcal{S}_{CP}$.(e) Fit value distribution of $K \pi \mathcal{A}_{CP}$.(f) Pull distribution of $K \pi \mathcal{A}_{CP}$.

Figure 4.43: Fit central value and pull distributions of the CP parameters in the PDF ensemble tests. The black dots including the error represent the results from the toy MC pseudo experiments. The solid black line is the result of a Gaussian fit. The red line indicates the generated value.

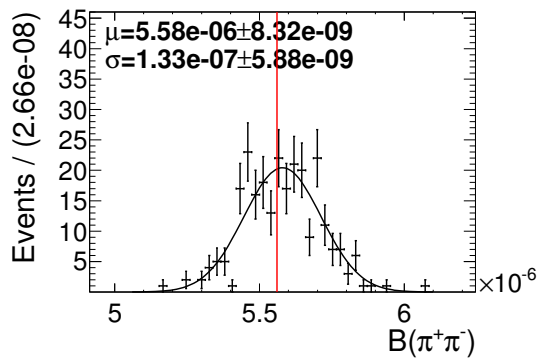
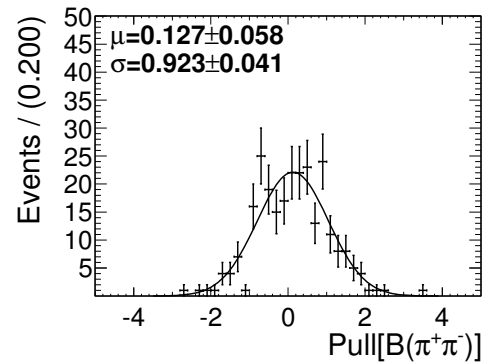
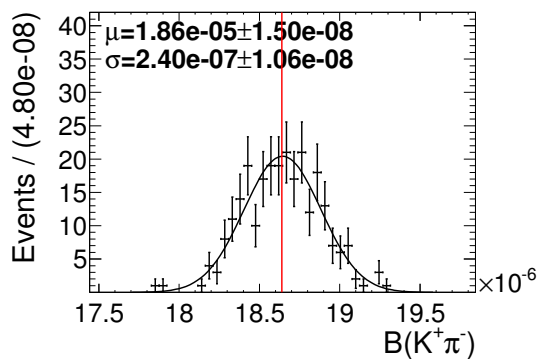
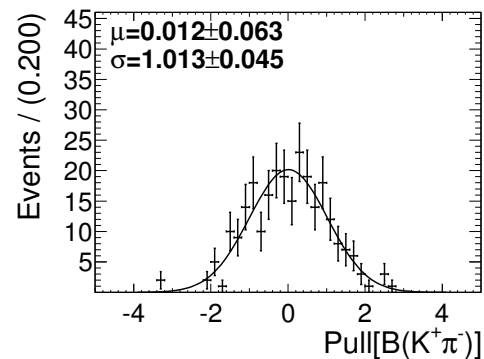
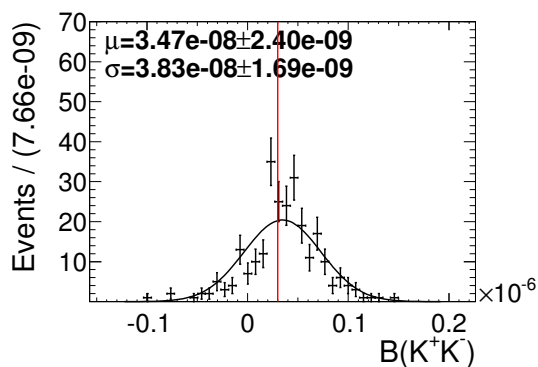
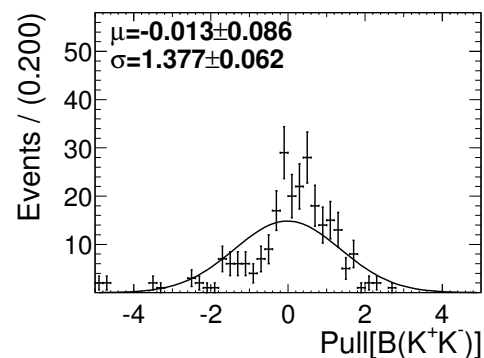
(a) *Fit value distribution of $\pi^+ \pi^-$ branching ratio.*(b) *Pull distribution of $\pi^+ \pi^-$ branching ratio.*(c) *Fit value distribution of $K \pi$ branching ratio.*(d) *Pull distribution of $K \pi$ branching ratio.*(e) *Fit value distribution of $K^+ K^-$ branching ratio.*(f) *Pull distribution of $K^+ K^-$ branching ratio.*

Figure 4.44: *Fit central value and pull distributions of the branching ratio in the PDF ensemble tests. The black dots including the error represent the results from the toy MC pseudo experiments. The solid black line is the result of a Gaussian fit. The red line indicates the generated value.*

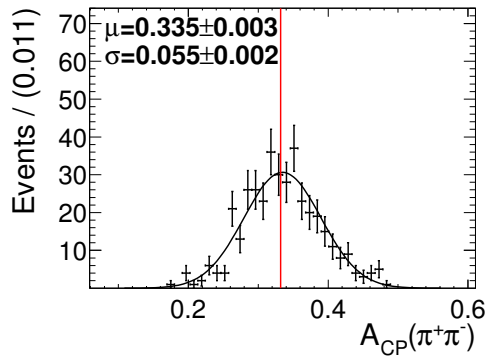
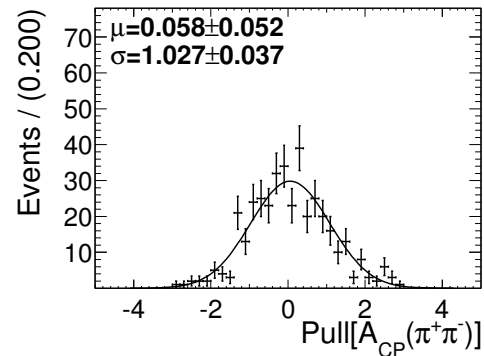
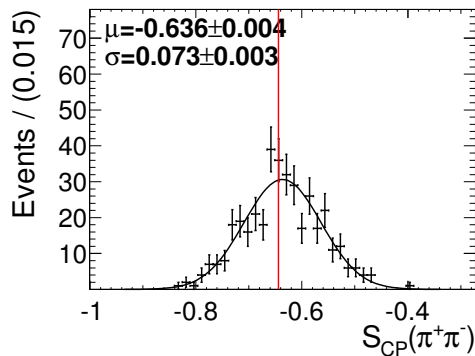
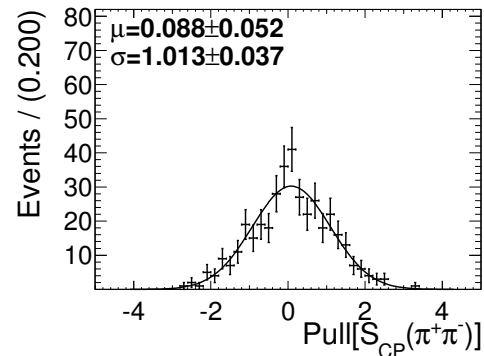
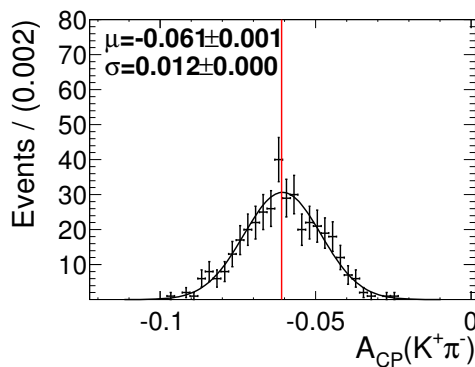
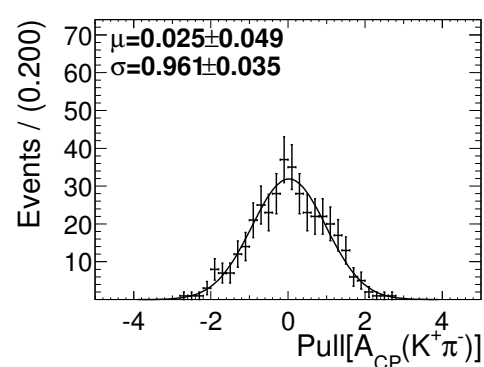
(a) Fit value distribution of $\pi^+ \pi^- \mathcal{A}_{CP}$.(b) Pull distribution of $\pi^+ \pi^- \mathcal{A}_{CP}$.(c) Fit value distribution of $\pi^+ \pi^- \mathcal{S}_{CP}$.(d) Pull distribution of $\pi^+ \pi^- \mathcal{S}_{CP}$.(e) Fit value distribution of $K \pi \mathcal{A}_{CP}$.(f) Pull distribution of $K \pi \mathcal{A}_{CP}$.

Figure 4.45: Fit central value and pull distributions of the CP parameters in the GSIM ensemble tests. The black dots including the error represent the results from the toy MC pseudo experiments. The solid black line is the result of a Gaussian fit. The read line indicates the generated value.

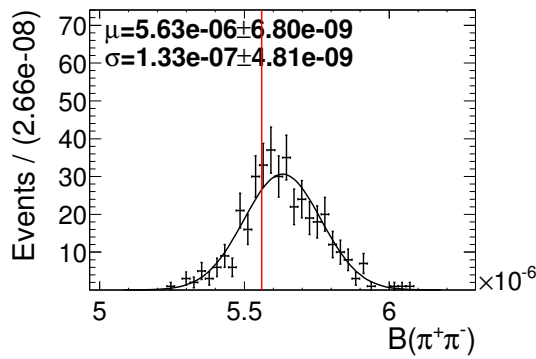
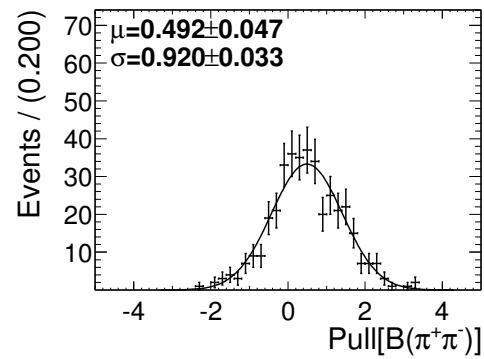
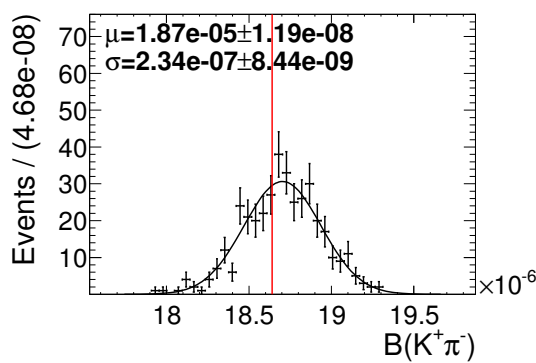
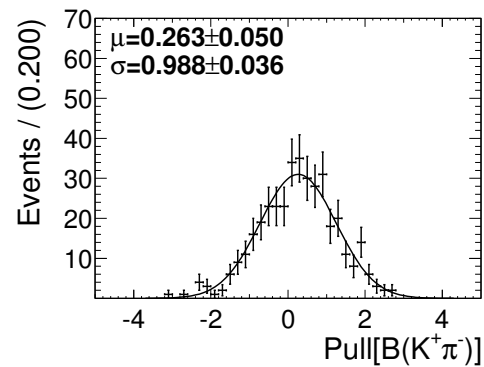
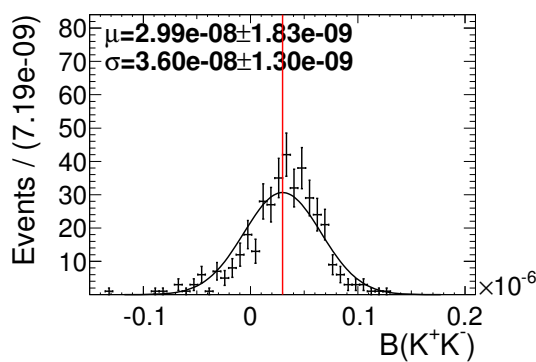
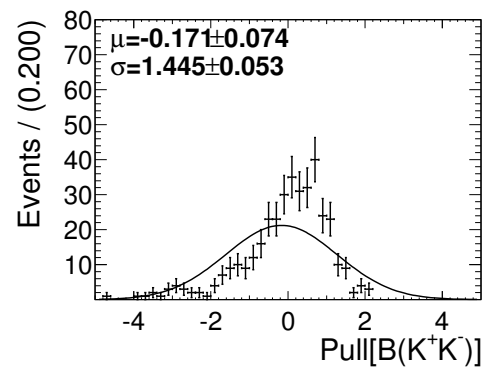
(a) Fit value distribution of $\pi^+ \pi^-$ branching ratio.(b) Pull distribution of $\pi^+ \pi^-$ branching ratio.(c) Fit value distribution of $K \pi$ branching ratio.(d) Pull distribution of $K \pi$ branching ratio.(e) Fit value distribution of $\pi^+ \pi^-$ branching ratio.(f) Pull distribution of $K^+ K^-$ branching ratio.

Figure 4.46: Fit central value and pull distributions of the branching ratio in the GSIM ensemble tests. The black dots including the error represent the results from the toy MC pseudo experiments. The solid black line is the result of a Gaussian fit. The red line indicates the generated value.

4.6.3 Interpretation

The pull distributions from PDF pseudo-experiments expose no bias except for the branching ratio of $B^0 \rightarrow K^+K^-$. The mean of the pull distribution of the branching ratio of $B^0 \rightarrow K^+K^-$ is not shifted, but the width of the distribution is wider than unity. The error calculation is done using the symmetric Gaussian errors from the minimisation procedure. Since the branching ratio is close to zero, the assumption of Gaussian errors is not satisfactory. When we use the asymmetric errors from a scan of the likelihood the pull distribution for the $B^0 \rightarrow K^+\pi^-$ branching ratio recovers a width of unity. Because the errors are underestimated, the width of the pull distribution is wider than unity. For GSIM pseudo-experiments the results are more diverse. The CP parameters show very little bias as in the case of PDF pseudo-experiments. On the other hand, the bias of the branching ratios is quite significant. The absolute size of the bias, however, is on a tolerable level and is included as a systematic error. Later in the calculation of the systematic uncertainties, we are going to see that only the $B^0 \rightarrow \pi^+\pi^-$ measurement is dominated by the uncertainty resulting from the bias. For future analyses, one would probably want to reduce the fit bias. Therefore we will study in the next section the source of the bias in the fitter and possible remedies.

4.6.4 Possible Sources of the Fit Biases

By systematically removing components from the pseudo-experiments, the bias was identified to be in the signal components $\pi^+\pi^-$ and $K\pi$ itself. In a next step, we removed the fit variable ΔE with the result of the bias vanishing. The same happens if the PID likelihoods are removed from the fit. Figure 4.47 shows the PID likelihood in slices of ΔE . Implementing these correlations and the correlation of ΔE with M_{BC} might lead to a reduced fit result. We leave the task to implement the correlations and search for an improvement open for future analyses.

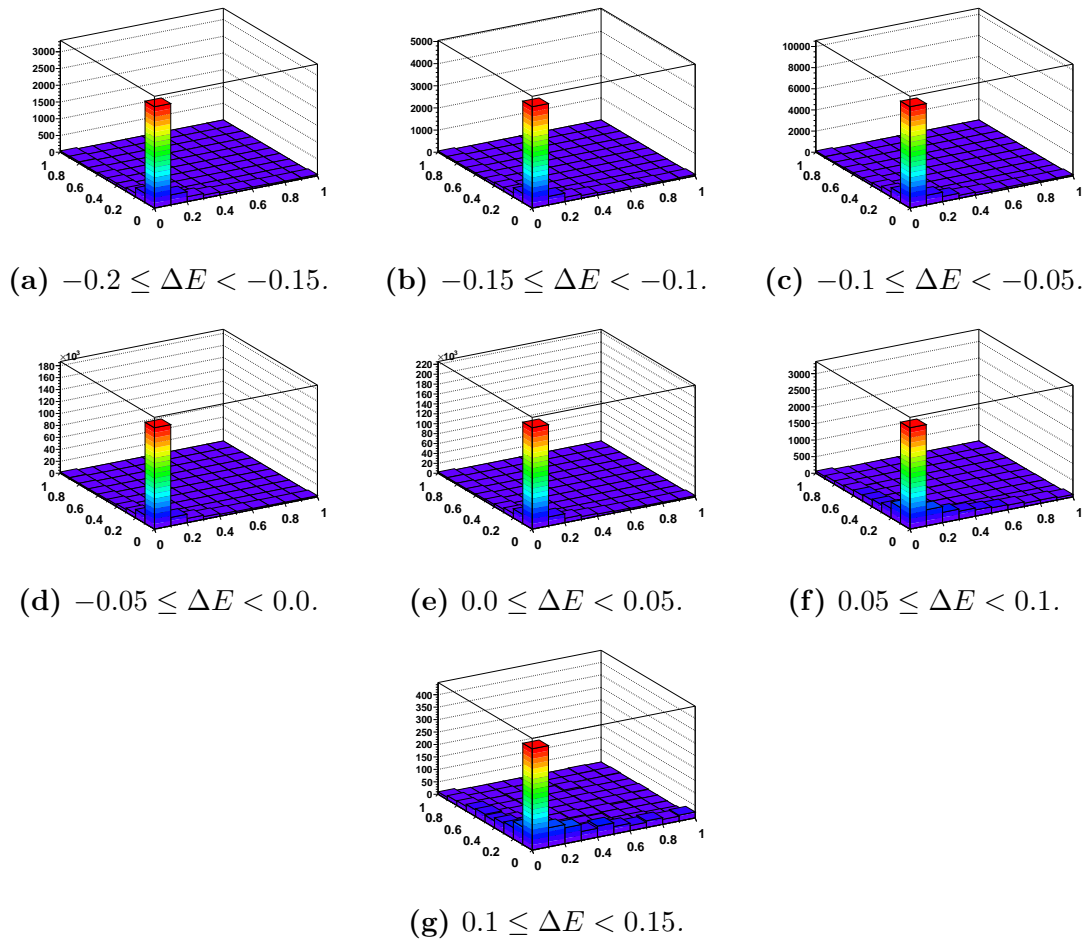


Figure 4.47: PID likelihood $\mathcal{L}_{K/\pi}^+$ and $\mathcal{L}_{K/\pi}^-$ for the $\pi^+ \pi^-$ component in slices of ΔE . When comparing the histograms starting with (a) going down to (g) one can observe an increase of events outside the peak at $(0,0)$. This feature is especially pronounced in the row defined by $\mathcal{L}_{K/\pi}^+ = 0$ and the row $\mathcal{L}_{K/\pi}^- = 0$.

Chapter 5

Differences between Monte-Carlo and Data

5.1 Control Sample Measurement

5.1.1 Control Sample $B \rightarrow D\pi$, $D \rightarrow K\pi$

Our main analysis is $B \rightarrow h^+h^-$ where h is either a pion or a kaon. This section shows a way of checking and correcting possible differences between the full Monte-Carlo simulation and the data. The signal models for the $B \rightarrow h^+h^-$ analysis are obtained purely from Monte-Carlo simulation. To correct these models, we are using the following method. We are identifying a decay channel which is as similar as possible to our main analysis. The data collected for this decay channel is called our control sample. We perform an event selection in a similar way as for the main analysis and build a model for the signal and the background components. It is important to keep the models for the main analysis and the control sample sufficiently similar. We introduce correction factors into the signal model which can account for differences (shifts, change in shapes) between the signal model and the data. In a fit to the control sample, we float the correction factors. The obtained corrections can then be applied to the main analysis signal models. We extract correction factors for the mean and width of the M_{BC} , ΔE and $\mathcal{F}_{S/B}$ of the signal model. Because the fisher discriminant $\mathcal{F}_{S/B}$, is different in every r -bin, we are extracting seven sets of correction factors. Corrections to the yields in every r -bin (r -bin fractions) are also obtained.

The main analysis examines a scalar particle decay into two scalar particles where both resulting scalar particles are charged. As a suitable control sample, we look into decays with a similar topology and a sufficiently high branching ratio to exclusively reconstruct it. The obvious candidate is $B^\pm \rightarrow \bar{D}^0\pi^\pm$ where the D^0 decays into charged pion and kaon ($D^0 \rightarrow K^-\pi^+$). The branching ratios are reasonably high with $(4.81 \pm 0.15) \times 10^{-3}$ for

$B^+ \rightarrow \bar{D}^0\pi^+$ or $B^- \rightarrow D^0\pi^-$ and $(3.88 \pm 0.05) \times 10^{-2}$ for $D^0 \rightarrow K^-\pi^+$. This allows us to use tight cuts on the D^0 mass to obtain a clean sample.

5.1.2 Event Selection

Basically the same event selection is used as for the main analysis $B \rightarrow h^+h^-$ (see section 4.3). This is necessary to transfer the obtained correction factors from the control channel to the main analysis. The differences and similarities are discussed in the following.

The reconstruction of $B^+ \rightarrow \bar{D}^0\pi^+$ begins with the reconstruction of the D^0 or \bar{D}^0 meson from a charged pion and a charged kaon. We apply a loose requirement on the likelihood ratio between the kaon likelihood and the sum of the kaon and pion likelihoods,

$$\frac{\mathcal{L}_K}{\mathcal{L}_K + \mathcal{L}_\pi} < 0.4 \text{ for pions,} \quad (5.1)$$

$$\frac{\mathcal{L}_K}{\mathcal{L}_K + \mathcal{L}_\pi} > 0.6 \text{ for kaons.} \quad (5.2)$$

In addition, an electron veto is placed on the tracks used for reconstruction,

$$\mathcal{L}_{e^\pm} > 0.9. \quad (5.3)$$

The analysis window of ΔE is chosen to be the same as it is in the $\pi^+ \pi^-$ study,

$$-0.2 \text{ GeV} < \Delta E < 0.15 \text{ GeV}. \quad (5.4)$$

An additional 3σ cut on the mass of the D meson is placed,

$$1.828 \text{ GeV}/c^2 < m(D^0) < 1.9 \text{ GeV}/c^2. \quad (5.5)$$

The resulting distribution is shown in figure 5.1.

5.1.3 Data Model

The branching fraction and the correction factors for the shape are extracted from a 5 dimensional extended unbinned maximum likelihood fit. We fit ΔE , M_{BC} , $\mathcal{F}_{S/B}$, q and Δt in every r -bin and SVD configuration l, s . The first three variables are in the fit for obvious reasons because we want to obtain correction factors for the signal shapes. The variables q and Δt are included because they are strongly correlated with the B -tagging quality r and we want to cross check that no time-dependent CP violation is present in the control sample. To obtain correct r -bin fractions we want to keep the model for the control sample as close as possible to model of the main analysis.

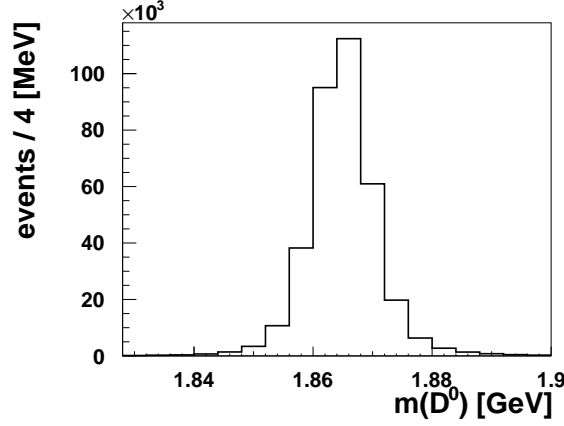


Figure 5.1: Distribution of the D^0 mass inside the analysis window.

Truth Model

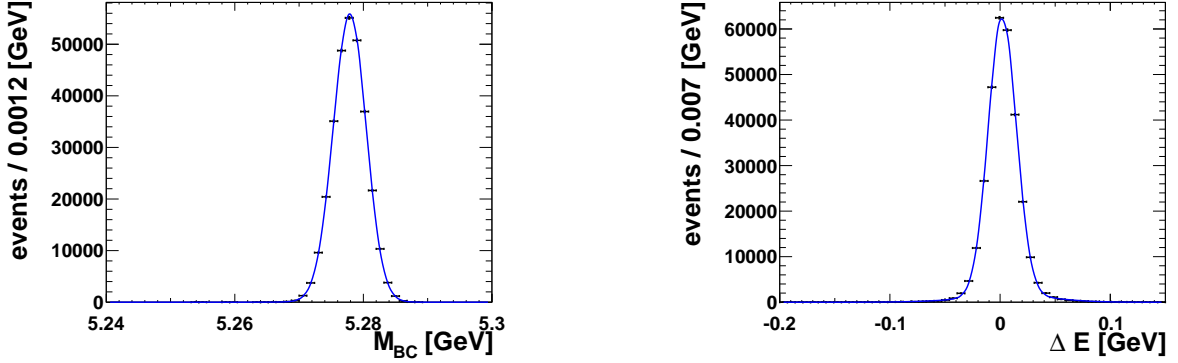
The model is determined from correctly reconstructed signal MC events. A sample of 1×10^6 events was generated with full detector simulation [66], taking into account the effect of final state radiation. Then all events were processed as described in Sec. 5.1.2. In the remaining events, only 3.00 % were found misreconstructed according to Monte-Carlo truth information. Therefore we can neglect the misreconstructed events and build the signal truth model from the correctly reconstructed events.

The PDF for M_{BC} and ΔE is modelled by the sum of three Gaussians that are defined the following way,

$$\begin{aligned} \mathcal{P}_{D\pi}(M_{BC}) \equiv & f_1 \cdot G(M_{BC}, \mu_1^l + \mu_1^{\text{CF},l}, \sigma_1^l \cdot \sigma_1^{\text{CF},l}) \\ & + f_2 \cdot G(M_{BC}, \mu_1^l + \mu_1^{\text{CF},l} + \mu_2^l, \sigma_1^l \cdot \sigma_1^{\text{CF},l} \cdot \sigma_2^l) \\ & + (1 - f_1 - f_2) \cdot G(M_{BC}, \mu_1^l + \mu_1^{\text{CF},l} + \mu_2^l + \mu_3^l, \sigma_1^l \cdot \sigma_1^{\text{CF},l} \cdot \sigma_2^l \cdot \sigma_3^l), \end{aligned} \quad (5.6)$$

$$\begin{aligned} \mathcal{P}_{D\pi}(\Delta E) \equiv & f_1 \cdot G(\Delta E, \mu_1^l + \mu_1^{\text{CF},l}, \sigma_1^l \cdot \sigma_1^{\text{CF},l}) \\ & + f_2 \cdot G(\Delta E, \mu_1^l + \mu_1^{\text{CF},l} + \mu_2^l, \sigma_1^l \cdot \sigma_1^{\text{CF},l} \cdot \sigma_2^l) \\ & + (1 - f_1 - f_2) \cdot G(\Delta E, \mu_1^l + \mu_1^{\text{CF},l} + \mu_2^l + \mu_3^l, \sigma_1^l \cdot \sigma_1^{\text{CF},l} \cdot \sigma_2^l \cdot \sigma_3^l). \end{aligned} \quad (5.7)$$

This is the same definition used for the signal models in the main analysis. The triple Gaussian also incorporates correction factors that may be floated in a fit to data to compensate differences between data and Monte-Carlo (MC). These correction factors are then applied to the signal models of the $B \rightarrow hh$ PDFs in the main analysis. For the fit to $D\pi$ signal Monte-Carlo, the correction factors that modify the mean are fixed to zero while the correction factors that change the width are fixed to unity. The fit results can be found in figure 5.2. Later in the fit to the control sample data, these correction factors are floated.



(a) Fit projection of the variable M_{BC} , from full detector simulation Monte-Carlo.

(b) Fit projection of the variable ΔE , from full detector simulation Monte-Carlo.

Figure 5.2: Fit results for the variables M_{BC} and ΔE , for the component $D\pi$. Data points with errors represent the MC from full detector simulation and the solid blue line represents the fit result.

The Fisher discriminant that distinguishes between signal (B decays) and continuum ($e^+e^- \rightarrow q\bar{q}$, where $q = u, d, s, c$) $\mathcal{F}_{S/B}$, is modelled by the same parametrisation throughout the whole analysis. In every component j , the $\mathcal{F}_{S/B}$ is modelled by the sum of three Gaussians in every r -bin l , containing correction factors which can correct differences between data and MC where necessary. The parameters for of the three Gaussians are the same for all B decays and are different for the continuum background,

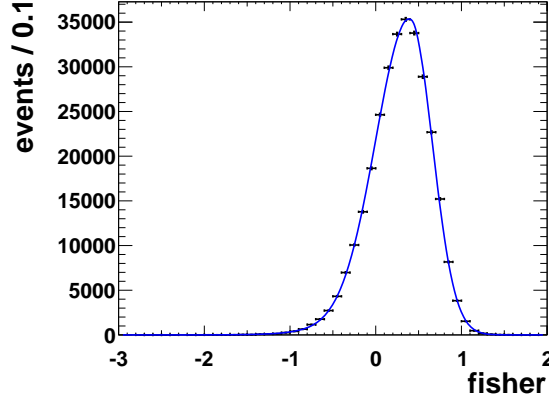
$$\begin{aligned} \mathcal{P}_j^l(\mathcal{F}_{S/B}) \equiv & f_1 \cdot G(\mathcal{F}_{S/B}, \mu_1^l + \mu_1^{\text{CF},l}, \sigma_1^l \cdot \sigma_1^{\text{CF},l}) \\ & + f_2 \cdot G(\mathcal{F}_{S/B}, \mu_1^l + \mu_1^{\text{CF},l} + \mu_2^l, \sigma_1^l \cdot \sigma_1^{\text{CF},l} \cdot \sigma_2^l) \\ & + (1 - f_1 - f_2) \cdot G(\mathcal{F}_{S/B}, \mu_1^l + \mu_1^{\text{CF},l} + \mu_2^l + \mu_3^l, \sigma_1^l \cdot \sigma_1^{\text{CF},l} \cdot \sigma_2^l \cdot \sigma_3^l). \end{aligned} \quad (5.8)$$

The fit results can be found in figure 5.3.

The time-dependent CP parameters \mathcal{A}_{CP} and \mathcal{S}_{CP} , are by including the following PDF,

$$\begin{aligned} \mathcal{P}_{D\pi}^l(\Delta t, q) \equiv & \frac{e^{-|\Delta t|/\tau_{B^\pm}}}{4\tau_{B^\pm}} \{(1 - q\Delta w_l + q(1 - 2w_l)) \times \\ & \left[(\mathcal{A}_{CP} \cos \Delta m_d \Delta t + \mathcal{S}_{CP} \sin \Delta m_d \Delta t) \right] \} \otimes R_{B^+B^-}(\Delta t). \end{aligned} \quad (5.9)$$

Although we know that there is no mixing of charged B mesons, we interpret the data as if there could be mixing as a cross check. The PDF accounts for the dilution from probability of incorrect flavour tagging w_l , and the difference in incorrect tagging between B^0 and \bar{B}^0 , Δw_l . The CP asymmetry PDF is convoluted with the detector resolution function $R_{B^+B^-}(\Delta t)$, for charged B mesons. The resolution function [68] is explained in appendix C.



(a) PDF and full detector simulation Monte-Carlo for variable $\mathcal{F}_{S/B}$.

Figure 5.3: Fit results for the variable $\mathcal{F}_{S/B}$, for the component $D\pi$. Data points with errors represent the MC from full detector simulation and the solid blue line represents the fit result.

The PDF also depends on the B lifetime τ_{B^\pm} , and the mass difference between B_H and \bar{B}_L , Δm_d . The following values were used to generate the $D\pi$ signal Monte-Carlo,

$$\begin{aligned}\tau_{B^\pm} &= 1.638 \text{ ps}, \\ \Delta m_d &= 0.507 \times 10^{12} \text{ } \hbar\text{s}^{-1}, \\ \mathcal{A}_{CP} &= 0.0, \\ \mathcal{S}_{CP} &= 0.0.\end{aligned}$$

The fit results can be found in figure 5.4.

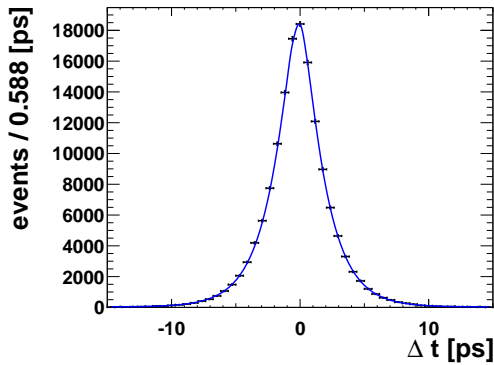
The total PDF for the $D\pi$ component is constructed to be

$$\mathcal{P}_{D\pi}^l(M_{BC}, \Delta E, \mathcal{F}_{S/B}, q, \Delta t) \equiv \mathcal{P}_{D\pi}(M_{BC}, \Delta E) \mathcal{P}_{D\pi}(\mathcal{F}_{S/B}) \mathcal{P}_{D\pi}^l(q, \Delta t). \quad (5.10)$$

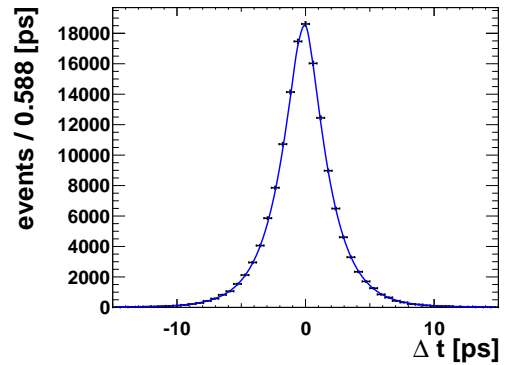
Its shape can be determined by maximizing the following likelihood,

$$\mathcal{L}_j \equiv \prod_{l,s} \frac{e^{N_j^s \sum_{l,s} f_j^{l,s}}}{N_{l,s}!} \prod_{i=0}^{N_{l,s}} N_j^s f_j^{l,s} \mathcal{P}_j^{l,s}(M_{BC}^i, \Delta E^i, \mathcal{F}_{S/B}^i, q^i, \Delta t^i), \quad (5.11)$$

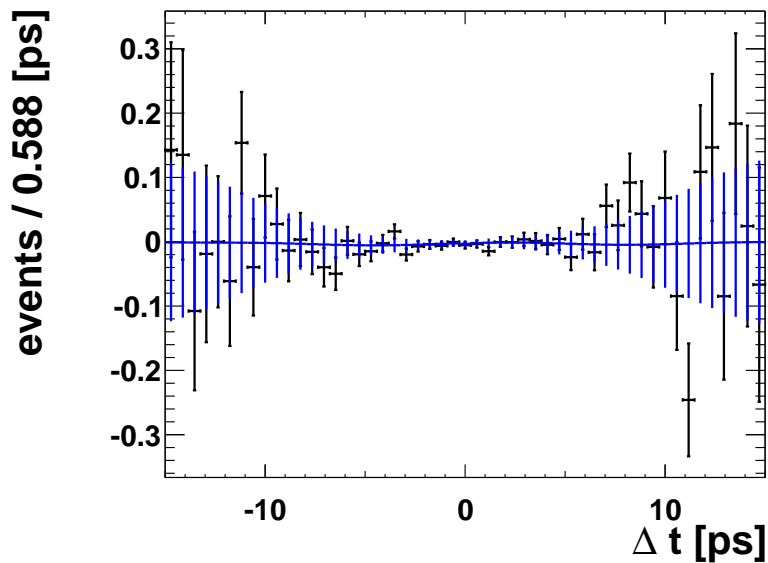
where j is the component. The parameter N is the signal yield and f is the fraction of events in r -bin and SVD configuration l, s . The fit results to $D\pi$ signal Monte-Carlo are shown in figs. 5.2, 5.3, 5.4.



(a) Δt PDF on full detector simulation Monte-Carlo for events tagged as B^0 ($q = 1$).



(b) Δt PDF on full detector simulation Monte-Carlo for events tagged as \bar{B}^0 ($q = -1$).



(c) $D \pi \Delta t$ asymmetry.

Figure 5.4: Fit results for variable Δt , for the component $D\pi$. Data points with errors represent the MC from full detector simulation and the solid blue line represents the fit result.

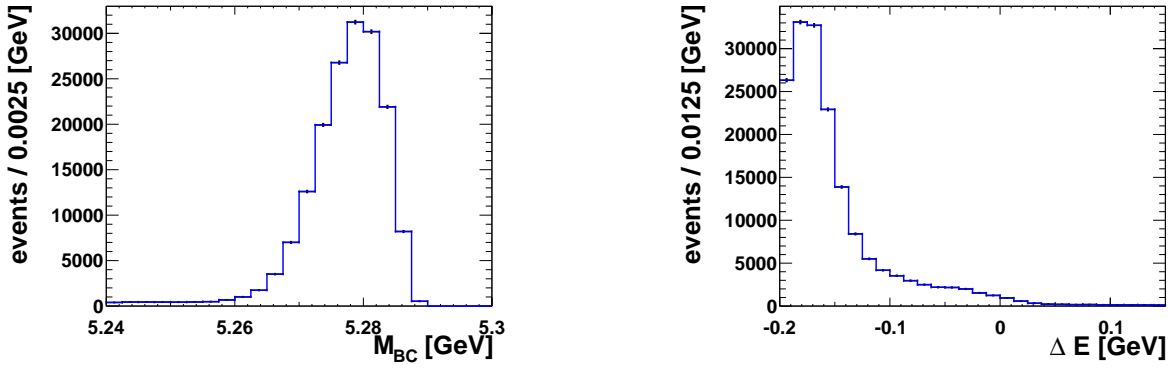
Charmed B^+B^- Model

The charmed B^+B^- Monte-Carlo events were taken from full detector simulation. A Monte-Carlo sample corresponding to ten times the Belle statistics is generated. Then all events were processed according to Sec. 5.1.2.

The PDF for M_{BC} and ΔE is modelled by a 2D histogram to incorporate the correlation between M_{BC} and ΔE ,

$$\mathcal{P}_{B^+B^-}(M_{BC}, \Delta E) \equiv \mathcal{H}(M_{BC}, \Delta E). \quad (5.12)$$

In figure 5.5, the resulting fit and projections into 1D for M_{BC} and ΔE are shown.



(a) Projection of the variable M_{BC} , from the 2D PDF on full detector simulation Monte-Carlo.

(b) Projection of the variable ΔE , from the 2D PDF on full detector simulation Monte-Carlo.

Figure 5.5: Fit results for the variables M_{BC} and ΔE , for the charmed B^+B^- component. Data points with errors represent the MC from full detector simulation and the solid blue line represents the fit result.

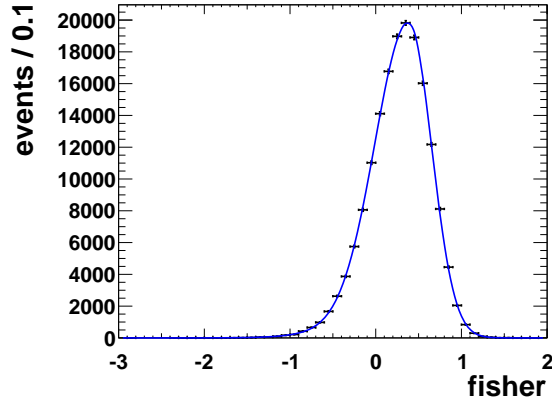
We are using the same triple Gaussian PDF for the fisher discriminant $\mathcal{F}_{S/B}$, as we use in the truth signal model. The parameters including the mean, width and fractions, are also shared between all B meson components in the control sample,

$$\begin{aligned} \mathcal{P}_j^l(\mathcal{F}_{S/B}) \equiv & f_1 \cdot G(\mathcal{F}_{S/B}, \mu_1^l + \mu_1^{\text{CF},l}, \sigma_1^l \cdot \sigma_1^{\text{CF},l}) \\ & + f_2 \cdot G(\mathcal{F}_{S/B}, \mu_1^l + \mu_1^{\text{CF},l} + \mu_2^l, \sigma_1^l \cdot \sigma_1^{\text{CF},l} \cdot \sigma_2^l) \\ & + (1 - f_1 - f_2) \cdot G(\mathcal{F}_{S/B}, \mu_1^l + \mu_1^{\text{CF},l} + \mu_2^l + \mu_3^l, \sigma_1^l \cdot \sigma_1^{\text{CF},l} \cdot \sigma_2^l \cdot \sigma_3^l). \end{aligned} \quad (5.13)$$

The fit results can be found in figure 5.6.

The Δt PDF is modelled by a lifetime PDF with an effective lifetime τ_{eff} , as free parameter,

$$\mathcal{P}_{\text{generic}B^+B^-}^l(\Delta t) \equiv \frac{e^{-|\Delta t|/\tau_{B^0}}}{4\tau_{B^0}} \otimes R_{B^0\bar{B}^0}(\Delta t). \quad (5.14)$$



(a) PDF on full detector simulation Monte-Carlo for the variable $\mathcal{F}_{S/B}$.

Figure 5.6: Fit results of the variable $\mathcal{F}_{S/B}$, for the charmed B^+B^- component. Data points with errors represent the MC from full detector simulation and the solid blue line represents the fit result.

The lifetime PDF is convoluted with the detector resolution function $R_{B^+B^-}(\Delta t)$, for charged B mesons. The resolution function [68] is explained in appendix C. The lifetime PDF depends on the effective B lifetime τ_{eff} . The fit results can be found in figure 5.7.

The total PDF for the charmed B^+B^- component is constructed to be

$$\mathcal{P}_{B^+B^-}^l(M_{\text{BC}}, \Delta E, \mathcal{F}_{S/B}, q, \Delta t) \equiv \mathcal{P}_{B^+B^-}(M_{\text{BC}}, \Delta E) \mathcal{P}_{B^+B^-}(\mathcal{F}_{S/B}) \mathcal{P}_{B^+B^-}^l(\Delta t). \quad (5.15)$$

The fit results to charmed B^+B^- signal Monte-Carlo are shown in figs. 5.5, 5.6, 5.7.

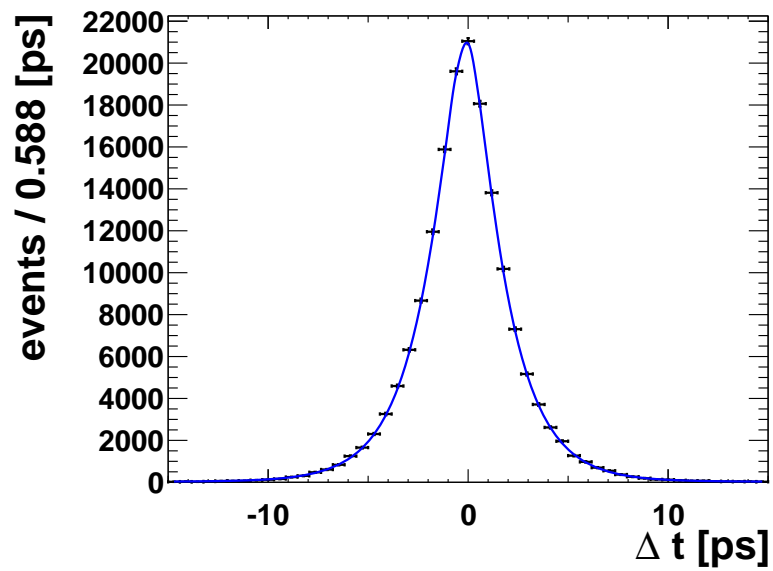


Figure 5.7: *Fit results for the variable Δt , for the charmed B^+B^- component. Data points with errors represent the MC from full detector simulation and the solid blue line represents the fit result.*

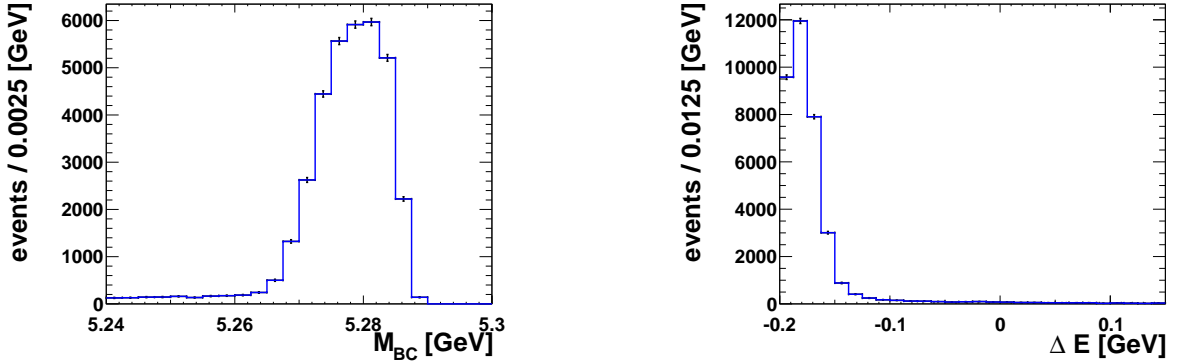
Charmed $B^0\bar{B}^0$ Model

The charmed $B^0\bar{B}^0$ Monte-Carlo events were taken from full detector simulation. A Monte-Carlo sample corresponding to ten times the Belle statistics is generated. Then all events were processed according to Sec. 5.1.2.

The PDF for M_{BC} and ΔE is modelled by a 2D histogram to incorporate the correlation between M_{BC} and ΔE ,

$$\mathcal{P}_{\text{generic}B^0\bar{B}^0}(M_{BC}, \Delta E) \equiv \mathcal{H}(M_{BC}, \Delta E). \quad (5.16)$$

In figure 5.8, the resulting fit and projections into 1D histograms for M_{BC} and ΔE are shown.



(a) Fit projection of the variable M_{BC} , from the 2D PDF on full detector simulation Monte-Carlo.

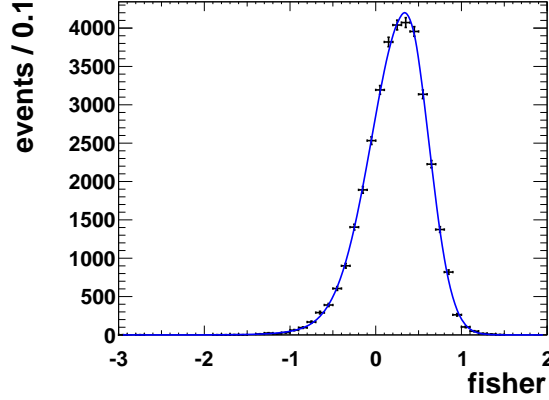
(b) Fit projection of the variable ΔE , from the 2D PDF on full detector simulation Monte-Carlo.

Figure 5.8: Fit results for the variables M_{BC} and ΔE , for the charmed $B^0\bar{B}^0$ component. Data points with errors represent the MC from full detector simulation and the solid blue line represents the fit result.

We are using the same triple Gaussian PDF for the fisher discriminant $\mathcal{F}_{S/B}$, as we use in the truth signal model. The parameters including the mean, width and fractions, are also shared between all B meson components in the control sample,

$$\begin{aligned} \mathcal{P}_j^l(\mathcal{F}_{S/B}) \equiv & f_1 \cdot G(\mathcal{F}_{S/B}, \mu_1^l + \mu_1^{\text{CF},l}, \sigma_1^l \cdot \sigma_1^{\text{CF},l}) \\ & + f_2 \cdot G(\mathcal{F}_{S/B}, \mu_1^l + \mu_1^{\text{CF},l} + \mu_2^l, \sigma_1^l \cdot \sigma_1^{\text{CF},l} \cdot \sigma_2^l) \\ & + (1 - f_1 - f_2) \cdot G(\mathcal{F}_{S/B}, \mu_1^l + \mu_1^{\text{CF},l} + \mu_2^l + \mu_3^l, \sigma_1^l \cdot \sigma_1^{\text{CF},l} \cdot \sigma_2^l \cdot \sigma_3^l). \end{aligned} \quad (5.17)$$

The fit results can be found in figure 5.9.



(a) PDF on full detector simulation Monte-Carlo for the variable $\mathcal{F}_{S/B}$.

Figure 5.9: Fit results for the variable $\mathcal{F}_{S/B}$, for the charmed $B^0\bar{B}^0$ component. Data points with errors represent the MC from full detector simulation and the solid blue line represents the fit result.

The time-dependent CP parameters \mathcal{A}_{CP} and \mathcal{S}_{CP} , are determined by multiplying by the following PDF,

$$\mathcal{P}_{\text{generic } B^0\bar{B}^0}^l(\Delta t, q) \equiv \frac{e^{-|\Delta t|/\tau_{\text{eff}}}}{4\tau_{\text{eff}}} \{(1 - q\Delta w_l + q(1 - 2w_l)) \times \left[(\mathcal{A}_{CP} \cos \Delta m_d \Delta t + \mathcal{S}_{CP} \sin \Delta m_d \Delta t) \right] \} \otimes R_{B^0\bar{B}^0}(\Delta t). \quad (5.18)$$

The PDF accounts for the dilution from probability of incorrect flavor tagging w_l , and the difference in wrong tagging between B^0 and \bar{B}^0 , Δw_l . The CP asymmetry PDF is convoluted with the detector resolution function $R_{B^0\bar{B}^0}(\Delta t)$, for neutral B mesons. The resolution function [68] is explained in appendix C. The lifetime PDF depends on the effective B lifetime τ_{eff} , and the mass difference between B_H and \bar{B}_L , Δm_d . The following values were used to generate the charmed $B^0\bar{B}^0$ signal Monte-Carlo,

$$\begin{aligned} \tau_{B^0} &= 1.53439 \text{ ps}, \\ \Delta m_d &= 0.507 \times 10^{12} \text{ } \hbar\text{s}^{-1}. \end{aligned}$$

The fit results from the Δt dimension can be found in figure 5.10.

The total PDF for the charmed $B^0\bar{B}^0$ component is constructed to be

$$\mathcal{P}_{B^0\bar{B}^0}^l(M_{BC}, \Delta E, \mathcal{F}_{S/B}, q, \Delta t) \equiv \mathcal{P}_{B^0\bar{B}^0}(M_{BC}, \Delta E) \mathcal{P}_{B^0\bar{B}^0}(\mathcal{F}_{S/B}) \mathcal{P}_{B^0\bar{B}^0}^l(q, \Delta t). \quad (5.19)$$

The fit results to charmed $B\bar{B}$ Monte-Carlo are shown in figs. 5.8, 5.9, 5.10.

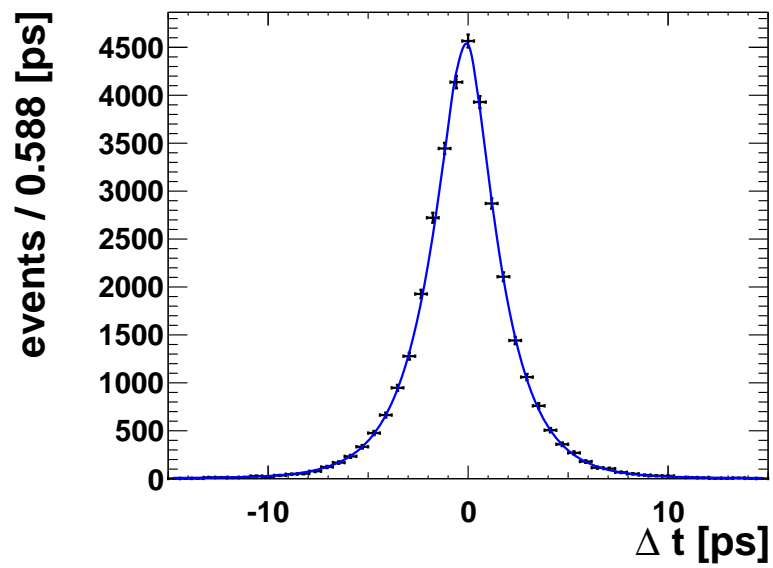


Figure 5.10: Fit results for the variable Δt for the charmed $B^0\bar{B}^0$ component. Data points with errors represent the MC from full detector simulation and the solid blue line represents the fit result.

Continuum Model

The model is determined from off-resonance data taken a 80 MeV below the $\Upsilon(4S)$ resonance. All events were processed with the procedure described in section 5.1.2. We used the same parametrisation as for the continuum model of the main analysis.

The PDF for M_{BC} is modelled by a Argus function [72],

$$\mathcal{P}_{\text{cont}}(M_{BC}) \equiv M_{BC} \cdot \sqrt{1 - \left(\frac{M_{BC}}{E_{\text{beam}}}\right)^2} \cdot e^{-a_{\text{eff}} \cdot \left(1 - \left(\frac{M_{BC}}{E_{\text{beam}}}\right)^2\right)}. \quad (5.20)$$

The fit results for M_{BC} can be found in figure 5.11a.

Because ΔE in the signal region has no structure, we model it by a first order Chebyshev polynomial. To incorporate the correlation between ΔE and qr , we fit ΔE in every r -bin,

$$\mathcal{P}_{\text{cont}}^l(\Delta E) \equiv 1 + c_{\text{eff}}^l \Delta E. \quad (5.21)$$

The fit results for ΔE can be found in figure 5.11b.

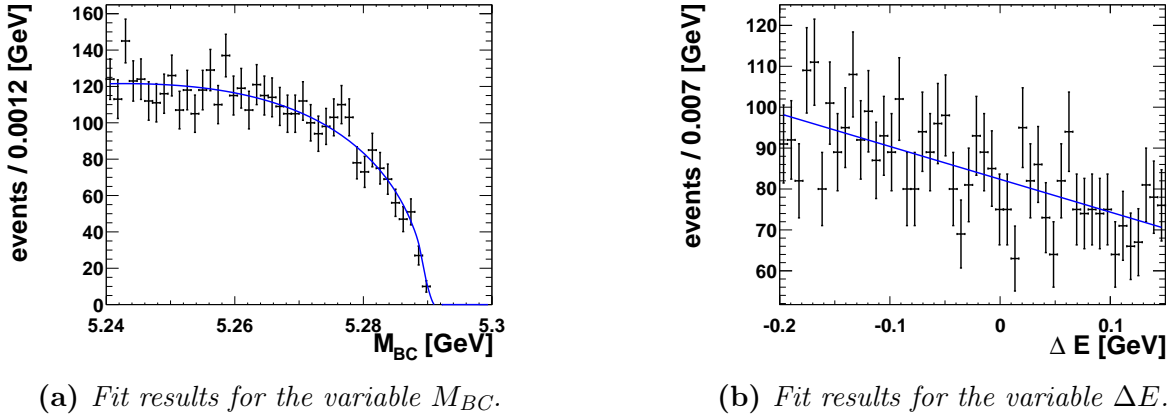
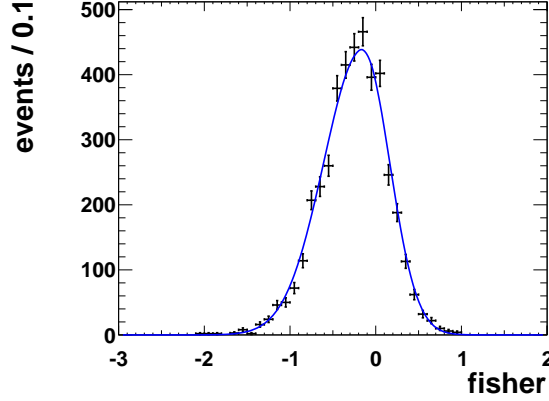


Figure 5.11: Fit results of the continuum component of the $D\pi$ control sample. Data points with errors represent the off-resonance data and the solid blue line represents the fit result.

The Fisher discriminant that distinguishes between signal (B decays) and continuum ($e^+e^- \rightarrow q\bar{q}$, where $q = u, d, s, c$) $\mathcal{F}_{S/B}$, is modelled by the same parametrisation throughout the whole analysis. The parameters of the Gaussians, however, are different for the continuum model compared to the B decay models. In every component j , the $\mathcal{F}_{S/B}$ is modelled by the sum of three Gaussians in every r -bin, l .

$$\begin{aligned} \mathcal{P}_j^l(\mathcal{F}_{S/B}) \equiv & f_1 \cdot G(\mathcal{F}_{S/B}, \mu_1^l + \mu_1^{\text{CF},l}, \sigma_1^l \cdot \sigma_1^{\text{CF},l}) \\ & + f_2 \cdot G(\mathcal{F}_{S/B}, \mu_1^l + \mu_1^{\text{CF},l} + \mu_2^l, \sigma_1^l \cdot \sigma_1^{\text{CF},l} \cdot \sigma_2^l) \\ & + (1 - f_1 - f_2) \cdot G(\mathcal{F}_{S/B}, \mu_1^l + \mu_1^{\text{CF},l} + \mu_2^l + \mu_3^l, \sigma_1^l \cdot \sigma_1^{\text{CF},l} \cdot \sigma_2^l \cdot \sigma_3^l) \end{aligned} \quad (5.22)$$

But there is no need for correction factors because the continuum model is built from off-resonance data as we do not expect a difference between off-resonance data and on-resonance data in the continuum. The fit results can be found in figure 5.12.



(a) PDF and data for variable $\mathcal{F}_{S/B}$

Figure 5.12: Fit results for the variable $\mathcal{F}_{S/B}$, for the continuum component of the $D\pi$ control sample. Data points with errors represent the off-resonance data and the solid blue line represents the fit result.

The Δt for continuum consists of a broad lifetime component which accounts for long lived particles, for example charmed particles, and a delta function component for single vertex events (prompt decays),

$$\mathcal{P}_{\text{cont}}^l(\Delta t) \equiv f_{\text{prompt}} \cdot \mathcal{P}_{\text{prompt}} + (1 - f_{\text{prompt}}) \cdot \mathcal{P}_{\text{lifetime}}^l, \quad (5.23)$$

where the lifetime PDF $\mathcal{P}_{\text{lifetime}}^l$, is given by

$$\mathcal{P}_{\text{lifetime}}^l(\Delta t) \equiv \frac{e^{-|\Delta t|/\tau_{\text{eff}}}}{4\tau_{\text{eff}}} \otimes R_{B^+B^-}^l(\Delta t). \quad (5.24)$$

The detector resolution function $R_{\text{cont}}^l(\Delta t)$, for continuum is convoluted onto the exponential function modelling the lifetime. For the prompt component, the convolution of the detector resolution function with the delta function yields the sum of two Gaussians as a model,

$$\begin{aligned} \mathcal{P}_{\text{prompt}}(\Delta t) \equiv & f \cdot G(\mathcal{F}_{S/B}, \mu_{\text{main}}, \sigma_{\text{main}}) \\ & + (1 - f) \cdot G(\mathcal{F}_{S/B}, \mu_{\text{main}} + \mu_{\text{tail}}, \sigma_{\text{main}} \cdot \sigma_{\text{tail}}). \end{aligned} \quad (5.25)$$

The fit results can be found in figure 5.13.

The total PDF for the continuum component is constructed to be

$$\mathcal{P}_{\text{cont}}^l(M_{\text{BC}}, \Delta E, \mathcal{F}_{S/B}, q, \Delta t) \equiv \mathcal{P}_{\text{cont}}(M_{\text{BC}}, \Delta E) \mathcal{P}_{\text{cont}}(\mathcal{F}_{S/B}) \mathcal{P}_{\text{cont}}^l(\Delta t). \quad (5.26)$$

The fit results to off resonance data are shown in Figs. 5.11a, 5.11b, 5.12, 5.13.

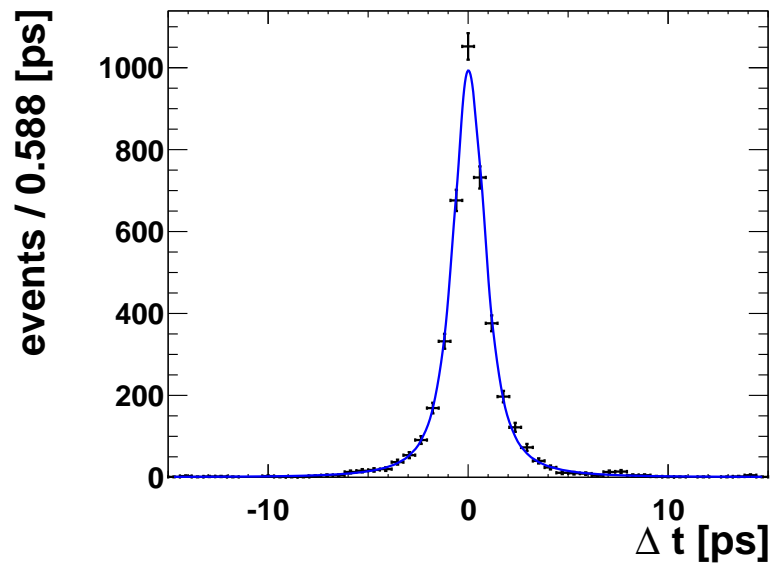


Figure 5.13: *Fit results for the variable Δt , for the continuum component of the $D\pi$ control sample. Data points with errors represent the off-resonance data and the solid blue line represents the fit result.*

5.1.4 Fit of $D\pi$ Model to the Control Sample

To correct the differences between Monte-Carlo and data, we use a two step procedure. First we obtain our $D\pi$ model from full detector simulation Monte-Carlo. In a second step, we fit our Model to data and free correction factors that allow changes in the shape of the model. This way we can obtain correction factors for M_{BC} , ΔE , $\mathcal{F}_{S/B}$ and the r -bin fractions. We assume that our main analysis channel $B \rightarrow \pi^+\pi^-$ is similar enough to the control sample to carry the correction factors over and apply them to the shapes there as well.

We include correction factors into our $D\pi$ model of M_{BC} , ΔE and $\mathcal{F}_{S/B}$. The correction factor for the mean of the primary Gaussian is added onto the mean obtained from the fit to the $D\pi$ signal sample. The correction factor for the width, however, is multiplied onto the width obtained from the fit to the signal sample. Allowing the correction factors to float in the fit to data enables us to determine them. The plots show a good agreement between data and MC after floating the correction factors (Fig. 5.14). The correction factors obtained from the fit are applied to the full-fitter ($\pi^+ \pi^-$) for the final fit to data. Corrections for ΔE , M_{BC} , $\mathcal{F}_{S/B}$ and the r -bin fractions obtained from the $D\pi$ -truth-model are applied to the PDF shape of the signal component $\pi^+ \pi^-$, $K \pi$ and $K K$. The correction factors for the $\mathcal{F}_{S/B}$ PDF shape are also applied to the $\mathcal{F}_{S/B}$ PDF shape of the charged and neutral B meson components. Table 5.1 shows a summary of the correction factors obtained on the $D\pi$ sample.

The correction factor and the corresponding errors with more digits can be found in the parameter listing in the appendix D.

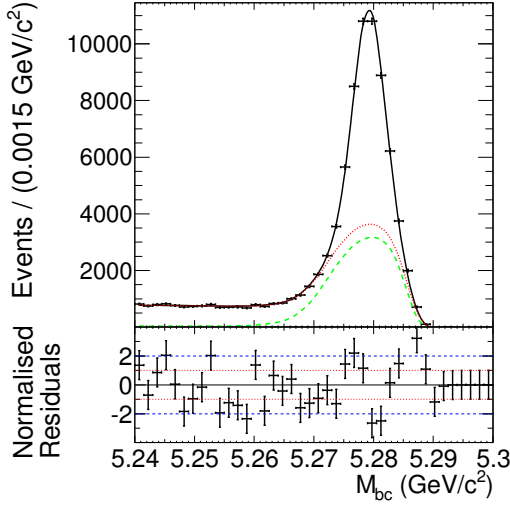
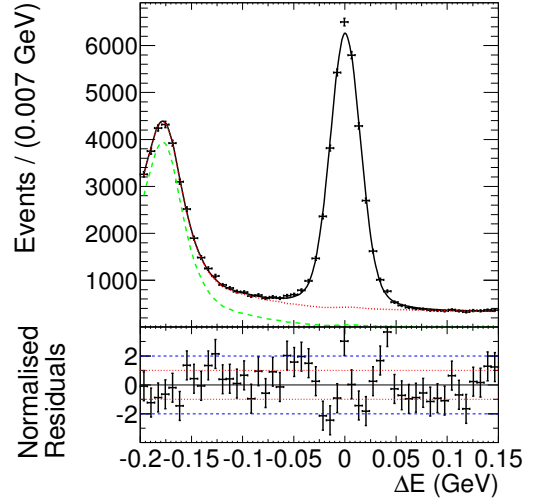
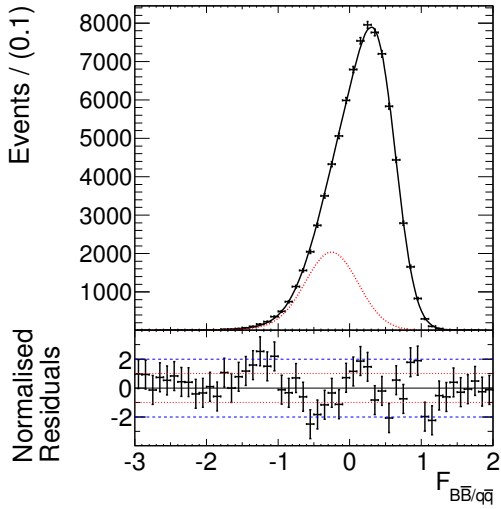
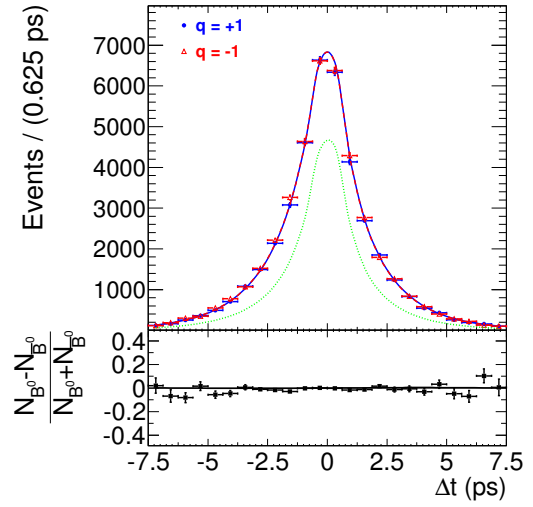
(a) M_{BC} projection.(b) ΔE projection.(c) $\mathcal{F}_{S/B}$ projection.(d) Δt projection.

Figure 5.14: Fit projections of all variables to the control sample. The black points show the data of the full Belle statistics including the errors. The black solid line represents the total PDF of all components. The red dotted line represents the total background while the green broken line is the background from three body charmed decays.

Table 5.1: *Correction factors obtained from truth model of the $D\pi$ fit.*

model parameter	r -bin	CF for SVD1	CF for SVD2
r -bin frac.	0	0.98	1.02
r -bin frac.	1	1.07	1.03
r -bin frac.	2	0.99	0.98
r -bin frac.	3	0.96	1.03
r -bin frac.	4	0.98	0.98
r -bin frac.	5	1.05	0.95
M_{BC} mean		1.59 MeV	1.37 MeV
M_{BC} σ		96 %	101 %
ΔE mean		-3.94 MeV	-1.29 MeV
ΔE σ		117 %	122 %
$\mathcal{F}_{S/B}$ mean	0	0.00	-0.01
$\mathcal{F}_{S/B}$ σ	0	100 %	100 %
$\mathcal{F}_{S/B}$ mean	1	-0.02	-0.01
$\mathcal{F}_{S/B}$ σ	1	103 %	102 %
$\mathcal{F}_{S/B}$ mean	2	-0.01	-0.01
$\mathcal{F}_{S/B}$ σ	2	104 %	102 %
$\mathcal{F}_{S/B}$ mean	3	0.00	-0.01
$\mathcal{F}_{S/B}$ σ	3	98 %	103 %
$\mathcal{F}_{S/B}$ mean	4	-0.01	-0.01
$\mathcal{F}_{S/B}$ σ	4	103 %	105 %
$\mathcal{F}_{S/B}$ mean	5	-0.00	-0.01
$\mathcal{F}_{S/B}$ σ	5	105 %	103 %
$\mathcal{F}_{S/B}$ mean	6	0.01	-0.01
$\mathcal{F}_{S/B}$ σ	6	108 %	103 %

5.2 Corrections to the Particle Identification

In this analysis, we incorporate the particle identification (PID) likelihood ratios $\mathcal{L}_{K/\pi}^+$ and $\mathcal{L}_{K/\pi}^-$, into the fit. The PID likelihood ratio of the kaon over the sum of kaon and pion likelihoods are described as histograms in all components. The histograms, however, are determined from Monte-Carlo for $B\bar{B}$ components and we expect a difference between data and Monte-Carlo. In contrary to the previous analysis, we intend to correct for the differences between data and Monte-Carlo. There is a set of correction factors ρ , available from an independent analysis (PID group). These correction factors are meant to correct the efficiency calculation. The correction factors can be used for a discrete set of cut values, 0.1, 0.2, 0.3, 0.4, 0.5, 0.6, 0.7, 0.8, 0.9. Also, the correction factors are given as a function of the angle of the particle to the detector z -axis θ , and the particle momentum, p . The correction factors are obtained in the independent analysis from an inclusive $D^*(2010)^\pm$ sample. The flavour of the D meson can be determined from the charge of the slow pion in the decays $D^*(2010)^\pm \rightarrow D^0\pi^\pm$ and $D^*(2010)^\mp \rightarrow \bar{D}^0\pi^\mp$. Since the D^0 (\bar{D}^0) decays into $K^+\pi^-$ ($K^-\pi^+$), we know whether the positive or negative track is the kaon or vice versa. This information is compared to the information from the PID system. The analysis is performed in bins of the particle momentum and polar angle θ , in the detector.

In the following we will show how to calculate the expected bin heights in data of the $\mathcal{L}_{K/\pi}^+$ and $\mathcal{L}_{K/\pi}^-$ histogram from the cut correction factors.

We want to introduce the method in the simpler one dimensional case and then later generalize it to the two dimensional case. Now imagine a histogram that looks like the one shown in figure 5.15. The number of events in the first bin is N_1^{MC} and is known from Monte-Carlo. Now imagine we would cut at the bin border, 0.1, we would be left with only these events in the first bin. Then using the correction factor for this cut ρ_1 , we can obtain the expected number of events in data N_1 ,

$$N_1 = N_1^{MC} \cdot \rho_1. \quad (5.27)$$

Moving on to a cut at the bin border of the second bin, 0.2, we can set up the following equation

$$N_1 + N_2 = (N_1^{MC} + N_2^{MC}) \cdot \rho_2, \quad (5.28)$$

$$N_2 = (N_1^{MC} + N_2^{MC}) \cdot \rho_2 - N_1. \quad (5.29)$$

The value of N_2 depends now only on N^{MC} , which is known from Monte-Carlo, ρ_2 , which is our input from the PID experts group, and N_1 , which we calculated above. We can generalize this recursive procedure and obtain

$$N_i = \sum_u^i N_u^{MC} \cdot \rho_i - \sum_u^{i-1} N_u. \quad (5.30)$$

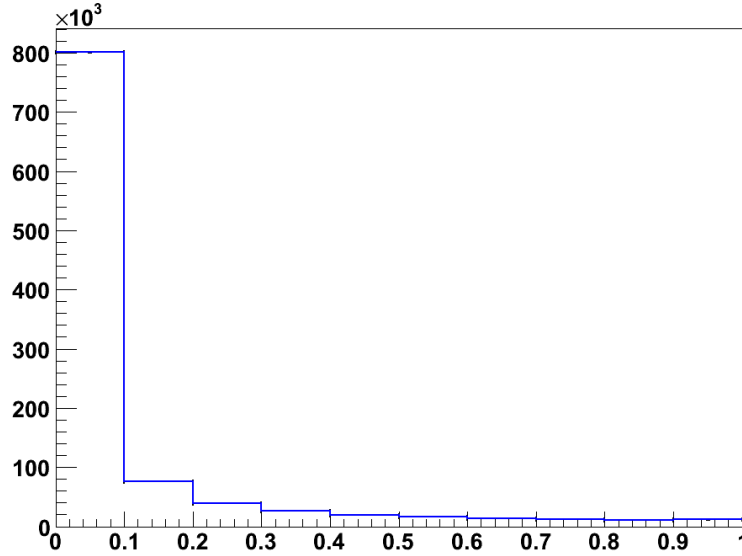


Figure 5.15: Likelihood ratio of a kaon given the pion hypothesis in a $B^0 \rightarrow \pi^+\pi^-$ Monte-Carlo sample.

In the extension to the 2D case we are looking at the PID likelihood ratio of the kaon given the pion hypothesis again, but this time for the positive and the negative particles that together form the B meson. Figure 5.16 shows the distribution obtained from Monte-Carlo. We need to redefine slightly the variables that we introduced for the 1D case. The correction factors for cuts on $\mathcal{L}_{K/\pi}^+$ or $\mathcal{L}_{K/\pi}^-$ are combined into a single ρ_{ij} ,

$$\rho_{ij} = \rho_i^+ \cdot \rho_j^-, \quad (5.31)$$

$$\Delta\rho_{ij}^2 = (\Delta\rho^+\rho^-)^2 + (\Delta\rho^-\rho^+)^2. \quad (5.32)$$

Then we can start our recursive procedure with the bin (1, 1),

$$N_{11} = N_{11}^{MC} \cdot \rho_{11}. \quad (5.33)$$

Moving away from this bin to the neighboring bins yields the same equations as for the 1D case. Finally we obtain

$$N_{ij} = \sum_u^i \sum_v^j N_{uv}^{MC} \cdot \rho_{ij} - \sum_u^i \sum_v^j N_{uv} + N_{ij}, \quad (5.34)$$

for the general case. Please note that the expression on the right is independent from N_{ij} because it is subtracted in the sum, but explicitly added afterwards to make it vanish from the term. By using the relation

$$\sum_u^i \sum_v^j N_{uv} = \sum_u^i \sum_v^j N_{uv} \cdot \rho_{ij}, \quad (5.35)$$

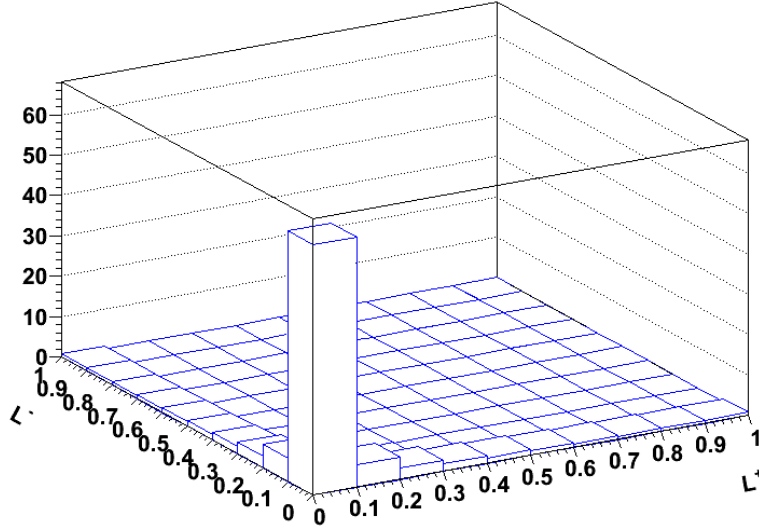


Figure 5.16: Likelihood ratio of the kaon given the pion hypothesis for the positive particle L^+ , and the negative particle L^- .

which is just the definition of the correction factors for the cuts ρ , we can remove the recursion from the formula and obtain the final result,

$$\begin{aligned}
 N_{ij} = & \sum_u^i \sum_v^j N_{uv}^{MC} \cdot \rho_{ij} - \sum_u^{i-1} \sum_v^j N_{uv}^{MC} \cdot \rho_{i-1j} \\
 & - \sum_u^i \sum_v^{j-1} N_{uv}^{MC} \cdot \rho_{ij-1} + \sum_u^{i-1} \sum_v^{j-1} N_{uv}^{MC} \cdot \rho_{i-1j-1}.
 \end{aligned}$$

Another question is the error of the expected number of events in each bin. This can be calculated using error propagation. The resulting error in each bin for the 2D case is

$$\begin{aligned}
 \Delta N_{ij}^2 = & \left[\sum_u^i \sum_v^j N_{uv}^{MC} \right] \cdot \Delta \rho_{ij}^2 - \left[\sum_u^{i-1} \sum_v^j N_{uv}^{MC} \right] \cdot \Delta \rho_{i-1j}^2 \\
 & - \left[\sum_u^i \sum_v^{j-1} N_{uv}^{MC} \right] \cdot \Delta \rho_{ij-1}^2 + \left[\sum_u^{i-1} \sum_v^{j-1} N_{uv}^{MC} \right] \cdot \Delta \rho_{i-1j-1}^2.
 \end{aligned}$$

This statement holds only if the number of events in each bin are uncorrelated. Because this is not necessarily true we did some Toy Monte-Carlo studies where we modelled the correlation explicitly (Data not shown). We used, however, a different method for calculating the systematic errors of this procedure (Sec. 6.2) which is even more conservative. For the

component $\pi^+ \pi^-$, the procedure is illustrated now with the aid of plots. The correction factors in each bin ρ_{ij}^N , are provided by an independent analysis as a function of θ and p for every particle N . The average in every bin is shown in figure 5.17. The errors of those

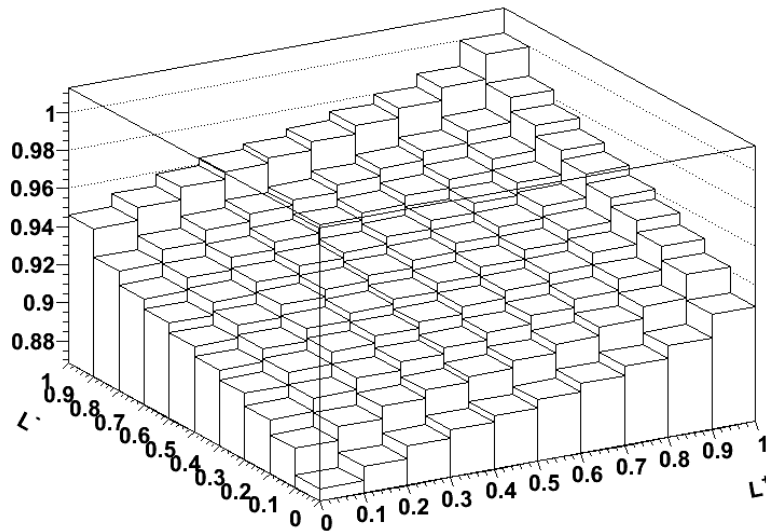


Figure 5.17: *Cut efficiency correction factors (ρ) for each bin in the L^+L^- histogram.*

correction factors $\Delta\rho_{ij}$ (Fig. 5.18), are also provided by the PID expert group as a function of θ and p . They are needed as input to the error propagation to determine the final error on the number of events. Finally the applied recursive procedure produces the following expectation for the data histogram (Fig. 5.19). The blue lines indicate the Monte-Carlo histogram while the black crosses show the expectation in data with the corresponding error estimation. To get a better feeling about the differences between data and Monte-Carlo we build a ratio (Fig. 5.20). Please note that the biggest discrepancies are in the bins with the lowest statistics.

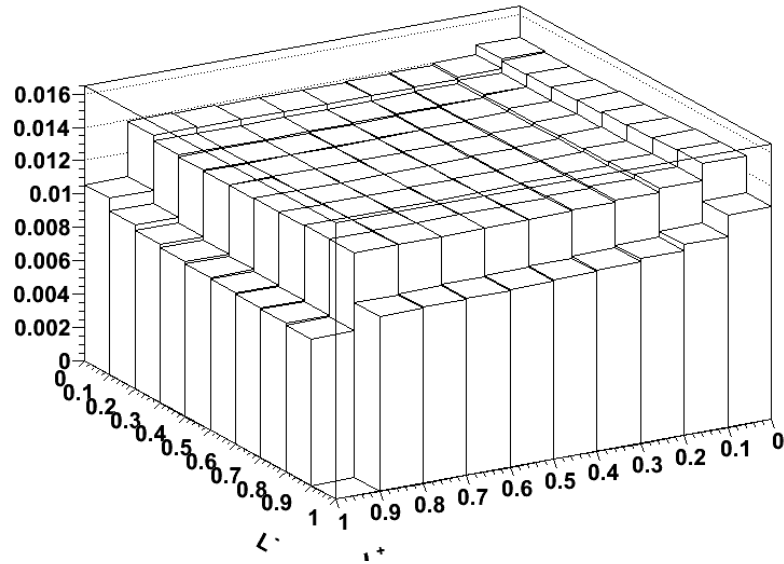


Figure 5.18: Errors of the correction factors for each bin in the L^+L^- histogram.

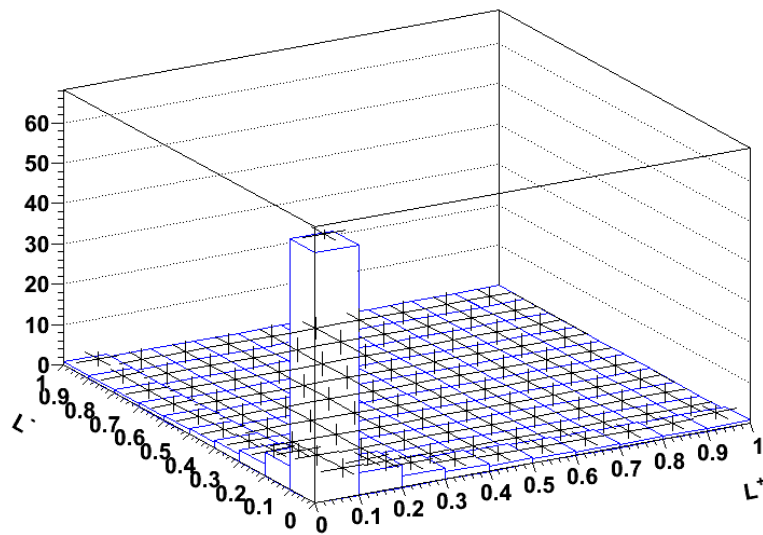


Figure 5.19: Monte-Carlo histogram (blue) and corrected data-like histogram with errors (black) of L^+L^- .

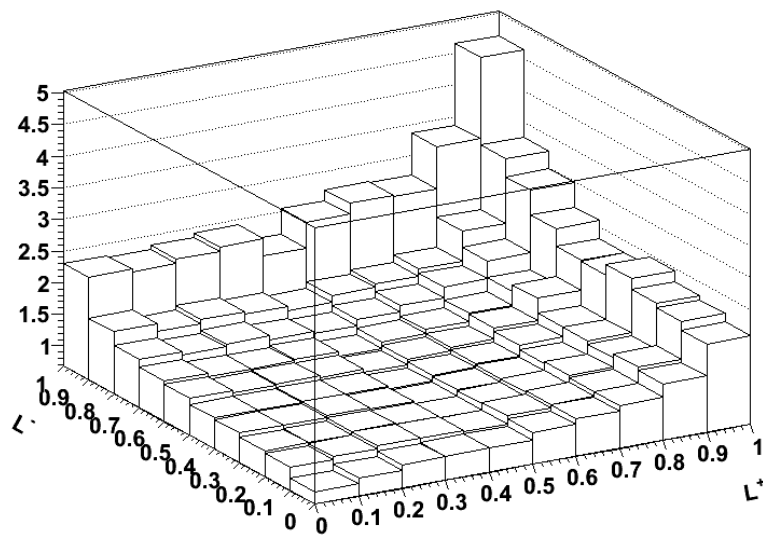


Figure 5.20: *Bin-wise ratio between data-like histogram and Monte-Carlo histogram of L^+L^- .*

Chapter 6

Results from $B^0 \rightarrow h^+ h^-$

6.1 Measurement of $B^0 \rightarrow h^+ h^-$ from the full Data Sample

6.1.1 Box Opening

The previous time-dependent CP violation analysis [39] analysed at a dataset of 535×10^6 $B\bar{B}$ events. We are using the full Belle dataset which contains 772×10^6 $B\bar{B}$ events. This will enable us to compare our results with the results of the previous analysis on the same dataset. First we performed a fit without correcting the PID histograms obtained from Monte-Carlo. The PID histogram correction accounts for the differences between data and Monte-Carlo and is described in section 5.2. In the fit to data, we float the branching ratios and the CP parameters.

It turns out that the fit of the signal components $\pi^+ \pi^-$, $K \pi$ and $K K$ to on-resonance data shows a discrepancy between the PDF and the data in the variable M_{BC} , particularly. This demonstrates that the $B^0 \rightarrow h^+ h^-$ decays and the $D\pi$ decay are kinematically not similar enough to obtain perfect correction factors. Therefore the correction factors for M_{BC} are floated on the final fit to data. The control sample analysis is still useful because start parameters for the fit of all signal components can be obtained. The correction factors obtained from the control channel for the mean and the width of ΔE and $\mathcal{F}_{S/B}$ are applied and fixed. Also, the ratio between the yield of the charmless B^0 and B^\pm decays is fixed while floating the combined yield. The yield of the continuum is floated. Because we are strongly dominated by continuum events, we can determine the continuum shape in the fit to data. Therefore we float the ΔE slope in all r -bin's. Also for the M_{BC} PDF, the parameters of the Argus function are determined from the fit. The chance is also taken to float the $\mathcal{F}_{S/B}$ shape and the r -bin fractions. A complete list of all floated parameters in the final fit can be found in the appendix D.

Table 6.1: Cuts applied to data to enhance the $B^0 \rightarrow \pi^+\pi^-$ signal.

Dimension	lower limit	upper limit
M_{BC}	5.27 GeV	5.29 GeV
ΔE	-0.04 GeV	0.04 GeV
$\mathcal{F}_{S/B}$	0.0	
r	0.5	
$\mathcal{L}_{K/\pi}^+$		0.4
$\mathcal{L}_{K/\pi}^-$		0.4

Table 6.2: Cuts applied to data to enhance the $B \rightarrow K^\pm\pi^\mp$ signal. The colour code in the cuts of the likelihood ratios means $(\mathcal{L}_{K/\pi}^+ > 0.6 \wedge \mathcal{L}_{K/\pi}^- < 0.4) \vee (\mathcal{L}_{K/\pi}^+ < 0.4 \wedge \mathcal{L}_{K/\pi}^- > 0.6)$.

Dimension	lower limit	upper limit
M_{BC}	5.27 GeV	5.29 GeV
ΔE	-0.08 GeV	0.00 GeV
$\mathcal{F}_{S/B}$	0.5	
r	0.0	
$\mathcal{L}_{K/\pi}^+$	0.6	0.4
$\mathcal{L}_{K/\pi}^-$	0.6	0.4

Table 6.3: Cuts applied to data to enhance the $B^0 \rightarrow K^+K^-$ signal.

Dimension	lower limit	upper limit
M_{BC}	5.27 GeV	5.29 GeV
ΔE	-0.12 GeV	-0.08 GeV
$\mathcal{F}_{S/B}$	0.0	
r	0.5	
$\mathcal{L}_{K/\pi}^+$	0.6	
$\mathcal{L}_{K/\pi}^-$	0.6	

The following plots show projections of the data and the PDF onto the various fit dimensions e.g. M_{BC} , ΔE , etc. The plots are signal enhanced by applying various cut to amplify one of the three signal modes $B^0 \rightarrow \pi^+\pi^-$, $B^0 \rightarrow K^+\pi^-$ and $B^0 \rightarrow K^+K^-$. To enhance $B^0 \rightarrow \pi^+\pi^-$, we apply the cuts shown in Tbl. 6.1.

For the decays $B^0 \rightarrow K^+\pi^-$ and $\bar{B}^0 \rightarrow K^-\pi^+$, we differentiate between the decays by the charge on the kaon. Therefore we have to cut on the PID variables which we connect with a logical or. This is shown in Tbl. 6.2.

The cuts for the decay $B^0 \rightarrow K^+K^-$ are very much the same as for $B^0 \rightarrow \pi^+\pi^-$, except for the ΔE region and the PID likelihood cuts (see Tbl. 6.3).

The following plots are all using the same color code, showing the data points with their corresponding errors in black. The solid black line shows the total PDF being the sum of all separate component PDFs. The continuum PDF is shown as a red slashed line. The green line is the sum of the PDFs of the charmless decays. Possible peaking backgrounds are indicated with a blue area. Beneath the plot, we decided to put a plot showing the normalized residuals in every bin. The normalized residual is the difference between data and PDF in the bin of interest divided by the error of the data point. The red and blue dotted lines in the normalized residual plot show the 1 and 2 sigma deviation levels, respectively.

Table 6.4: *Physics results from the full Belle data set of 772×10^6 $B\bar{B}$ -pairs.*

Observable	Value $\times 10^6$	Statistical error
$\mathcal{BR}(\pi^+\pi^-)$	5.63	± 0.16
$\mathcal{BR}(K\pi)$	18.71	± 0.25
$\mathcal{BR}(K^+K^-)$	0.03	± 0.05
$\mathcal{A}_{CP}(\pi^+\pi^-)$	0.33	± 0.06
$\mathcal{S}_{CP}(\pi^+\pi^-)$	-0.64	± 0.08
$\mathcal{A}_{CP}(K\pi)$	-0.061	± 0.014

By studying the projections of the data and PDF in the plots (Fig. 6.3-6.19), we can summarize that the agreement between data and the PDF is within the statistical uncertainties. Table 6.4 shows the physics results from the fit. For all physics observables, we determine the asymmetric error by examining the Likelihood function (MINOS). Because the statistical uncertainties are close to symmetric, we symmetrise the statistical error by taking the larger one. One side effect of the determination of the six physics observables in one likelihood maximization, is that we can obtain a full correlation matrix. The correlation parameters are interesting for a later isospin analysis. The correlation matrix of the physics observables is shown in table 6.5. The two strongest correlations are between the \mathcal{A}_{CP} and \mathcal{S}_{CP} parameters for $\pi^+\pi^-$, and the branching ratios between the decays $B^0 \rightarrow \pi^+\pi^-$ and $B \rightarrow K\pi$. Both are in the order of 10%. The fit of the likelihood ratios $\mathcal{L}_{K/\pi}^+$ and $\mathcal{L}_{K/\pi}^-$ are shown in Fig. 6.13,6.14 for $K^+\pi^-$ and Fig. 6.18 6.19 for K^+K^- . We observe that the normalisation of the total PDF is not optimal. The reason is that we project out the PID

likelihood by cutting on the fisher discriminant. The continuum model of the PDF of the fisher discriminant seems to mismatch the data which results in a bad normalization of the total PDF after the cut. This is also believed to be the reason for the shape of the residuals in Fig. 6.3.

Table 6.5: Correlation factors obtained from a simultaneous fit of all 6 physics observables.

	$\mathcal{BR}(\pi\pi)$	$\mathcal{BR}(K\pi)$	$\mathcal{BR}(KK)$	$\mathcal{A}_{CP}(\pi\pi)$	$\mathcal{S}_{CP}(\pi\pi)$	$\mathcal{A}_{CP}(K\pi)$
$\mathcal{BR}(\pi\pi)$	1					
$\mathcal{BR}(K\pi)$	-0.093	1				
$\mathcal{BR}(KK)$	+0.009	-0.063	1			
$\mathcal{A}_{CP}(\pi\pi)$	-0.058	+0.017	-0.001	1		
$\mathcal{S}_{CP}(\pi\pi)$	+0.034	-0.010	+0.001	+0.095	1	
$\mathcal{A}_{CP}(K\pi)$	-0.003	+0.006	-0.003	-0.041	-0.000	1

6.1.2 Comparison with previous Results

At the Belle experiment, the branching ratios and the CP parameters have been measured before with a data set of 532 million $B\bar{B}$ pairs. The results are summarized in section 2.9. For better comparison, we again divided the full data set into a first part of 532 million $B\bar{B}$ pairs and a second part containing the remaining 237 million $B\bar{B}$ pairs. In the following, the first part is going to be called partial box and the second part, the new data set. With our analysis, we obtain the values shown in table 6.6 from the partial box measurement. In addition we provide the signal enhanced Δt plot, showing the results from our fit on the partial box data in Fig. 6.9. We observe a difference in the branching ratio measurement

Table 6.6: Physics results from the partial box opening of 535×10^6 $B\bar{B}$ -pairs.

Observable	Value $\times 10^6$	stat. error
$\mathcal{BR}(\pi^+\pi^-)$	5.57	0.18
$\mathcal{BR}(K\pi)$	18.43	0.29
$\mathcal{BR}(K^+K^-)$	0.077	0.06
$\mathcal{A}_{CP}(\pi^+\pi^-)$	0.47	0.07
$\mathcal{S}_{CP}(\pi^+\pi^-)$	-0.63	0.08
$\mathcal{A}_{CP}(K\pi)$	-0.073	0.016

of $\mathcal{BR}(\pi^+\pi^-)$ and $\mathcal{BR}(K\pi)$ with respect to the previous measurement. Judging from the numbers, it seems to be a migration of $K\pi$ events to $\pi^+\pi^-$ events. The CP parameters are in agreement within the statistical errors. Now we performed a separate fit of the new data set and found the results given in table 6.7. We can clearly see that the difference in the CP parameters shows a downward fluctuation in the new data set. Fig. 6.10 shows the signal

enhanced projections of the Δt dimension for the last 237×10^6 $B\bar{B}$ pairs. An independent Belle analysis [73] is observing the same down fluctuation in the CP parameters in this last data set. This independent analysis is using cuts on the Kaon-Pion Likelihood ratio to obtain the data sample which is then used in a three dimensional maximum likelihood fit. The branching ratios are unchanged in the old and new dataset within the statistical errors. To estimate the probability for a statistical fluctuation of $\mathcal{A}_{CP}(\pi^+\pi^-)$ and $\mathcal{S}_{CP}(\pi^+\pi^-)$, the

Table 6.7: *Physics results from the last 237×10^6 $B\bar{B}$ -pairs taken at Belle. This is the data set that has not been analysed in previous analyses*

Observable	Value $\times 10^6$	stat. error
$\mathcal{BR}(\pi^+\pi^-)$	5.82	0.28
$\mathcal{BR}(K\pi)$	19.41	0.45
$\mathcal{BR}(K^+K^-)$	-0.12	0.078
$\mathcal{A}_{CP}(\pi^+\pi^-)$	0.058	0.10
$\mathcal{S}_{CP}(\pi^+\pi^-)$	-0.62	0.13
$\mathcal{A}_{CP}(K\pi)$	-0.034	0.023

data set was divided into the first 535×10^6 $B\bar{B}$ -pairs and the last 237×10^6 $B\bar{B}$ -pairs. We performed Toy-Monte-Carlo experiments with the central values obtained from the full data set. The values obtained from the previous analyses we marked with arrows. The previous analysis used data with a different track reconstruction procedure, called case A. This analysis uses data processed with an improved track reconstruction procedure, called case B. For better comparability with the previous analysis we colour coded the expectations from case A data and case B data with blue and red respectively. We obtain the probabilities for statistical fluctuations shown in table 6.8. The corresponding plots are

Table 6.8: *Chances for statistical fluctuation of the $\mathcal{A}_{CP}(\pi^+\pi^-)$ value in various data sets.*

Dataset	quantity	probability
535×10^6 case B	$\mathcal{A}_{CP} = +0.47$	3.2%
535×10^6 case A	$\mathcal{A}_{CP} = +0.55$	0.1%
237×10^6 case B	$\mathcal{A}_{CP} = +0.058$	0.47%

shown in Figs. 6.1 6.2.

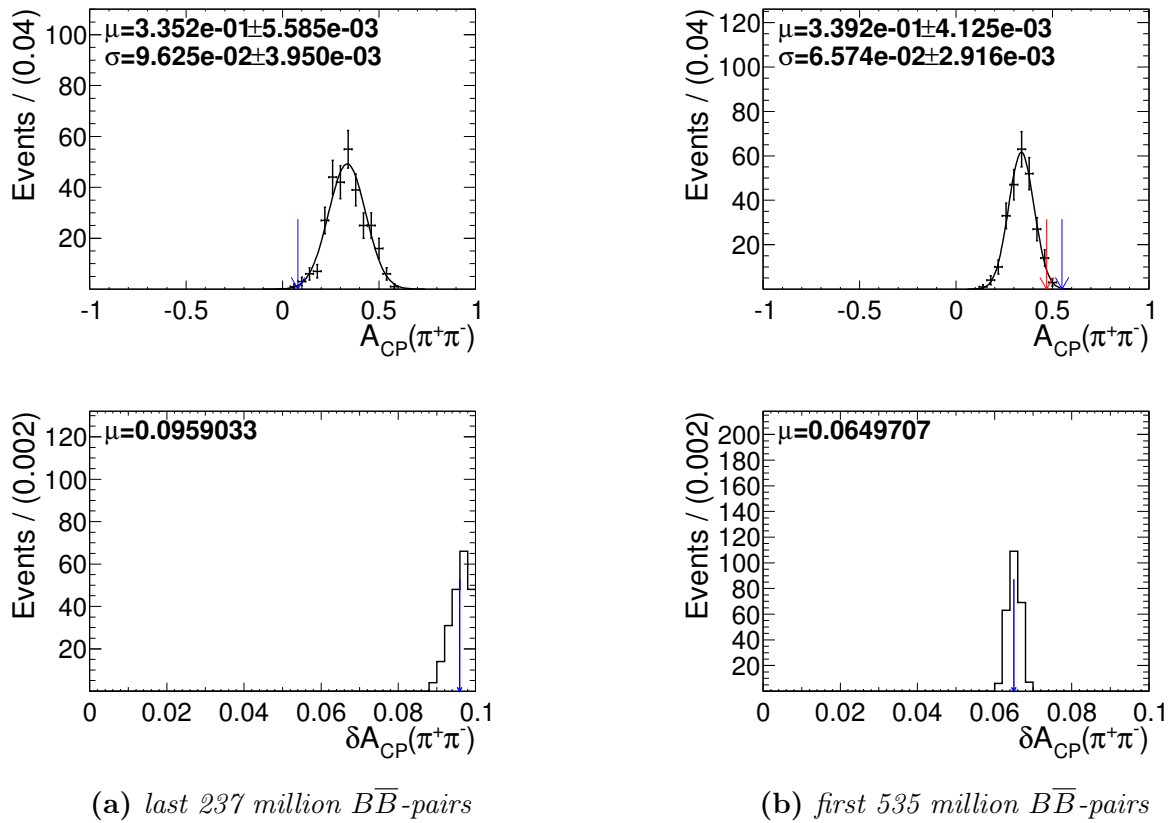


Figure 6.1: Distribution of $\mathcal{A}_{CP}(\pi^+\pi^-)$ (top) and its error (bottom) from Toy-Monte-Carlo studies in the first 535 million (b) and the remaining 237 (a) million $B\bar{B}$ pairs. The blue arrow denotes expectations from case A while the red arrow denotes expectations from case B.

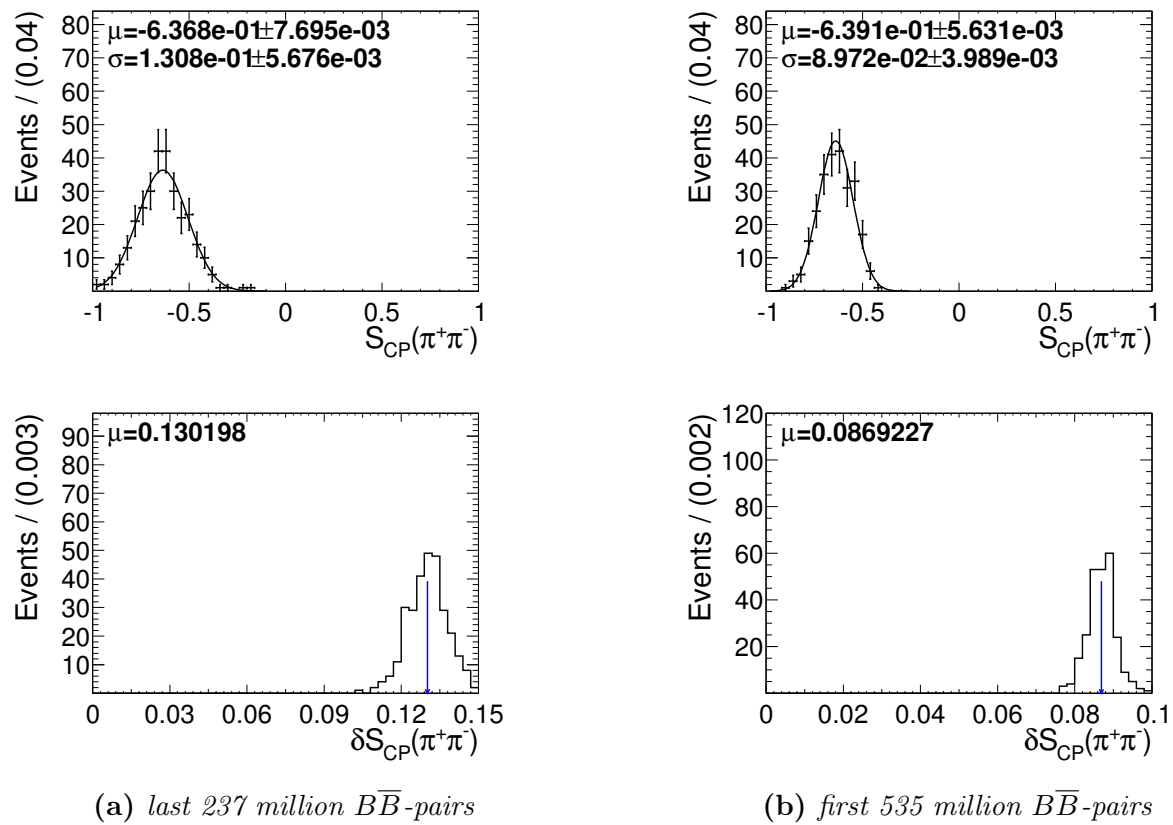


Figure 6.2: Distribution of $\mathcal{A}_{CP}(\pi^+\pi^-)$ (top) and its error (bottom) from Toy-Monte-Carlo studies in the first 535 million (b) and the remaining 237 (a) million $B\bar{B}$ pairs. The blue arrow denotes the expected values from the full dataset.

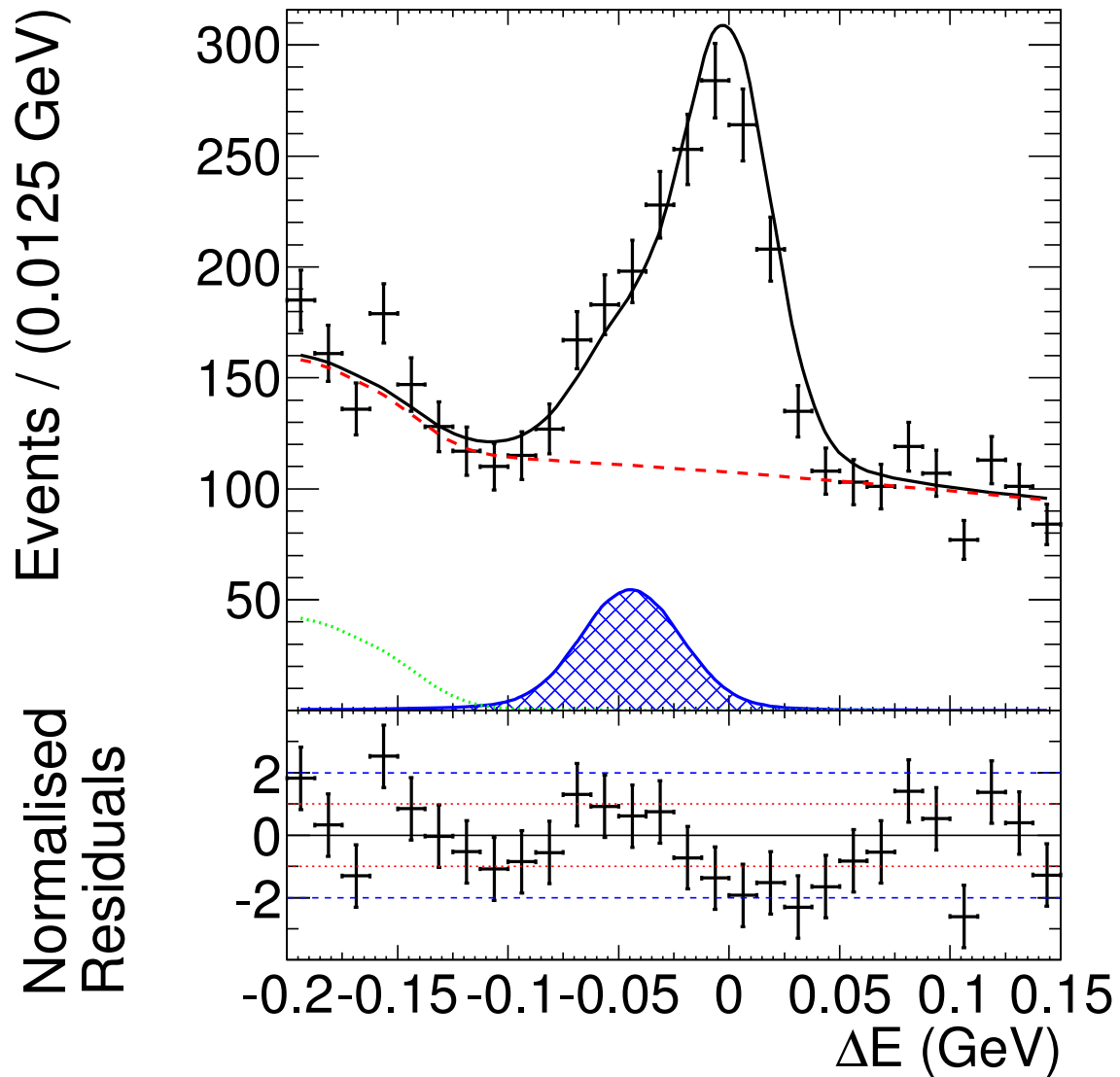


Figure 6.3: ΔE distribution of the $\pi^+ \pi^-$ signal enhanced data from the full Belle data set. Black crosses denote the data; the total PDF is shown as a black solid line. The total background is the red dashed line, containing the background from charmless B decays displayed as green dotted line. The blue hashed area is the contribution from the peaking background of $B^0 \rightarrow K^+\pi^-$ decays.

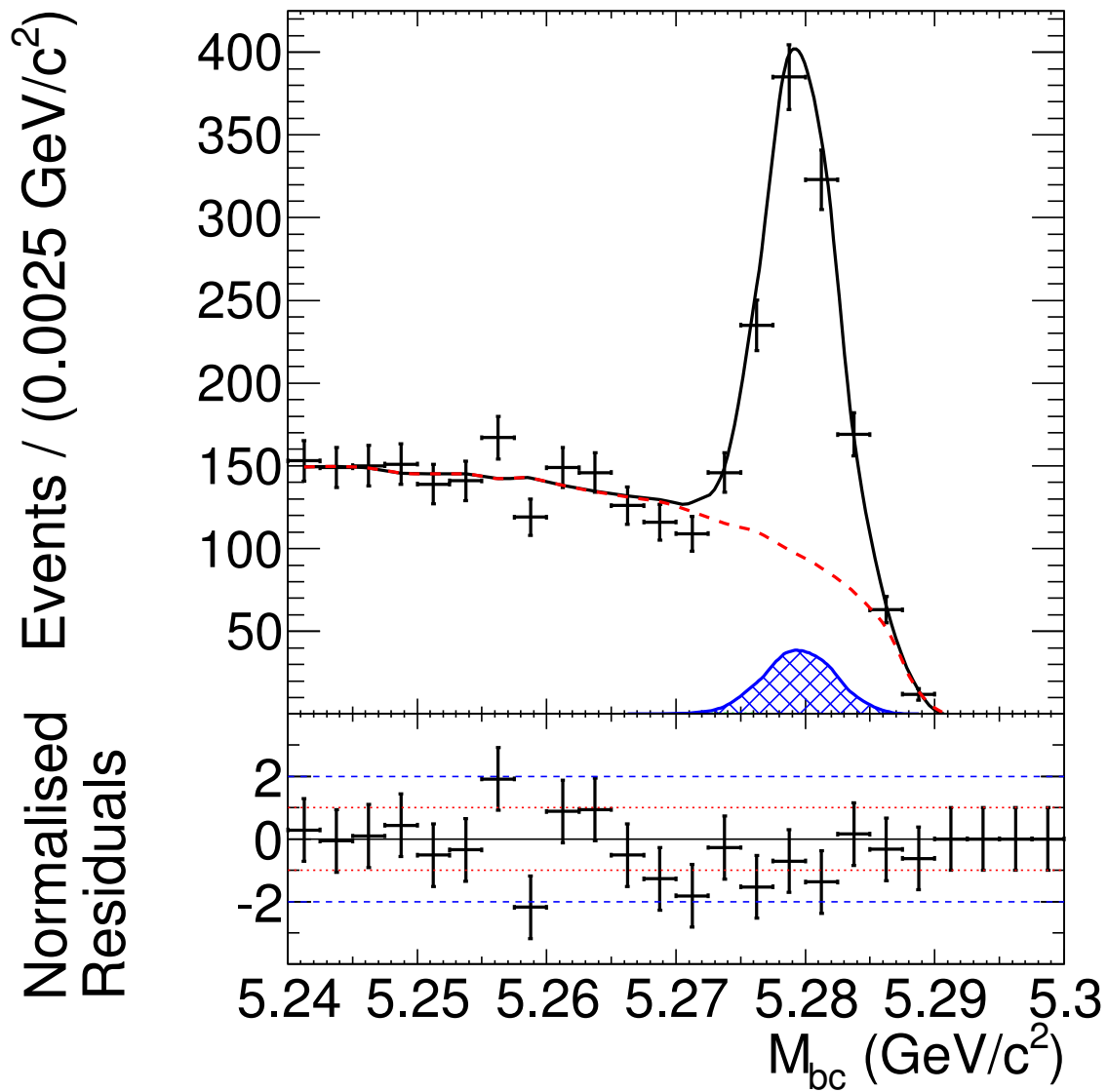


Figure 6.4: M_{BC} distribution of the $\pi^+ \pi^-$ signal enhanced data from the full Belle data set. Black crosses denote the data; the total PDF is shown as a black solid line. The total background is the red dashed line. The blue hashed area is the contribution from the peaking background of $B^0 \rightarrow K^+\pi^-$ decays.

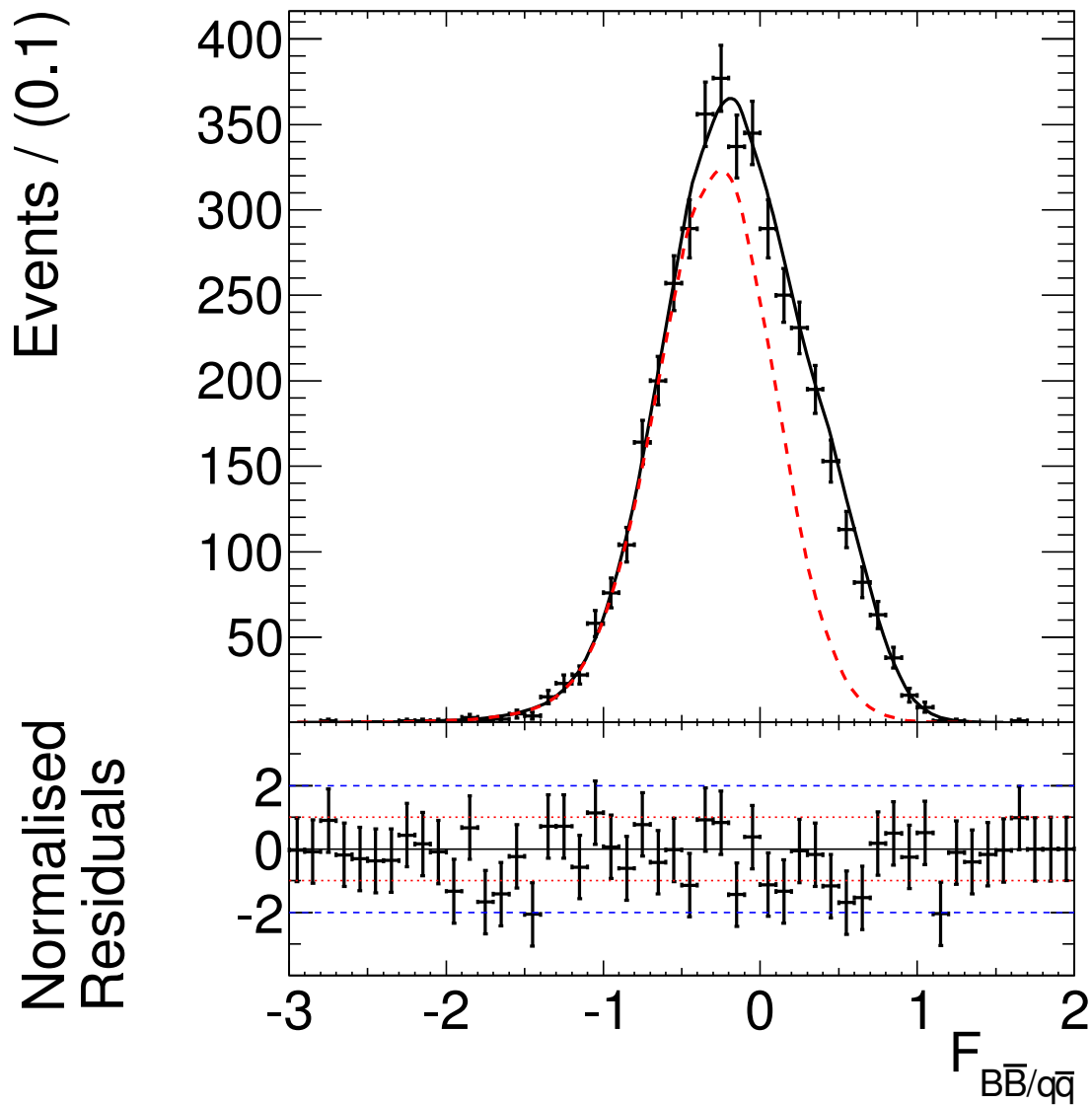


Figure 6.5: $\mathcal{F}_{S/B}$ distribution of the $\pi^+ \pi^-$ signal enhanced data from the full Belle data set. Black crosses denote the data; the total PDF is shown as a black solid line. The total background is the red dashed line. The blue hashed area is the contribution from the peaking background of $B^0 \rightarrow K^+\pi^-$ decays.

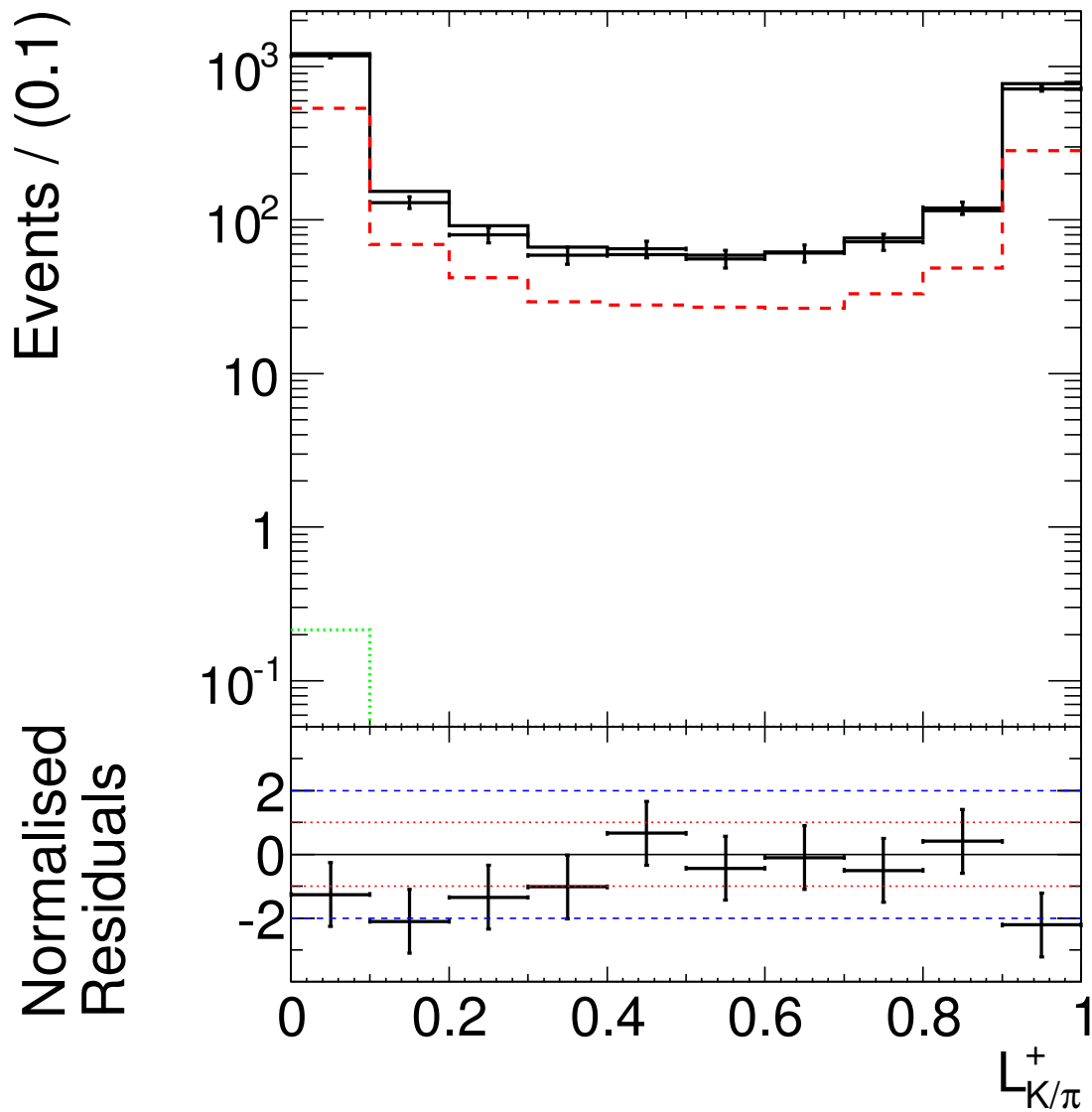


Figure 6.6: $\mathcal{L}_{K/\pi}^+$ distribution of the $\pi^+ \pi^-$ signal enhanced data from the full Belle data set. Black crosses denote the data; the total PDF is shown as a black solid line. The total background is the red dashed line, containing the background from charmless B decays displayed as green dotted line.

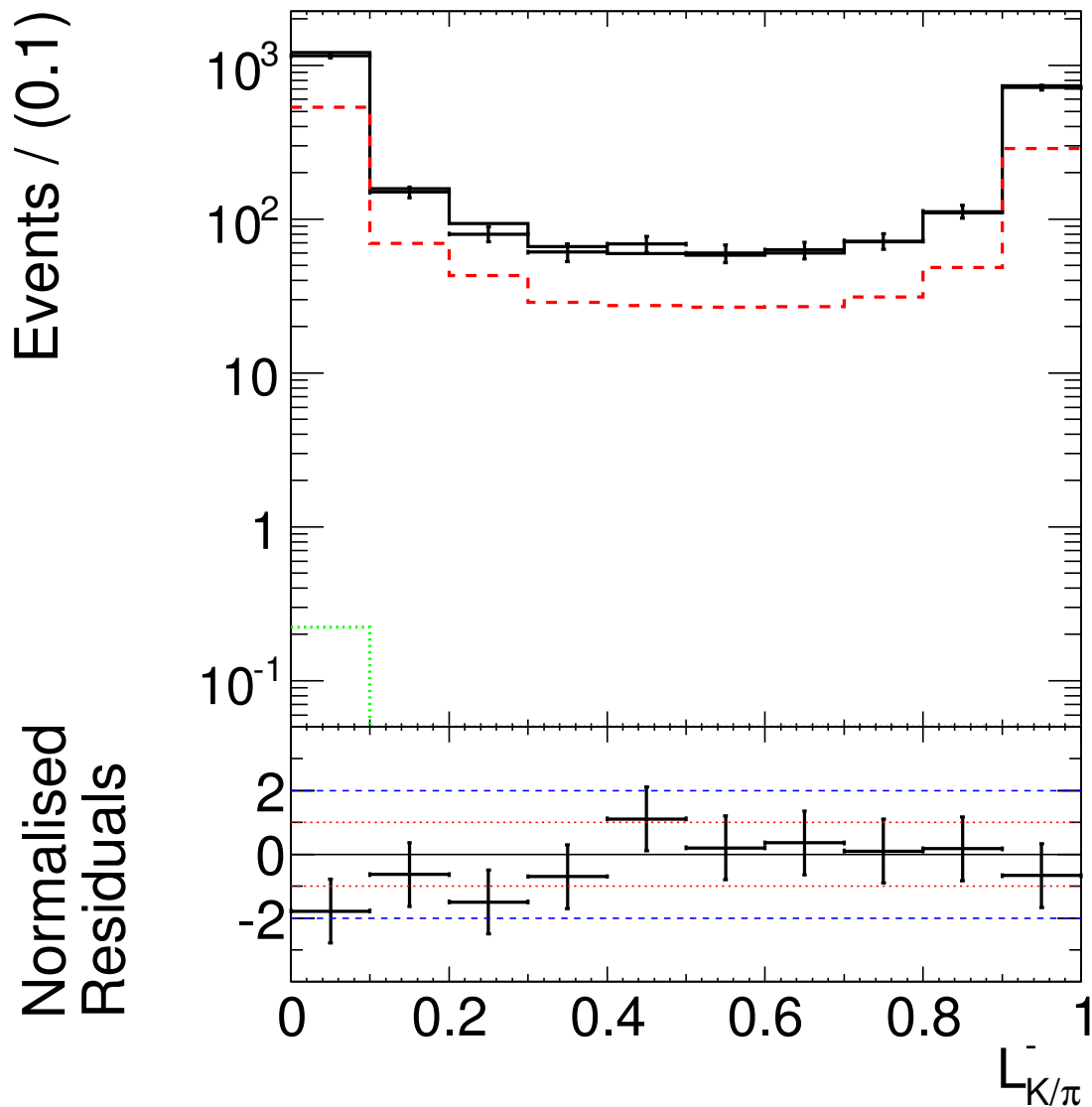


Figure 6.7: $L_{K/\pi}^-$ distribution of the $\pi^+ \pi^-$ signal enhanced data from the full Belle data set. Black crosses denote the data; the total PDF is shown as a black solid line. The total background is the red dashed line, containing the background from charmless B decays displayed as green dotted line.

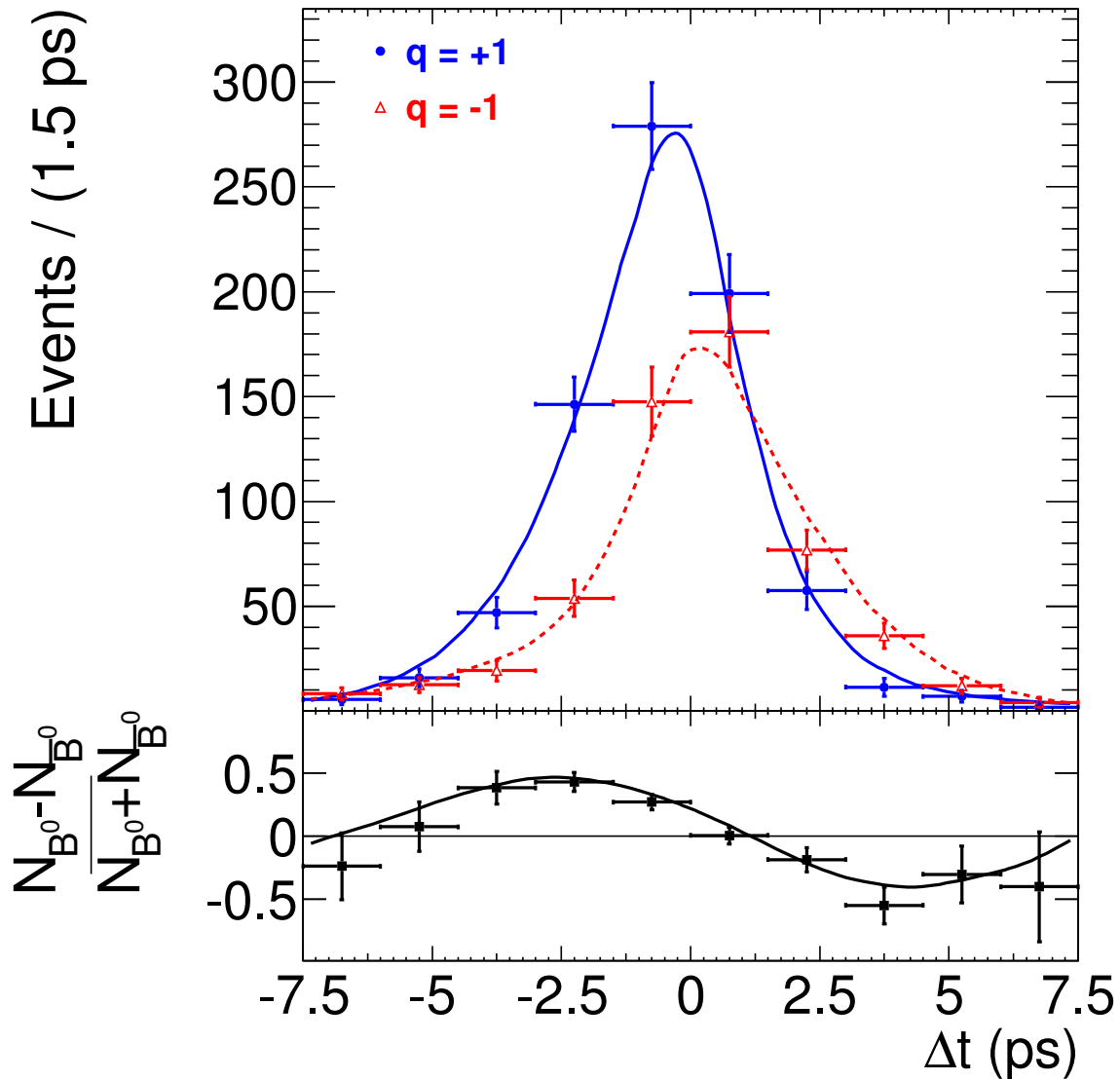


Figure 6.8: Δt distribution of the $\pi^+\pi^-$ signal enhanced data from the full Belle data set. The blue points correspond to data with a B_{tag} identified as B^0 , the red triangles correspond to data with a B_{tag} identified as \bar{B}^0 . The solid lines show the PDF for the given class of events. The time-dependent asymmetry is shown in the lower part of the plot.

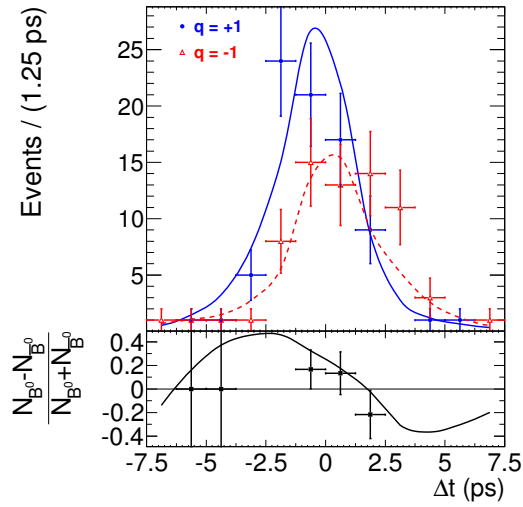


Figure 6.9: Δt distribution of the $\pi^+\pi^-$ signal enhanced data from the data set of the previous analysis of 535 million $B\bar{B}$ pairs. The blue points correspond to data with a B_{tag} identified as B^0 , the red triangles correspond to data with a B_{tag} identified as \bar{B}^0 . The solid lines show the PDF for the given class of events. The time-dependent asymmetry is shown in the lower part of the plot.

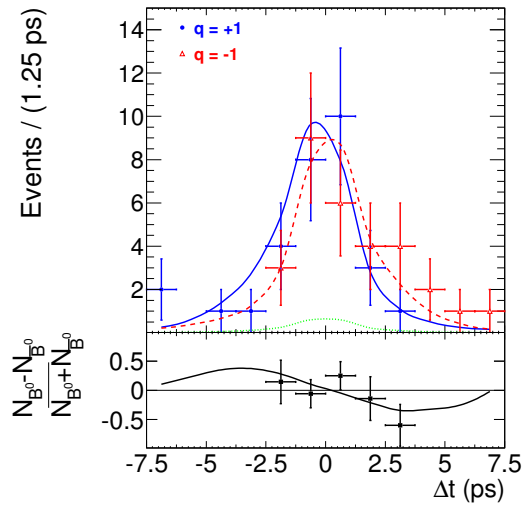


Figure 6.10: Δt distribution of the $\pi^+\pi^-$ signal enhanced data from the new data set of the latest 237 million $B\bar{B}$ pairs. The blue points correspond to data with a B_{tag} identified as B^0 , the red triangles correspond to data with a B_{tag} identified as \bar{B}^0 . The solid lines show the PDF for the given class of events. The green dotted line is the contribution from backgrounds. The time-dependent asymmetry is shown in the lower part of the plot.

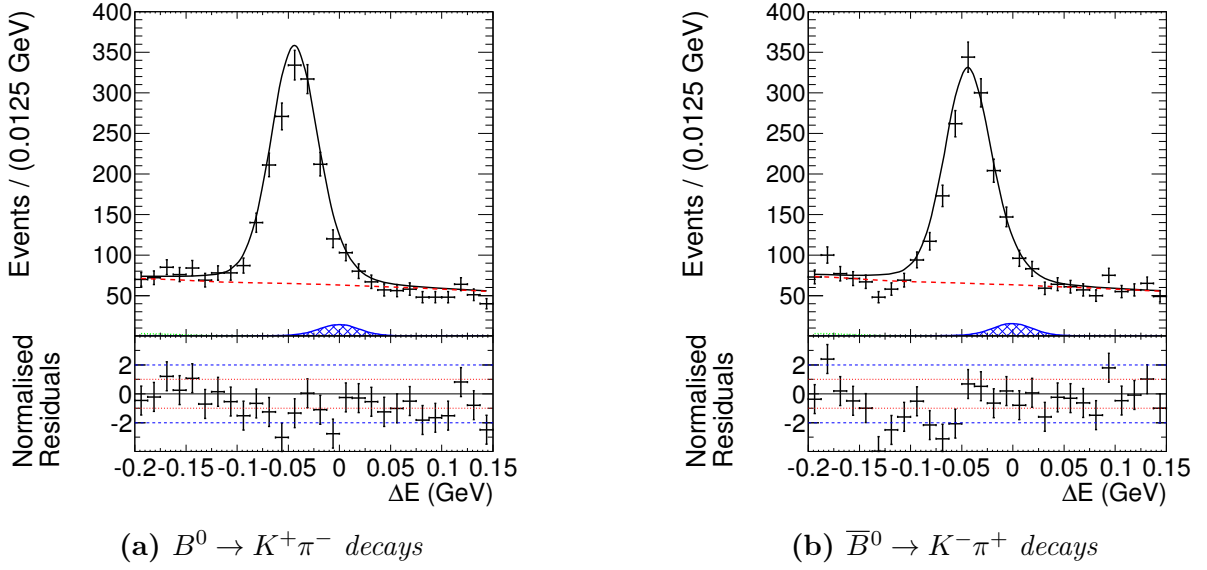


Figure 6.11: ΔE distribution of the $K^+\pi^-$ signal enhanced data from the full Belle data set. Data is shown as black crosses; the total PDF is the solid black line; the total background is the red dashed line which includes the contribution from charmless B decays in green. The hashed blue area is the peaking background contribution from the decay $B^0 \rightarrow \pi^+\pi^-$.

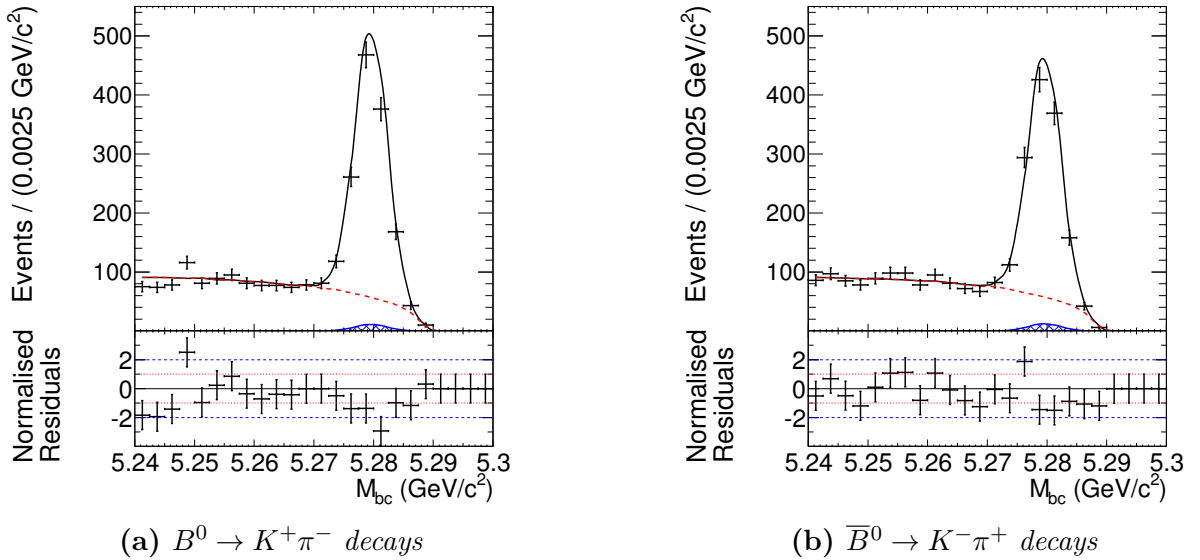


Figure 6.12: M_{BC} distribution of the $K^+\pi^-$ signal enhanced data from the full Belle data set. Data is shown as black crosses; the total PDF is the solid black line. The hashed blue area is the peaking background contribution from the decay $B^0 \rightarrow \pi^+\pi^-$.

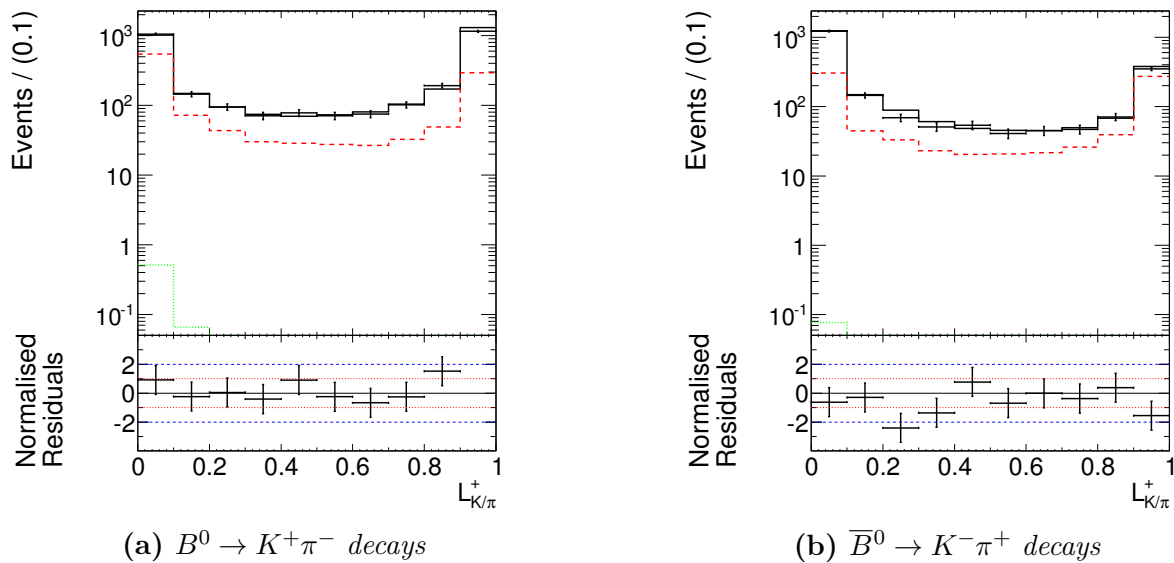


Figure 6.13: $\mathcal{L}_{K/\pi}^+$ distribution of the $K^+\pi^-$ signal enhanced data from the full Belle data set. Data as black crosses; the total PDF as solid black line; the total background is the red dashed line which includes the contribution from charmless B decays in green. The hashed blue area is the peaking background contribution from the decay $B^0 \rightarrow \pi^+\pi^-$.

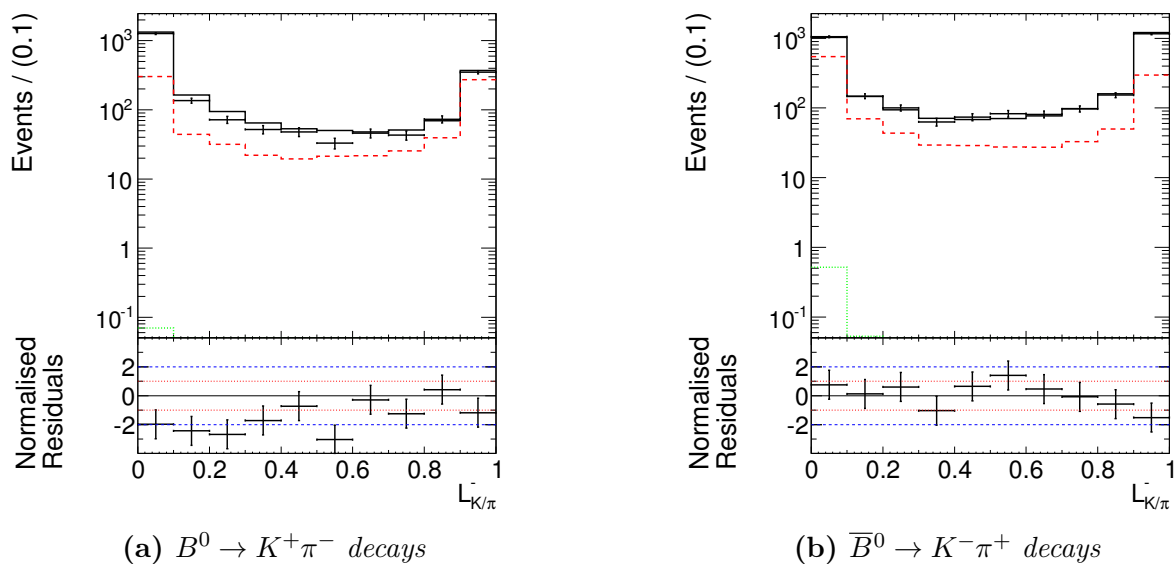


Figure 6.14: $\mathcal{L}_{K/\pi}^-$ distribution of the $K^+\pi^-$ signal enhanced data from the full Belle data set. Data as black crosses; the total PDF as solid black line; the total background is the red dashed line which includes the contribution from charmless B decays in green. The hashed blue area is the peaking background contribution from the decay $B^0 \rightarrow \pi^+\pi^-$.

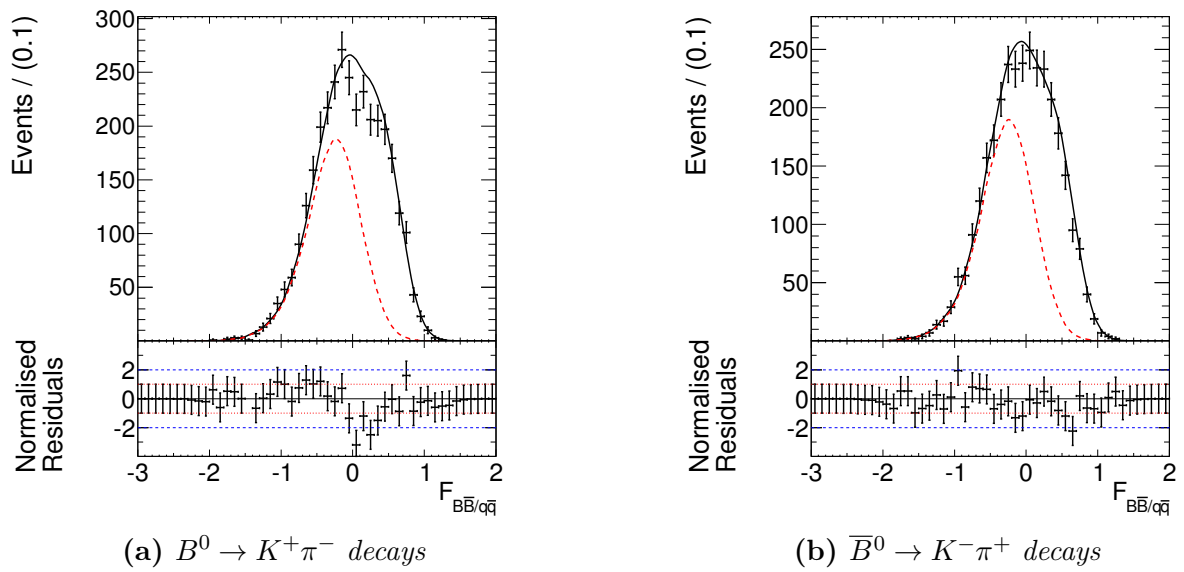


Figure 6.15: $\mathcal{F}_{S/B}$ distribution of the $K^+\pi^-$ signal enhanced data from the full Belle data set. Data is shown as black crosses; the total PDF is the solid black line; the total background is the red dashed line. The hashed blue area is the peaking background contribution from the decay $B^0 \rightarrow \pi^+\pi^-$.

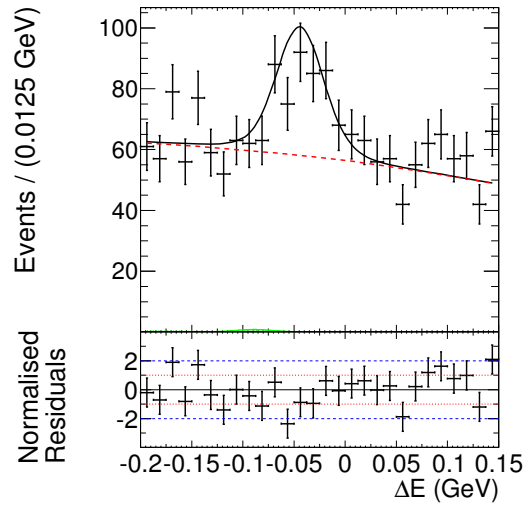


Figure 6.16: ΔE distribution of the K^+K^- signal enhanced data from the full Belle data set. Data is shown as black crosses; the total PDF is the solid black line; the total background is the red dashed line. The green solid line is the signal component from the $B^0 \rightarrow K^+K^-$ decay.

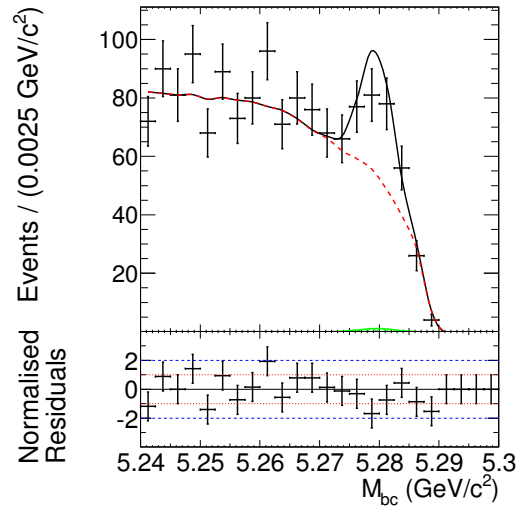


Figure 6.17: M_{BC} distribution of the K^+K^- signal enhanced data from the full Belle data set. Data is shown as black crosses; the total PDF is the solid black line; the total background is the red dashed line. The green solid line is the signal component from the $B^0 \rightarrow K^+K^-$ decay.

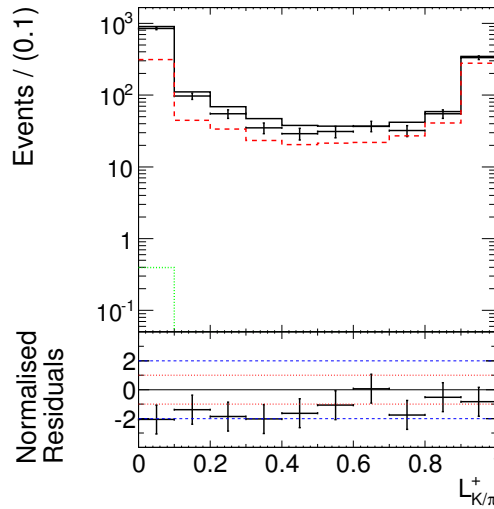


Figure 6.18: $\mathcal{L}_{K/\pi}^+$ distribution of the K^+K^- signal enhanced data from the full Belle data set. Data is shown as black crosses; the total PDF is the solid black line; the total background is the red dashed line including the background from charmless B decays displayed as green dashed line.

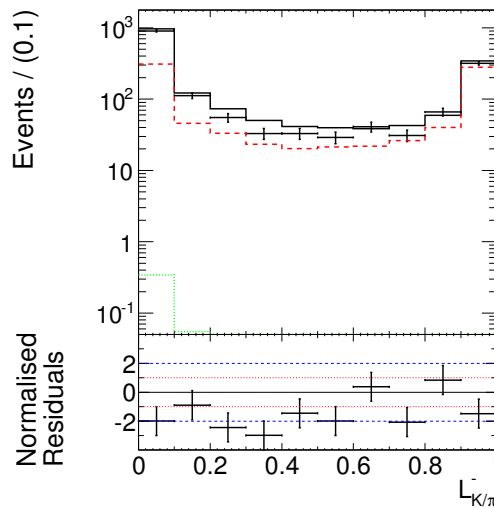


Figure 6.19: $\mathcal{L}_{K/\pi}^-$ distribution of the K^+K^- signal enhanced data from the full Belle data set. Data is shown as black crosses; the total PDF is the solid black line; the total background is the red dashed line including the background from charmless B decays displayed as green dashed line.

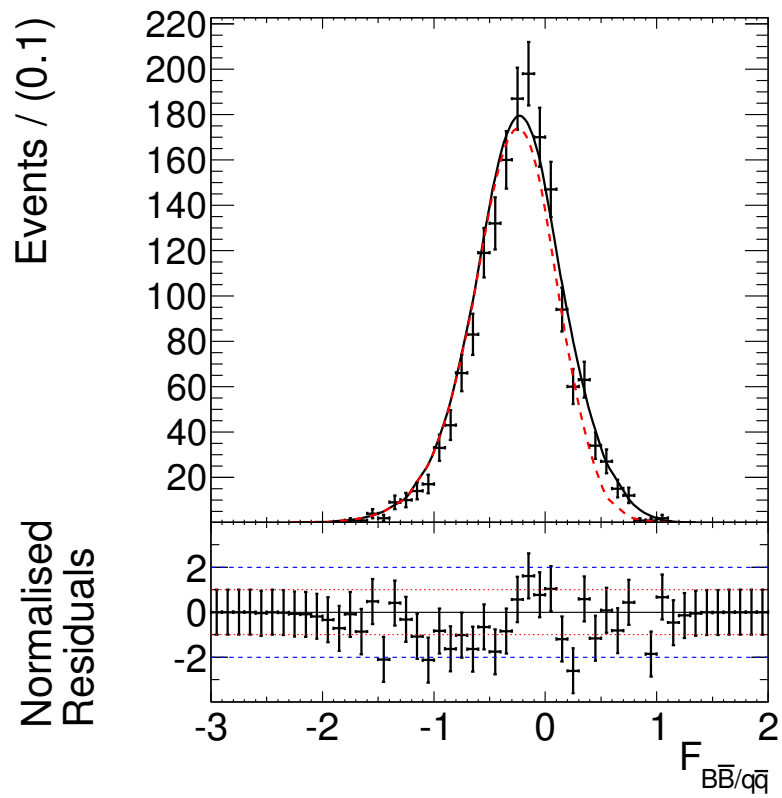


Figure 6.20: $\mathcal{F}_{S/B}$ distribution of the K^+K^- signal enhanced data from the full Belle data set. Data is shown as black crosses; the total PDF is the solid black line; the total background is the red dashed line.

6.2 Estimation of Systematic Uncertainties

To carefully estimate the systematic errors, we are closely following the procedures that have been established in the Belle collaboration. For those cases where we introduced new analysis methods, e.g. the particle identification histogram corrections (see section 5.2), we devote more time in the discussion of the calculations performed to evaluate the systematic uncertainty. Many procedures are standard procedures performed at the Belle experiment. This chapter explains all the contributions to the systematic error of both the branching fractions and the CP parameters. In a final section, a table of all the contributions to the systematic uncertainty are presented and we are discussing the relative size of them.

6.2.1 Number of $B\bar{B}$ pairs

The determination of the number of $B\bar{B}$ pairs is done directly with the Belle detector. Basically it is determined from the increase in the cross section when recording data 80 MeV below the $\Upsilon(4S)$ resonance (off-resonance) from on the $\Upsilon(4S)$ resonance (on-resonance).

$$N(B\bar{B}) = N(\text{on}) - acN(\text{off}) \quad (6.1)$$

The ratio c , of efficiency for recording background $q\bar{q}$ events in an on and off-resonance sample is determined from Monte-Carlo. The scale factor a , for on and off-resonance $q\bar{q}$ background is calculated from Bhabha pairs and muon pairs from data. Systematics are determined globally for the final data set of Belle. The procedure is described elsewhere [74].

6.2.2 Tracking Systematics

The tracking systematics is an uncertainty that effects the efficiency of the reconstruction. Depending on the momentum of a particle track, there is an uncertainty that a track is found or not. This uncertainty is 0.35% for a particle track with a momentum higher than 200 MeV. For the two body decay of our channel $B \rightarrow hh$, the particles always have more than 200 MeV. Nevertheless we estimated the average tracking systematic on a per event basis on the Monte-Carlo sample which we used for the calculation of the reconstruction efficiency. The resulting systematic error is 0.7% of the resulting branching fraction for all channels.

6.2.3 IP Profile

In the reconstruction of the event, we are performing a beam tube constrained fit on the z -vertex of the CP side and tag side B meson. The beam tube constrained fit is explained in

more detail in Sec. 4.3.3, but basically it is a vertex fit which constrains the tracks to come from a common vertex lying on the interaction point but being free in the z direction. The IP or beam spot, however, is defined as an ellipsoid with a central point and uncertainties giving the size of the principal axes. In the $r - \phi$ plane the IP ellipsoid has a uncertainty of $21 \mu\text{m}$. By varying the uncertainty by $\pm 10 \mu\text{m}$, we are accounting for the finite lifetime of the B meson.

6.2.4 Selection Criteria of the B -tagging Algorithm

Once the reconstruction of the CP side B meson is done, we run the tagging algorithm on the event. The tagging algorithm tries to extract the information about the flavour and vertex of the other B meson which is sometimes named the tag B meson. Therefore a set of selection criteria depending on decay vertex of the CP side B meson is used to remove tracks with poor z -position measurements. The selection criteria in the z direction are $\sigma_z < 0.5 \text{ mm}$ and $dr < 0.5 \text{ mm}$ in the $r - \phi$ plane. The effect on the physics results is investigated by a variation of $\pm 10\%$ of the selection criteria.

6.2.5 Track Helix Error

The tracking which is done in the full simulation of the Belle detector is taking many detector effects into account. But it is still a simplification of the real detector. Therefore the resolution of the helix parameters is too optimistic. Correct errors for the tracks are obtained by studying cosmic ray data. During the simulation, the track helix errors are scaled up. To estimate the systematic uncertainty coming from this procedure, we are performing the reconstruction with and without the error scaling applied and compare the results.

6.2.6 Δt Selection

During the reconstruction, we are applying a cut on the Δt variable to veto cosmic particles or misreconstructed tracks ($|\Delta t| < 70 \text{ ps}$). By varying the cuts by $\pm 30 \text{ ps}$ we evaluate the impact of the selection criterion.

6.2.7 Vertex Quality

Since the vertex fit of the CP side and tag side is crucial to the Δt measurement, we are estimating systematic effects due to the quality of the fit. Therefore we vary the selection criteria, $h < 50$ and the $z_{\text{err}} < 200(500) \mu\text{m}$ of the multi (single) track vertices. The selection

of the fit quality h , is varied by ${}_{-25}^{+50}$ and z_{err} is varied by $\pm 100 \mu\text{m}$. The impact on the fit result with respect to the nominal fit result is taken as a systematic uncertainty.

6.2.8 Δz Bias

The Δz bias is observed due to intrinsic detector effects and misalignment between SVD and CDC and many other sources. Moreover, it directly affects the extraction of the time-dependent CP parameters. We can use the golden channel $B^0 \rightarrow J/\psi K_S^0$ to measure the bias of the Δz distribution. The bias is depending on charge, momentum and the angle of the track. Because it is thought to be independent of the decay channel, the systematic uncertainty study is taken from the golden channel.

6.2.9 Misalignment

The effects of not perfectly aligned silicon and gas detectors has a big impact on tracking. Although alignment of the detector is performed and taken into account, we still have uncertainties. In addition, the alignment can change during the data taking. To study the effect of a misaligned detector on the physics quantities, we use a special Monte-Carlo data set which is misaligned intentionally.

6.2.10 Physics Parameters

In the models for the Δt PDFs, we are using parameters like the lifetime τ_{B^0} , of the B meson or the mass difference Δm_d , between the heavy and light eigenstates of the B meson. These parameters are not measured in this analysis. Therefore we are using the current world averages from the particle data group [4]. By changing these parameters by their error we study the effect of these uncertainties on our results.

6.2.11 Data/MC Shape

For the signal components, we determine the systematic error due to imperfections of the model. Therefore all parameters that are obtained from Monte-Carlo or the control channel are varied according to their uncertainties. For the histogram of $\mathcal{L}_{K/\pi}^+$ and $\mathcal{L}_{K/\pi}^-$, we are using a different approach. The procedure of correcting this PID histogram bin-wise is explained in Sec. 5.2 in more detail. If one looks at Fig. 5.17 in that section, one can see how the efficiency correction parameters ascend and reach unity in the last bin. To incorporate the uncertainty of this procedure in our systematic error estimation, we are assuming, depending on the error of the first bin ($\mathcal{L}_{K/\pi}^+ = 0 \wedge \mathcal{L}_{K/\pi}^- = 0$), two different sloped planes. To incorporate effects that act differently depending on the charge of the particle,

we repeat this procedure for the two bins, $\mathcal{L}_{K/\pi}^+ = 1 \wedge \mathcal{L}_{K/\pi}^- = 0$ and $\mathcal{L}_{K/\pi}^+ = 0 \wedge \mathcal{L}_{K/\pi}^- = 1$. This change is propagated back into our PDF. With these changed PDFs, we are refitting the data and calculate the difference of the fit results with the nominal fit result. These differences are added in quadrature to determine the systematic error coming from the PID correction procedure.

6.2.12 Δt Resolution Function

The detector resolution function is depending on parameters that are obtained from Monte-Carlo and Data. These parameters are varied within 1σ or 2σ depending on whether the parameters are obtained from data or from Monte-Carlo. The change of our measurement results is a direct measure for the systematic uncertainty due to the determination of the detector resolution function.

6.2.13 Flavour Tagging

In the time-dependent part of our analysis, we are using the data binned in the B -tag quality r . Within these bins, the fractions of wrongly tagged events w , and the wrong tag fraction difference between B^0 and \bar{B}^0 , Δw , is determined. The error of this method is determined by the Belle flavour tagging group [69]. We are varying the wrong tag fractions according the errors and determine this way the impact on the physics results.

6.2.14 Parametric Shape

In this analysis we try to use analytical functions everywhere possible in the background model to describe the background shapes. We determine the parameters of these analytical function PDFs by fitting a Monte-Carlo set or off-resonance data. The maximum Likelihood method does not only provide us with the central value for our model parameters but also yields an uncertainty on every parameter. To determine the systematic error due to the determination of the model parameters, we vary the parameters of the PDFs by their errors and repeat the fit to data. The uncertainties on the results are given by the difference to the nominal fit results. The total systematic error on the parametric shape is calculated by adding up the uncertainties of all fits in quadrature.

6.2.15 Non-parametric Shape

In all background models, we describe some dimensions of the PDF by histograms. For example, the ΔE and M_{BC} PDFs for the rare decays of neutral and charged B mesons are described by histograms. These histograms are created from a Monte-Carlo data set

that corresponds to 50 times the luminosity of the Belle experiment. For the continuum model, data taken slightly below the $\Upsilon(4S)$ resonance (off-resonance) with statistics of approximately 1/10 of the on-resonance dataset is used. An uncertainty can be assigned to every bin due to the statistical Poisson distribution of the events in our counting experiment. In analogy to the parametric shapes, we vary every bin by its error and refit our data. The differences of our fitting results with the nominal fit result are added in quadrature and are our measure of the uncertainty due our choice of a histogram PDF. For the histogram of $\mathcal{L}_{K/\pi}^+$ and $\mathcal{L}_{K/\pi}^-$ determined from Monte-Carlo, we are using a different approach. The procedure of correcting this PID histogram bin-wise is explained in Sec. 5.2 in more detail. Fig. 5.17 in that section shows how the efficiency correction parameters ascend and reach unity in the last bin. To incorporate the uncertainty of this procedure in our systematic error estimation, we are assuming, depending on the error of the first bin ($\mathcal{L}_{K/\pi}^+ = 0 \wedge \mathcal{L}_{K/\pi}^- = 0$), two different sloped planes. To incorporate effects which act differently depending on the charge of the particle, we repeat this procedure for the two bins $\mathcal{L}_{K/\pi}^+ = 1 \wedge \mathcal{L}_{K/\pi}^- = 0$ and $\mathcal{L}_{K/\pi}^+ = 0 \wedge \mathcal{L}_{K/\pi}^- = 1$. This change is propagated back into our PDF. With these changed PDF we are refitting the data and calculate the difference of the fit results with the nominal fit result. These differences are added in quadrature to determine the systematic error coming from the PID correction procedure.

6.2.16 Fit Bias

To determine the fit bias of our model, we performed Toy-Monte-Carlo ensemble tests (see Sec. 4.6). Using events from full simulation, we showed that we are expecting biased results due to imperfections of our parametric description of the Monte-Carlo. These biases can, in principal, be determined with arbitrary precision. One, however, cannot know if the bias is the same on data as it is on Monte-Carlo. Therefore we are using the following method to determine a systematic error for this fitting bias. Our systematic error calculation is based on the assumption that a small bias or no bias is a hint for a good PDF description of the Monte-Carlo and therefore also deserves the assignment of a small error. We are confident in the source of the fit bias being the parametric description of the PDF and the neglecting of some correlations. We do not correct the fit bias and assign the full bias as systematic uncertainty.

6.2.17 Tag-side Interference

The B -tagging algorithm tries to identify the flavour of a B meson by identifying the charges of the decay products. For example, one observes the decay of $\overline{B}^0 \rightarrow D^+\pi^-$ on the tag-side where the D^+ decays into $K^-\pi^+\pi^+$. This decay would be usually associated with a \overline{B}^0 meson. But the same final state can be reached through a $\overline{b} \rightarrow \overline{u}c\overline{d}$ transition. The probability for the later process is in the order of a few percent of the dominant decay

amplitude. Long *et al.* [75] propose a procedure of how to estimate the uncertainties that come from neglecting the tag-side interferences.

6.2.18 Discussion of the Contributions of the total Systematic Error

After performing all the studies that were mentioned in the previous sections, we obtain the full table of systematic uncertainties for our 6 physics observables (Table 6.9). Every physics observable measurement is dominated by one or more systematic errors. In the following, we want to discuss this for every observable.

The measurement of the branching ratio of $\pi^+ \pi^-$ is dominated by the fit bias. This fit bias is discussed in Sec. 4.6. In future analyses, we suggest to further increase the number of correlations that are modelled in the PDFs. The second biggest contribution the systematic errors is the error on the measurement of the number of $B \bar{B}$ pairs.

The systematic uncertainty on the branching ratio of the decay $B^0 \rightarrow K\pi$ is dominated by the number of $B \bar{B}$ pairs.

The search for the decay $B^0 \rightarrow K^+K^-$ obtains its biggest systematic uncertainties from the PDF model shape that we use. Also, a noteworthy contribution comes from the Δt resolution function.

The CP parameters for the $\pi^+ \pi^-$ decay are dominated by different sources. For $\mathcal{A}_{CP}(\pi^+\pi^-)$, the tag-side interference is the largest contribution. For $\mathcal{S}_{CP}(\pi^+\pi^-)$, however, the systematic uncertainties originate mainly from the uncertainties on the Δt resolution function. Not surprisingly, the IP profile is a big contributor for the systematic error for the time-dependent quantity of $\mathcal{S}_{CP}(\pi^+\pi^-)$.

Finally the dominant systematic error by far for $\mathcal{A}_{CP}(K\pi)$, is the shape of the $\mathcal{L}_{K/\pi}^+ \mathcal{L}_{K/\pi}^-$ histogram obtained from off-resonance data.

In table 6.10, we are showing the absolute systematic error for every physics observable. The statistical error (see table 6.4) is also shown for comparison. The results including the correlations are also used by the Heavy Flavour Averaging Group (HFAG) to create a plot of the error ellipse for the various experiments including this analysis, denoted as Belle (Fig. 6.21). The new world average is shown in red.

Table 6.9: Contributions to the total systematic uncertainty by various effects. The systematic uncertainty for branching ratios are given in percent. The systematic uncertainties for the CP parameters are given as absolute errors in units of 10^{-2} .

Sys. error	$\mathcal{B}(\pi^+\pi^-)$ [%]	$\mathcal{B}(\pi K)$ [%]	$\mathcal{B}(K^+K^-)$ [%]	$\mathcal{A}_{CP}(\pi^+\pi^-)$ [10^{-2}]	$\mathcal{S}_{CP}(\pi^+\pi^-)$ [10^{-2}]	$\mathcal{A}_{CP}(\pi K)$ [10^{-2}]
NBB	1.23	1.23	1.23	N/A	N/A	N/A
Tracking	0.7	0.7	0.7	N/A	N/A	N/A
IP-profile	0.42	0.15	14.28	0.13	1.19	0.06
Btag selection	0.47	0.24	44.71	0.30	0.33	0.09
Track helix error	0.02	0.02	5.00	0.00	0.01	0.01
Dt selection	0.10	0.16	16.97	0.01	0.03	0.02
Vtx quality	0.63	0.39	33.47	0.37	0.23	0.13
Dz bias	N/A	N/A	N/A	0.5	0.4	N/A
Misalignment	N/A	N/A	N/A	0.4	0.2	N/A
Physics parameters	0.14	0.10	10.14	0.12	0.09	0.00
Data/MC shape	0.79	0.37	47.48	0.15	0.19	0.24
Dt resolution function	1.09	0.75	67.96	0.83	2.02	0.04
Flavour tagging	0.01	0.02	18.67	0.40	0.31	0.01
Parametric shape	0.90	0.50	69.53	0.15	0.28	0.01
Non-parametric shape	1.00	0.55	96.07	0.37	0.57	0.75
Fit bias	1.30	0.60	5.71	0.54	0.86	0.07
Tag-side interference	N/A	N/A	N/A	3.18	0.17	N/A
Total sys. error	2.86	1.97	158.30	3.48	2.68	0.81

Table 6.10: Summary of absolute systematic and statistical uncertainties on the physics observables.

Physics observable	Central value	statistical error	systematic error
$\mathcal{B}(\pi^+\pi^-)[10^{-6}]$	5.63	± 0.16	± 0.16
$\mathcal{B}(\pi K)[10^{-6}]$	18.71	± 0.25	± 0.37
$\mathcal{B}(K^+K^-)[10^{-6}]$	0.03	± 0.05	± 0.05
$\mathcal{A}_{CP}(\pi^+\pi^-)$	0.33	± 0.06	± 0.03
$\mathcal{S}_{CP}(\pi^+\pi^-)$	-0.64	± 0.08	± 0.03
$\mathcal{A}_{CP}(\pi K)$	-0.061	± 0.014	± 0.008

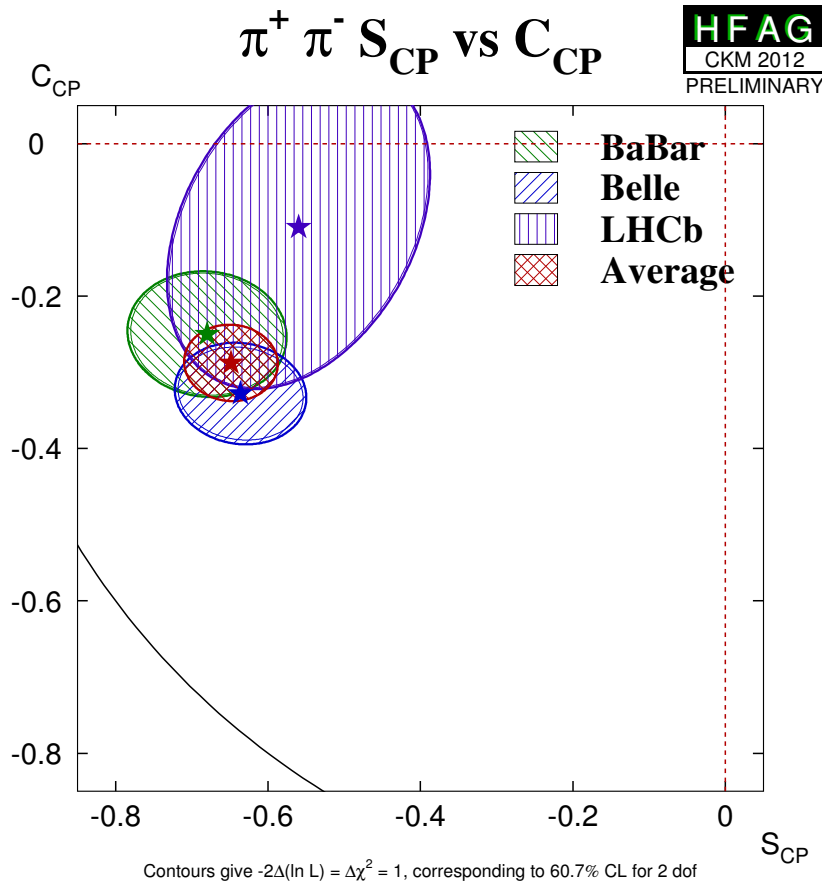


Figure 6.21: Direct CP violation vs. mixing induced CP violation parameters for the decay $B^0 \rightarrow \pi^+\pi^-$ determined from this analysis, BaBar and LHCb experiments [59]. This can be compared to the results from the previous measurement in Fig. 2.10. Other experiments use a different definition of the direct CP violation parameter $\mathcal{A}_{CP} = -C_{CP}$.

6.3 Upper Limit Calculation for $B^0 \rightarrow K^+K^-$

The branching ratio of the decay $B^0 \rightarrow K^+K^-$, was observed to be compatible with zero. As a consequence, we determined the upper limit bound for the branching ratio. We use the method of likelihood scans which yields a more accurate result. For the likelihood scan, we are fixing the branching ratio of K^+K^- in the range $0 \leq \mathcal{B}(K^+K^-) \leq 30 \times 10^{-8}$ in steps of 1×10^{-8} . At each fixed point, the other physics observables are floated and a new parameter set that maximizes the likelihood is determined. In practice, we are minimizing the inverted quantity $-2 \log \mathcal{L}$ which has two important mathematical properties. On one hand, the $-2 \log \mathcal{L}$ behaves like a χ^2 quantity, meaning that the change by 1 or 4 marks the 1 or 2σ confidence interval for a normally distributed quantity. The absolute value of $-2 \log \mathcal{L}$ is meaningless. On the other hand, the minimization of the logarithm of the likelihood is numerically much more stable because the likelihood is sharply peaking close to the maximum and is almost flat everywhere else. Figure 6.22 shows the $-2 \log \mathcal{L}$ in the above range. It is interesting to note that the black solid line is taking the blue line and convoluting it with the systematic error. We assume the systematic error to be of Gaussian shape. Converting the $-2 \log \mathcal{L}$ back to a likelihood results in Fig. 6.23. We find the 90%

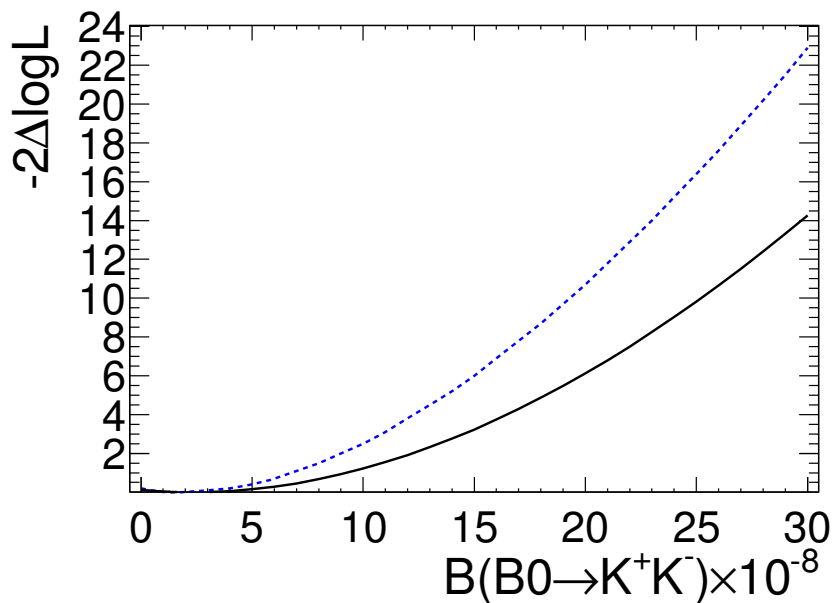


Figure 6.22: *Logarithm of the likelihood as a function of the branching ratio $\mathcal{B}(K^+K^-)$. The blue dotted line shows only the statistical likelihood. The solid black line shows the statistical likelihood convoluted with the systematic error modelled as a Gaussian.*

confidence level from the likelihood convoluted with the systematic Gaussian determined as

being the point where area under the curve from zero corresponds to 90%. The confidence level is $\mathcal{B}(K^+K^-) < 13 \times 10^{-8}$.

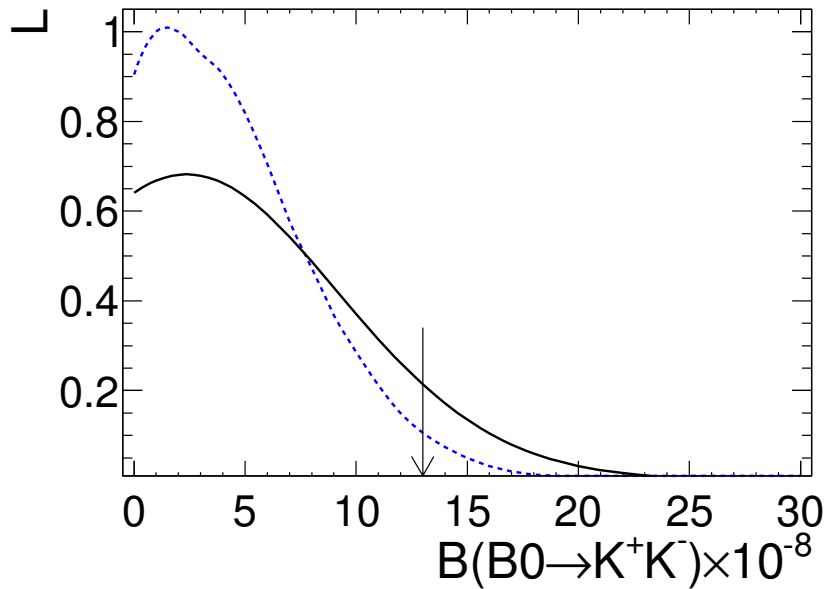


Figure 6.23: Likelihood as a function of the branching ratio $\mathcal{B}(K^+K^-)$. The blue dotted line shows only the statistical likelihood. The solid black line shows the likelihood convoluted with the systematic error modelled as a Gaussian. The black arrow denotes the position of the 90% exclusion limit

6.4 Results from Isospin Analysis of $B \rightarrow \pi\pi$

The isospin analysis is aimed at isolating the contributions of penguin level diagrams from the measurement of the angle ϕ_2 of the unitarity triangle. The theoretical derivation of the method is found in Sec. 2.5. For the first time, we are using only quantities measured at the Belle detector to perform the measurement of ϕ_2 and the contribution from the penguin diagrams causing $\Delta\phi_2$. All branching ratios and CP parameters of decays which are associated to the decay $B^0 \rightarrow \pi^+\pi^-$, by isospin symmetry are used. The isospin triangle (Fig. 6.24) shows how the different amplitudes add up in the complex space. We are performing a χ^2 minimisation to obtain the best value for ϕ_2 and $\Delta\phi_2$.

In order to construct such a χ^2 quantity, we look at the difference between the theoretical predictions of the isospin analysis and the experimental results divided by the experimental uncertainties. In table 6.11, all experimental results taken from the publications [73][76] are summarised including their errors. All results from the decay of $B^0 \rightarrow \pi^+\pi^-$ are taken from our analysis. In addition to the bare parameters, we can implement correlations into the

Table 6.11: Branching ratios and CP parameters of decays associated by isospin symmetry.

Quantity	central value	stat. error	sys. error
$\mathcal{B}(\pi^+\pi^-)$	5.63×10^{-6}	$\pm 0.16 \times 10^{-6}$	$\pm 0.16 \times 10^{-6}$
$\mathcal{B}(\pi^0\pi^0)$	2.30×10^{-6}	0.50×10^{-6}	0.30×10^{-6}
$\mathcal{B}(\pi^+\pi^0)$	5.86×10^{-6}	0.26×10^{-6}	0.38×10^{-6}
$\mathcal{A}_{CP}(\pi^+\pi^-)$	0.33	± 0.06	± 0.03
$\mathcal{S}_{CP}(\pi^+\pi^-)$	-0.64	± 0.08	± 0.03
$\mathcal{A}_{CP}(\pi^0\pi^0)$	0.44	0.53	0.17

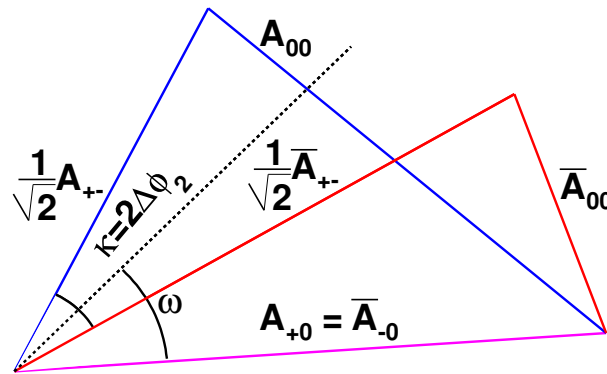


Figure 6.24: The isospin triangles for the B^0 decay and the CP conjugated \bar{B}^0 decay. The contribution of the penguin diagram to the ϕ_2 measurement can be geometrically obtained by measuring $\Delta\phi_2$.

isospin analysis. The correlation coefficient between $\mathcal{A}_{CP}(\pi^+\pi^-)$ and $\mathcal{S}_{CP}(\pi^+\pi^-)$ is usually known because it is extracted in the same analysis. But for the first time in Belle, we also obtained the correlation between the branching ratio and the CP parameters (Tbl. 6.12). From the correlations ρ , in table 6.12 and the total error $\sigma = \sqrt{\sigma_{\text{stat.}}^2 + \sigma_{\text{sys.}}^2}$, from table

Table 6.12: Correlation matrix of branching ratios and CP parameters of the decay $B^0 \rightarrow \pi^+\pi^-$.

	$\mathcal{B}(\pi^+\pi^-)$	$\mathcal{A}_{CP}(\pi^+\pi^-)$	$\mathcal{S}_{CP}(\pi^+\pi^-)$
$\mathcal{B}(\pi^+\pi^-)$	1		
$\mathcal{A}_{CP}(\pi^+\pi^-)$	-0.057	1	
$\mathcal{S}_{CP}(\pi^+\pi^-)$	+0.032	+0.097	1

6.11, we obtain the correlation matrix Σ .

We are using a $-2 \log \mathcal{L}$ ansatz and use a multivariate normal distribution as a likelihood. The $-2 \log \mathcal{L}$ is equal to the χ^2 definition in the case of normal distributed values,

$$\chi^2 = -2 \log \mathcal{L} = -2 \log \left[\frac{1}{(2\pi)^{n/2} |\Sigma|^{1/2}} \exp \left(-\frac{1}{2} (x_{\text{theo}} - x_{\text{exp}})^T \Sigma^{-1} (x_{\text{theo}} - x_{\text{exp}}) \right) \right]. \quad (6.2)$$

The vector of the predictions made by the fitter constrained by theory x_{theo} , of dimension $n = 6$, is subtracted from the vector of experimental results x_{exp} . It is multiplied by the inverted covariance matrix Σ^{-1} and normalized by the determinant of the covariance matrix. In the minimisation procedure, we are varying the geometrical parameters in the two isospin triangles (Fig. 6.24) of the B^0 decay and the \bar{B}^0 decay. These parameters are related to the length of the sides of the triangles, a_{+-} , a_{+0} (which is the same as a_{-0}) and $\mathcal{A}_{CP} = \mathcal{A}_{CP}(\pi^+\pi^-)$, and these represent internal angles, ω , $\kappa = 2\Delta\phi_2$ and ϕ_2 . The amplitudes are constructed from the geometrical parameters as shown in Eqn. 6.8.

$$A_{+-} = \sqrt{a_{+-}(1 - \mathcal{A}_{CP})}, \quad (6.3)$$

$$\bar{A}_{+-} = \sqrt{a_{+-}(1 + \mathcal{A}_{CP})}, \quad (6.4)$$

$$A_{+0} = \sqrt{a_{+0}}, \quad (6.5)$$

$$A_{00}^2 = \frac{A_{+-}^2}{2} + A_{+0}^2 - \sqrt{2} A_{+-} A_{+0} \cos(\omega - \frac{\kappa}{2}), \quad (6.6)$$

$$\bar{A}_{00}^2 = \frac{\bar{A}_{+-}^2}{2} + A_{+0}^2 - \sqrt{2} \bar{A}_{+-} A_{+0} \cos(\omega + \frac{\kappa}{2}). \quad (6.7)$$

$$(6.8)$$

Knowing the theoretical amplitudes from the geometrical parameters, we can then calculate the theoretical observables as shown in Eqn. 6.14. These observables can then be compared

to the experimental results in the χ^2 minimization.

$$\mathcal{B}(\pi^+\pi^-) = \frac{1}{2}(\bar{A}_{+-}^2 + A_{+-}^2), \quad (6.9)$$

$$\mathcal{B}(\pi^0\pi^0) = \frac{1}{2}(\bar{A}_{00} + A_{00}), \quad (6.10)$$

$$\mathcal{B}(\pi^+\pi^0) = A_{+0}^2 \cdot \tau_{B^+}/\tau_{B^0}, \quad (6.11)$$

$$\mathcal{A}_{CP}(\pi^+\pi^-) = \mathcal{A}_{CP}, \quad (6.12)$$

$$\mathcal{S}_{CP}(\pi^+\pi^-) = \sqrt{1 - \mathcal{A}_{CP}^2} \cdot \sin(2\phi_2 + \kappa), \quad (6.13)$$

$$\mathcal{A}_{CP}(\pi^0\pi^0) = \frac{\bar{A}_{00} - A_{00}}{\bar{A}_{00} + A_{00}}. \quad (6.14)$$

To create a plot of the confidence level (CL) as a function of the angle ϕ_2 , we have to scan through all possible values of ϕ_2 . At every value of ϕ_2 , we re-minimise the χ_2 , determining a new set of parameters. In a second step we can translate the χ_2 for 1 degree of freedom into a confidence level,

$$1 - \text{CL} = \frac{1}{\sqrt{2^n}\Gamma(n/2)} \int_{\Delta\chi^2}^{\text{inf}} e^{-\frac{t}{2}} t^{\frac{n}{2}-1} dt. \quad (6.15)$$

The result is shown in Figure 6.25. Our measurement excludes a range of $23.8^\circ < \phi_2 < 66.8^\circ$ at the 1σ level. With a similar method, we create a plot of the confidence level of the penguin contribution $\Delta\phi_2$, to the $\phi_{2\text{eff}}$ measurement (Fig. 6.26). The shift of the ϕ_2 measurement due to the penguin contribution is constrained to be $|\Delta\phi_2| < 44.8^\circ$ at a 1σ level.

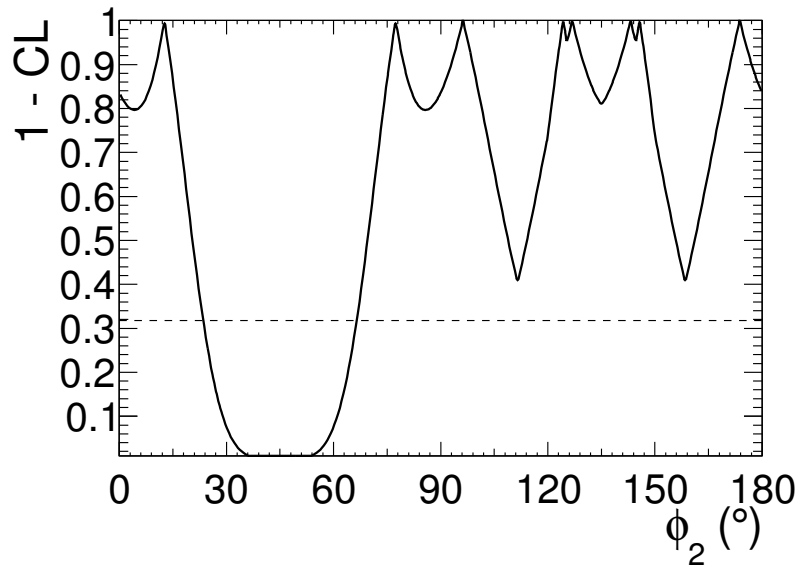


Figure 6.25: $1 - CL$ plot of the angle ϕ_2 . The eightfold solution can clearly be seen. There is no clear preference for one of the solutions visible.

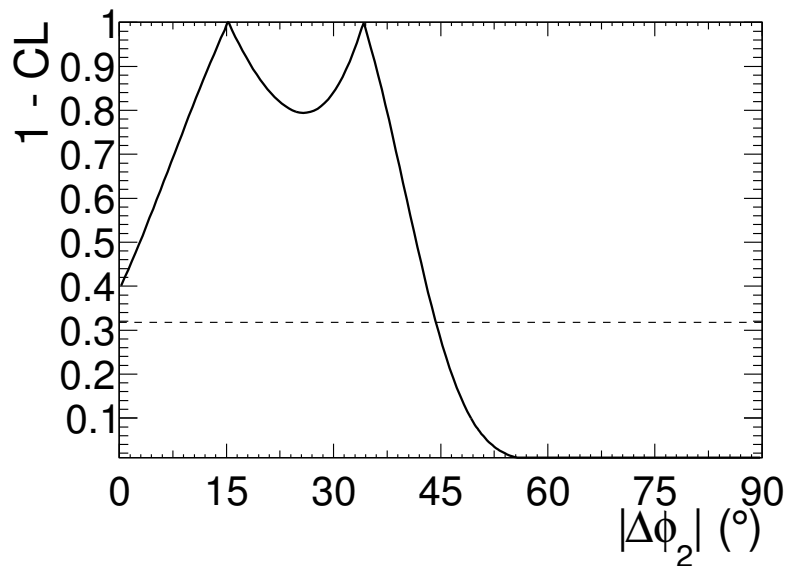


Figure 6.26: $1 - CL$ plot of the angle $|\Delta\phi_2|$.

6.5 Results from the $K\pi$ Sum Rule

Direct CP violating asymmetries have been studied rigorously in $B \rightarrow K\pi$ decays. The observation that the direct CP violation in $B^0 \rightarrow K^+\pi^-$ differs from the direct CP violation that is found in $B^+ \rightarrow K^+\pi^0$ decays is very puzzling. This is especially fascinating because the two decay diagrams differ only by the spectator quark. This feature could be explained by either an enhanced colour-suppressed tree contribution [30, 77] or could indicate significant contributions from electroweak penguins in various NP scenarios [78–81]. A short introduction on the origin of the $K\pi$ sum rule is given in section 2.6. A violation of the relation (Eq. 6.16) between branching fractions and CP violation asymmetries of $K\pi$ decays,

$$\mathcal{A}_{CP}(K^+\pi^-) + \mathcal{A}_{CP}(K^0\pi^+) \frac{\mathcal{B}(K^0\pi^+)}{\mathcal{B}(K^+\pi^-)} = \mathcal{A}_{CP}(K^+\pi^0) \frac{2\mathcal{B}(K^+\pi^0)}{\mathcal{B}(K^+\pi^-)} + \mathcal{A}_{CP}(K^0\pi^0) \frac{2\mathcal{B}(K^0\pi^0)}{\mathcal{B}(K^+\pi^-)}, \quad (6.16)$$

would be a model-independent indication of new physics (NP).

To evaluate the $K\pi$ sum rule we use a Monte-Carlo method. We generate sets of all 8 observables found in Eq. 2.58. The observables and their corresponding uncertainties are taken from this analysis and other Belle results [82, 83]. The distribution of the observables is modelled using a Gaussian distribution with the mean being the central value of the measured observable and the width corresponding to the statistical uncertainty of the observable. If we encounter correlations between the observables, we are using a multivariate Gaussian to model the distribution. For each set, we calculate the sum rule and take the central values and their uncertainties. The systematic error is evaluated with the same procedure by generating uncorrelated distributions of observables with a width corresponding to their respective systematic errors. Comparing the left and right side of Eq. 2.58 we obtain a deviation from zero of $-0.289 \pm 0.139(\text{stat}) \pm 0.064(\text{syst})$ with a 1.9σ significance.

Chapter 7

Summary and Outlook

Summary

One of the most puzzling questions in modern physics is the large matter antimatter asymmetry observed in our universe today. The matter dominated universe can be explained by a large asymmetry in the decay rates of particles and anti-particles, so-called CP asymmetry or CP violation, after the Big Bang. Our currently best model of the elementary physics is the Standard Model of particle physics (SM). But the CP violation explained by the SM is too small to account for the large matter antimatter asymmetry observed today. Therefore we look for new physics beyond the SM. We are performing precision measurements on the time dependent decay rates of B and anti- B mesons to verify the predictions of the standard model and to observe possible deviations. The CP violation in the SM comes from the mixing of quark flavours, described by the **CKM** matrix. One way to test the standard model is to check whether the **CKM** matrix is unitary. A unitary matrix ensures that the sum of all probabilities for all processes is unity. The unitarity condition can be visualised as a unitarity triangle in complex space. The method of choice is to overconstrain the unitarity triangle for B decays by experimentally measuring the sides and angles independently and searching for tensions.

The Belle experiment in Japan is dedicated to CP violation measurements. It is located at the KEKB storage ring. The KEKB is an electron positron collider and is the world record holder in both the instantaneous and the integrated luminosity. The KEKB is an asymmetric collider with an electron beam energy of 8 GeV and a positron beam energy of 3.5 GeV. Therefore the $\Upsilon(4S)$ resonance, which is produced almost at rest in the center-of-mass system is boosted. This resonance decays exclusively into quantum mechanically entangled $B\bar{B}$ pairs.

The Belle detector has recorded 1 ab^{-1} of integrated luminosity mostly at the $\Upsilon(4S)$ resonance. This analysis uses the final Belle dataset of 772×10^6 $B\bar{B}$ pairs to measure the

angle ϕ_2 of the unitarity triangle and search for new physics beyond the Standard Model. To access this angle, we are reconstructing B meson decays from light charged hadrons like pions and kaons.

A new analysis strategy is used in this thesis. We are minimising the amount of data quality requirements (cuts) used during the event selection of our data sample. As a result, the reconstruction efficiency is 10% higher (0.67) than in the previous Belle analyses (0.57) [39], which means that we are effectively analysing more events. This can reduce the statistical error on the branching fraction measurements. The drawback of the new method is that the purity of the reconstructed data sample is lower than with tight cuts. We try to compensate this with an increase in the fitting dimensions. This also implies that a more precise study of the background is needed. We try to find 2500 $B \rightarrow \pi^+\pi^-$ decay events on an enormous background of 450000 continuum events after the event selection. To extract the branching ratios and CP parameters in such an environment is extremely challenging. We use a multi-variate maximum likelihood fit to simultaneously extract the branching ratio of the decays $B \rightarrow \pi^+\pi^-$, $B \rightarrow K^+\pi^-$ and $B \rightarrow K^+K^-$, but also the time-dependent CP violation parameters $\mathcal{A}_{CP}(\pi^+\pi^-)$ and $\mathcal{S}_{CP}(\pi^+\pi^-)$ and $\mathcal{A}_{CP}(K^+\pi^-)$.

To counteract the background increase, we increased the number of dimensions of the maximum likelihood fit. We are using the beam constrained mass of the B meson M_{BC} , and the difference of the reconstructed energy with the beam energy ΔE , as primary dimensions. Then we added information from the particle identification systems that discriminates kaons from pions. The likelihood ratio of the kaon likelihood and the pion likelihood is obtained for the positive ($\mathcal{L}_{K/\pi}^+$) and the negative ($\mathcal{L}_{K/\pi}^-$) constituent of the reconstructed B meson. To discriminate B decays from the continuum background, we exploit the topology of the decays. B mesons decay with no preferred direction spherically, while continuum background ($e^+e^- \rightarrow q\bar{q}$ events) have a jet-like topology. Event shape variables contain the information about the event topology. We combine several of these event shape variables into a fisher discriminant $\mathcal{F}_{S/B}$, which is then used in the maximum likelihood fit. Finally, we are partially reconstructing the other B meson which originates from the $\Upsilon(4S)$ decay. If the other B decays into a flavour specific final state, we can determine the flavour of the reconstructed B at the decay time of the other B . The flavour q , of the B meson is included as one dimension of the maximum likelihood fit. This is possible because the two B mesons coming from the $\Upsilon(4S)$ resonance are quantum mechanically entangled. For the determination of the time-dependent CP parameters, we are also calculating the difference of the decay vertex of the reconstructed B meson and the other B meson. This spatial difference can be converted to a time difference because we know the boost of the center-of-mass system. The time difference Δt , is crucial in the determination of the time-dependent CP parameters of the signal decays.

The observables connected to the decay of $B \rightarrow \pi^+\pi^-$ are needed to determine the angle ϕ_2 of the unitarity triangle, while the $K\pi$ branching ratio and CP asymmetry is used in a sum rule to perform a model independent search for new physics (NP). The combined approach to all these quantities is tried for the first time at Belle in this thesis. In addition to the bare

branching fractions and CP parameters, the correlation coefficients are also determined. The correlation coefficients between the branching ratios and the CP parameters are included in the calculation of the angle ϕ_2 , and the $K\pi$ sum rule. Taking into account the full covariance matrix yields more precise results than ignoring the correlations coefficients as the previous analyses have done.

A major part of the analysis is to determine the fit biases which arise from imperfections in the parametric modeling of the signal and background components. Toy Monte-Carlo ensemble tests were performed to check the impact of such imperfections on the physics observables. Correlations between the different fit dimensions have to be modeled with great care, especially. We incorporated more correlations than any Belle analysis before to reduce the bias due to model imperfections to an acceptable level. We had to model every correlation down to 2% to ensure that the systematic uncertainty due to model imperfections is not the dominant one.

A weak point of many blind analysis is the dependence on Monte-Carlo simulations. We tried to use parametric models of signal and background components wherever possible. Afterwards, we tried to determine as many parameters as possible in the final fit to the data itself. Where this was not possible, we determined correction factors from the control sample $B^\pm \rightarrow D^0\pi^\pm$. A bin-wise correction to the non-parametric histogram shapes of $\mathcal{L}_{K/\pi}^+$ and $\mathcal{L}_{K/\pi}^-$ was developed in this analysis.

All these new techniques and careful studying of systematic effects render it possible to simultaneously obtain the branching fractions for the decays $B \rightarrow \pi^+\pi^-$ and $B \rightarrow K^+\pi^-$, and the world's most precise CP parameters $\mathcal{A}_{CP}(\pi^+\pi^-)$ and $\mathcal{S}_{CP}(\pi^+\pi^-)$. Also we obtain a very restrictive upper limit on the decay $B \rightarrow K^+K^-$. Our results rule out the angle ϕ_2 of the unitarity triangle in the range $23.8^\circ < \phi_2 < 66.8^\circ$ at the 1σ level. A model independent test of new physics using a sum rule in the $K\pi$ system finds a mild deviation from the Standard Model expectation of zero of $-0.289 \pm 0.139(\text{stat}) \pm 0.064(\text{syst})$ with a 1.9σ significance.

Outlook

In the near future, we are expecting results from the LHCb experiment in the channels $B \rightarrow h^+h^-$. The LHCb experiment has collected 1.79 fb^{-1} of data as at October 2012. This corresponds to a signal yield of approximately 5205 events extrapolated from Ref. [58]. This is already almost twice of our signal yield with the full Belle statistics. We are expecting the statistical uncertainties of the branching fraction measurement to become smaller than the Belle uncertainties very soon. The systematic uncertainties, however, are going to dominate the LHCb results. This is because LHCb does not know the total number of $B\bar{B}$ pairs created. Only ratios between branching fractions are measured. To obtain an absolute measurement of the branching fractions, the ratios have to be normalised by an

absolute branching fraction measured at a B-factory. The uncertainty of the absolute branching fraction is inherent in the LHCb measurement and can be taken as an irreducible error on the branching fraction measurement. The time-dependent CP parameters for $B^0 \rightarrow \pi^+\pi^-$ can be measured at LHCb as well. For the time-dependent measurement, we are crucially depending on the tagging algorithm which identifies B^0 and \bar{B}^0 decays. The tagging efficiency for Belle is about 30% [69], while it is 4.5% [84] for LHCb. To reach a similar statistical precision LHCb has to collect about 10 times more data than a B-factory.

A way out to reach even higher precision is a super-B-factory like Belle II [85]. The main goal of Belle II is to search for new physics beyond the Standard Model. To reach this goal, it is planned to record 50 times more integrated luminosity than Belle. This can be achieved by upgrading the accelerator to provide 20 times more instantaneous luminosity ($8.5 \times 10^{35} \text{ cm}^{-2}\text{s}^{-1}$) than the KEKB collider used for the Belle experiment. This can be achieved by the accelerator by using even smaller beam diameters in the order of nano meters (Nano-beam option). The statistical errors on the branching fractions are expected to shrink to 14% of the current values. For the time-dependent CP parameters the effect is expected to be even more dramatic. Due to a new silicon-pixel-vertex-detector(PXD), the time resolution is going to increase by a factor of 2. This comes in addition to the reduction of the statistical uncertainties to 14% of the Belle level. In contrast to LHCb, the Belle II experiment is capable of studying decays that contain photons and neutrinos. This holds exciting, rich, new physics ready for us, just waiting to be explored.

Appendix A

Toy Monte-Carlo Plotting Method

The standard method for plotting correlated probability density functions (PDFs) is the following. For every dimension of the plots e.g. M_{BC} , ΔE or Δt we want to plot a projection of the PDF. When plotting e.g. M_{BC} we have to evaluate the PDF at several points in our plotting window. We commonly want to compare to binned data and therefore evaluate the PDF at the bin center of every bin. Because we have correlations with other dimensions we also have to loop over the bins of the other dimensions. This leads to nested for-loops which mean the number of evaluations of the PDF exponentially grows with the number of dimensions. In addition we have to loop over all events if we are plotting an event-dependent PDF like Δt . The Δt resolution depends on the goodness of the vertex-fit of CP- and tag-side and because of this the PDF is different for every event. In our case the plotting of our 7D PDF takes weeks for one plot.

Generating a big toy Monte-Carlo sample from the PDF with the values obtained from the fit to data takes only a few hours. In the limit of infinitely high statistics in the toy MC sample it describes the PDF perfectly. Our toy Monte-Carlo ensemble tests show that there is no discrepancy between the PDF and the toy Monte-Carlo. To plot the data and the PDF we perform the following steps. First we generate a sufficiently large toy Monte-Carlo sample. Then we plot the binned data points with their corresponding error. On top we are plotting the binned toy MC sample normalized to the yield obtained from the fit to data. We choose a continuous drawing style to distinguish between data and PDF. One has to make sure that the same cuts are applied to data and the toy MC sample. This is especially important when producing signal enhanced plots by cutting e.g. on the particle identification likelihood ratio.

Appendix B

Flavour Tagging

Flavour tagging is the method of determining whether a B meson is a B^0 or a \bar{B}^0 meson. This information, “tag”, can be obtained if the B meson decays into a flavour specific final state. This appendix closely follows the description in Ref. [86]. A more detailed information can be found in Ref. [69].

B.1 Track-Level Flavour Tagging

Flavour tagging is a Belle procedure common to many analyses. It is implemented in the Hamlet software package. After a B_{Rec} meson is reconstructed the remaining final state particles are assumed to belong to the other B meson, B_{Tag} . The tracks belonging to the B_{Tag} meson are used to determine the flavour of the B meson. The basic procedure is to search for particular charged tracks within the set of final state particles to determine the flavour, q . The Feynman diagrams of some of the processes are shown in Fig. B.1. In general the tracks are required to originate from the IP within 2 cm in the $r - \phi$ plane and 10 cm in the z direction. An exception are the tracks which are associated to the kaon or Λ categories which are described in the following.

B.1.1 Slow Pion Category

Tracks with a momentum smaller than 0.25 GeV/c in the center of mass system (CMS) are assigned to this category. The charge of the slow pion track is used to identify the b -flavour of the tag side. Several variables are used to discriminate the slow pion from background processes: The charge of the track, the momentum in the laboratory frame, the polar angle in the laboratory frame, the angle between the slow pion and the thrust axis of the rest of the tag side particles in the CMS, θ_{thr} , and a pion/electron identification likelihood ratio, $R_{\pi/e}$. The angle, θ_{thr} is used to suppress the background from non- D decays. The ratio,

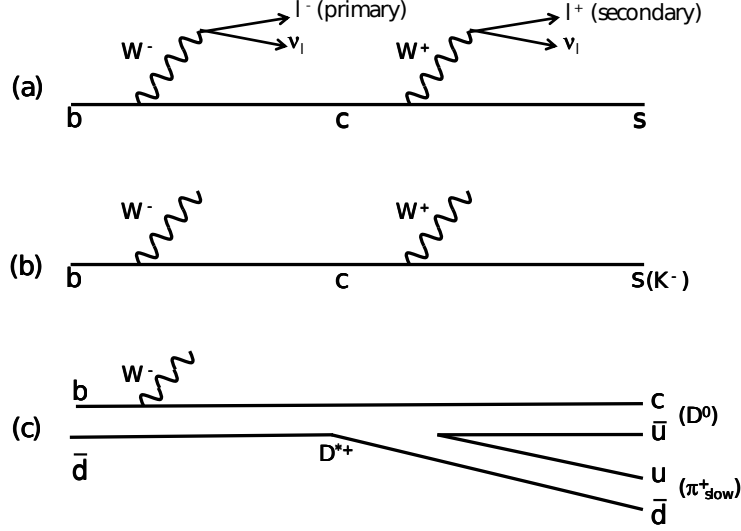


Figure B.1: Some of the decay processes from which the flavour of the B_{tag} can be determined.

$R_{\pi/e}$, is used to remove fake slow pions. These fake slow pions mainly originate from photon conversions into electrons. This category has a low tagging efficiency and poor tagging quality. A major effort is ongoing for the Belle II experiment to improve especially the tagging efficiency in this category. This is going to be achieved by an increased track finding capability in the low momentum regime.

B.1.2 Lambda Category

If two tracks from oppositely charged particles can be combined to have an invariant mass, $M_{p\pi}$, between $1.1108 \text{ GeV}/c^2$ and $1.1208 \text{ GeV}/c^2$ it is assigned to the Λ category. The flavour information from the Λ , Λ or $\bar{\Lambda}$, is used to determine the b -flavour of the tag side. In addition to the matching invariant mass, one of the tracks has to be identified as a proton. The angle between the momentum vector of the Λ candidate and the vector formed by the IP and the vertex of the Λ candidate, θ_{defl} , must be less than 30° . The minimum distance between the tracks in the z axis, Δz , is required to be less than 4 cm, and the flight length of the Λ in the $r - \phi$ plane must be less than 0.5 cm. The flavour of Λ , $M_{p\pi}$, θ_{defl} and the presence of K_S^0 candidates are included as discriminants.

B.1.3 Kaon Category

A charged track that is not positively identified as a lepton or proton is assigned to this category. The decays $b \rightarrow c \rightarrow s$ carry over the b -flavour information to the kaon. From the charge of the kaon we can obtain the b -flavour. Since no kaon identification is required also the fast pions from the decay of $B \rightarrow D^{(*)}\pi^\pm$ are included. The charge of the kaon, the presence of K_S^0 candidates, the kaon momentum in the CMS, the polar angle of the kaon in the laboratory frame and the K/π ID likelihood ratio are included as discriminants. This category has a high tagging efficiency but a poor tagging quality.

B.1.4 Lepton Category

This category differs between electron candidates and muon candidates. The electron candidates are required to have a momentum larger than 0.4 GeV/c and an electron likelihood larger than 0.8. The muon candidates are required to have a momentum of 0.8 GeV/c or larger and a muon likelihood larger than 0.95. It is assumed that the high momentum leptons originate from the decay $B \rightarrow X\ell^\pm\nu$ and intermediate momentum leptons from $B \rightarrow D \rightarrow K\ell^\pm\nu$. Again the charge of the lepton is used to determine the b -flavour on the tag side. Several variables are included as discriminants: the lepton momentum in the CMS, $p\ell^{\text{CMS}}$, the polar angle of the leptons in the laboratory frame, θ_{lab} , the recoil mass, M_{recoil} and the missing momentum in the CMS, $p_{\text{miss}}^{\text{CMS}}$. We discriminate between primary and secondary leptons using the variable $p\ell^{\text{CMS}}$. The recoil mass, M_{recoil} , can indicate the presence of a D meson. If neutrinos are present their momentum cannot be reconstructed. Therefore missing momentum in the CMS can indicate the presence of neutrinos in the decay. This category has a low tagging efficiency but a high tagging quality.

B.2 Event-Level Flavour Tagging

From the track level flavour tagging we obtain several flavour tag informations. It is also obvious that the track level flavour information is not always accurate due to incorrect particle identification of suppressed physics processes. The task of the event-level flavour tagging is to combine all the information and provide a flavour information and a measure for the reliability of the flavour information, also called flavour tag quality. We define a flavour reliability, r , which is defined as

$$q \cdot r \equiv \frac{N(B^0) - N(\bar{B}^0)}{N(B^0) + N(\bar{B}^0)}, \quad (\text{B.1})$$

and ranges from $r = 0$ for no flavour discrimination to $r = 1$ for unambiguous flavour assignment. The flavour reliability is determined from Monte-Carlo and the variables $N(B^0)$ and $N(\bar{B}^0)$ are the number of B^0 and \bar{B}^0 events that occupy a “bin”. A bin is meant to

be an element in a multi-dimensional flavour tagging histogram prepared from MC. The histogram depends on the flavour tagging category and the discriminates described above.

The event-level flavour tagging combines the results, $(q \cdot r)_x$ where x is the tagging category for each track to determine a single highest $q \cdot r$ output for each event. For the lepton and slow pion categories, the track with the highest r in each category is chosen as an input. For the kaon and Λ categories, the flavour and dilution factors of each track are combined by calculating the product of the flavour dilution factors in order to account for possible cases where there are multiple s quarks in the final state. By using a three-dimensional look-up table, the correlations between the flavour information for the four categories in track-level are correctly taken into account. A schematic of these procedures is shown in Fig. B.2.

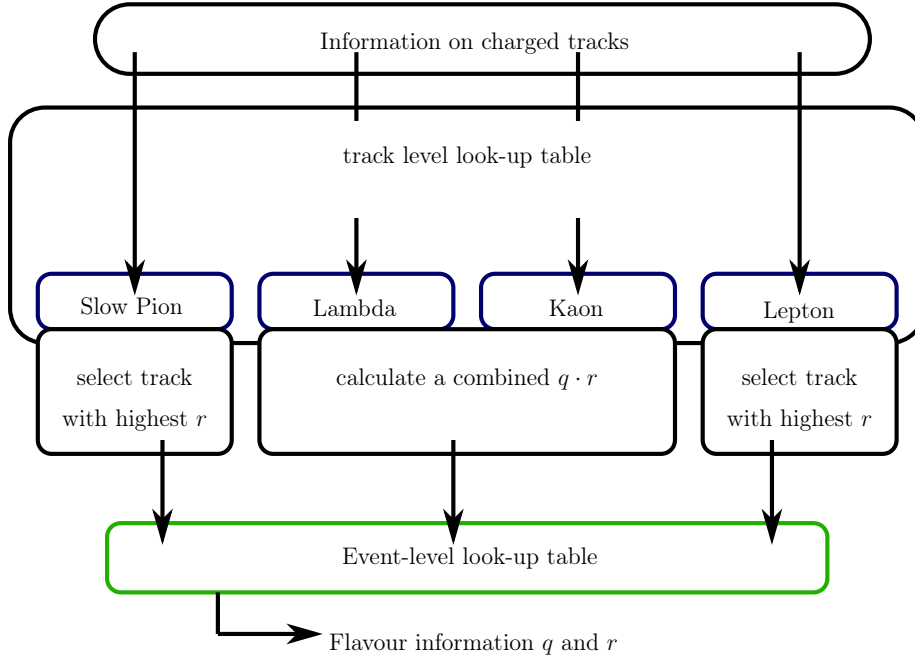


Figure B.2: *Flavour tagging algorithm.*

B.2.1 Flavour Tagging Performance

We define two parameters to describe the tagging performance, ϵ and w . The parameter ϵ is the uncorrected tagging efficiency and parameter w is defined to be wrong tag fraction, which is the probability that a obtained flavour tag is wrong.

In this analysis we are observing time-dependent CP violation as a combined function of Δt and the b -flavour q ,

$$\mathcal{P}_{\text{Sig}}^{\text{obs}}(\Delta t, q, \epsilon, w) = \epsilon \cdot [(1 - w)\mathcal{P}_{\text{Sig}}(\Delta t, q) + w(\mathcal{P}_{\text{Sig}}(\Delta t, -q))] \quad (\text{B.2})$$

taking into account the imperfect flavour tag we have to rewrite the observed CP violation as

$$\mathcal{A}_{CP}^{\text{obs}} = \frac{\mathcal{P}_{\text{Sig}}^{\text{obs}}(\Delta t, q, \epsilon, w) - \mathcal{P}_{\text{Sig}}^{\text{obs}}(\Delta t, -q, \epsilon, w)}{\mathcal{P}_{\text{Sig}}^{\text{obs}}(\Delta t, q, \epsilon, w) + \mathcal{P}_{\text{Sig}}^{\text{obs}}(\Delta t, -q, \epsilon, w)} = (1 - 2w)\mathcal{A}_{CP}. \quad (\text{B.3})$$

The statistical significance of the asymmetry is proportional to the square root of the effective number of events, $(1 - 2w)\sqrt{\epsilon}$. We can introduce an effective efficiency which takes into account both the raw efficiency and also the effective reduction of the statistics due to the wrong tag fractions,

$$\epsilon_{\text{eff}} = \epsilon(1 - 2w)^2 \quad (\text{B.4})$$

The effective efficiency, ϵ_{eff} , was the figure of merit when optimizing the tagging algorithm. The total effective efficiency for MC is estimated to be $29.72 \pm 0.17\%$.

The average flavour reliability can be determined to be $r = 1 - 2w$ if the MC represents data perfectly. A procedure which is totally dependent on the quality of the MC is not desirable because there is no way of checking the quality of the MC. Therefore also data is used to check the tagging efficiency and the wrong tag fractions. The data is subdivided into seven regions, r -bins, depending on their r values: $0 < r \leq 0.1$, $0.1 < r \leq 0.25$, $0.25 < r \leq 0.5$, $0.5 < r \leq 0.625$, $0.625 < r \leq 0.75$, $0.75 < r \leq 0.875$ and $0.875 < r \leq 1$. These r -bins are labeled in this analysis from $l = 0$ to $l = 6$. The wrong tag fractions, w , and the difference in w between B^0 and \bar{B}^0 , Δw , are obtained by fitting the time-dependent $B^0\bar{B}^0$ mixing oscillation of $B^0 \rightarrow D^{*-}\ell^+\nu_\ell$, $B^0 \rightarrow D^{(*)-}\pi^+$ and $B^0 \rightarrow D^{*-}\rho^+$ self tagging events as shown in Fig. B.3. The data channels used for obtaining the wrong tag fractions are self tagging, which means that we can determine the flavour from the final state. This flavour can be compared to the flavour determined from the tagging algorithm and the events can be grouped by whether the reconstructed side and the tag side have the same flavour (SF) or the opposite flavour (OF). The time evolution of the $B\bar{B}$ pairs is given by

$$\mathcal{P}^{\text{OF}} = \frac{e^{-|\Delta t|/\tau_{B^0}}}{4\tau_{B^0}} [1 - q\Delta w + (1 - 2w) \cos(\Delta m_d \Delta t)] \quad (\text{B.5})$$

$$\mathcal{P}^{\text{SF}} = \frac{e^{-|\Delta t|/\tau_{B^0}}}{4\tau_{B^0}} [1 + q\Delta w - (1 - 2w) \cos(\Delta m_d \Delta t)], \quad (\text{B.6})$$

and the OF-SF asymmetry is given by

$$\mathcal{A}_{\text{Mix}} = \frac{\mathcal{P}^{\text{OF}} - \mathcal{P}^{\text{SF}}}{\mathcal{P}^{\text{OF}} + \mathcal{P}^{\text{SF}}} = -q\Delta w + (1 - 2w) \cos(\Delta m_d \Delta t). \quad (\text{B.7})$$

We summarize the obtained wrong tag fractions, w , and the differences of the wrong tag fractions for B^0 and \bar{B}^0 , Δw in Tbl. B.1. w and Δw are determined independently for SVD1 and SVD2 data samples. The total effective tagging efficiency for data is determined to be $29.20 \pm 1.37\%$.

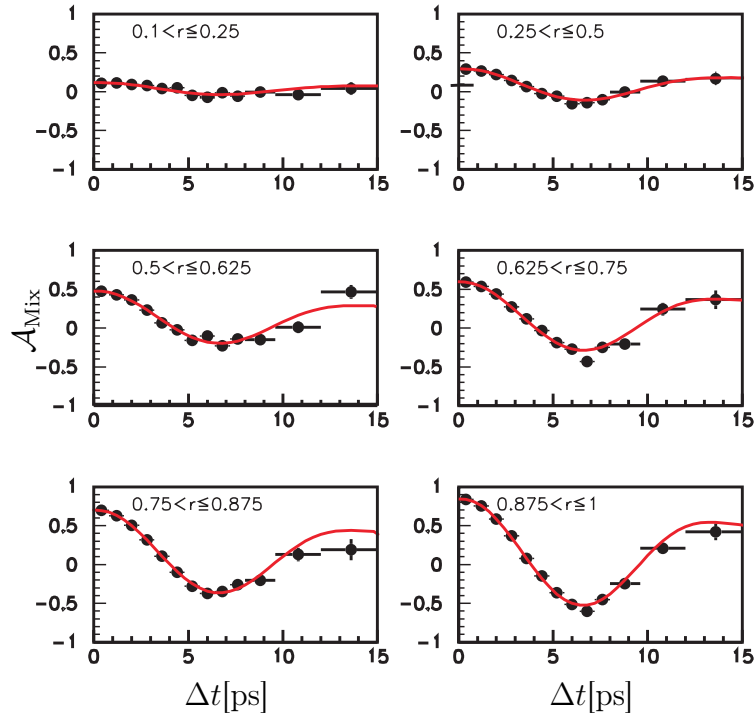


Figure B.3: Time-dependent $B^0\bar{B}^0$ mixing oscillation fit result to the control sample data. Each plot from the top-left to the bottom right, corresponds to the subsample in each r -bin region from 1 to 6. The amplitudes in the oscillation become larger due to less dilution from incorrect tagging.

Table B.1: Wrong tag fractions and wrong tag fraction differences for each r -bin.

r -bin	w (SVD1)	w (SVD2)	Δw (SVD1)	Δw (SVD2)
$0.0 < r \leq 0.1$	0.5 ± 0.0	0.5 ± 0.0	0.0 ± 0.0	0.0 ± 0.0
$0.1 < r \leq 0.25$	$0.423^{+0.008}_{-0.007}$	0.429 ± 0.005	$0.058^{+0.010}_{-0.009}$	$-0.039^{+0.006}_{-0.007}$
$0.25 < r \leq 0.5$	0.337 ± 0.008	0.327 ± 0.006	0.012 ± 0.010	-0.036 ± 0.006
$0.5 < r \leq 0.625$	$0.235^{+0.010}_{-0.008}$	$0.223^{+0.011}_{-0.006}$	-0.012 ± 0.010	0.018 ± 0.007
$0.625 < r \leq 0.75$	$0.166^{+0.008}_{-0.007}$	$0.161^{+0.010}_{-0.006}$	$-0.011^{+0.010}_{-0.009}$	0.002 ± 0.006
$0.75 < r \leq 0.875$	$0.105^{+0.008}_{-0.007}$	$0.105^{+0.007}_{-0.008}$	0.008 ± 0.009	-0.027 ± 0.006
$0.875 < r \leq 1.0$	$0.026^{+0.006}_{-0.005}$	$0.019^{+0.004}_{-0.005}$	0.003 ± 0.006	-0.001 ± 0.004

Appendix C

Δt Resolution Function

The Δt distribution obtained from the measurement differs in many aspects from the theoretical predictions. The reasons are mainly the smearing because of the detector resolution, the vertex smearing on the tag side because of inclusion of secondary tracks into the primary vertex and the approximation that the B mesons are at rest in the center of mass frame. We provide a brief description in the following closely following Ref. [86]. The detailed information can be found in Ref. [68].

C.1 Detector Resolution

We differentiate the detector resolution for B mesons originating from the reconstructed side, R_{Rec} , and from the other B or tag-side, R_{Tag} . The vertex of these B mesons can be determined by a multi-track vertex fit or a single-track vertex fit using the beam tube constraint. Because the resolution for multi-track vertex fits is significantly different from the resolution for single-track vertex fits, they are treated separately.

The detector resolution function for the B_{Rec} for a multi-track event is given by a double Gaussian,

$$R_{\text{Rec}}(\delta z_{\text{Rec}}) \equiv (1 - f_{\text{Rec}}^{\text{tail}})G(\delta z_{\text{Rec}}, (S_{\text{Rec}}^0 + \xi_{\text{Rec}}S_{\text{Rec}}^1)\sigma_{\text{Rec}}) + f_{\text{Rec}}^{\text{tail}}G(\delta z_{\text{Rec}}, S_{\text{Rec}}^{\text{tail}}S_{\text{Rec}}^{\text{main}}). \quad (\text{C.1})$$

The corresponding resolution function for multi-track events for the tag side B_{Tag} is modeled with a single Gaussian,

$$R_{\text{Tag}}(\delta z_{\text{Tag}}) \equiv G(\delta z_{\text{Tag}}, (S_{\text{Tag}}^0 + \xi_{\text{Tag}}S_{\text{Tag}}^1)\sigma_{\text{Tag}}). \quad (\text{C.2})$$

The single-track vertex resolution is described by the same model, a double Gaussian, for both the reconstructed B meson and the tag side B meson,

$$R_i(\delta z_i) \equiv (1 - f_i^{\text{tail}})G(\delta z_i, S_i^{\text{main}}\sigma_i) + f_i^{\text{tail}}G(\delta z_i, S_i^{\text{tail}}\sigma_i), \quad i = \text{Rec, Tag}. \quad (\text{C.3})$$

Table C.1: R_{Det} resolution function parameters for single-track and multi-track vertices

Track Multiplicity	Parameter	Value(SVD1)	Value(SVD2)
Mutli-track	S_{Rec}^0	$0.910^{+0.463}_{-0.080}$	$0.656^{+0.453}_{-0.098}$
	S_{Rec}^1	0.023 ± 0.004	$0.035^{+0.008}_{-0.006}$
	f_{Rec}^{tail}	-	$0.101^{+0.040}_{-0.053}$
	S_{Tag}^0	$0.667^{+0.339}_{-0.398}$	$0.790^{+0.494}_{-0.260}$
	S_{Tag}^1	$0.010^{+0.001}_{-0.004}$	$0.014^{+0.003}_{-0.006}$
	Single-track	S_i^{main}	$0.906^{+0.278}_{-0.069}$
f_i^{tail}		-	$0.108^{+0.042}_{-0.045}$
S_i^{tail}		-	$3.596^{+4.462}_{-0.803}$

In the equations C.1-C.3 δz is defined as the difference between the true position of the vertex and the reconstructed position. The vertex quality, ξ , and the z-positional error, σ , are event dependent quantities. The vertex quality, ξ , is basically a projection of the χ^2 of the vertex fit onto the z -direction of the detector and defined as

$$\xi \equiv \frac{1}{2n} \sum_{i=1}^n \left[\frac{z_{before}^i - z_{after}^i}{\epsilon_{before}^i} \right]^2. \quad (C.4)$$

The parameters z_{before}^i and z_{after}^i are the vertex position of each track before and after the fit, respectively. The error of the z -position of every track before the vertex fit is given by ϵ_{before}^i . Please note that ξ cannot be defined for single-track vertices because the information content on the z -position is not increased by the vertex fit. It is also interesting to note that the correlation between the multi-track resolution function width, $S_i^{main} \equiv (S_i^0 + \xi_i S_i^1) \sigma_i$, and the vertex error, σ_i , is corrected with a linear polynomial in the vertex quality. The detector resolution parameters are determined from the lifetime fit to the data of control samples like, $B^0 \rightarrow D^* \ell \nu_\ell$, $B^0 \rightarrow D^{(*)} \pi$ and $B^0 \rightarrow D^* \rho$. A summary is given in Tbl. C.1.

C.2 B_{Tag} Vertex Smearing from Non-Primary Tracks

The vertex of the tag-side B meson can be smeared by the inclusion of additional tracks from secondary vertices. These vertices are displaced from the primary vertex because of the finite lifetime of the decay products. The simple algorithm for tag-side vertex finding is explained in Sec. 4.3.3.

To cover the effect of the tracks from non-primary tracks we define a resolution function, R_{NP} , to be

$$R_{NP}(\delta z_{Tag}) \equiv f_\delta \delta(\delta z_{Tag}) + (1 - f_\delta) [f^+ E^+(\delta z_{Tag}, \tau_{NP}^+) + (1 - f^+) E^-(\delta z_{Tag}, \tau_{NP}^-)]. \quad (C.5)$$

The first part of the equation is a Dirac delta function which models the vertices without contamination from non-primary tracks. The second part describes vertices which have a contribution from non-primary tracks. These non-primary tracks originate from decay products with a finite lifetime which create a secondary vertex. Therefore their distribution is modeled by two exponential functions, E^+ and E^- , on both sides of the delta function,

$$E^+(\delta z_{\text{Tag}}, \tau_{\text{NP}}^+) \equiv \begin{cases} \frac{1}{\tau_{\text{NP}}^+} \exp -\delta z_{\text{Tag}}/\tau_{\text{NP}} & \text{if } \delta z_{\text{Tag}} > 0 \\ 0 & \text{if } \delta z_{\text{Tag}} < 0 \end{cases} \quad (\text{C.6})$$

$$E^-(\delta z_{\text{Tag}}, \tau_{\text{NP}}^-) \equiv \begin{cases} \frac{1}{\tau_{\text{NP}}^-} \exp -\delta z_{\text{Tag}}/\tau_{\text{NP}} & \text{if } \delta z_{\text{Tag}} > 0 \\ 0 & \text{if } \delta z_{\text{Tag}} < 0. \end{cases} \quad (\text{C.7})$$

In both equations C.5 and C.7 δz_{Tag} is defined as the reconstructed vertex with and without contamination from non-primary tracks. The effective decay length, τ_{NP}^\pm , is depending on the vertex quality, ξ_{NP} , because the secondary tracks which are further away from the other tracks also contribute more to ξ_{NP} and the vertex has a larger error, σ_{NP} . For a multi-track vertex we model this correlation between σ_{NP} , ξ_{NP} and τ_{NP}^\pm ,

$$\tau_{\text{NP}}^+ \equiv S_{\text{NP}}^3 [\tau_0^+ + \tau_1^+ (1 + S_{\text{Tag}}^2 \xi) \sigma_{\text{Tag}}], \quad (\text{C.8})$$

$$\tau_{\text{NP}}^- \equiv S_{\text{NP}}^3 [\tau_0^- + \tau_1^- (1 - S_{\text{Tag}}^2 \xi) \sigma_{\text{Tag}}]. \quad (\text{C.9})$$

The effective decay length, τ_{NP} , for single-track vertices is must be defined differently because ξ_{NP} is not defined,

$$\tau_{\text{NP}}^+ \equiv S_{\text{Tag}}^3 [\tau_0^+ + \tau_1^+ \sigma_{\text{Tag}}], \quad (\text{C.10})$$

$$\tau_{\text{NP}}^- \equiv S_{\text{Tag}}^3 [\tau_0^- + \tau_1^- \sigma_{\text{Tag}}]. \quad (\text{C.11})$$

To determine the parameters of R_{NP} we compare two Monte-Carlo sets. One MC set contains B decays into charmed particles and the second MC set contains the same decays but with the lifetime of all daughter particles artificially set to zero. With the second Monte-Carlo set it is possible to study the δz_{Tag} distribution separately. The parameters obtained from this procedure are given in the tables C.2 and C.3.

C.3 Kinematic Approximation

The Δt distribution is calculated from Eq. 4.4 which assumes that the B mesons are at rest in the rest frame of the $\Upsilon(4S)$ resonance. We can analytically derive the smearing due to this approximation. One can show that the difference between the reconstructed Δt , Eq. 4.4, and the true Δt , $\Delta t_{\text{True}} \equiv t_{\text{Rec}} - t_{\text{Tag}}$, is given by

$$x \equiv \Delta t_{\text{Rec}} - \Delta t_{\text{True}} = [(\beta\gamma)_{\text{Rec}}/(\beta\gamma)_{\Upsilon(4S)} - 1] t_{\text{Rec}} - [(\beta\gamma)_{\text{Tag}}/(\beta\gamma)_{\Upsilon(4S)} - 1] t_{\text{Tag}}, \quad (\text{C.12})$$

Table C.2: R_{NP} resolution function parameters for B^0 .

	Parameter	Value (SVD1)	Value (SVD2)
Global	S_{Tag}^2	0.020 ± 0.0004	0.034 ± 0.0004
	S_{Tag}^3	$0.954^{+0.104}_{-0.053}$	$0.877^{+0.201}_{-0.077}$
Multi-track	f_δ	$0.251^{+0.062}_{-0.067}$	$0.297^{+0.088}_{-0.038}$
	f^+	0.792 ± 0.005	0.770 ± 0.002
	τ_0^+ (cm)	0.071 ± 0.004	0.111 ± 0.002
	τ_1^+	0.070 ± 0.005	0.101 ± 0.002
	τ_0^- (cm)	0.062 ± 0.008	0.129 ± 0.004
	τ_1^-	0.011 ± 0.009	0.092 ± 0.004
Single-track	f_δ	$0.598^{+0.041}_{-0.141}$	$0.706^{+0.029}_{-0.082}$
	f^+	0.734 ± 0.010	0.841 ± 0.012
	τ_0^+ (cm)	0.641 ± 0.047	1.450 ± 0.030
	τ_1^+	$0.314^{+0.066}_{-0.063}$	0.886 ± 0.033
	τ_0^- (cm)	$0.314^{+0.065}_{-0.060}$	$1.002^{+0.074}_{-0.070}$
	τ_1^-	$0.196^{+0.097}_{-0.085}$	$0.519^{+0.081}_{-0.073}$

Table C.3: R_{NP} resolution function parameters for B^+ .

	Parameter	Value (SVD1)	Value (SVD2)
Global	S_{Tag}^2	0.020 ± 0.0004	0.034 ± 0.0004
	S_{Tag}^3	$0.954^{+0.104}_{-0.053}$	$0.877^{+0.201}_{-0.077}$
Multi-track	f_δ	$0.166^{+0.090}_{-0.077}$	$0.385^{+0.082}_{-0.052}$
	f^+	0.775 ± 0.007	0.762 ± 0.003
	τ_0^+ (cm)	0.607 ± 0.009	0.640 ± 0.006
	τ_1^+	0.627 ± 0.010	0.571 ± 0.006
	τ_0^- (cm)	0.530 ± 0.016	0.589 ± 0.009
	τ_1^-	0.617 ± 0.020	0.561 ± 0.010
Single-track	f_δ	-	-
	f^+	0.745 ± 0.017	0.834 ± 0.028
	τ_0^+ (cm)	$1.045^{+0.055}_{-0.028}$	-
	τ_1^+	$1.057^{+0.086}_{-0.083}$	-
	τ_0^- (cm)	1.199 ± 0.089	-
	τ_1^-	1.307 ± 0.155	-

where the Lorentz boost factors of B_{Tag} and B_{Rec} are $(\beta\gamma)_{\text{Tag}}$ and $(\beta\gamma)_{\text{Rec}}$, respectively. Their ratios to the $\Upsilon(4S)$ Lorentz boost are,

$$\frac{(\beta\gamma)_{\text{Rec}}}{(\beta\gamma)_{\Upsilon(4S)}} = \frac{E_B^{\text{CMS}}}{m_B} + \frac{p_B^{\text{CMS}} \cos \theta_B^{\text{CMS}}}{\beta_{\Upsilon(4S)} m_B} \equiv a_K + c_K, \quad (\text{C.13})$$

$$\frac{(\beta\gamma)_{\text{Tag}}}{(\beta\gamma)_{\Upsilon(4S)}} = \frac{E_B^{\text{CMS}}}{m_B} - \frac{p_B^{\text{CMS}} \cos \theta_B^{\text{CMS}}}{\beta_{\Upsilon(4S)} m_B} \equiv a_K - c_K, \quad (\text{C.14})$$

where E_B^{CMS} , m_B , p_B^{CMS} and θ_B^{CMS} are the energy, mass, momentum and polar angle of the reconstructed B in the center of mass frame. The probability density of simultaneous obtaining x and Δt_{True} incorporates the exponential distribution, E_i^+ , of t_{Rec} and t_{Tag} and is calculated to be

$$\mathcal{P}(x, \Delta t_{\text{True}}) = \int_0^\infty \int_0^\infty dt_{\text{Rec}} dt_{\text{Tag}} E^+(t_{\text{Rec}}, \tau_B) E^+(t_{\text{Tag}}, \tau_B) \delta(\Delta t_{\text{True}} - [t_{\text{Rec}} - t_{\text{Tag}}]) \delta(x - \{[a_k + c_k - 1]t_{\text{Rec}} - [a + k - c_k - 1]t_{\text{Tag}}\}), \quad (\text{C.15})$$

and the probability density function for only obtaining Δt_{True} is

$$\mathcal{P}(\Delta t_{\text{True}}) = \int_0^\infty \int_0^\infty dt_{\text{Rec}} dt_{\text{Tag}} E^+(t_{\text{Rec}}, \tau_B) E^+(t_{\text{Tag}}, \tau_B) \delta(\Delta t_{\text{True}} - [t_{\text{Rec}} - t_{\text{Tag}}]). \quad (\text{C.16})$$

Using the previous results we obtain the resolution function that accounts for the kinematic approximation, R_K . R_K is defined as the probability density of obtaining x for a given Δt_{True} . Thus, it is expressed as $R_K = \mathcal{P}(x, \Delta t_{\text{True}})/\mathcal{P}(\Delta t_{\text{True}})$, which evaluates to,

$$R_K = \begin{cases} E^+(x - \{(a_k - 1)\Delta t_{\text{True}} + c_k|\Delta t_{\text{True}}|\}, |c_k|\tau_B) & \text{if } c_k > 0 \\ \delta(x - a_k - 1\Delta t_{\text{True}}) & \text{if } c_k = 0 \\ E^-(x - \{(a_k - 1)\Delta t_{\text{True}} + c_k|\Delta t_{\text{True}}|\}, |c_k|\tau_B) & \text{if } c_k < 0. \end{cases} \quad (\text{C.17})$$

C.4 Outlier

Although the above resolution functions cover many effects but there still exists a long tail in Δt which is not described. We model these outlier tail with a Gaussian with zero mean and a width independent of the event,

$$P_{\text{Out}}(\Delta t) \equiv G(\Delta t, \sigma_{\text{Out}}). \quad (\text{C.18})$$

Vertices reconstructed from single-tracks contain a larger outlier contribution. One reason may be the worse resolution of the single-track vertices. We model this by a different outlier fraction, f_{Out} , depending on whether the vertex was reconstructed by a single-track or by multiple tracks.

The parameters of the outlier fraction are determined in the same fit as the detector resolution function, R_{Det} . The parameters are summarised in Tbl. C.4.

Table C.4: P_{Out} resolution function parameters.

	Parameter	Value (SVD1)	Value (SVD2)
Global	σ_{Out} (ps)	$37.4^{+6.8}_{-9.0}$	$33.6^{+6.8}_{-9.0}$
Multi-track	f_{Out}	0.0003 ± 0.0001	0.0002 ± 0.0001
Single-track	f_{Out}	$0.042^{+0.007}_{-0.008}$	$0.026^{+0.007}_{-0.004}$

C.5 Combined Resolution Function

The total resolution function R_{Sig} is a convolution of the three individual resolution functions explained earlier,

$$R_{Sig} \equiv R_{Det} \otimes R_{NP} \otimes R_K. \quad (C.19)$$

When we are describing the data modeling in section 4.4 the total resolution function R_{Sig} is simply referred to as the detector resolution function. But one should keep in mind that e.g. R_{Det} and R_{NP} are event depending because they strongly depend on the vertex quality. Also the resolution function differs between $B^0\bar{B}^0$ decays and B^+B^- decays.

Appendix D

Parameters of the Fit Model for all Components

In the following section we are presenting all parameters used in the fit to data. This information is useful if a future analysis is going to analyse the same channel e.g. at the Belle II experiment. A few conventions are used for naming the parameters. The first digit of the parameter defines if the parameter is used for the SVD1 or the SVD2 model. This is usually followed by an abbreviation for the channel e.g. pp for the $\pi^+\pi^-$ model or qq for the continuum model. The fit dimension e.g. M_{BC} or ΔE is appended and followed by the parameter names found in the data model section 4.4. The yields or branching fractions are abbreviated with N followed by the channel abbreviation. In an analogous way the r -bin fractions are indicated with an f.

We list all parameters with their value and the corresponding error. If no error is given the parameter is fixed or shared with a different channel.

1fpp0	0.2053065802	0.000393811877	1ppfd_w30	0.1626803473	0.005719708969
1fpp1	0.15665738	0.0003699359917	1ppfd_m30	-0.2803395484	0.007477390539
1fpp2	0.1658681365	0.0003750737667	1ppfd_s30	1.357608662	0.01550670621
1fpp3	0.1085028493	0.0003350694246	1ppfd_mcf0	0.003737445979	0.007507143136
1fpp4	0.1110208858	0.0003372919992	1ppfd_scf0	1.000690204	0.0210988573
1fpp5	0.1002164375	0.0003272581352	1ppfd_m11	0.4040907646	0.001127866942
1fpp0cf	0.9810084669	0.0241639286	1ppfd_s11	0.2678691865	0.0008220255119
1fpp1cf	1.065950901	0.03013802718	1ppfd_w21	0.6076233498	0.01028132541
1fpp2cf	0.9935780143	0.02945832917	1ppfd_m21	-0.3067106406	0.002495400411
1fpp3cf	0.9602534745	0.03495795201	1ppfd_s21	1.189982175	0.007198543914
1fpp4cf	0.9765015789	0.03321150162	1ppfd_w31	0.07045736554	0.002762818092
1fpp5cf	1.048709131	0.0385354408	1ppfd_m31	-0.2784340799	0.0115941109
1Npp	504.117567	751.3986864	1ppfd_s31	1.392820912	0.02493504837
1ppbc_m1	5.279534084	5.668206883e-06	1ppfd_mcf1	-0.01589990901	0.008252104797
1ppbc_s1	0.002555746847	3.819761887e-06	1ppfd_scf1	1.029618852	0.0226756241
1ppbc_w2	0.03412890947	0.001642520179	1ppfd_m12	0.4583800356	0.001194480362
1ppbc_m2	-0.003638930221	8.373150431e-05	1ppfd_s12	0.2586402596	0.0008464039227
1ppbc_s2	1.29921321	0.02552783539	1ppfd_w22	0.906947981	0.02602553331
1ppbc_w3	0.004026454872	0.0001798093324	1ppfd_m22	-0.3153866418	0.004008878424
1ppbc_m3	-0.00543851886	0.0003022252212	1ppfd_s22	1.167585219	0.009008402524
1ppbc_s3	1.816033905	0.04018803989	1ppfd_w32	0.1605560797	0.007465115141
1ppbc_mcf	-8.760225961e-05	7.527385047e-05	1ppfd_m32	-0.3099020454	0.01062660548
1ppbc_scf	1.004937328	0.02377332719	1ppfd_s32	1.337713584	0.01758960101
1ppe_m1	0.002175037128	2.501795568e-05	1ppfd_mcf2	-0.005790521321	0.009011971521
1ppe_s1	0.01545676471	2.016066309e-05	1ppfd_scf2	1.039878033	0.02591663879
1ppe_w2	0.1522790735	0.001811597795	1ppfd_m13	0.4755045668	0.00218284263
1ppe_m2	-0.008816553637	0.0001883000468	1ppfd_s13	0.2506055767	0.001140982072
1ppe_s2	2.153300051	0.009640456158	1ppfd_w23	0.7956016374	0.02785402363
1ppe_w3	0.08633293287	0.0006912064109	1ppfd_m23	-0.3202348589	0.003456855406
1ppe_m3	-0.06541118388	0.0008722801171	1ppfd_s23	1.095555794	0.009700380365
1ppe_s3	2.909939161	0.02038146426	1ppfd_w33	0.3638719507	0.01361158671
1ppe_mcf	-0.003939033354	0.0002099344503	1ppfd_m33	-0.1966136919	0.006239057589
1ppe_scf	1.169582257	0.01461227109	1ppfd_s33	1.483964717	0.01470066358
1ppd_m10	0.4247118248	0.0009753378315	1ppfd_mcf3	0.003112051188	0.01002517687
1ppd_s10	0.2559778743	0.0007188758709	1ppfd_scf3	0.9826006372	0.02989110688
1ppd_w20	0.8344163386	0.01634475707	1ppfd_m14	0.4569952858	0.001344637352
1ppd_m20	-0.2750991938	0.00226999142	1ppfd_s14	0.2637851404	0.001012825251
1ppd_s20	1.183307451	0.005978417123	1ppfd_w24	0.8225757145	0.01985285718

1ppfd_m24	-0.3174026627	0.003246344349	2fpp2cf	0.9816255597	0.0125018558
1ppfd_s24	1.179778848	0.008351536584	2fpp3cf	1.02510383	0.01597833981
1ppfd_w34	0.1616969667	0.005707747572	2fpp4cf	0.975676463	0.01684059545
1ppfd_m34	-0.2635680094	0.009562399335	2fpp5cf	0.9455046339	0.01773270878
1ppfd_s34	1.333159308	0.01987370154	2Npp	5.49255298e-06	1.821348966e-07
1ppfd_mcf4	-0.008184970868	0.01016867552	2ppmbc_m1	5.279449652	4.116695755e-06
1ppfd_scf4	1.028959353	0.02780057372	2ppmbc_s1	0.002561677519	2.55257452e-06
1ppfd_m15	0.5424607022	0.001350072245	2ppmbc_w2	0.04586437634	0.002179635419
1ppfd_s15	0.2475726693	0.001241704285	2ppmbc_m2	-0.002858668059	6.94819658e-05
1ppfd_w25	1.600832421	0.1144232997	2ppmbc_s2	1.249097731	0.01273865186
1ppfd_m25	-0.3145396173	0.003949389687	2ppmbc_w3	0.005397911348	0.0001943346318
1ppfd_s25	1.257784966	0.01947377739	2ppmbc_m3	-0.005311242661	0.0001395953831
1ppfd_w35	0.4762610566	0.01603322569	2ppmbc_s3	1.782963345	0.03145329899
1ppfd_m35	-0.2641887892	0.01508047719	2ppmbc_mcf	0.0002174012535	4.673319575e-05
1ppfd_s35	1.359216878	0.01752733863	2ppmbc_scf	1.009871054	0.01488065122
1ppfd_mcf5	-0.002927912233	0.01159974372	2ppde_m1	0.001360343619	2.377021116e-05
1ppfd_scf5	1.052867645	0.02955589223	2ppde_s1	0.01542607159	1.917596383e-05
1ppfd_m16	0.6234460843	0.001352608949	2ppde_w2	0.1688231158	0.001799128927
1ppfd_s16	0.2304147216	0.001051345078	2ppde_m2	-0.004447379793	0.0001661850414
1ppfd_w26	1.635267604	0.06868056036	2ppde_s2	2.177713149	0.008297586947
1ppfd_m26	-0.3601490753	0.002581583531	2ppde_w3	0.09277613731	0.0006530641462
1ppfd_s26	1.314649125	0.01519763903	2ppde_m3	-0.06378709354	0.0007306830257
1ppfd_w36	0.498899441	0.002632874406	2ppde_s3	2.916553075	0.01930542717
1ppfd_m36	-0.3577105806	0.00646539851	2ppde_mcf	-0.001293523411	0.00010157266
1ppfd_s36	1.256963969	0.01530688979	2ppde_scf	1.215711704	0.007055243918
1ppfd_mcf6	0.004210374623	0.009603832093	2ppfd_m10	0.4154373483	0.0009114190887
1ppfd_scf6	1.078201959	0.02776558893	2ppfd_s10	0.2471547619	0.000646062536
1pptau	0	0	2ppfd_w20	0.790362953	0.01039370571
1ppAcp	0	0	2ppfd_m20	-0.3057155384	0.001891123519
1ppScp	0	0	2ppfd_s20	1.311166138	0.005689296742
2fpp0	0.2039714517	0.0003742774573	2ppfd_w30	0.107296346	0.0030575766
2fpp1	0.1419882003	0.0003428301818	2ppfd_m30	-0.2535161043	0.009672790758
2fpp2	0.1816914971	0.0003645894493	2ppfd_s30	1.690440367	0.01877468613
2fpp3	0.1211196758	0.000328182091	2ppfd_mcf0	-0.005125849673	0.003392306942
2fpp4	0.09655388785	0.0003067991068	2ppfd_scf0	1.004672072	0.009604049238
2fpp5	0.0948478439	0.0003050335388	2ppfd_m11	0.4142409389	0.00108890951
2fpp0cf	1.015941117	0.01120581976	2ppfd_s11	0.2476852461	0.0007783445681
2fpp1cf	1.031345514	0.01448397607	2ppfd_w21	0.7813140446	0.01195960724

2ppfd_m21	-0.313223203	0.002285912627	2ppfd_s15	0.2276036613	0.0008982476892
2ppfd_s21	1.310132967	0.006911347678	2ppfd_w25	1.276125751	0.02320552633
2ppfd_w31	0.0964416587	0.003376114034	2ppfd_m25	-0.3335697744	0.00233306242
2ppfd_m31	-0.2757396004	0.01224919725	2ppfd_s25	1.382526433	0.007652453597
2ppfd_s31	1.692565741	0.0239831112	2ppfd_w35	0.1563136587	0.00601456147
2ppfd_mcf1	-0.01286999305	0.004048884831	2ppfd_m35	-0.2933432966	0.01266074117
2ppfd_scf1	1.018927829	0.011558486	2ppfd_s35	1.661362346	0.02547309011
2ppfd_m12	0.4528869895	0.001018793555	2ppfd_mcf5	-0.008605887176	0
2ppfd_s12	0.2395191652	0.0006898095569	2ppfd_scf5	1.033846636	0
2ppfd_w22	1.211532335	0.01800622599	2ppfd_m16	0.5602306956	0.00127134192
2ppfd_m22	-0.3032705471	0.001785736919	2ppfd_s16	0.1991881025	0.0008834264265
2ppfd_s22	1.338011031	0.005703465751	2ppfd_w26	1.787983752	0.0380022393
2ppfd_w32	0.1435224114	0.003900249857	2ppfd_m26	-0.3380161648	0.001835376699
2ppfd_m32	-0.3366902771	0.009519766491	2ppfd_s26	1.511714836	0.008143789083
2ppfd_s32	1.655291512	0.01934291146	2ppfd_w36	0.2220277607	0.005915227504
2ppfd_mcf2	-0.01297608026	0	2ppfd_m36	-0.2986876463	0.008124253895
2ppfd_scf2	1.023758481	0	2ppfd_s36	1.487432743	0.017536824
2ppfd_m13	0.4478087785	0.001221295677	2ppfd_mcf6	-0.009678363912	0
2ppfd_s13	0.2389645151	0.0008128542567	2ppfd_scf6	1.02926003	0
2ppfd_w23	1.147984665	0.02030911423	2ppta	1.525	0
2ppfd_m23	-0.3098451603	0.00234065256	2ppAcp	0.4771534598	0.07176432274
2ppfd_s23	1.357401029	0.006897219016	2ppScp	-0.6375034223	0.08719935748
2ppfd_w33	0.133977609	0.004848291865	1fkpi0	0.2039053445	0.0005470891697
2ppfd_m33	-0.2956675428	0.01276975892	1fkpi1	0.1569596417	0.0004929962884
2ppfd_s33	1.663661591	0.02417752809	1fkpi2	0.1667821068	0.0005054395272
2ppfd_mcf3	-0.01451155145	0	1fkpi3	0.108593088	0.00042066642
2ppfd_scf3	1.028552501	0	1fkpi4	0.1105571922	0.0004240289696
2ppfd_m14	0.4751150571	0.001466955819	1fkpi5	0.1006680134	0.0004066530666
2ppfd_s14	0.2297291999	0.0009611479156	1fkpi0cf	0.9810084669	0.001
2ppfd_w24	1.386187875	0.03362071646	1fkpi1cf	1.065950901	0.001
2ppfd_m24	-0.3092328476	0.002673429603	1fkpi2cf	0.9935780143	0.001
2ppfd_s24	1.358860646	0.008248137694	1fkpi3cf	0.9602534745	0.001
2ppfd_w34	0.1929978218	0.00685505673	1fkpi4cf	0.9765015789	0.001
2ppfd_m34	-0.2774668869	0.01157718886	1fkpi5cf	1.048709131	0.001
2ppfd_s34	1.640400332	0.02322903304	1fkpi	1655.448393	744.2681968
2ppfd_mcf4	-0.01334090263	0	1kpiAcp	0	0
2ppfd_scf4	1.05132212	0	1kpimbc_m1	5.279688897	5.736448616e-05
2ppfd_m15	0.4898888368	0.001352793348	1kpimbc_s1	0.002501139143	1.610759958e-05

1kpimbc_w2	0.149512731	0.03048059282	1kpifd_mi2	0.4583800356	0.001194480362
1kpimbc_m2	-0.002246426671	0.000128990623	1kpifd_s12	0.2586402596	0.0008464039227
1kpimbc_s2	1.144085825	0.04569313403	1kpifd_w22	0.906947981	0.02602553331
1kpimbc_w3	0.004162592956	0.0007912386509	1kpifd_m22	-0.3153864148	0.004008878424
1kpimbc_m3	-0.005652146989	0.0004617822103	1kpifd_s22	1.167585219	0.009008402524
1kpimbc_s3	2.151898376	0.06447320515	1kpifd_w32	0.1605560797	0.007465115141
1kpimbc_mcf	-8.760225961e-05	0	1kpifd_m32	-0.3099020454	0.01062660548
1kpimbc_scf	1.004937328	0	1kpifd_s32	1.337713584	0.01758960101
1kpide_m1	-0.04178928058	3.33077895e-05	1kpifd_mcf2	-0.005790521321	0
1kpide_s1	0.01790292777	3.963091199e-05	1kpifd_scf2	1.039878033	0
1kpide_w2	0.1096720618	0.003284042897	1kpifd_mi3	0.4755045668	0.00218284263
1kpide_m2	-0.01099264531	0.0005302270789	1kpifd_si3	0.2506055767	0.001140982072
1kpide_s2	2.20338904	0.03263572679	1kpifd_w23	0.7956016374	0.02785402363
1kpide_w3	0.06942345609	0.001129546784	1kpifd_m23	-0.3202348589	0.003456855406
1kpide_m3	-0.07161972571	0.003704264179	1kpifd_s23	1.095555794	0.009700380365
1kpide_s3	2.96355074	0.05206059006	1kpifd_w33	0.3638719507	0.01361158671
1kpide_mcf	-0.003939033354	0	1kpifd_m33	-0.1966136919	0.006239057589
1kpide_scf	1.169582257	0	1kpifd_s33	1.483964717	0.01470066358
1kpifd_m10	0.4247118248	0.0009753378315	1kpifd_mcf3	0.003112051188	0
1kpifd_s10	0.2559778743	0.0007188758709	1kpifd_scf3	0.9826006372	0
1kpifd_w20	0.8344163386	0.01634475707	1kpifd_m14	0.4569952858	0.001344637352
1kpifd_m20	-0.2750991938	0.00226999142	1kpifd_s14	0.2637851404	0.001012825251
1kpifd_s20	1.183307451	0.005978417123	1kpifd_w24	0.8225757145	0.01985285718
1kpifd_w30	0.1626803473	0.005719708969	1kpifd_m24	-0.3174026627	0.003246344349
1kpifd_m30	-0.2803395484	0.007477390539	1kpifd_s24	1.179778848	0.008351536584
1kpifd_s30	1.357608662	0.01550670621	1kpifd_w34	0.1616969667	0.005707747572
1kpifd_mcf0	0.003737445979	0	1kpifd_m34	-0.2635680094	0.009562399335
1kpifd_scf0	1.000690204	0	1kpifd_s34	1.333159308	0.01987370154
1kpifd_m11	0.4040907646	0.001127866942	1kpifd_mcf4	-0.008184970868	0
1kpifd_s11	0.2678691865	0.0008220255119	1kpifd_scf4	1.028959353	0
1kpifd_w21	0.6076233498	0.01028132541	1kpifd_m15	0.5424607022	0.001350072245
1kpifd_m21	-0.3067106406	0.002495400411	1kpifd_s15	0.2475726693	0.001241704285
1kpifd_s21	1.189982175	0.007198543914	1kpifd_w25	1.600832421	0.1144232997
1kpifd_w31	0.07045736554	0.002762818092	1kpifd_m25	-0.3145396173	0.003949389687
1kpifd_m31	-0.2784340799	0.0115941109	1kpifd_s25	1.257784966	0.01947377739
1kpifd_s31	1.392820912	0.02493504837	1kpifd_w35	0.4762610566	0.01603322569
1kpifd_mcf1	-0.01589990901	0	1kpifd_m35	-0.2641887892	0.01508047719
1kpifd_scf1	1.029618852	0	1kpifd_s35	1.359216878	0.01752733863

1kpidf_mcf5	-0.002927912233	0	2kptide_s1	0.01788952627	4.07762585e-05
1kpidf_scf5	1.052867645	0	2kptide_w2	0.1234849968	0.003576953531
1kpidf_m16	0.6234460843	0.001352608949	2kptide_m2	-0.006311481006	0.0004259966714
1kpidf_s16	0.2304147216	0.001051345078	2kptide_s2	2.209015778	0.03159082222
1kpidf_w26	1.635267604	0.06868056036	2kptide_w3	0.06869530672	0.001213701852
1kpidf_m26	-0.3601490753	0.002581583531	2kptide_m3	-0.06495186483	0.003151017489
1kpidf_s26	1.314649125	0.01519763903	2kptide_s3	2.734598702	0.04509390673
1kpidf_w36	0.498899441	0.002632874406	2kptide_mcf	-0.001293523411	0
1kpidf_m36	-0.3577105806	0.00646539851	2kptide_scf	1.215711704	0
1kpidf_s36	1.256963969	0.01530688979	2kpidf_m10	0.4154373483	0.0009114190887
1kpidf_mcf6	0.004210374623	0	2kpidf_s10	0.2471547619	0.000646062536
1kpidf_scf6	1.078201959	0	2kpidf_w20	0.790362953	0.01039370571
1kpitau	0	0	2kpidf_m20	-0.3057155384	0.001891123519
2fkpi0	0.2037044909	0.0005152376661	2kpidf_s20	1.311166138	0.005689296742
2fkpi1	0.1420836513	0.0004456384663	2kpidf_w30	0.107296346	0.0030575766
2fkpi2	0.1814894263	0.0004927026617	2kpidf_m30	-0.2535161043	0.009672790758
2fkpi3	0.1214432235	0.0004165601142	2kpidf_s30	1.690440367	0.01877468613
2fkpi4	0.09763110035	0.0003781171782	2kpidf_mcf0	-0.005125849673	0
2fkpi5	0.09383258378	0.0003714024162	2kpidf_scf0	1.004672072	0
2fkpi0cf	1.015941117	0.001	2kpidf_m11	0.4142409389	0.00108890951
2fkpi1cf	1.031345514	0.001	2kpidf_s11	0.2476852461	0.0007783445681
2fkpi2cf	0.9816255597	0.001	2kpidf_w21	0.7813140446	0.01195960724
2fkpi3cf	1.02510383	0.001	2kpidf_m21	-0.313223203	0.002285912627
2fkpi4cf	0.975676463	0.001	2kpidf_s21	1.310132967	0.006911347678
2fkpi5cf	0.9455046339	0.001	2kpidf_w31	0.0964416587	0.003376114034
2Nkpi	1.835046945e-05	2.927003391e-07	2kpidf_m31	-0.2757396004	0.01224919725
2kpiAcp	-0.07390012861	0.01620372058	2kpidf_s31	1.6925665741	0.0239831112
2kpiabc_m1	5.279601359	4.849048771e-05	2kpidf_mcf1	-0.01286999305	0
2kpiabc_s1	0.002512450962	1.330956325e-05	2kpidf_scf1	1.018927829	0
2kpiabc_w2	0.1578096554	0.02479359205	2kpidf_m12	0.4528869895	0.001018793555
2kpiabc_m2	-0.002207198171	0.0001433022413	2kpidf_s12	0.2395191652	0.0006898095569
2kpiabc_s2	1.131608458	0.03903356748	2kpidf_w22	1.211532335	0.01800622599
2kpiabc_w3	0.004574439511	0.0007964970811	2kpidf_m22	-0.3032705471	0.001785736919
2kpiabc_m3	-0.005169471519	0.0004563679583	2kpidf_s22	1.388011031	0.005703465751
2kpiabc_s3	1.959826255	0.06055387564	2kpidf_w32	0.1435224114	0.003900249857
2kpiabc_mcf	0.0002174012535	0	2kpidf_m32	-0.3366902771	0.009519766491
2kpiabc_scf	1.009871054	0	2kpidf_s32	1.655291512	0.01934291146
2kptide_m1	-0.0425565743	3.102971136e-05	2kpidf_mcf2	-0.01297608026	0

2kpidf_scf2	1.023758481	0	2kpidf_s36	1.487432743	0.017536824
2kpidf_m13	0.4478087785	0.001221295677	2kpidf_mcf6	-0.009678363912	0
2kpidf_s13	0.2389645151	0.0008128542567	2kpidf_scf6	1.02926003	0
2kpidf_w23	1.147984665	0.02030911423	2kpitau	1.525	0
2kpidf_m23	-0.3098451603	0.00234065256	1fkk0	0.2039566641	0.0005541052506
2kpidf_s23	1.357401029	0.006897219016	1fkk1	0.1568917912	0.0004990929316
2kpidf_w33	0.133977609	0.004848291865	1fkk2	0.1661812804	0.0005110599283
2kpidf_m33	-0.2956675428	0.01276975892	1fkk3	0.1086999821	0.0004261608419
2kpidf_s33	1.663661591	0.02417752809	1fkk4	0.1107277039	0.0004296541569
2kpidf_mcf3	-0.01451155145	0	1fkk5	0.1006619253	0.0004117585752
2kpidf_scf3	1.028552501	0	1fkk0cf	0.9810084669	0.001
2kpidf_m14	0.4751150571	0.001466955819	1fkk1cf	1.065950901	0.001
2kpidf_s14	0.2297291999	0.0009611479156	1fkk2cf	0.9935780143	0.001
2kpidf_w24	1.386187875	0.03362071646	1fkk3cf	0.9602534745	0.001
2kpidf_m24	-0.3092328476	0.002673429603	1fkk4cf	0.9765015789	0.001
2kpidf_s24	1.358860646	0.008248137694	1fkk5cf	1.048709131	0.001
2kpidf_w34	0.1929978218	0.00685505673	1Nkk	6.374535583	734.9000357
2kpidf_m34	-0.2774668869	0.01157718886	1kkmbc_m1	5.280245891	3.047333805e-05
2kpidf_s34	1.640400332	0.02322903304	1kkmbc_s1	0.002380379304	8.811292077e-06
2kpidf_mcf4	-0.01334090263	0	1kkmbc_w2	0.7706890422	0.009721126768
2kpidf_scf4	1.05132212	0	1kkmbc_m2	-0.002147281574	6.754104442e-05
2kpidf_m15	0.489888368	0.001352793348	1kkmbc_s2	1.143493728	0.007363452493
2kpidf_s15	0.2276036613	0.0008982476892	1kkmbc_w3	0.00644829279	0.0006111806146
2kpidf_w25	1.276125751	0.02320552633	1kkmbc_m3	-0.006113083187	0.0004050676434
2kpidf_m25	-0.3335697744	0.00233306242	1kkmbc_s3	2.209906536	0.05569335622
2kpidf_s25	1.382526433	0.007652453597	1kkmbc_mcf	-8.760225961e-05	0
2kpidf_w35	0.1563136587	0.00601456147	1kkmbc_scf	1.004937328	0
2kpidf_m35	-0.2933432966	0.01266074117	1kkde_m1	-0.08641937052	2.927317194e-05
2kpidf_s35	1.661362346	0.02547309011	1kkde_s1	0.01529340609	4.210533357e-05
2kpidf_mcf5	-0.008605887176	0	1kkde_w2	0.1589512882	0.005245803508
2kpidf_scf5	1.033846636	0	1kkde_m2	-0.003686441225	0.0002814494669
2kpidf_m16	0.5602306956	0.00127134192	1kkde_s2	2.128304334	0.02517634019
2kpidf_s16	0.1991881025	0.0008834264265	1kkde_w3	0.09856497509	0.003765151949
2kpidf_w26	1.787983752	0.0380022393	1kkde_m3	-0.1461584536	0.007447213039
2kpidf_m26	-0.3380161648	0.001835376699	1kkde_s3	4.763576462	0.08656947443
2kpidf_s26	1.511714836	0.008143789083	1kkde_mcf	-0.003939033354	0
2kpidf_w36	0.2220277607	0.005915227504	1kkde_scf	1.169582257	0
2kpidf_m36	-0.2986876463	0.008124253895	1kkfd_m10	0.4247118248	0.0009753378315

1kkfd_s10	0.2559778743	0.0007188758709	1kkfd_scf3	0.9826006372	0
1kkfd_w20	0.8344163386	0.01634475707	1kkfd_m14	0.4569952858	0.0013444637352
1kkfd_m20	-0.2750991938	0.00226999142	1kkfd_s14	0.2637851404	0.001012825251
1kkfd_s20	1.183307451	0.005978417123	1kkfd_w24	0.8225757145	0.01985285718
1kkfd_w30	0.1626803473	0.005719708969	1kkfd_m24	-0.3174026627	0.003246344349
1kkfd_m30	-0.2803395484	0.007477390539	1kkfd_s24	1.179778848	0.008351536584
1kkfd_s30	1.357608662	0.01550670621	1kkfd_w34	0.1616969667	0.005707747572
1kkfd_mcf0	0.003737445979	0	1kkfd_m34	-0.2635680094	0.009562399335
1kkfd_scf0	1.000690204	0	1kkfd_s34	1.333159308	0.01987370154
1kkfd_m11	0.4040907646	0.001127866942	1kkfd_mcf4	-0.008184970868	0
1kkfd_s11	0.2678691865	0.0008220255119	1kkfd_scf4	1.028959353	0
1kkfd_w21	0.6076233498	0.01028132541	1kkfd_m15	0.5424607022	0.001350072245
1kkfd_m21	-0.3067106406	0.002495400411	1kkfd_s15	0.2475726693	0.001241704285
1kkfd_s21	1.189982175	0.007198543914	1kkfd_w25	1.600832421	0.1144232997
1kkfd_w31	0.07045736554	0.002762818092	1kkfd_m25	-0.3145396173	0.003949389687
1kkfd_m31	-0.2784340799	0.0115941109	1kkfd_s25	1.257784966	0.01947377739
1kkfd_s31	1.392820912	0.02493504837	1kkfd_w35	0.4762610566	0.01603322569
1kkfd_mcf1	-0.01589990901	0	1kkfd_m35	-0.2641887892	0.01508047719
1kkfd_scf1	1.029618852	0	1kkfd_s35	1.359216878	0.01752733863
1kkfd_m12	0.4583800356	0.001194480362	1kkfd_mcf5	-0.002927912233	0
1kkfd_s12	0.2586402596	0.0008464039227	1kkfd_scf5	1.052867645	0
1kkfd_w22	0.906947981	0.02602553331	1kkfd_m16	0.6234460843	0.001352608949
1kkfd_m22	-0.3153864148	0.004008878424	1kkfd_s16	0.2304147216	0.001051345078
1kkfd_s22	1.167585219	0.009008402524	1kkfd_w26	1.635267604	0.06868056036
1kkfd_w32	0.1605560797	0.007465115141	1kkfd_m26	-0.3601490753	0.002581583531
1kkfd_m32	-0.3099020454	0.01062660548	1kkfd_s26	1.314649125	0.01519763903
1kkfd_s32	1.337713584	0.01758960101	1kkfd_w36	0.498899441	0.002632874406
1kkfd_mcf2	-0.005790521321	0	1kkfd_m36	-0.3577105806	0.00646539851
1kkfd_scf2	1.039878033	0	1kkfd_s36	1.256963969	0.01530688979
1kkfd_m13	0.4755045668	0.00218284263	1kkfd_mcf6	0.004210374623	0
1kkfd_s13	0.2506055767	0.001140982072	1kkfd_scf6	1.078201959	0
1kkfd_w23	0.7956016374	0.02785402363	1kkftau	0	0
1kkfd_m23	-0.3202348589	0.003456855406	1kkacp	0	0
1kkfd_s23	1.095555794	0.009700380365	1kkScp	0	0
1kkfd_w33	0.3638719507	0.01361158671	2fkk0	0.2035696716	0.0005213586631
1kkfd_m33	-0.1966136919	0.006239057589	2fkk1	0.1417171414	0.0004507053087
1kkfd_s33	1.483964717	0.01470066358	2fkk2	0.1817423247	0.0004989511007
1kkfd_mcf3	0.003112051188	0	2fkk3	0.1214635328	0.0004217016705

2fkk4	0.09664283266	0.0003809874203	2kkfd_scf0	1.004672072	0
2fkk5	0.09363563354	0.0003756449162	2kkfd_m11	0.4142409389	0.00108890951
2fkk0cf	1.015941117	0.001	2kkfd_s11	0.2476852461	0.0007783445681
2fkk1cf	1.031345514	0.001	2kkfd_w21	0.7813140446	0.01195960724
2fkk2cf	0.9816255597	0.001	2kkfd_m21	-0.313223203	0.002285912627
2fkk3cf	1.02510383	0.001	2kkfd_s21	1.310132967	0.006911347678
2fkk4cf	0.975676463	0.001	2kkfd_w31	0.0964416587	0.003376114034
2fkk5cf	0.9455046339	0.001	2kkfd_m31	-0.2757396004	0.01224919725
2Nkk	7.221082737e-08	5.914731357e-08	2kkfd_s31	1.692565741	0.0239831112
2kkmbc_m1	5.280062198	3.059051495e-05	2kkfd_mcf1	-0.01286999305	0
2kkmbc_s1	0.002418260732	8.185507503e-06	2kkfd_scf1	1.018927829	0
2kkmbc_w2	0.6984193381	0.01619515837	2kkfd_m12	0.4528869895	0.001018793555
2kkmbc_m2	-0.002065691409	7.051557812e-05	2kkfd_s12	0.2395191652	0.0006898095569
2kkmbc_w3	1.141937545	0.007997303164	2kkfd_w22	1.211532335	0.01800622599
2kkmbc_m3	0.006256226822	0.000606732424	2kkfd_m22	-0.3032705471	0.001785736919
2kkmbc_s3	-0.005957881396	0.0003975368733	2kkfd_s22	1.338011031	0.005703465751
2kkmbc_mcf	2.137169565	0.05257726455	2kkfd_w32	0.1435224114	0.003900249857
2kkmbc_scf	0.0002174012535	0	2kkfd_m32	-0.3366902771	0.009519766491
2kkde_m1	1.009871054	0	2kkfd_s32	1.655291512	0.01934291146
2kkde_s1	-0.08722994532	2.727360127e-05	2kkfd_mcf2	-0.01297608026	0
2kkde_w2	0.01537783831	4.024127838e-05	2kkfd_scf2	1.023758481	0
2kkde_m2	0.1492886383	0.00473402526	2kkfd_m13	0.4478087785	0.001221295677
2kkde_s2	-0.002110694513	0.0002672258962	2kkfd_s13	0.2389645151	0.0008128542567
2kkde_w3	2.16971697	0.0272349494	2kkfd_w23	1.147984665	0.02030911423
2kkde_m3	0.07962454497	0.002483162622	2kkfd_m23	-0.3098451603	0.00234065256
2kkde_s3	-0.1140504642	0.006347843563	2kkfd_s23	1.357401029	0.006897219016
2kkde_mcf	4.06724641	0.07422377004	2kkfd_w33	0.133977609	0.004848291865
2kkde_scf	-0.001293523411	0	2kkfd_m33	-0.2956675428	0.01276975892
2kkfd_m10	1.215711704	0	2kkfd_s33	1.663661591	0.02417752809
2kkfd_s10	0.4154373483	0.0009114190887	2kkfd_mcf3	-0.01451155145	0
2kkfd_w20	0.2471547619	0.000646062536	2kkfd_scf3	1.028552501	0
2kkfd_m20	0.790362953	0.01039370571	2kkfd_m14	0.4751150571	0.001466955819
2kkfd_s20	-0.3057155384	0.001891123519	2kkfd_s14	0.2297291999	0.0009611479156
2kkfd_w30	1.311166138	0.005689296742	2kkfd_w24	1.386187875	0.03362071646
2kkfd_m30	0.107296346	0.0030575766	2kkfd_m24	-0.3092328476	0.002673429603
2kkfd_s30	-0.2535161043	0.009672790758	2kkfd_s24	1.358860646	0.008248137694
2kkfd_wcf0	1.690440367	0.01877468613	2kkfd_w34	0.1929978218	0.00685505673
2kkfd_mcf0	-0.005125849673	0	2kkfd_m34	-0.2774668869	0.01157718886

2kafd_s34	1.640400332	0.02322903304	1Mqq	89520.15249	295.1689456
2kafd_mcf4	-0.01334090263	0	1qqmbc_a	-24.80156671	0.6831115168
2kafd_scf4	1.05132212	0	1qqde_c10	-0.665553086	0.03930468476
2kafd_m15	0.4898888368	0.001352793348	1qqde_c20	-1.758585307	0.1336505281
2kafd_s15	0.2276036613	0.0008982476892	1qqde_c11	-0.801339048	0.04897842075
2kafd_w25	1.276125751	0.02320552633	1qqde_c21	0	0.001
2kafd_m25	-0.3335697744	0.00233306242	1qqde_c12	-0.7216799188	0.05674207984
2kafd_s25	1.382526433	0.007652453597	1qqde_c22	0	0.001
2kafd_w35	0.1563136587	0.00601456147	1qqde_c13	-0.697506361	0.06921610728
2kafd_m35	-0.2933432966	0.01266074117	1qqde_c23	0	0.001
2kafd_s35	1.661362346	0.02547309011	1qqde_c14	-0.8134075245	0.06940705183
2kafd_mcf5	-0.008605887176	0	1qqde_c24	0	0.001
2kafd_scf5	1.033846636	0	1qqde_c15	-0.7980241043	0.08183909754
2kafd_m16	0.5602306956	0.00127134192	1qqde_c25	0	0.001
2kafd_s16	0.1991881025	0.0008834264265	1qqde_c16	-1.120601342	0.1560557532
2kafd_w26	1.787983752	0.0380022393	1qqde_c26	0	0.001
2kafd_m26	-0.3380161648	0.001835376699	1qqfd_pm10	-0.06632586254	0.00339603453
2kafd_s26	1.511714836	0.008143789083	1qqfd_ps10	0.274878651	0.002027527764
2kafd_w36	0.2220277607	0.005915227504	1qqfd_pw20	1.631879689	0.3519341889
2kafd_m36	-0.2986876463	0.008124253895	1qqfd_pm20	-0.3760664419	0.03601990743
2kafd_s36	1.487432743	0.017536824	1qqfd_ps20	1.441154283	0.07438701892
2kafd_mcf6	-0.009678363912	0	1qqfd_pw30	0	0.001
2kafd_scf6	1.02926003	0	1qqfd_pm30	0	0.001
2kktau	1.525	0	1qqfd_ps30	1	0.001
2kkaCp	0	0.002072776374	1qqfd_pmcF0	0	0
2kksCp	0	0.003005630055	1qqfd_pscF0	1	0
1fq0	0.3598788319	0.01280556971	1qqfd_pm11	-0.08296442276	0.004164582777
1fq1	0.2327065992	0.00781910384	1qqfd_ps11	0.28816801	0.002544182428
1fq2	0.1505968834	0.004992410317	1qqfd_pw21	1.953890732	0.5852442107
1fq3	0.08849358116	0.00329709576	1qqfd_pm21	-0.34105794	0.047569276
1fq4	0.09877858922	0.003562935372	1qqfd_ps21	1.344325708	0.08418459185
1fq5	0.05543989608	0.002439809453	1qqfd_pw31	0	0.001
1fq0cf	1.002039138	0.0121738733	1qqfd_pm31	0	0.001
1fq1cf	0.9854729684	0.01292737245	1qqfd_ps31	1	0.001
1fq2cf	0.9873615231	0.01149505978	1qqfd_pmcF1	0	0
1fq3cf	1.057037604	0.01338485712	1qqfd_pscF1	1	0
1fq4cf	0.9660031911	0.01216354595	1qqfd_pm12	-0.1061916455	0.00530652137
1fq5cf	1.052439403	0.01567609338	1qqfd_ps12	0.2902184499	0.003424387332

1qqfd_pw22	1.383225424	0.310530789	1qqfd_pm16	-0.1614921172	0.02107577138
1qqfd_pm22	-0.3892829774	0.03816353542	1qqfd_ps16	0.3340829802	0.01367662563
1qqfd_ps22	1.338095918	0.06863767529	1qqfd_pw26	0	0.001
1qqfd_pw32	0	0.001	1qqfd_pm26	0	0.001
1qqfd_pm32	0	0.001	1qqfd_ps26	1	0.001
1qqfd_ps32	1	0.001	1qqfd_pw36	0	0.001
1qqfd_pmcf2	0	0	1qqfd_pm36	0	0.001
1qqfd_pscf2	1	0	1qqfd_ps36	1	0.001
1qqfd_pm13	-0.08434059068	0.006813128961	1qqfd_pmcf6	0	0
1qqfd_ps13	0.2878586588	0.004385450415	1qqfd_pscf6	1	0
1qqfd_pw23	0	0.001	1qqfd_km10	-0.09725014948	0.002731202928
1qqfd_pm23	0	0.001	1qqfd_ks10	0.2995656299	0.001901066709
1qqfd_ps23	1	0.001	1qqfd_kw20	0.7440431601	0.1610034106
1qqfd_pw33	0	0.001	1qqfd_km20	-0.354653325	0.04303501018
1qqfd_pm33	0	0.001	1qqfd_ks20	1.314434879	0.06491400744
1qqfd_ps33	1	0.001	1qqfd_kw30	0	0.001
1qqfd_pmcf3	0	0	1qqfd_km30	0	0.001
1qqfd_pscf3	1	0	1qqfd_ks30	1	0.001
1qqfd_pm14	-0.09727657335	0.006597102586	1qqfd_kmcf0	0	0
1qqfd_ps14	0.2817530063	0.00426440555	1qqfd_kscf0	1	0
1qqfd_pw24	0	0.001	1qqfd_km11	-0.07636466177	0.003414728072
1qqfd_pm24	0	0.001	1qqfd_ks11	0.2954511013	0.002294671517
1qqfd_ps24	1	0.001	1qqfd_kw21	1.0702665387	0.1813074485
1qqfd_pw34	0	0.001	1qqfd_km21	-0.339461765	0.02831437475
1qqfd_pm34	0	0.001	1qqfd_ks21	1.29132585	0.04516146462
1qqfd_ps34	1	0.001	1qqfd_kw31	0	0.001
1qqfd_pmcf4	0	0	1qqfd_km31	0	0.001
1qqfd_pscf4	1	0	1qqfd_ks31	1	0.001
1qqfd_pm15	-0.1565502683	0.008865612266	1qqfd_kmcf1	0	0
1qqfd_ps15	0.288633253	0.005759382625	1qqfd_kscf1	1	0
1qqfd_pw25	0	0.001	1qqfd_km12	-0.1085300197	0.004301226077
1qqfd_pm25	0	0.001	1qqfd_ks12	0.2992106084	0.002894633742
1qqfd_ps25	1	0.001	1qqfd_kw22	0	0.001
1qqfd_pw35	0	0.001	1qqfd_km22	0	0.001
1qqfd_pm35	0	0.001	1qqfd_ks22	1	0.001
1qqfd_ps35	1	0.001	1qqfd_kw32	0	0.001
1qqfd_pmcf5	0	0	1qqfd_km32	0	0.001
1qqfd_pscf5	1	0	1qqfd_ks32	1	0.001

1qqfd_kmcf2	0	0	1qqfd_km36	0	0.001
1qqfd_kscf2	1	0	1qqfd_ks36	1	0.001
1qqfd_km13	-0.08679497739	0.005322965725	1qqfd_kmcf6	0	0
1qqfd_ks13	0.299306608	0.003577450399	1qqfd_kscf6	1	0
1qqfd_kw23	0	0.001	1qppid_c10	0.02074016165	0.01020492976
1qqfd_km23	0	0.001	1qppid_c20	1.062353467	0.08305688703
1qqfd_ks23	1	0.001	1qppid_c11	0.1125124778	0.01298319609
1qqfd_kw33	0	0.001	1qppid_c21	0	0
1qqfd_km33	0	0.001	1qppid_c12	0.135189381	0.01600690755
1qqfd_ks33	1	0.001	1qppid_c22	0	0
1qqfd_kmcf3	0	0	1qppid_c13	0.2550281548	0.01960584988
1qqfd_kscf3	1	0	1qppid_c23	0	0
1qqfd_km14	-0.1141663671	0.005208775445	1qppid_c14	0.4589124118	0.01844205535
1qqfd_ks14	0.2939777195	0.003499187887	1qppid_c24	0	0
1qqfd_kw24	0	0.001	1qppid_c15	0.6137318267	0.0209348856
1qqfd_km24	0	0.001	1qppid_c25	0	0
1qqfd_ks24	1	0.001	1qppid_c16	0.6527628541	0.0403060917
1qqfd_kw34	0	0.001	1qppid_c26	0	0
1qqfd_km34	0	0.001	1qptaueff	0.450389138	0.04534668833
1qqfd_ks34	1	0.001	1qqpmu	-0.06011173831	0.01974488666
1qqfd_kmcf4	0	0	1qqfp	0.6134561257	0.0653378572
1qqfd_kscf4	1	0	1qqmresmu	-0.002120667554	0.04113516794
1qqfd_km15	-0.1855289684	0.006875923697	1qqmress1	1.096171118	0.02140900409
1qqfd_ks15	0.3069007443	0.004642713073	1qqmftail	0.08412076979	0.0130286761
1qqfd_kw25	0	0.001	1qqmress2	3.330834338	0.2055974652
1qqfd_km25	0	0.001	1qqsresmu	-0.0726344024	0.06648168648
1qqfd_ks25	1	0.001	1qqsress1	1.030954914	0.03083108628
1qqfd_kw35	0	0.001	1qqsftail	0.1128160898	0.02484643843
1qqfd_km35	0	0.001	1qqsress2	2.833230559	0.2794400381
1qqfd_ks35	1	0.001	2fqq0	0.3620474121	0.001715827395
1qqfd_kmcf5	0	0	2fqq1	0.2016097547	0.001491213731
1qqfd_kscf5	1	0	2fqq2	0.1835281021	0.00144926662
1qqfd_km16	-0.2438537526	0.01400293447	2fqq3	0.1059321359	0.001196242994
1qqfd_ks16	0.3067923175	0.009694558368	2fqq4	0.0828246709	0.001085631114
1qqfd_kw26	0	0.001	2fqq5	0.05016570204	0.000877647606
1qqfd_km26	0	0.001	2fqq0cf	0.9923279311	0.002618483037
1qqfd_ks26	1	0.001	2fqq1cf	0.9965643586	0.003855772137
1qqfd_kw36	0	0.001	2fqq2cf	1.008579044	0.004095439356

2fqg3cf	0.9774704119	0.005473223834	2qqfd_pscf1	1	0
2fqg4cf	1.027428504	0.006382936672	2qqfd_pm12	-0.2483613183	0.002685474431
2fqg5cf	1.038286805	0.008336660232	2qqfd_ps12	0.3515118041	0.002028856362
2Nqq	276254.0225	519.1824949	2qqfd_pw22	0.1401191851	0.0348503427
2qqmbc_a	-25.43537195	0.3870257843	2qqfd_pm22	-0.4740889878	0.083032674
2qqde_c10	-0.6881004701	0.02425257288	2qqfd_ps22	1.415832491	0.0984551702
2qqde_c20	-1.407331356	0.06917021455	2qqfd_pw32	0	0.001
2qqde_c11	-0.8623490279	0.03208629583	2qqfd_pm32	0	0.001
2qqde_c21	0	0.001	2qqfd_ps32	1	0.001
2qqde_c12	-0.8899427861	0.03351076719	2qqfd_pmcf2	0	0
2qqde_c22	0	0.001	2qqfd_pscf2	1	0
2qqde_c13	-0.8966878254	0.04280746955	2qqfd_pm13	-0.2655419483	0.003645183327
2qqde_c23	0	0.001	2qqfd_ps13	0.3632276383	0.002776726855
2qqde_c14	-0.9197032742	0.04642366343	2qqfd_pw23	0.06778719368	0.02414082843
2qqde_c24	0	0.001	2qqfd_pm23	-0.5760585117	0.1279419353
2qqde_c15	-1.070676577	0.05762411334	2qqfd_ps23	1.644883117	0.1609667369
2qqde_c25	0	0.001	2qqfd_pw33	0	0.001
2qqde_c16	-1.044603269	0.105664586	2qqfd_pm33	0	0.001
2qqde_c26	0	0.001	2qqfd_ps33	1	0.001
2qqfd_pm10	-0.2084681416	0.002015168356	2qqfd_pmcf3	0	0
2qqfd_ps10	0.3516095412	0.001499666724	2qqfd_pscf3	1	0
2qqfd_pw20	0.2631661563	0.04029181329	2qqfd_pm14	-0.2949655683	0.003980645898
2qqfd_pm20	-0.4240206803	0.03830784583	2qqfd_ps14	0.3702955158	0.00302148015
2qqfd_ps20	1.353660442	0.04608576503	2qqfd_pw24	0.01847935754	0.01034771194
2qqfd_pw30	0	0.001	2qqfd_pm24	-0.9592034715	0.3784081929
2qqfd_pm30	0	0.001	2qqfd_ps24	2.099616608	0.4864315665
2qqfd_ps30	1	0.001	2qqfd_pw34	0	0.001
2qqfd_pmcf0	0	0	2qqfd_pm34	0	0.001
2qqfd_pscf0	1	0	2qqfd_ps34	1	0.001
2qqfd_pm11	-0.2415983248	0.002648356227	2qqfd_pmcf4	0	0
2qqfd_ps11	0.3707462999	0.002012082714	2qqfd_pscf4	1	0
2qqfd_pw21	0.1254763563	0.03603773372	2qqfd_pm15	-0.2905309928	0.005162546905
2qqfd_pm21	-0.4575326433	0.07944545901	2qqfd_ps15	0.3523097453	0.003967355775
2qqfd_ps21	1.285337743	0.0910227801	2qqfd_pw25	0.07346572832	0.03615223727
2qqfd_pw31	0	0.001	2qqfd_pm25	-0.6305623692	0.1501954129
2qqfd_pm31	0	0.001	2qqfd_ps25	1.031965815	0.202288138
2qqfd_ps31	1	0.001	2qqfd_pm25	0	0.001
2qqfd_pmcf1	0	0	2qqfd_pw35	0	0.001
			2qqfd_pm35	0	0.001

2qqfd_ps35	1	0.001	2qqfd_kw32	0	0.001
2qqfd_pmcf5	0	0	2qqfd_km32	0	0.001
2qqfd_pscf5	1	0	2qqfd_ks32	1	0.001
2qqfd_pm16	-0.2876008041	0.0104572822	2qqfd_kmcf2	0	0
2qqfd_ps16	0.3556612632	0.008055607781	2qqfd_kscf2	1	0
2qqfd_pw26	0	0.001	2qqfd_kmi3	-0.1673733702	0.002929618478
2qqfd_pm26	0	0.001	2qqfd_ks13	0.3349056744	0.002139998649
2qqfd_ps26	1	0.001	2qqfd_kw23	0.3588013128	0.08123855862
2qqfd_pw36	0	0.001	2qqfd_km23	-0.3553206491	0.05045602309
2qqfd_pm36	0	0.001	2qqfd_ks23	1.280435472	0.06297901455
2qqfd_ps36	1	0.001	2qqfd_kw33	0	0.001
2qqfd_pmcf6	0	0	2qqfd_km33	0	0.001
2qqfd_pscf6	1	0	2qqfd_ks33	1	0.001
2qqfd_km10	-0.1589393241	0.001614416516	2qqfd_kmcf3	0	0
2qqfd_ks10	0.3318303059	0.001171221851	2qqfd_kscf3	1	0
2qqfd_kw20	0.3134114526	0.03649255374	2qqfd_km14	-0.2414398306	0.003104106998
2qqfd_km20	-0.3848208316	0.0249194754	2qqfd_ks14	0.3462951875	0.002358469257
2qqfd_ks20	1.433069398	0.03452492632	2qqfd_kw24	0.08281096544	0.02700964936
2qqfd_kw30	0	0.001	2qqfd_km24	-0.5110897743	0.09955075003
2qqfd_km30	0	0.001	2qqfd_ks24	1.531676607	0.128833654
2qqfd_ks30	1	0.001	2qqfd_kw34	0	0.001
2qqfd_kmcf0	0	0	2qqfd_km34	0	0.001
2qqfd_kscf0	1	0	2qqfd_ks34	1	0.001
2qqfd_km11	-0.1939895357	0.002139027973	2qqfd_kmcf4	0	0
2qqfd_ks11	0.3489865744	0.001589532957	2qqfd_kscf4	1	0
2qqfd_kw21	0.1631272491	0.03353635961	2qqfd_km15	-0.2159286157	0.003956008489
2qqfd_km21	-0.389357451	0.05163616433	2qqfd_ks15	0.31086889	0.002767406149
2qqfd_ks21	1.468928161	0.06716122024	2qqfd_kw25	0.444656886	0.1038812215
2qqfd_kw31	0	0.001	2qqfd_km25	-0.3380871305	0.05105532294
2qqfd_km31	0	0.001	2qqfd_ks25	1.4289333197	0.08130582357
2qqfd_ks31	1	0.001	2qqfd_kw35	0	0.001
2qqfd_kmcf1	0	0	2qqfd_km35	0	0.001
2qqfd_kscf1	1	0	2qqfd_ks35	1	0.001
2qqfd_km12	-0.2031197085	0.002222759602	2qqfd_kmcf5	0	0
2qqfd_ks12	0.345152324	0.001673493298	2qqfd_kscf5	1	0
2qqfd_kw22	0.1511782935	0.02907105184	2qqfd_km16	-0.2301461331	0.007684148755
2qqfd_km22	-0.4664794192	0.05812414044	2qqfd_ks16	0.3149102673	0.00537088907
2qqfd_ks22	1.465735943	0.07287083572	2qqfd_kw26	0	0.001

2qffd_km26	0	0.001	1frb00cf	1	0.001
2qffd_ks26	1	0.001	1frb01cf	1	0.001
2qffd_kw36	0	0.001	1frb02cf	1	0.001
2qffd_km36	0	0.001	1frb03cf	1	0.001
2qffd_ks36	1	0.001	1frb04cf	1	0.001
2qffd_kmcf6	0	0	1frb05cf	1	0.001
2qffd_kscf6	1	0	1Nrb0	198.0886343	21.38165179
2qppid_c10	0.04199293118	0.005882499206	1rb0fd_mi0	0.4045844877	0.006086405333
2qppid_c20	1.101038063	0.0498215013	1rb0fd_s10	0.2605471635	0.004491202358
2qppid_c11	0.09691605534	0.007945914837	1rb0fd_w20	0.8344163386	0.01634475707
2qppid_c21	0	0	1rb0fd_m20	-0.2750991938	0.00226999142
2qppid_c12	0.1334021389	0.008286951305	1rb0fd_s20	1.183307451	0.005978417123
2qppid_c22	0	0	1rb0fd_w30	0.1626803473	0.005719708969
2qppid_c13	0.3126330553	0.01075722835	1rb0fd_m30	-0.2803395484	0.007477390539
2qppid_c23	0	0	1rb0fd_s30	1.357608662	0.01550670621
2qppid_c14	0.4723133501	0.01119272888	1rb0fd_mcf0	0.003737445979	0
2qppid_c24	0	0	1rb0fd_scf0	1.000690204	0
2qppid_c15	0.5871519406	0.0132414117	1rb0fd_mi1	0.391541599	0.006796868665
2qppid_c25	0	0	1rb0fd_s11	0.2673849777	0.005133258706
2qppid_c16	0.6870829711	0.02257150351	1rb0fd_w21	0.6076233498	0.01028132541
2qppid_c26	0	0	1rb0fd_m21	-0.3067106406	0.002495400411
2qptaueff	0.5392416919	0.01524164502	1rb0fd_s21	1.189982175	0.007198543914
2qppmu	0.004476809746	0.006047551736	1rb0fd_w31	0.07045736554	0.002762818092
2qfp	0.5614534169	0.0168787468	1rb0fd_m31	-0.2784340799	0.0115941109
2qpmresmu	-0.04940942118	0.01145856977	1rb0fd_s31	1.392820912	0.02493504837
2qpmress1	1.175518864	0.01074844428	1rb0fd_mcf1	-0.01589990901	0
2qpmftail	0.07650439098	0.00521758902	1rb0fd_scf1	1.029618852	0
2qpmress2	3.904511577	0.1061633998	1rb0fd_mi2	0.4295546631	0.007150298307
2qpsresmu	-0.07579395752	0.02936696732	1rb0fd_s12	0.2662871935	0.005410747131
2qpsress1	1.060729691	0.02030161104	1rb0fd_w22	0.906947981	0.02602553331
2qpsftail	0.1404310933	0.01267011381	1rb0fd_m22	-0.3153864148	0.004008878424
2qpsress2	3.538169351	0.1600867145	1rb0fd_s22	1.167585219	0.009008402524
1frb00	0.2063430754	0.0033335345868	1rb0fd_w32	0.1605560797	0.007465115141
1frb01	0.1634463189	0.003039333231	1rb0fd_m32	-0.3099020454	0.01062660548
1frb02	0.1635771723	0.003040337179	1rb0fd_s32	1.337713584	0.01758960101
1frb03	0.1086581464	0.002547289853	1rb0fd_mcf2	-0.005790521321	0
1frb04	0.1066873868	0.002526463738	1rb0fd_scf2	1.039878033	0
1frb05	0.1028780469	0.002485456344	1rb0fd_mi3	0.4539274556	0.008471535956

1rb0fd_s13	0.2435806378	0.006396285027	1rb0fd_scf6	1.078201959	0
1rb0fd_w23	0.7956016374	0.02785402363	1rb0pid_c10	-0.00610380094	0.05921322762
1rb0fd_m23	-0.3202348589	0.003456855406	1rb0pid_c20	1.813124905	0.3836060328
1rb0fd_s23	1.095555794	0.009700380365	1rb0pid_c11	0.1037017469	0.06534173436
1rb0fd_w33	0.3638719507	0.01361158671	1rb0pid_c21	0	0
1rb0fd_m33	-0.1966136919	0.006239057589	1rb0pid_c12	0.153744158	0.06091294782
1rb0fd_s33	1.483964717	0.01470066358	1rb0pid_c22	0	0
1rb0fd_mcf3	0.003112051188	0	1rb0pid_c13	0.4383788798	0.07596209059
1rb0fd_scf3	0.9826006372	0	1rb0pid_c23	0	0
1rb0fd_m14	0.4293170459	0.008818353279	1rb0pid_c14	0.4500439293	0.07441035268
1rb0fd_s14	0.2672954439	0.006618189015	1rb0pid_c24	0	0
1rb0fd_w24	0.8225757145	0.01985285718	1rb0pid_c15	0.4696794234	0.07952708892
1rb0fd_m24	-0.3174026627	0.003246344349	1rb0pid_c25	0	0
1rb0fd_s24	1.179778848	0.008351536584	1rb0pid_c16	0.5650421271	0.06119227348
1rb0fd_w34	0.1616969667	0.005707747572	1rb0pid_c26	0	0
1rb0fd_m34	-0.2635680094	0.009562399335	1rb0taueff	0	0
1rb0fd_s34	1.333159308	0.01987370154	1rb0Acp	0	0
1rb0fd_mcf4	-0.008184970868	0	1rb0Scp	0	0
1rb0fd_scf4	1.028959353	0	2frb00	0.2003961526	0.00153984613
1rb0fd_m15	0.54118984	0.009255045323	2frb01	0.1421875389	0.001341317726
1rb0fd_s15	0.2466556132	0.006222337962	2frb02	0.1847600736	0.001492361271
1rb0fd_w25	1.600832421	0.1144232997	2frb03	0.1216453394	0.001254602094
1rb0fd_m25	-0.3145396173	0.003949389687	2frb04	0.09643214922	0.001132008572
1rb0fd_s25	1.257784966	0.01947377739	2frb05	0.0955416426	0.001127290581
1rb0fd_w35	0.4762610566	0.01603322569	2frb00cf	1	0.001
1rb0fd_m35	-0.2641887892	0.01508047719	2frb01cf	1	0.001
1rb0fd_s35	1.359216878	0.01752733863	2frb02cf	1	0.001
1rb0fd_mcf5	-0.002927912233	0	2frb03cf	1	0.001
1rb0fd_scf5	1.052867645	0	2frb04cf	1	0.001
1rb0fd_m16	0.6005540377	0.007966421127	2frb05cf	1	0.001
1rb0fd_s16	0.2308386597	0.00542779596	2Nrb0	525.335805	36.33431121
1rb0fd_w26	1.635267604	0.06868056036	2rb0fd_m10	0.389540351	0.002992442192
1rb0fd_m26	-0.3601490753	0.002581583531	2rb0fd_s10	0.2537569773	0.002108915621
1rb0fd_s26	1.314649125	0.01519763903	2rb0fd_w20	0.790362953	0.01039370571
1rb0fd_w36	0.498899441	0.002632874406	2rb0fd_m20	-0.3057155384	0.001891123519
1rb0fd_m36	-0.3577105806	0.00646539851	2rb0fd_s20	1.311166138	0.0056689296742
1rb0fd_s36	1.256963969	0.01530688979	2rb0fd_w30	0.107296346	0.0030575766
1rb0fd_mcf6	0.004210374623	0	2rb0fd_m30	-0.2535161043	0.009672790758

2rb0fd_s30	1.690440367	0.01877468613	2rb0fd_w34	0.1929978218	0.00685505673
2rb0fd_mcf0	-0.005125849673	0	2rb0fd_m34	-0.2774668869	0.01157718886
2rb0fd_scf0	1.004672072	0	2rb0fd_s34	1.640400332	0.02322903304
2rb0fd_m11	0.3851364979	0.003543776149	2rb0fd_mcf4	-0.01334090263	0
2rb0fd_s11	0.2533492458	0.002506264812	2rb0fd_scf4	1.05132212	0
2rb0fd_w21	0.7813140446	0.01195960724	2rb0fd_m15	0.4634082643	0.004477397992
2rb0fd_m21	-0.313223203	0.002285912627	2rb0fd_s15	0.2380595883	0.002954429978
2rb0fd_s21	1.310132967	0.006911347678	2rb0fd_w25	1.276125751	0.02320552633
2rb0fd_w31	0.0964416587	0.003376114034	2rb0fd_m25	-0.3335697744	0.00233306242
2rb0fd_m31	-0.2757396004	0.01224919725	2rb0fd_s25	1.382526433	0.007652453597
2rb0fd_s31	1.692565741	0.0239831112	2rb0fd_w35	0.1563136587	0.00601456147
2rb0fd_mcf1	-0.01286999305	0	2rb0fd_m35	-0.2933432966	0.01266074117
2rb0fd_scf1	1.018927829	0	2rb0fd_s35	1.661362346	0.02547309011
2rb0fd_m12	0.4296123519	0.003131039997	2rb0fd_mcf5	-0.008605887176	0
2rb0fd_s12	0.2415542719	0.002112128173	2rb0fd_scf5	1.033846636	0
2rb0fd_w22	1.211532335	0.01800622599	2rb0fd_m16	0.5446731749	0.003270221347
2rb0fd_m22	-0.3032705471	0.001785736919	2rb0fd_s16	0.2030304603	0.001949768267
2rb0fd_s22	1.338011031	0.005703465751	2rb0fd_w26	1.787983752	0.0380022393
2rb0fd_w32	0.1435224114	0.003900249857	2rb0fd_m26	-0.3380161648	0.001835376699
2rb0fd_m32	-0.3366902771	0.009519766491	2rb0fd_s26	1.511714836	0.008143789083
2rb0fd_s32	1.655291512	0.01934291146	2rb0fd_w36	0.2220277607	0.005915227504
2rb0fd_mcf2	-0.01297608026	0	2rb0fd_m36	-0.2986876463	0.008124253895
2rb0fd_scf2	1.023758481	0	2rb0fd_s36	1.487432743	0.017536824
2rb0fd_m13	0.4264568732	0.003891610542	2rb0fd_mcf6	-0.009678363912	0
2rb0fd_s13	0.2430254551	0.00260144063	2rb0fd_scf6	1.02926003	0
2rb0fd_w23	1.147984665	0.02030911423	2rb0pid_c10	0.0261312276	0.03016088486
2rb0fd_m23	-0.3098451603	0.00234065256	2rb0pid_c20	2.950582643	0.2965048216
2rb0fd_s23	1.357401029	0.006897219016	2rb0pid_c11	0.03904886549	0.03574439428
2rb0fd_w33	0.133977609	0.004848291865	2rb0pid_c21	0	0
2rb0fd_m33	-0.2956675428	0.01276975892	2rb0pid_c12	0.254996993	0.03166856207
2rb0fd_s33	1.663661591	0.02417752809	2rb0pid_c22	0	0
2rb0fd_mcf3	-0.01451155145	0	2rb0pid_c13	0.3417881048	0.03746963402
2rb0fd_scf3	1.028552501	0	2rb0pid_c23	0	0
2rb0fd_m14	0.4572144291	0.004311238952	2rb0pid_c14	0.4034943614	0.04147300279
2rb0fd_s14	0.231429332	0.002821314754	2rb0pid_c24	0	0
2rb0fd_w24	1.386187875	0.03362071646	2rb0pid_c15	0.4531126696	0.04155343177
2rb0fd_m24	-0.3092328476	0.002673429603	2rb0pid_c25	0	0
2rb0fd_s24	1.358860646	0.008248137694	2rb0pid_c16	0.6201543482	0.03039944555

2rb0pid_c26	0			1rbpfd_s12	0.2675645769	0.01026328313
2rb0taueff	1.518008812	0	0.006025524531	1rbpfd_w22	0.906947981	0.02602553331
2rb0Acp	0	0	0	1rbpfd_m22	-0.3153864148	0.004008878424
2rb0Scp	0	0	0	1rbpfd_s22	1.167585219	0.009008402524
1frbp0	0.1619248845	0.005823923766	0.005823923766	1rbpfd_w32	0.1605560797	0.007465115141
1frbp1	0.1629065795	0.005838429108	0.005838429108	1rbpfd_m32	-0.3099020454	0.01062660548
1frbp2	0.1687851496	0.005923627694	0.005923627694	1rbpfd_s32	1.337713584	0.01758960101
1frbp3	0.1048491411	0.004828299383	0.004828299383	1rbpfd_mcf2	-0.005790521321	0
1frbp4	0.1085231274	0.004903125487	0.004903125487	1rbpfd_scf2	1.039878033	0
1frbp5	0.1205280975	0.005135871567	0.005135871567	1rbpfd_mi3	0.437993758	0.01748388463
1frbp0cf	1	0.001	0.001	1rbpfd_si3	0.26364207	0.01310149164
1frbp1cf	1	0.001	0.001	1rbpfd_w23	0.7956016374	0.02785402363
1frbp2cf	1	0.001	0.001	1rbpfd_m23	-0.3202348589	0.003456855406
1frbp3cf	1	0.001	0.001	1rbpfd_s23	1.095555794	0.009700380365
1frbp4cf	1	0.001	0.001	1rbpfd_w33	0.3638719507	0.01361158671
1frbp5cf	1	0.001	0.001	1rbpfd_m33	-0.1966136919	0.006239057589
1Nrbp	0.2681641778	63.89070418	63.89070418	1rbpfd_s33	1.483964717	0.01470066358
1rbpfd_m10	0.4309282766	0.01346088428	0.01346088428	1rbpfd_mcf3	0.003112051188	0
1rbpfd_s10	0.2659007249	0.009882323917	0.009882323917	1rbpfd_scf3	0.9826006372	0
1rbpfd_w20	0.8344163386	0.01634475707	0.01634475707	1rbpfd_m14	0.4119839018	0.01815518029
1rbpfd_m20	-0.2750991938	0.00226999142	0.00226999142	1rbpfd_s14	0.294124334	0.01326823607
1rbpfd_s20	1.183307451	0.005978417123	0.005978417123	1rbpfd_w24	0.8225757145	0.01985285718
1rbpfd_w30	0.1626803473	0.005719708969	0.005719708969	1rbpfd_m24	-0.3174026627	0.003246344349
1rbpfd_m30	-0.2803395484	0.007477390539	0.007477390539	1rbpfd_s24	1.179778848	0.008351536584
1rbpfd_s30	1.357608662	0.01550670621	0.01550670621	1rbpfd_w34	0.1616969667	0.005707747572
1rbpfd_mcf0	0.003737445979	0	0	1rbpfd_m34	-0.2635680094	0.009562399335
1rbpfd_scf0	1.000690204	0	0	1rbpfd_s34	1.333159308	0.01987370154
1rbpfd_m11	0.3942560214	0.01305531896	0.01305531896	1rbpfd_mcf4	-0.008184970868	0
1rbpfd_s11	0.2647343129	0.009893946118	0.009893946118	1rbpfd_scf4	1.028959353	0
1rbpfd_w21	0.6076233498	0.01028132541	0.01028132541	1rbpfd_m15	0.5346069496	0.01698368181
1rbpfd_m21	-0.3067106406	0.002495400411	0.002495400411	1rbpfd_s15	0.2546851871	0.01136189301
1rbpfd_s21	1.189982175	0.007198543914	0.007198543914	1rbpfd_w25	1.600832421	0.1144232997
1rbpfd_w31	0.07045736554	0.002762818092	0.002762818092	1rbpfd_m25	-0.3145396173	0.003949389687
1rbpfd_m31	-0.2784340799	0.0115941109	0.0115941109	1rbpfd_s25	1.257784966	0.01947377739
1rbpfd_s31	1.392820912	0.02493504837	0.02493504837	1rbpfd_w35	0.4762610566	0.01603322569
1rbpfd_mcf1	-0.01589990901	0	0	1rbpfd_m35	-0.2641887892	0.01508047719
1rbpfd_scf1	1.029618852	0	0	1rbpfd_s35	1.359216878	0.01752733863
1rbpfd_m12	0.4188253694	0.01365610354	0.01365610354	1rbpfd_mcf5	-0.002927912233	0

1rbpfd_scf5	1.052867645	0	2Nrbp	0.2692351951	135.7977209
1rbpfd_m16	0.5962389819	0.01467303616	2rbpfd_m10	0.3777718554	0.006736230461
1rbpfd_s16	0.2454364631	0.01029733749	2rbpfd_s10	0.2689320922	0.004758213929
1rbpfd_w26	1.635267604	0.06868056036	2rbpfd_w20	0.790362953	0.01039370571
1rbpfd_m26	-0.3601490753	0.002581583531	2rbpfd_m20	-0.3057155384	0.001891123519
1rbpfd_s26	1.314649125	0.01519763903	2rbpfd_s20	1.311166138	0.005689296742
1rbpfd_w36	0.498899441	0.002632874406	2rbpfd_w30	0.107296346	0.0030575766
1rbpfd_m36	-0.3577105806	0.00646539851	2rbpfd_m30	-0.2535161043	0.009672790758
1rbpfd_s36	1.256963969	0.01530688979	2rbpfd_s30	1.690440367	0.01877468613
1rbpfd_w36	0.004210374623	0	2rbpfd_w30	-0.005125849673	0
1rbpfd_mcf6	1.078201959	0	2rbpfd_mcf0	1.004672072	0
1rbpfd_scf6	-0.05607233141	0.1221450956	2rbpfd_scf0	0.3897512377	0.006950411778
1rbppid_c10	1.978714273	0.4016391283	2rbpfd_m11	0.2649720607	0.004920290572
1rbppid_c20	0.0653243069	0.1274911978	2rbpfd_s11	0.7813140446	0.01195960724
1rbppid_c11	0	0	2rbpfd_w21	-0.313223203	0.002285912627
1rbppid_c21	0.2770480856	0.1209684287	2rbpfd_m21	1.310132967	0.006911347678
1rbppid_c12	0	0	2rbpfd_s21	0.0964416587	0.003376114034
1rbppid_c22	0.4835255201	0.1487269657	2rbpfd_w31	-0.2757396004	0.01224919725
1rbppid_c13	0	0	2rbpfd_m31	1.692565741	0.0239831112
1rbppid_c23	0.9007094777	0.09731290626	2rbpfd_s31	-0.01286999305	0
1rbppid_c14	0	0	2rbpfd_mcf1	1.018927829	0
1rbppid_c24	0.6807814573	0.1139171218	2rbpfd_scf1	0.4315024647	0.006087425994
1rbppid_c15	0	0	2rbpfd_m12	0.250753357	0.004052869678
1rbppid_c25	0.9603041772	0.05791809681	2rbpfd_s12	1.211532335	0.01800622599
1rbppid_c16	0	0	2rbpfd_w22	-0.3032705471	0.001785736919
1rbppid_c26	0	0	2rbpfd_m22	1.338011031	0.005703465751
1rbptaueff	0.1621388693	0.002726784347	2rbpfd_s22	0.1435224114	0.003900249857
2frbp0	0.148363481	0.002628880929	2rbpfd_w32	-0.3366902771	0.009519766491
2frbp1	0.190063915	0.002904386707	2rbpfd_m32	1.655291512	0.01934291146
2frbp2	0.114094403	0.002349262258	2rbpfd_s32	-0.01297608026	0
2frbp3	0.1034639581	0.002249873134	2rbpfd_mcf2	1.023758481	0
2frbp4	0.1085614528	0.002298387278	2rbpfd_scf2	0.419578935	0.007882988393
2frbp5	1	0.001	2rbpfd_m13	0.2495224854	0.005265422223
2frbp0cf	1	0.001	2rbpfd_s13	1.147984665	0.02030911423
2frbp1cf	1	0.001	2rbpfd_w23	-0.3098451603	0.00234065256
2frbp2cf	1	0.001	2rbpfd_m23	1.357401029	0.006897219016
2frbp3cf	1	0.001	2rbpfd_s23	0.133977609	0.004848291865
2frbp4cf	1	0.001	2rbpfd_w33	-0.2956675428	0.01276975892
2frbp5cf	1	0.001	2rbpfd_m33		

2rbpfd_s33	1.663661591	0.02417752809	2rbpfd_s16	0.2139756777	0.003695886389
2rbpfd_mcf3	-0.01451155145	0	2rbpfd_w26	1.787983752	0.0380022393
2rbpfd_scf3	1.028552501	0	2rbpfd_m26	-0.3380161648	0.001835376699
2rbpfd_m14	0.4480685804	0.00837966912	2rbpfd_s26	1.511714836	0.008143789083
2rbpfd_s14	0.243729563	0.005526505803	2rbpfd_w36	0.2220277607	0.005915227504
2rbpfd_w24	1.386187875	0.03362071646	2rbpfd_m36	-0.2986876463	0.008124253895
2rbpfd_m24	-0.3092328476	0.002673429603	2rbpfd_s36	1.487432743	0.017536824
2rbpfd_s24	1.358860646	0.008248137694	2rbpfd_mcf6	-0.009678363912	0
2rbpfd_w34	0.1929978218	0.00685505673	2rbpfd_scf6	1.02926003	0
2rbpfd_m34	-0.2774668869	0.01157718886	2rbppid_c10	-0.02182102471	0.06556395306
2rbpfd_s34	1.640400332	0.02322903304	2rbppid_c20	2.988557657	0.3590611005
2rbpfd_mcf4	-0.01334090263	0	2rbppid_c11	0.219615515	0.06947819342
2rbpfd_scf4	1.05132212	0	2rbppid_c21	0	0
2rbpfd_m15	0.4563078607	0.00833477718	2rbppid_c12	0.5043979171	0.05251700785
2rbpfd_s15	0.244888066	0.005487096345	2rbppid_c22	0	0
2rbpfd_w25	1.276125751	0.02320552633	2rbppid_c13	0.5832071006	0.07058562735
2rbpfd_m25	-0.3335697744	0.00233306242	2rbppid_c23	0	0
2rbpfd_s25	1.382526433	0.007652453597	2rbppid_c14	0.7609502903	0.06536856572
2rbpfd_w35	0.1563136587	0.00601456147	2rbppid_c24	0	0
2rbpfd_m35	-0.2933432966	0.01266074117	2rbppid_c15	0.8297426454	0.05805741363
2rbpfd_s35	1.661362346	0.02547309011	2rbppid_c25	0	0
2rbpfd_mcf5	-0.008605887176	0	2rbppid_c16	0.8615949397	0.04259665181
2rbpfd_scf5	1.033846636	0	2rbppid_c26	0	0
2rbpfd_m16	0.5289145476	0.006271081149	2rbptaueff	1.642398627	0.01218039382

List of Figures

1.1	History of the universe in the Standard Model of cosmology [4].	2
1.2	Summary of experimental results to constrain the unitarity triangle by the CKMfitter group [14]	4
2.1	The normalized unitarity triangle.	14
2.2	Feynman box diagram showing the predominant time-dependent flavour mixing diagrams	15
2.3	Theoretical Δt distribution for maximal direct (a) and mixing induced (b) CP violation. The red line indicates the distribution for B^0 mesons while the blue line indicates the distribution for \bar{B}^0 mesons. (a),(b) shows the Δt distributions for a decay to a CP final state with the CP parameters $\mathcal{A}_{CP} = 1$ and $\mathcal{S}_{CP} = 0$ [$\mathcal{A}_{CP} = 0$ and $\mathcal{S}_{CP} = 1$].	19
2.4	Two entangled B mesons are produced from the $\Upsilon(4S)$ resonance. One decays into CP eigenstate at time t_2 (CP -side). The other B meson decays into a flavour specific state at time t_1 (tag-side). From the charge of the decay products on the tag-side, the flavour of both B mesons can be determined at time t_1	21
2.5	Feynman diagrams illustrating the tree and penguin decay of the decay $B \rightarrow \pi\pi$	23
2.6	Isospin triangles.	25
2.7	tree and penguin diagram of the decay $B^0 \rightarrow K^+\pi^-$	27
2.8	The dominant Feynman diagram for the decay $B^0 \rightarrow K^+K^-$	29
2.9	Current results of branching fraction measurements from various experiments [59]	32
2.10	Direct CP violation vs. mixing induced CP violation parameters for the decay $B^0 \rightarrow \pi^+\pi^-$ determined from the Belle, BaBar and LHCb experiments [59]. Other experiments use a different definition of the direct CP violation parameter $\mathcal{A}_{CP} = -C_{CP}$	32
3.1	The KEKB accelerator ring. The Belle detector is located at the Tsukuba area.	36

3.2	In the left diagram, crab cavities compensate for the finite crossing angle. Effectively, the whole bunch collides head-on, as would be the case without a crossing angle. The right diagram shows luminosity improvements as a function of the bunch current.	37
3.3	The Belle detector with all subdetector components.	37
3.4	Geometry of the Belle beam pipe used for data taking of the first 152×10^6 million $B \bar{B}$ pairs.	39
3.5	Geometry of the Silicon vertex detector (SVD1) of Belle is illustrated on the upper left. Acceptance of the Belle tracking system and the mechanical setup of a SVD ladder is shown in the upper right and lower center respectively.	40
3.6	Impact parameter resolution for charged muons from cosmic ray data for SVD1. Each track is required to have associated SVD hits. The effective momentum \hat{p} is $\hat{p} \equiv p\beta \sin^{3/2} \theta$ in the left plot and $\hat{p} \equiv p\beta \sin^{5/2} \theta$ in the right plot. The red solid line indicates a fit to the data points with the parameters shown in the plot.	40
3.7	The track parameters $d_\rho, d_z, \kappa, \phi, \lambda$	41
3.8	Mechanical design of the CDC including the acceptance angles.	42
3.9	Energy depositions and tracking performance of the CDC.	43
3.10	Arrangement of the ACC modules in the barrel part and the endcap.	44
3.11	Plot showing the distribution of pulse heights for pions (in blue) and kaons (in red) in units of photo electrons. The four plots show the discrimination between pions and kaons for different optical densities.	45
3.12	TOF module mechanical design.	46
3.13	Performance plots for the TOF.	47
3.14	The overall geometrical layout of the ECL.	48
3.15	Energy and position resolution of the ECL.	49
3.16	Layout of the superconducting solenoid magnet of Belle including the cryostat.	50
3.17	Cut-out of a KLM super layer.	51
3.18	Trigger system of the Belle detector.	52
3.19	Flow chart of the global decision logic (GDL) of the Belle trigger.	53
3.20	Event display of a $B \rightarrow J/\psi K_S^0$ decay candidate (http://www.belle.jp/belle/events/). Cut through the detector $r - \phi$ plane.	55
4.1	Production cross sections around the center-of-mass energies of the Υ resonances.	60
4.2	Distribution of input variables for the Fisher discriminant. We are showing normalized distributions of Monte-Carlo $B^0 \rightarrow \pi^+ \pi^-$ events and off-resonance data in red and blue, respectively.	67
4.3	Event multiplicity for different channels.	68
4.4	Bayesian probability network for the component $\pi^+ \pi^-$. The directed acyclic graph shows the fit variables as nodes and the modelled correlations as arrows.	71

4.5	Fit results for the variables M_{BC} and ΔE for component $\pi^+ \pi^-$. Data points with errors represent the MC from full detector simulation and the solid blue line represents the fit result.	72
4.6	Fit results for the variables $\mathcal{L}_{K/\pi}^+$ and $\mathcal{L}_{K/\pi}^-$ for component $\pi^+ \pi^-$. Data points with errors represent the MC from full detector simulation and the solid blue histogram represents the fit result.	73
4.7	Fit results for the variable $\mathcal{F}_{S/B}$ for component $\pi^+ \pi^-$. The PDF is shown in blue while the full detector simulation Monte-Carlo is plotted in black including errors.	73
4.8	Fit results for the variable Δt for component $\pi^+ \pi^-$. Data points with errors represent the MC from full detector simulation and the solid blue line (or histogram) represents the fit result.	75
4.9	Bayesian probability network for the $K \pi$ components. The directed acyclic graph shows the fit variables as nodes and the modelled correlations as arrows.	77
4.10	Fit results for the variables M_{BC} and ΔE , for component $K^+ \pi^-$. Data points with errors represent the MC from full detector simulation and the solid blue line represents the fit result.	78
4.11	Fit results for the variables $\mathcal{L}_{K/\pi}^+$ and $\mathcal{L}_{K/\pi}^-$ for component $K^+ \pi^-$. Data points with errors represent the MC from full detector simulation and the solid blue histogram represents the fit result.	79
4.12	Fit results for the variable $\mathcal{F}_{S/B}$ for component $K^+ \pi^-$. The PDF is shown in blue while the full detector simulation Monte-Carlo is plotted in black including errors.	79
4.13	Fit results for variable Δt , for component $K^+ \pi^-$. Data points with errors represent the MC from full detector simulation and the solid blue line represents the fit result.	81
4.14	Bayesian probability network for the component $K^+ K^-$. The directed acyclic graph shows the fit variables as nodes and the modelled correlations as arrows.	82
4.15	Fit results for the variables M_{BC} and ΔE , for component $K^+ K^-$. Data points with errors represent the MC from full detector simulation and the solid blue line represents the fit result.	83
4.16	Fit results for the variables $\mathcal{L}_{K/\pi}^+$ and $\mathcal{L}_{K/\pi}^-$, for component $K^+ K^-$. Data points with errors represent the MC from full detector simulation and the solid blue histogram represents the fit result.	84
4.17	Fit results for the variable $\mathcal{F}_{S/B}$ for component $K^+ K^-$. The PDF is shown in blue while the full detector simulation Monte-Carlo is plotted in black including errors.	84
4.18	Fit results for variable Δt for component $K^+ K^-$. Data points with errors represent the MC from full detector simulation and the solid blue line represents the fit result.	86

4.19	Bayesian probability network for the continuum component. The directed acyclic graph shows the fit variables as nodes and the modelled correlations as arrows.	87
4.20	Fit results of M_{BC} and ΔE for continuum. Data points with errors represent the off-resonance data and the solid blue line represents the fit result. . . .	88
4.21	Fit results of the variable ΔE , for the continuum component. Data points with errors represent the off-resonance data and the solid blue line represents the fit result. The slope of the first order Chebyshev polynome is different in every r -bin. This is especially visible in plot (g), the r -bin with the best B tagging purity, compared to the other plots.	89
4.22	Fit results for the variables $\mathcal{L}_{K/\pi}^+$ and $\mathcal{L}_{K/\pi}^-$, for the continuum component cumulated integrated over all r -bins. Data points with errors represent the off-resonance data and the solid blue histogram represents the fit result. . . .	89
4.23	The figure shows the bins of a 2D histogram of $\mathcal{L}_{K/\pi}^+$ and $\mathcal{L}_{K/\pi}^-$. The area is divided according to the conditions from Tbl. 4.9. The blue area corresponds to $k = 1$ while the larger orange area corresponds to $k = 2$	90
4.24	Fit results for the variable $\mathcal{F}_{S/B}$ for the continuum component. The PDF is shown in blue while the off-resonance data is plotted in black including errors.	91
4.25	Δt fit results for the continuum component. Data points with errors represent the off-resonance data and the solid blue line represents the fit result. . . .	92
4.26	Detailed fit results of the variables $\mathcal{L}_{K/\pi}^+$ and $\mathcal{L}_{K/\pi}^-$, for the continuum component in every r -bin. Data points with errors represent the off-resonance data and the solid blue line represents the fit result.	93
4.27	Bayesian probability network for the charmless B^+B^- component. The directed acyclic graph shows the fit variables as nodes and the modelled correlations as arrows.	94
4.28	Fit results for the variables M_{BC} and ΔE , for the charmless B^+B^- component. Data points with errors represent the MC from full detector simulation and the solid blue line represents the fit result.	96
4.29	Fit results for the variables $\mathcal{L}_{K/\pi}^+$ and $\mathcal{L}_{K/\pi}^-$, for the charmless B^+B^- component. Data points with errors represent the MC from full detector simulation and the solid blue histogram represents the fit result.	97
4.30	The figure shows the bins of a 2D histogram of $\mathcal{L}_{K/\pi}^+$ and $\mathcal{L}_{K/\pi}^-$. We observe an excess of events in the blue bin (1,0) if we select events with a B tag of $q = +1$. For events with a B tag of $q = -1$ an excess in the green bin (0,1) is observed.	97
4.31	Manta-ray function to correct the particle identification histogram for its correlation with q . In the plot, $a = 1$ and $c = 5$ are taken for illustrative purposes.	98
4.32	Fit results for the variable $\mathcal{F}_{S/B}$ for component charmless B^+B^- . The PDF is shown in blue while the full detector simulation Monte-Carlo is plotted in black including errors.	98

4.33	Δt fit results for the charmless B^+B^- component. Data points with errors represent the MC from full detector simulation and the solid blue line represents the fit result.	99
4.34	Bayesian probability network for the charmless $B^0\bar{B}^0$ component. The directed acyclic graph shows the fit variables as nodes and the modelled correlations as arrows.	100
4.35	Fit results for the variables M_{BC} and ΔE , for the charmless $B^0\bar{B}^0$ component. Data points with errors represent the MC from full detector simulation and the solid blue line represents the fit result.	101
4.36	Fit results for the variables $\mathcal{L}_{K/\pi}^+$ and $\mathcal{L}_{K/\pi}^-$, for the charmless $B^0\bar{B}^0$ component. Data points with errors represent the MC from full detector simulation and the solid blue histogram represents the fit result.	102
4.37	Fit results for the variable $\mathcal{F}_{S/B}$, for the charmless $B^0\bar{B}^0$ component. The PDF is shown in blue while the full detector simulation Monte-Carlo is plotted in black including errors.	103
4.38	Δt fit results for the charmless $B^0\bar{B}^0$ component. Data points with errors represent the MC from full detector simulation and the solid blue line represents the fit result.	104
4.39	M_{BC} and ΔE projections from a fit to Toy Monte-Carlo. The Toy MC is shown as black crosses including the errors. The black histogram represents the summed PDFs of all components. The individual components are the continuum (red), the $B^0 \rightarrow K^+\pi^-$ decay(magenta), the $B^0 \rightarrow \pi^+\pi^-$ decay (gold), the charmless decays of B^0 (green) and B^\pm (blue).	106
4.40	$\mathcal{L}_{K/\pi}^+$ and $\mathcal{L}_{K/\pi}^-$ projections from a fit to Toy Monte-Carlo. The Toy MC is shown as black crosses including the errors. The black histogram represents the summed PDFs of all components. The individual components are the continuum (red), the $B^0 \rightarrow K^+\pi^-$ decay(magenta), the $B^0 \rightarrow \pi^+\pi^-$ decay (gold), the charmless decays of B^0 (green) and B^\pm (blue).	106
4.41	$\mathcal{F}_{S/B}$ projection from a fit to Toy Monte-Carlo. The Toy MC is shown as black crosses including the errors. The black histogram represents the summed PDFs of all components. The individual components are the continuum (red), the $B^0 \rightarrow K^+\pi^-$ decay(magenta), the $B^0 \rightarrow \pi^+\pi^-$ decay (gold), the charmless decays of B^0 (green) and B^\pm (blue).	107
4.42	Δt projection from a fit to Toy Monte-Carlo. The Toy MC is shown as black crosses including the errors. The black histogram represents the summed PDFs of all components. The individual components are the continuum (red), the $B^0 \rightarrow K^+\pi^-$ decay(magenta), the $B^0 \rightarrow \pi^+\pi^-$ decay (gold), the charmless decays of B^0 (green) and B^\pm (blue).	107
4.43	Fit central value and pull distributions of the CP parameters in the PDF ensemble tests. The black dots including the error represent the results from the toy MC pseudo experiments. The solid black line is the result of a Gaussian fit. The read line indicates the generated value.	110

4.44	Fit central value and pull distributions of the branching ratio in the PDF ensemble tests. The black dots including the error represent the results from the toy MC pseudo experiments. The solid black line is the result of a Gaussian fit. The read line indicates the generated value.	111
4.45	Fit central value and pull distributions of the CP parameters in the GSIM ensemble tests. The black dots including the error represent the results from the toy MC pseudo experiments. The solid black line is the result of a Gaussian fit. The read line indicates the generated value.	112
4.46	Fit central value and pull distributions of the branching ratio in the GSIM ensemble tests. The black dots including the error represent the results from the toy MC pseudo experiments. The solid black line is the result of a Gaussian fit. The read line indicates the generated value.	113
4.47	PID likelihood $\mathcal{L}_{K/\pi}^+$ and $\mathcal{L}_{K/\pi}^-$ for the $\pi^+ \pi^-$ component in slices of ΔE . When comparing the histograms starting with (a) going down to (g) one can observe an increase of events outside the peak at (0,0). This feature is especially pronounced in the row defined by $\mathcal{L}_{K/\pi}^+ = 0$ and the row $\mathcal{L}_{K/\pi}^- = 0$.	115
5.1	Distribution of the D^0 mass inside the analysis window.	119
5.2	Fit results for the variables M_{BC} and ΔE , for the component $D\pi$. Data points with errors represent the MC from full detector simulation and the solid blue line represents the fit result.	120
5.3	Fit results for the variable $\mathcal{F}_{S/B}$, for the component $D\pi$. Data points with errors represent the MC from full detector simulation and the solid blue line represents the fit result.	121
5.4	Fit results for variable Δt , for the component $D\pi$. Data points with errors represent the MC from full detector simulation and the solid blue line represents the fit result.	122
5.5	Fit results for the variables M_{BC} and ΔE , for the charmed B^+B^- component. Data points with errors represent the MC from full detector simulation and the solid blue line represents the fit result.	123
5.6	Fit results of the variable $\mathcal{F}_{S/B}$, for the charmed B^+B^- component. Data points with errors represent the MC from full detector simulation and the solid blue line represents the fit result.	124
5.7	Fit results for the variable Δt , for the charmed B^+B^- component. Data points with errors represent the MC from full detector simulation and the solid blue line represents the fit result.	125
5.8	Fit results for the variables M_{BC} and ΔE , for the charmed $B^0\bar{B}^0$ component. Data points with errors represent the MC from full detector simulation and the solid blue line represents the fit result.	126
5.9	Fit results for the variable $\mathcal{F}_{S/B}$, for the charmed $B^0\bar{B}^0$ component. Data points with errors represent the MC from full detector simulation and the solid blue line represents the fit result.	127

5.10	Fit results for the variable Δt for the charmed $B^0\bar{B}^0$ component. Data points with errors represent the MC from full detector simulation and the solid blue line represents the fit result.	128
5.11	Fit results of the continuum component of the $D\pi$ control sample. Data points with errors represent the off-resonance data and the solid blue line represents the fit result.	129
5.12	Fit results for the variable $\mathcal{F}_{S/B}$, for the continuum component of the $D\pi$ control sample. Data points with errors represent the off-resonance data and the solid blue line represents the fit result.	130
5.13	Fit results for the variable Δt , for the continuum component of the $D\pi$ control sample. Data points with errors represent the off-resonance data and the solid blue line represents the fit result.	131
5.14	Fit projections of all variables to the control sample. The black points show the data of the full Belle statistics including the errors. The black solid line represents the total PDF of all components. The red dotted line represents the total background while the green broken line is the background from three body charmed decays.	133
5.15	Likelihood ratio of a kaon given the pion hypothesis in a $B^0 \rightarrow \pi^+\pi^-$ Monte-Carlo sample.	136
5.16	Likelihood ratio of the kaon given the pion hypothesis for the positive particle L^+ , and the negative particle L^-	137
5.17	Cut efficiency correction factors (ρ) for each bin in the L^+L^- histogram.	138
5.18	Errors of the correction factors for each bin in the L^+L^- histogram.	139
5.19	Monte-Carlo histogram(blue) and corrected data-like histogram with errors(black) of L^+L^-	139
5.20	Bin-wise ratio between data-like histogram and Monte-Carlo histogram of L^+L^-	140
6.1	Distribution of $\mathcal{A}_{CP}(\pi^+\pi^-)$ (top) and its error (bottom) from Toy-Monte-Carlo studies in the first 535 million (b) and the remaining 237 (a) million $B\bar{B}$ pairs. The blue arrow denotes expectations from case A while the red arrow denotes expectations from case B.	146
6.2	Distribution of $\mathcal{A}_{CP}(\pi^+\pi^-)$ (top) and its error (bottom) from Toy-Monte-Carlo studies in the first 535 million (b) and the remaining 237 (a) million $B\bar{B}$ pairs. The blue arrow denotes the expected values from the full dataset.	147
6.3	ΔE distribution of the $\pi^+\pi^-$ signal enhanced data from the full Belle data set. Black crosses denote the data; the total PDF is shown as a black solid line. The total background is the red dashed line, containing the background from charmless B decays displayed as green dotted line. The blue hashed area is the contribution from the peaking background of $B^0 \rightarrow K^+\pi^-$ decays.	148

- 6.4 M_{BC} distribution of the $\pi^+ \pi^-$ signal enhanced data from the full Belle data set. Black crosses denote the data; the total PDF is shown as a black solid line. The total background is the red dashed line. The blue hashed area is the contribution from the peaking background of $B^0 \rightarrow K^+ \pi^-$ decays. . . . 149
- 6.5 $\mathcal{F}_{S/B}$ distribution of the $\pi^+ \pi^-$ signal enhanced data from the full Belle data set. Black crosses denote the data; the total PDF is shown as a black solid line. The total background is the red dashed line. The blue hashed area is the contribution from the peaking background of $B^0 \rightarrow K^+ \pi^-$ decays. . . . 150
- 6.6 $\mathcal{L}_{K/\pi}^+$ distribution of the $\pi^+ \pi^-$ signal enhanced data from the full Belle data set. Black crosses denote the data; the total PDF is shown as a black solid line. The total background is the red dashed line, containing the background from charmless B decays displayed as green dotted line. 151
- 6.7 $\mathcal{L}_{K/\pi}^-$ distribution of the $\pi^+ \pi^-$ signal enhanced data from the full Belle data set. Black crosses denote the data; the total PDF is shown as a black solid line. The total background is the red dashed line, containing the background from charmless B decays displayed as green dotted line. 152
- 6.8 Δt distribution of the $\pi^+ \pi^-$ signal enhanced data from the full Belle data set. The blue points correspond to data with a B_{tag} identified as B^0 , the red triangles correspond to data with a B_{tag} identified as \bar{B}^0 . The solid lines show the PDF for the given class of events. The time-dependent asymmetry is shown in the lower part of the plot. 153
- 6.9 Δt distribution of the $\pi^+ \pi^-$ signal enhanced data from the data set of the previous analysis of 535 million $B\bar{B}$ pairs. The blue points correspond to data with a B_{tag} identified as B^0 , the red triangles correspond to data with a B_{tag} identified as \bar{B}^0 . The solid lines show the PDF for the given class of events. The time-dependent asymmetry is shown in the lower part of the plot. 154
- 6.10 Δt distribution of the $\pi^+ \pi^-$ signal enhanced data from the new data set of the latest 237 million $B\bar{B}$ pairs. The blue points correspond to data with a B_{tag} identified as B^0 , the red triangles correspond to data with a B_{tag} identified as \bar{B}^0 . The solid lines show the PDF for the given class of events. The green dotted line is the contribution from backgrounds. The time-dependent asymmetry is shown in the lower part of the plot. 154
- 6.11 ΔE distribution of the $K^+ \pi^-$ signal enhanced data from the full Belle data set. Data is shown as black crosses; the total PDF is the solid black line; the total background is the red dashed line which includes the contribution from charmless B decays in green. The hashed blue area is the peaking background contribution from the decay $B^0 \rightarrow \pi^+ \pi^-$ 155
- 6.12 M_{BC} distribution of the $K^+ \pi^-$ signal enhanced data from the full Belle data set. Data is shown as black crosses; the total PDF is the solid black line; the total background is the red dashed line. The hashed blue area is the peaking background contribution from the decay $B^0 \rightarrow \pi^+ \pi^-$ 155

- 6.13 $\mathcal{L}_{K/\pi}^+$ distribution of the $K^+\pi^-$ signal enhanced data from the full Belle data set. Data as black crosses; the total PDF as solid black line; the total background is the red dashed line which includes the contribution from charmless B decays in green. The hashed blue area is the peaking background contribution from the decay $B^0 \rightarrow \pi^+\pi^-$ 156
- 6.14 $\mathcal{L}_{K/\pi}^-$ distribution of the $K^+\pi^-$ signal enhanced data from the full Belle data set. Data as black crosses; the total PDF as solid black line; the total background is the red dashed line which includes the contribution from charmless B decays in green. The hashed blue area is the peaking background contribution from the decay $B^0 \rightarrow \pi^+\pi^-$ 156
- 6.15 $\mathcal{F}_{S/B}$ distribution of the $K^+\pi^-$ signal enhanced data from the full Belle data set. Data is shown as black crosses; the total PDF is the solid black line; the total background is the red dashed line. The hashed blue area is the peaking background contribution from the decay $B^0 \rightarrow \pi^+\pi^-$ 157
- 6.16 ΔE distribution of the K^+K^- signal enhanced data from the full Belle data set. Data is shown as black crosses; the total PDF is the solid black line; the total background is the red dashed line. The green solid line is the signal component from the $B^0 \rightarrow K^+K^-$ decay. 158
- 6.17 M_{BC} distribution of the K^+K^- signal enhanced data from the full Belle data set. Data is shown as black crosses; the total PDF is the solid black line; the total background is the red dashed line. The green solid line is the signal component from the $B^0 \rightarrow K^+K^-$ decay. 158
- 6.18 $\mathcal{L}_{K/\pi}^+$ distribution of the K^+K^- signal enhanced data from the full Belle data set. Data is shown as black crosses; the total PDF is the solid black line; the total background is the red dashed line including the background from charmless B decays displayed as green dashed line. 159
- 6.19 $\mathcal{L}_{K/\pi}^-$ distribution of the K^+K^- signal enhanced data from the full Belle data set. Data is shown as black crosses; the total PDF is the solid black line; the total background is the red dashed line including the background from charmless B decays displayed as green dashed line. 159
- 6.20 $\mathcal{F}_{S/B}$ distribution of the K^+K^- signal enhanced data from the full Belle data set. Data is shown as black crosses; the total PDF is the solid black line; the total background is the red dashed line. 160
- 6.21 Direct CP violation vs. mixing induced CP violation parameters for the decay $B^0 \rightarrow \pi^+\pi^-$ determined from this analysis, BaBar and LHCb experiments [59]. This can be compared to the results from the previous measurement in Fig. 2.10. Other experiments use a different definition of the direct CP violation parameter $\mathcal{A}_{CP} = -C_{CP}$ 168
- 6.22 Logarithm of the likelihood as a function of the branching ratio $\mathcal{B}(K^+K^-)$. The blue dotted line shows only the statistical likelihood. The solid black line shows the statistical likelihood convoluted with the systematic error modelled as a Gaussian. 169

6.23	Likelihood as a function of the branching ratio $\mathcal{B}(K^+K^-)$. The blue dotted line shows only the statistical likelihood. The solid black line shows the likelihood convoluted with the systematic error modelled as a Gaussian. The black arrow denotes the position of the 90% exclusion limit	170
6.24	The isospin triangles for the B^0 decay and the CP conjugated \bar{B}^0 decay. The contribution of the penguin diagram to the ϕ_2 measurement can be geometrically obtained by measuring $\Delta\phi_2$	171
6.25	$1 - CL$ plot of the angle ϕ_2 . The eightfold solution can clearly be seen. There is no clear preference for one of the solutions visible.	174
6.26	$1 - CL$ plot of the angle $ \Delta\phi_2 $	174
B.1	Some of the decay processes from which the flavour of the B_{tag} can be determined.	184
B.2	Flavour tagging algorithm.	186
B.3	Time-dependent $B^0\bar{B}^0$ mixing oscillation fit result to the control sample data. Each plot from the top-left to the bottom right, corresponds to the subsample in each r -bin region from 1 to 6. The amplitudes in the oscillation become larger due to less dilution from incorrect tagging.	188

List of Tables

2.1	Elementary spin-1/2 particles (fermions) in the Standard Model.	8
2.2	Integer-spin bosons in the Standard Model.	8
2.3	Theory predictions for CP averaged branching fractions	30
2.4	Theory predictions for direct CP violation	30
3.1	Number of ladders in each layer and number of DSSDs in each half-ladder of the SVD1	41
3.2	Number of ladders in each layer and number of DSSDs in each half-ladder of the SVD2	41
4.1	Definition of the r -bins regions.	64
4.2	Event multiplicity for different channels from Monte-Carlo.	67
4.3	Reconstruction efficiencies for all decay channels.	69
4.4	Correlation matrix for the $\pi^+ \pi^-$ signal Monte-Carlo.	71
4.5	Correlation matrix for the $K^+ \pi^-$ signal Monte-Carlo.	76
4.6	Correlation matrix for the $K^- \pi^+$ signal Monte-Carlo.	76
4.7	Correlation matrix for the $K^+ K^-$ signal Monte-Carlo.	82
4.8	Correlation matrix for the continuum data taken from off resonance data.	87
4.9	Borders of the k -bin which are used to take into account the correlation between $\mathcal{L}_{K/\pi}^+, \mathcal{L}_{K/\pi}^-$ and $\mathcal{F}_{S/B}$. The bin borders are located where no discrimination between pion and kaon is possible.	90
4.10	Correlation matrix for the charmless $B^+ B^-$ Monte-Carlo.	94
4.11	Correlation matrix for the charmless $B^0 \bar{B}^0$ Monte-Carlo.	100
4.12	Expected yield in every component.	108
5.1	Correction factors obtained from truth model of the $D\pi$ fit.	134
6.1	Cuts applied to data to enhance the $B^0 \rightarrow \pi^+ \pi^-$ signal.	142
6.2	Cuts applied to data to enhance the $B \rightarrow K^\pm \pi^\mp$ signal. The colour code in the cuts of the likelihood ratios means $(\mathcal{L}_{K/\pi}^+ > 0.6 \wedge \mathcal{L}_{K/\pi}^- < 0.4) \vee (\mathcal{L}_{K/\pi}^+ < 0.4 \wedge \mathcal{L}_{K/\pi}^- > 0.6)$	142
6.3	Cuts applied to data to enhance the $B^0 \rightarrow K^+ K^-$ signal.	142
6.4	Physics results from the full Belle data set of 772×10^6 $B\bar{B}$ -pairs.	143

6.5	Correlation factors obtained from a simultaneous fit of all 6 physics observables.	144
6.6	Physics results from the partial box opening of 535×10^6 $B\bar{B}$ -pairs.	144
6.7	Physics results from the last 237×10^6 $B\bar{B}$ -pairs taken at Belle. This is the data set that has not been analysed in previous analysis	145
6.8	Chances for statistical fluctuation of the $\mathcal{A}_{CP}(\pi^+\pi^-)$ value in various data sets.	145
6.9	Contributions to the total systematic uncertainty by various effects. The systematic uncertainty for branching ratios are given in percent. The systematic uncertainties for the CP parameters are given as absolute errors in units of 10^{-2}	167
6.10	Summary of absolute systematic and statistical uncertainties on the physics observables.	168
6.11	Branching ratios and CP parameters of decays associated by isospin symmetry.	171
6.12	Correlation matrix of branching ratios and CP parameters of the decay $B^0 \rightarrow \pi^+\pi^-$	172
B.1	Wrong tag fractions and wrong tag fraction differences for each r -bin.	188
C.1	R_{Det} resolution function parameters for single-track and multi-track vertices	190
C.2	R_{NP} resolution function parameters for B^0	192
C.3	R_{NP} resolution function parameters for B^+	192
C.4	P_{Out} resolution function parameters.	194

Bibliography

- [1] R. A. Alpher, H. Bethe and G. Gamow. ‘The Origin of Chemical Elements’. In: *Phys. Rev.* 73 (1948), p. 803.
- [2] G. Gamow. ‘Expanding Universe and the Origin of Elements’. In: *Phys. Rev.* 70 (1946), p. 572. DOI: 10.1103/PhysRev.70.572.2. URL: <http://link.aps.org/doi/10.1103/PhysRev.70.572.2>.
- [3] A.D. Sakharov. ‘Violation of CP invariance, C asymmetry, and baryon asymmetry of the universe’. In: *Journal of Experimental and Theoretical Physics* 5 (1967), pp. 24–27.
- [4] K. Nakamura et al. ‘Review of particle physics’. In: *J.Phys.G* G37 (2010), p. 075021. DOI: 10.1088/0954-3899/37/7A/075021. URL: <http://pdg.lbl.gov/2011/download/rpp-2010-JPhys-G-37-075021.pdf>.
- [5] O. W. Greenberg. ‘CPT Violation Implies Violation of Lorentz Invariance’. In: *Phys. Rev. Lett.* 89 (23 Nov. 2002), p. 231602. DOI: 10.1103/PhysRevLett.89.231602. URL: <http://link.aps.org/doi/10.1103/PhysRevLett.89.231602>.
- [6] T. D. Lee and C. N. Yang. ‘Question of Parity Conservation in Weak Interactions’. In: *Phys. Rev.* 104 (1 Oct. 1956), pp. 254–258. DOI: 10.1103/PhysRev.104.254. URL: <http://link.aps.org/doi/10.1103/PhysRev.104.254>.
- [7] C. S. Wu et al. ‘Experimental Test of Parity Conservation in Beta Decay’. In: *Phys. Rev.* 105 (4 Feb. 1957), pp. 1413–1415. DOI: 10.1103/PhysRev.105.1413. URL: <http://link.aps.org/doi/10.1103/PhysRev.105.1413>.
- [8] J. H. Christenson et al. ‘Evidence for the 2π Decay of the k_2^0 Meson’. In: *Phys. Rev. Lett.* 13 (1964), pp. 138–140. DOI: 10.1103/PhysRevLett.13.138.
- [9] S. L. Glashow, J. Iliopoulos and L. Maiani. ‘Weak interactions with lepton-hadron symmetry’. In: *Phys. Rev.* D2.1285 (1970).
- [10] Peter W. Higgs. ‘Broken Symmetries and the Masses of Gauge Bosons’. In: *Phys. Rev. Lett.* 13 (16 Oct. 1964), pp. 508–509. DOI: 10.1103/PhysRevLett.13.508. URL: <http://link.aps.org/doi/10.1103/PhysRevLett.13.508>.
- [11] Steven Weinberg. ‘A Model of Leptons’. In: *Phys. Rev. Lett.* 19 (21 Nov. 1967), pp. 1264–1266. DOI: 10.1103/PhysRevLett.19.1264. URL: <http://link.aps.org/doi/10.1103/PhysRevLett.19.1264>.
- [12] Makoto Kobayashi and Toshihide Maskawa. ‘CP-Violation in the Renormalizable Theory of Weak Interaction’. In: *Progress of Theoretical Physics* 49.2 (1973), pp. 652–657. DOI: 10.1143/PTP.49.652. URL: <http://ptp.ipap.jp/link?PTP/49/652/>.

- [13] Antonio Riotto. ‘Theories of baryogenesis’. In: (1998), pp. 326–436. arXiv:hep-ph/9807454 [hep-ph].
- [14] J. Charles and CKMfitter Group. In: *Eur. Phys. J. C* 41 (2005), pp. 1–131. DOI: hep-ph/0406184. URL: <http://ckmfitter.in2p3.fr>.
- [15] ATLAS Collab. *ATLAS-CONF-2012-093*. 2012.
- [16] CMS Collab. *CMS-PAS-HIG-12-020*. 2012.
- [17] F. Gianotti. *Status of Standard Model Higgs Searches in ATLAS*. presentation given at CERN. on behalf of the ATLAS Collaboration. Apr. 2012.
- [18] J. Incandela. *Status of the CMS SM Higgs Search*. presentation given at CERN. on behalf of the CMS Collaboration. Apr. 2012.
- [19] G. Aad, T. Abajyan and B. Abbott. ‘Observation of a new particle in the search for the Standard Model Higgs boson with the ATLAS detector at the LHC’. In: *Physics Letters B* 716.1 (2012), pp. 1–29. ISSN: 0370-2693. DOI: 10.1016/j.physletb.2012.08.020. URL: <http://www.sciencedirect.com/science/article/pii/S037026931200857X>.
- [20] S. Chatrchyan et al. ‘Observation of a new boson at a mass of 125 GeV with the CMS experiment at the LHC’. In: *Physics Letters B* 716.1 (2012), pp. 30–61. ISSN: 0370-2693. DOI: 10.1016/j.physletb.2012.08.021. URL: <http://www.sciencedirect.com/science/article/pii/S0370269312008581>.
- [21] Lincoln Wolfenstein. ‘Parametrization of the Kobayashi-Maskawa Matrix’. In: *Phys. Rev. Lett.* 51 (21 Nov. 1983), pp. 1945–1947. DOI: 10.1103/PhysRevLett.51.1945. URL: <http://link.aps.org/doi/10.1103/PhysRevLett.51.1945>.
- [22] Nicola Cabibbo. ‘Unitary Symmetry and Leptonic Decays’. In: *Phys. Rev. Lett.* 10 (12 June 1963), pp. 531–533. DOI: 10.1103/PhysRevLett.10.531. URL: <http://link.aps.org/doi/10.1103/PhysRevLett.10.531>.
- [23] Andrzej J. Buras, Matthias Jamin and Peter H. Weisz. ‘Leading and next-to-leading QCD corrections to ϵ -parameter and mixing in the presence of a heavy top quark’. In: *Nuclear Physics B* 347.3 (1990), pp. 491–536. ISSN: 0550-3213. DOI: 10.1016/0550-3213(90)90373-L. URL: <http://www.sciencedirect.com/science/article/pii/055032139090373L>.
- [24] F. Gilman and M. Wise. ‘ $K^0\text{-}\bar{K}^0$ mixing in the six-quark model’. In: *Physical* 27 (1983), p. 1128. URL: <http://resolver.caltech.edu/CaltechAUTHORS:GILprd83>.
- [25] John S. Hagelin. ‘Mass mixing and CP violation in the $B^0\text{-}\bar{B}^0$ system’. In: *Nuclear Physics B* 193.1 (1981), pp. 123–149. ISSN: 0550-3213. DOI: 10.1016/0550-3213(81)90521-6. URL: <http://www.sciencedirect.com/science/article/pii/0550321381905216>.
- [26] Takeo Inami and C. S. Lim. ‘Effects of Superheavy Quarks and Leptons in Low-Energy Weak Processes $K_L \rightarrow \mu\mu$, $K^+ \rightarrow \pi^+\nu\nu$ and $K^0 \leftrightarrow \bar{K}^0$ ’. In: *Progress of Theoretical Physics* 65 (1981), pp. 297–314. DOI: 10.1143/PTP.65.297. URL: <http://ptp.ipap.jp/link?PTP/65/297/>.
- [27] Christian W. Bauer et al. ‘An Effective field theory for collinear and soft gluons: Heavy to light decays’. In: *Phys.Rev.* D63 (2001), p. 114020. DOI: 10.1103/PhysRevD.63.114020. arXiv:hep-ph/0011336 [hep-ph].

- [28] Martin Beneke and Matthias Neubert. ‘QCD factorization for $B \rightarrow PP$ and $B \rightarrow PV$ decays’. In: *Nucl.Phys.* B675 (2003), pp. 333–415. DOI: 10.1016/j.nuclphysb.2003.09.026. arXiv:hep-ph/0308039 [hep-ph].
- [29] Andrzej J. Buras et al. ‘Anatomy of prominent B and K decays and signatures of CP violating new physics in the electroweak penguin sector’. In: *Nucl.Phys.* B697 (2004), pp. 133–206. DOI: 10.1016/j.nuclphysb.2004.07.009. arXiv:hep-ph/0402112 [hep-ph].
- [30] Cheng-Wei Chiang et al. ‘Charmless $B \rightarrow PP$ decays using flavor $SU(3)$ symmetry’. In: *Phys.Rev.* D70 (2004), p. 034020. DOI: 10.1103/PhysRevD.70.034020. arXiv:hep-ph/0404073 [hep-ph].
- [31] Marco Ciuchini et al. ‘Charming penguins strike back’. In: *Phys.Lett.* B515 (2001), pp. 33–41. DOI: 10.1016/S0370-2693(01)00700-6. arXiv:hep-ph/0104126 [hep-ph]. URL: <http://arxiv.org/pdf/hep-ph/0104126.pdf>.
- [32] M. Davier et al. ‘Updated estimate of the muon magnetic moment using revised results from e^+e^- annihilation’. In: *Eur.Phys.J.* C31 (2003), pp. 503–510. DOI: 10.1140/epjc/s2003-01362-6. arXiv:hep-ph/0308213 [hep-ph].
- [33] Yong-Yeon Keum. ‘Phenomenological application of $k(T)$ factorization’. In: *Pramana* 63 (2004), pp. 1151–1170. DOI: 10.1007/BF02704888. arXiv:hep-ph/0410337 [hep-ph].
- [34] Andrzej J. Buras and Robert Fleischer. ‘A General analysis of gamma determinations from $B \rightarrow \pi K$ decays’. In: *Eur.Phys.J.* C11 (1999), pp. 93–109. DOI: 10.1007/s100520050617. arXiv:hep-ph/9810260 [hep-ph].
- [35] Robert Fleischer and Thomas Mannel. ‘Constraining the CKM angle gamma and penguin contributions through combined $B \rightarrow \pi K$ branching ratios’. In: *Phys.Rev.* D57 (1998), pp. 2752–2759. DOI: 10.1103/PhysRevD.57.2752. arXiv:hep-ph/9704423 [hep-ph].
- [36] Michael Gronau, Jonathan L. Rosner and David London. ‘Weak coupling phase from decays of charged B mesons to πK and $\pi\pi$ ’. In: *Phys.Rev.Lett.* 73 (1994), pp. 21–24. DOI: 10.1103/PhysRevLett.73.21. arXiv:hep-ph/9404282 [hep-ph].
- [37] Matthias Neubert and Jonathan L. Rosner. ‘New bound on gamma from $B^\pm \rightarrow \pi K$ decays’. In: *Phys.Lett.* B441 (1998), pp. 403–409. DOI: 10.1016/S0370-2693(98)01194-0. arXiv:hep-ph/9808493 [hep-ph].
- [38] S. W. Lin et al. ‘Difference in direct charge-parity violation between charged and neutral B meson decays’. In: *Nature* 452 (2008), pp. 332–335. DOI: 10.1038/nature06827.
- [39] H. Ishino et al. ‘Observation of Direct CP-Violation in $B^0 \rightarrow \pi^+\pi^-$ Decays and Model-Independent Constraints on ϕ_2 ’. In: *Phys. Rev. Lett.* 98 (2007), p. 211801. DOI: 10.1103/PhysRevLett.98.211801. arXiv:hep-ex/0608035.
- [40] Andrzej J. Buras et al. ‘ $B \rightarrow \pi\pi$, new physics in $B \rightarrow \pi K$ and implications for rare K and B decays’. In: *Phys.Rev.Lett.* 92 (2004), p. 101804. DOI: 10.1103/PhysRevLett.92.101804. arXiv:hep-ph/0312259 [hep-ph].
- [41] Michael Gronau and David London. ‘Isospin analysis of CP asymmetries in B decays’. In: *Phys. Rev. Lett.* 65 (27 Dec. 1990), pp. 3381–3384. DOI: 10.1103/PhysRevLett.65.3381. URL: <http://link.aps.org/doi/10.1103/PhysRevLett.65.3381>.

- [42] Yuuji Unno. ‘Experimental status and prospects of the ‘Kpi puzzle’’. In: (2011). arXiv:1101.0675 [hep-ex].
- [43] Christian W. Bauer, Ira Z. Rothstein and Iain W. Stewart. ‘SCET analysis of $B \rightarrow K\pi$, $B \rightarrow K\bar{K}$ and $B \rightarrow \pi\pi$ decays’. In: *Phys.Rev.* D74 (2006), p. 034010. DOI: 10.1103/PhysRevD.74.034010. arXiv:hep-ph/0510241 [hep-ph].
- [44] Michael Gronau. ‘A Precise sum rule among four $B \rightarrow K\pi$ CP asymmetries’. In: *Phys.Lett.* B627 (2005), pp. 82–88. DOI: 10.1016/j.physletb.2005.09.014. arXiv:hep-ph/0508047 [hep-ph].
- [45] Michael Gronau and Jonathan L. Rosner. ‘Combining CP asymmetries in $B \rightarrow K\pi$ decays’. In: *Phys.Rev.* D59 (1999), p. 113002. DOI: 10.1103/PhysRevD.59.113002. arXiv:hep-ph/9809384 [hep-ph].
- [46] Harry J. Lipkin. ‘A Useful approximate isospin equality for charmless strange B decays’. In: *Phys.Lett.* B445 (1999), pp. 403–406. DOI: 10.1016/S0370-2693(98)01471-3. arXiv:hep-ph/9810351 [hep-ph].
- [47] Y.Y. Keum and A.I. Sanda. ‘Possible large direct CP violations in charmless B decays: Summary report on the pQCD method’. In: *Phys.Rev.* D67 (2003), p. 054009. DOI: 10.1103/PhysRevD.67.054009. arXiv:hep-ph/0209014 [hep-ph].
- [48] Wei-Shu Hou, Makiko Nagashima and Andrea Soddu. ‘Difference in B^+ and B^0 direct CP asymmetry as effect of a fourth generation’. In: *Phys.Rev.Lett.* 95 (2005), p. 141601. DOI: 10.1103/PhysRevLett.95.141601. arXiv:hep-ph/0503072 [hep-ph].
- [49] Seungwon Baek et al. ‘The $B \rightarrow \pi K$ puzzle and new physics’. In: *Phys.Rev.* D71 (2005), p. 057502. DOI: 10.1103/PhysRevD.71.057502. arXiv:hep-ph/0412086 [hep-ph].
- [50] Sébastien Descotes-Genon, Joaquim Matias and Javier Virto. ‘Exploring $B_{d,s} \rightarrow KK$ Decays through Flavor Symmetries and QCD Factorization’. In: *Phys. Rev. Lett.* 97 (6 Aug. 2006), p. 061801. DOI: 10.1103/PhysRevLett.97.061801. URL: <http://link.aps.org/doi/10.1103/PhysRevLett.97.061801>.
- [51] Cai-Dian Lu, Yue-Long Shen and Wei Wang. ‘Final state interaction in $B \rightarrow KK$ decays’. In: *Phys.Rev.* D73 (2006), p. 034005. DOI: 10.1103/PhysRevD.73.034005. arXiv:hep-ph/0511255 [hep-ph].
- [52] K. Abe et al. ‘Measurements of branching fractions for $B^0 \rightarrow K^+\pi^-$ and $B^0 \rightarrow \pi^+\pi^-$ decays with 449 million B anti-B pairs’. In: *Phys. Rev. Lett.* 99 (2007), p. 121601. DOI: 10.1103/PhysRevLett.99.121601. arXiv:hep-ex/0609015.
- [53] K. Abe et al. ‘Observation of B decays to two kaons’. In: *Phys.Rev.Lett.* 98 (2007), p. 181804. DOI: 10.1103/PhysRevLett.98.181804. arXiv:hep-ex/0608049 [hep-ex].
- [54] Bernard Aubert et al. ‘Improved Measurements of the Branching Fractions for $B^0 \rightarrow \pi^+\pi^-$ and $B^0 \rightarrow K^+\pi^-$, and a Search for $B^0 \rightarrow K^+K^-$ ’. In: *Phys.Rev.* D75 (2007), p. 012008. DOI: 10.1103/PhysRevD.75.012008. arXiv:hep-ex/0608003 [hep-ex].
- [55] Bernard Aubert et al. ‘Observation of CP violation in $B^0 \rightarrow K^+\pi^-$ and $B^0 \rightarrow \pi^+\pi^-$ ’. In: *Phys. Rev. Lett.* 99 (2007), p. 021603. DOI: 10.1103/PhysRevLett.99.021603. arXiv:hep-ex/0703016.

- [56] T. Aaltonen et al. ‘Measurements of Direct CP Violating Asymmetries in Charmless Decays of Strange Bottom Mesons and Bottom Baryons’. In: *Phys.Rev.Lett.* 106 (2011), p. 181802. DOI: 10.1103/PhysRevLett.106.181802. arXiv:1103.5762 [hep-ex].
- [57] T. Aaltonen et al. ‘Evidence for the charmless annihilation decay mode $B_s^0 \rightarrow \pi^+\pi^-$ ’. In: *Phys.Rev.Lett.* 108 (2012), p. 211803. DOI: 10.1103/PhysRevLett.108.211803. arXiv:1111.0485 [hep-ex].
- [58] R Aaij et al. ‘Measurement of b -hadron branching fractions for two-body decays into charmless charged hadrons’. In: *JHEP* 1210 (2012), p. 037. DOI: 10.1007/JHEP10(2012)037. arXiv:1206.2794 [hep-ex].
- [59] Heavy Flavor Averaging Group et al. *Averages of b -hadron, c -hadron, and tau-lepton properties as of early 2012*. 2012. eprint: arXiv/1207.1158.
- [60] CDF collaboration. *CP Violating Asymmetries in Charmless Decays of Strange Bottom Mesons and Bottom Baryons with $9.3fb^{-1}$* . Tech. rep. 10726. CDF, June 2012.
- [61] LHCb collaboration. *Measurement of time-dependent CP violation in charmless two-body B decays*. Tech. rep. Linked to LHCb-ANA-2012-020. CERN, Feb. 2012.
- [62] R. Aaij et al. ‘First evidence of direct CP violation in charmless two-body decays of B_s mesons’. In: *Phys.Rev.Lett.* 108 (2012), p. 201601. DOI: 10.1103/PhysRevLett.108.201601. arXiv:1202.6251 [hep-ex].
- [63] A. Abashian et al. ‘The Belle detector’. In: *Nuclear Instruments and Methods in Physics Research Section A: Accelerators, Spectrometers, Detectors and Associated Equipment* 479.1 (2002). <ce:title>Detectors for Asymmetric B-factories</ce:title>, pp. 117 –232. ISSN: 0168-9002. DOI: 10.1016/S0168-9002(01)02013-7. URL: <http://www.sciencedirect.com/science/article/pii/S0168900201020137>.
- [64] Nobumasa Akasaka et al. ‘KEKB accelerator control system’. In: *Nuclear Instruments and Methods in Physics Research Section A: Accelerators, Spectrometers, Detectors and Associated Equipment* 499.1 (2003). <ce:title>KEK-B: The KEK B-factory</ce:title>, pp. 138 –166. ISSN: 0168-9002. DOI: 10.1016/S0168-9002(02)01786-2. URL: <http://www.sciencedirect.com/science/article/pii/S0168900202017862>.
- [65] B. Aubert et al. ‘The BABAR detector’. In: *Nuclear Instruments and Methods in Physics Research Section A: Accelerators, Spectrometers, Detectors and Associated Equipment* 479.1 (2002). <ce:title>Detectors for Asymmetric B-factories</ce:title>, pp. 1 –116. ISSN: 0168-9002. DOI: 10.1016/S0168-9002(01)02012-5. URL: <http://www.sciencedirect.com/science/article/pii/S0168900201020125>.
- [66] R. Brun et al. *GEANT 3.21*. Tech. rep. DD/EE/84-1. CERN, 1984.
- [67] Geoffrey Taylor. ‘The Belle silicon vertex detector: present performance and upgrade plans’. In: *Nuclear Instruments and Methods in Physics Research Section A: Accelerators, Spectrometers, Detectors and Associated Equipment* 501.1 (2003). <ce:title>Proceedings of the 10th International Workshop on Vertex Detectors</ce:title>, pp. 22 –31. ISSN: 0168-9002. DOI: 10.1016/S0168-9002(02)02006-5. URL: <http://www.sciencedirect.com/science/article/pii/S0168900202020065>.

- [68] H. Tajima et al. ‘Proper-time resolution function for measurement of time evolution of B mesons at the KEK B-Factory’. In: *Nuclear Instruments and Methods in Physics Research Section A: Accelerators, Spectrometers, Detectors and Associated Equipment* 533.3 (2004), pp. 370–386. ISSN: 0168-9002. DOI: 10.1016/j.nima.2004.07.199. URL: <http://www.sciencedirect.com/science/article/pii/S0168900204017401>.
- [69] H. Kakuno et al. ‘Neutral flavor tagging for the measurement of mixing-induced violation at Belle’. In: *Nuclear Instruments and Methods in Physics Research Section A: Accelerators, Spectrometers, Detectors and Associated Equipment* 533.3 (2004), pp. 516–531. ISSN: 0168-9002. DOI: 10.1016/j.nima.2004.06.159. URL: <http://www.sciencedirect.com/science/article/pii/S0168900204014482>.
- [70] R. A. Fisher. ‘THE USE OF MULTIPLE MEASUREMENTS IN TAXONOMIC PROBLEMS’. In: *Annals of Eugenics* 7.2 (1936), pp. 179–188. ISSN: 2050-1439. DOI: 10.1111/j.1469-1809.1936.tb02137.x. URL: <http://dx.doi.org/10.1111/j.1469-1809.1936.tb02137.x>.
- [71] Giovanni Punzi. ‘Comments on Likelihood fits with variable resolution’. In: *PHYSTAT2003*. Sept. 2003. URL: <http://arxiv.org/abs/physics/0401045v1>.
- [72] H. Albrecht et al. ‘SEARCH FOR HADRONIC $b \rightarrow u$ DECAYS’. In: *Phys.Lett.* B241 (1990), pp. 278–282. DOI: 10.1016/0370-2693(90)91293-K.
- [73] Y. -T. Duh et al. ‘Measurements of Branching Fractions and Direct CP Asymmetries for $B \rightarrow K\pi$, $B \rightarrow \pi\pi$ and $B \rightarrow KK$ Decays’. In: (2012). arXiv:1210.1348 [hep-ex].
- [74] Brendan Casey. *HadronB*. Belle-note 390. Belle, 2001.
- [75] Owen Long et al. ‘Impact of tag-side interference on time-dependent CP asymmetry measurements using coherent B^0B^0 pairs’. In: *Phys. Rev.* D68.034010 (2003). DOI: 10.1103/PhysRevD.68.034010.
- [76] Y. Chao et al. ‘Observation of $B^0 \rightarrow \pi^0\pi^0$ ’. In: *Phys. Rev. Lett.* 94 (18 May 2005), p. 181803. DOI: 10.1103/PhysRevLett.94.181803. URL: <http://link.aps.org/doi/10.1103/PhysRevLett.94.181803>.
- [77] Yeo-Yie Charng and Hsiang-nan Li. ‘Weak phases from the $B \rightarrow \pi\pi$, $K\pi$ decays’. In: *Phys.Rev.* D71 (2005), p. 014036. DOI: 10.1103/PhysRevD.71.014036. arXiv:hep-ph/0410005 [hep-ph].
- [78] Seungwon Baek and David London. ‘Is There Still a $B \rightarrow \pi K$ Puzzle?’ In: *Phys.Lett.* B653 (2007), pp. 249–253. DOI: 10.1016/j.physletb.2007.08.001. arXiv:hep-ph/0701181 [hep-ph].
- [79] Wei-Shu Hou et al. ‘Fourth generation CP violation effect on $B \rightarrow K\pi$, ϕK and ρK in NLO PQCD’. In: *Phys.Rev.Lett.* 98 (2007), p. 131801. DOI: 10.1103/PhysRevLett.98.131801. arXiv:hep-ph/0611107 [hep-ph].
- [80] Maxime Imbeault, Seungwon Baek and David London. ‘The $B \rightarrow \pi K$ Puzzle and Supersymmetry’. In: *Phys.Lett.* B663 (2008), pp. 410–415. DOI: 10.1016/j.physletb.2008.04.039. arXiv:0802.1175 [hep-ph].
- [81] S. Khalil, A. Masiero and H. Murayama. ‘ $B \rightarrow K\pi$ Puzzle and New Sources of CP Violation in Supersymmetry’. In: *Phys.Lett.* B682 (2009), pp. 74–77. DOI: 10.1016/j.physletb.2009.10.034. arXiv:0908.3216 [hep-ph].

-
- [82] Damir Becirevic and Andrey Tayduganov. ‘Impact of $B \rightarrow K_0^* \ell^+ \ell^-$ on the New Physics search in $B \rightarrow K^* \ell^+ \ell^-$ decay’. In: (2012). arXiv:1207.4004 [hep-ph].
- [83] M. Fujikawa et al. ‘Measurement of CP asymmetries in $B \rightarrow K^0 \pi^0$ decays’. In: *Phys.Rev.* D81 (2010), p. 011101. DOI: 10.1103/PhysRevD.81.011101. arXiv:0809.4366 [hep-ex].
- [84] Marta Calvi, Marco Musy and Oliver Leroy. ‘Flavour tagging algorithms and performances in LHCb’. In: (2007).
- [85] T. Abe. ‘Belle II Technical Design Report’. In: (2010). arXiv:1011.0352 [physics.ins-det].
- [86] Miyuki Fujikawa. ‘Measurement of Branching fraction and Time-dependent CP Asymmetry Parameters in $B^0 \rightarrow K^0 \pi^0$ Decays’. PhD thesis. School of Interdisciplinary Research of Scientific Phenomena, Information Graduate School of Humanities and Sciences Nara Women’s University, Jan. 2009. URL: <http://www.hepl.phys.nara-wu.ac.jp/thesis/doctor/miyuki/fujikawa-doctor-thesis2009.pdf>.

Acknowledgements

Three persons contributed mainly to the success of this thesis. I would like to thank my supervisor Ph.D. Jeremy Dalseno for his guidance and excellent ideas. Without his deep knowledge about analysis techniques such a thesis could not have been finished. Second I want to thank Prof. Dr. Kiesling for his belief in my capabilities which actually gave me the opportunity start my thesis at the Max-Planck-Institute. The discussions with him about various topics helped me to reach a deeper understanding of physics and always encouraged me. Last but not least I want to thank Dr. Frank Simon for his advice. Whenever I had questions he immediately took the time to answer them.

In the last years I have worked together with many people. The great majority was very helpful and I hope that I could always pay back. From the many I want to pick a few in the name of all those that I could not name here. Andreas Moll who accompanied me since the very beginning of my time at the Max-Planck-Institute and Zbynek Drasal from Charles University Prague. In a good team with both we perform the optimisation studies for the Belle II vertex detector. Martin Ritter for encouraging me to try new approaches also in computing and always cheering me up. Jeremy Dalseno for teaching me how to drive on the wrong side of the road in Japan. Stanislav Shushkevich for the nice discussions on quantum mechanics and gardening. And of course the whole Belle/Belle II and ILC group at the MPI.

I want to thank all participants of the Tea-times for the sometimes serious, sometimes funny and sometimes weird discussions of all kinds of topics during the breaks. I believe this to be the origin of the extremely good working atmosphere in our group.

Claudia thank you for all the love, care and encouragement.

And of course big thanks go to my parents for supporting me during my whole life especially in science.

Thank you